Energy Storage For Frequency Support In Weak Electrical Grids

Prasanthi Charmalee Jayamaha, M.Sc.

Thesis submitted to the University of Nottingham

for the degree of Doctor of Philosophy

March 2015

Abstract

INTEGRATING local renewable resources into the low voltage distribution system can create weak micro-grids with limited power capabilities and challenging control requirements. The low inertia in these micro-grids can result in significant frequency excursions when large load or generation changes are seen. Micro-grids may also be more susceptible to high harmonic distortion in their voltage due to non-negligible supply impedance. This calls for advance control techniques to regulate frequency and maintain voltage at the standards required of the utility grid. Failure to do so may incur disconnection of the weak grid from the main supply leading to cascading power disruptions to the consumers. This thesis explores one approach to improving the frequency control in weak grids in the presence of poor voltage quality by exploiting energy storage to independently and optimally dispatch active power to constrain frequency fluctuations within acceptable limits.

Power system frequency - a direct indication of generation-demand imbalance -is selected as the main control signal in the energy storage control system. The energy storage injects active power when the frequency falls below the lower threshold and absorbs active power when the frequency rises above the upper threshold. Imposing thresholds close to but not equal to the nominal frequency allows a sufficient speed error for the conventional speed governor of the prime movers of the power system to operate unhindered and acquire the full control of the load at the equilibrium. Frequency control by the energy storage support combined with the continuous speed governing acts to restrict the frequency excursions within the thresholds well within the primary frequency time requirements.

The power system frequency is detected directly from the measured supply voltage in order to eliminate the need for any communication between system elements and make the energy storage device plug-and-play. This has meant the investigation of a suitable frequency tracker which can respond quickly, and at the same time operate correctly in the presence of high supply voltage distortion. Frequency detection introduces a transient delay and a steady state ripple to the estimated frequency. Hence, a set of frequency detection requirements are defined that must be satisfied by any candidate frequency detection

method. In identifying the best technique(s), this thesis presents a comparative analysis of candidate frequency detection methods when applied specifically in a weak grid. The analysis revealed that the Double Second Order Generalised Integrator Frequency Locked Loop (DSOGI-FLL) displays optimum transient and steady state characteristics for the energy storage control application requirements, closely followed by a Discrete Fourier Transformation (DFT) technique generalised in the study.

The proposed frequency trackers and energy storage control techniques were validated experimentally and tuning of the key parameters to match user requirements was presented for both single and multiple energy storage systems.

Acknowledgements

I would like to acknowledge everyone, whose support, guidance and encouragement contributed to this thesis. In particular, there are some without whom this thesis would not have been possible:

My supervisor, Professor Mark Sumner has mentored me from the early stages of problem formulation to careful presentation of the concepts in this thesis. He has kept me in the right path, guiding me to discover the solutions to the problems encountered during the study. I am indebted to his excellent supervision and for the personal and moral support over the last four years.

My co-supervisors Professor Mark Johnson and Dr. Arthur Williams have been very helpful in our intellectual discussions and providing invaluable suggestions to improve my work. I would also like to thank Dr. Alessandro Costabeber for his valuable ideas, comments and friendship, during our brief period of interaction.

My fellows, Dr. Alex Agbedahunsi, Dr. Seksak Pholboon, Dr. Sung Oe, Chris Rose, Richard Davies, Petros Kounnos and Marco Hoyos of the FlexElec Laboratory have been immensely helpful at various stages of my research, generously sharing their hard earned knowledge with me. I would also like to give special thanks to Wasseem Mohammed and Colin Blackburn for their support during the experimental work. All members of the PEMC group whose presence has created an enjoyable working atmosphere deserve my sincere thanks too.

My best friends have always been there to encourage me, pull me through hard times and to make life lots of fun. My parents-in-law always believed in me and wished me well in all my undertakings. Hayley Luff has given me immense peace of mind to continue with my PhD as a new mom, with her first-class childcare.

My husband, who has been through his round in a doctoral thesis, has been my rock, not only in completing my PhD journey, but throughout my life since the day we met. His confidence in me and the patience have been incomparable and invaluable. To put it short, his endless love makes ***Impossible is Nothing***.

My son Binal, has been growing up during my PhD, and as a result his vocabulary is already rich with technical and philosophical terms. He was more checking on mommy about thesis writing and Matlab simulations than demanding time for him. It is Binal's unending love and laughter that made ***Everything Possible***.

My parents instilled in me a love of learning and encouraged my curiosity to explore. They planted the seeds of nearly everything I know today at a very young age. There was never anything I needed that they ever failed to provide. Their eternal love and dedication made the person I am today. Thank you for raising me to believe that ***Nothing is Impossible***.

Thank you from the bottom of my heart.

*

To My Dearest Parents
Chandrani & Jayatilaka Jayamaha.

Contents

List of Symbols

D Damping Factor in s.

Δf Frequency error in Hz.

f Power frequency in Hz.

f_{nom} Nominal frequency in Hz.

f_o Fundamental frequency in Hz.

f_s Sampling frequency in Hz.

f_{sH} Transfer function of the heavy filter.

f_{sL} Transfer function of the faster filter.

f_{TH} Frequency Threshold (Hz).

Γ Gain of FLL.

G_{CL} Closed Loop Transfer function.

G_{en} Transfer function of the engine.

G_{mech} Transfer function of the generator.

$G_{\omega PI}$ Transfer function of the PI speed governor.

H Inertia constant in s.

I Current in A.

I_d d-axis current in A.

$K_{d(PID)}$ Derivative gain of the PID controller.

K_{ES} Proportional gain of the energy storage controller.

K_i Integral gain of the PI speed governor.

$K_{i(PID)}$ Integral gain of the PID controller.

K_p Proportional gain of the PI speed governor.

$K_{p(PID)}$ Proportional gain of the PID controller.

$\tau_{R/L}$ Time constant of the RL circuit s.

L_s Source Inductance in H.

ω_n Natural Frequency.

P_d Power disturbance in W.

$V_{\alpha\beta}$ Voltage in $\alpha - \beta$ axis in V.

R_L Load resistance in Ω.

R_s Source resistance in Ω.

T_d Frequency detection delay in s.

T_{EN} Engine torque in Nm.

T_e Electrical torque in Nm.

T_{en} Engine time constant in s.

T_{ES} Energy Storage Torque Nm.

θ Angle of rotation in rad.

B Friction constant.

T_L Load torque in Nm.

T_m Mechanical torque in Nm.

t_{SOGI} time constant of SOGI s.

v_{abc} 3 phase voltage V.

v_α voltage of the α-axis V.

v_β voltage of the β-axis V.

T_v Vector control delay in s.

V_d d-axis voltage in V.

V_{pk} Peak voltage in V.

V_{ref} Reference voltage in V.

ω Angular frequency in rad/s.

T Window length in s.

ζ Damping factor.

Acronyms

AGC Automatic Generation Control.

AVR Automatic Voltage Regulation.

BESS Battery Energy Storage System.

DDSRF-PLL Double Decoupled Synchronous Reference Frame Phase Locked Loop.

DER Distributed Energy Resources.

DFT Discrete Fourier Transform.

DGR Distributed Generation Resources.

DNO Distributed Network Operator.

DSOGI-FLL Double Second Order Generalised Integrator Frequency Locked Loop.

EPLL Enhanced Phase Locked Loop.

ES Energy Storage.

FFT Fast Fourier Transform.

FLL Frequency Locked Loop.

IM Induction Motor.

LAM Load Acceptance Module.

LSE Least Square Estimation.

PCC Point of Common Coupling.

PFC Primary Frequency control.

PFR Primary Frequency Response.

PI Proportional Integral.

PID Proportional Integral Derivative.

PLL Phase Locked Loop.

QPLL Quadrature Phase Locked Loop.

QSG Quadrature Signal Generator.

ROCOF Rate of change of Frequency.

RTT Real Time Target.

SFC Secondary Frequency Control.

SFR System Frequency Response.

SMES Superconducting Magnetic Energy Storage.

SOC State of Charge.

SOGI Second Order Generalised Integrator.

SRF-PLL Synchronous Reference Frame-Phase Locked Loop.

STATCOM Static Compensator.

THD Total Harmonic Distortion.

VCO Voltage Controlled Oscillator.

List of Figures

List of Tables

CHAPTER 1

Introduction

Electricity is one of the fundamental necessities in the modern world. Not only does it power a large fraction of our everyday tasks but also keeps all sophisticated processes of the world active and alive.

Essentially, the market for electrical power is ever growing. Conventionally one centralised utility was responsible for managing the power generation, the distribution and the transmission to meet the growing demands. During the past few decades, this has mostly been associated with bulk generation of power by combustion of fossil fuels followed by radial transmission and distribution. On one hand, due to scarcity of fossil fuels, the generation is becoming increasingly uneconomical, while on the other hand, it is environmentally unappealing due to high carbon dioxide emissions amidst the growing concerns on global warming.

Most countries are pro-actively increasing the participation of renewable energy in power generation to diminish the harsh impacts of conventional power generation. While renewable sources such as hydro-power and geothermal are capable of producing large power outputs in large power stations, most renewable sources such as photovoltaic are more suited for relatively smaller sized power plants, either in isolation or as energy farms. Therefore, increasing amounts of renewable energy generators will be connected at the lower voltage distribution level in order to reap the maximum benefits, conveniently and efficiently. The technical term distributed generation refers to this scenario as a whole. The electric power is generated close to the consumers, harnessing locally available energy resources, this also fits well with the intermittent nature of renewable energy sources, where the main supply-grid can supplement any deficit.

This concept was modified and identified as a micro-gird, which essentially is a power supply network designed to supply power to a small community. A micro-grid may work independently of the main supply grid or connected to the grid. But in either case, as an individual power entity, it is required to maintain good technical and regulatory practices, such that it does not hinder either the consumers or the functioning of the main utility. This calls for various smart control and optimisation techniques specific to low voltage weak-grids/micro-grids, to achieve 'good citizen' standards in a large power grid.

1.1 Motivation

The sustained operation of any power system depends on the balance between the generation and the load. The power system frequency is a direct indicator of the power balance of the electrical grid. In the event of loading, the kinetic energy stored in the rotating generator is the immediate energy that supplies the load change. Therefore, a drop in speed is inevitable during load disturbances as kinetic energy is spent in supplying the demand. In centralised power distribution systems, the inertia of many large generators combine to provide a large 'system' inertia which keeps frequency excursions small. In a weak grid, or in a micro-grid with high renewable energy factor, this is further exacerbated by the typical low inertia, making the power system more frequency sensitive. The conventional governor action of synchronous generators to provide frequency regulation may be inadequate and extremely slow, such that the weak-grid/micro-grid is not able to maintain the statutory operational regulations of the utility. The result of this can be complete disconnection from the utility that may lead to cascading blackouts in the main grid.

The solution to this problem may lay in energy storage technologies. The role of energy storage in micro-grids is constantly growing. In fact, energy storage has improved the penetration of renewable energy in micro-grids not only by providing back-up energy reserves to counteract the intermittent supply, but also by facilitating ancillary services such as frequency regulation. This has further become viable as various energy storage technologies are now technically matured and financially favourable. For example, battery energy storage technologies such as Li-ion can be competitive against the conventional storage technologies such as flywheels and pumped storage in terms of economic aspects [11, 12].

Energy storage technologies exhibit many useful characteristics to alleviate the frequency sensitivity of weak grids. The ability to supply active power over relatively short periods is required to achieve frequency regulation. However, supplying the active power throughout the load transient to balance the frequency will hinder the generator's own speed regulation, in addition, a large energy storage unit with high power and energy density will be required to sustain the load until the generator can provide the active power on its own. On the other hand, if the energy storage is set to follow the traditional regulation signal defined by the system operator, the energy delivery function will be coupled to the grid it is connected to. In addition, there will not be enough provision for autonomous activation and deactivation of the energy storage supply for its optimal utilisation.

A solution to this problem is to use an energy storage, while allowing traditional governor generation to provide frequency support in weak grids/microgrids. In this way, Energy storage acts during the faster transient of the frequency fluctuations, while the traditional speed governing of the synchronous generator follows the general trend of the load. In this way, the frequency of the system is maintained within tight margins, while the speed governor has the full control to bring the power system back to the equilibrium (50 Hz). This may be achieved by using the power frequency of the grid as the main control input of the energy storage. If the energy storage is set to recover the frequency to a reasonable threshold frequency not equal to the equilibrium, the speed error between the threshold and the nominal can keep the speed governor working at the same time. If the power frequency is to be detected using the voltage of the power system, the control of the energy storage can be decoupled from the grid it is connected to. The frequency threshold can also be used for automatic activation and deactivation of the energy storage, making sure that the active power is optimally supplied.

1.2 Grid Frequency Regulation

Frequency regulation in the utility grid is one of the main responsibilities of the National Grid for the effective operation of the utility [13]. When a step change in load occurs, the generator inertia immediately works to restore the balance between the load demand and the generation. This is known as the inertial response. During the inertial response, the kinetic energy stored in the rotating

part of the generator is released to balance the required electrical power slowing down the generator. This change in frequency primarily depends upon the size of load change, the power system inertia and the power rating of the generator. This initial frequency droop is commonly referred to as the rate of change of frequency (ROCOF). The higher the inertia, the lower the experienced ROCOF. Consequently, the generator's speed governor brings the system to a new equilibrium known as the new power set-point. This process is known as the Primary Frequency Control (PFC). The inertial response is important to prevent the frequency from falling. An illustration of how the main utility achieves frequency regulation after a major disruption is shown in Fig.1.1. The figure shows the values declared in the grid-code for Great Britain.

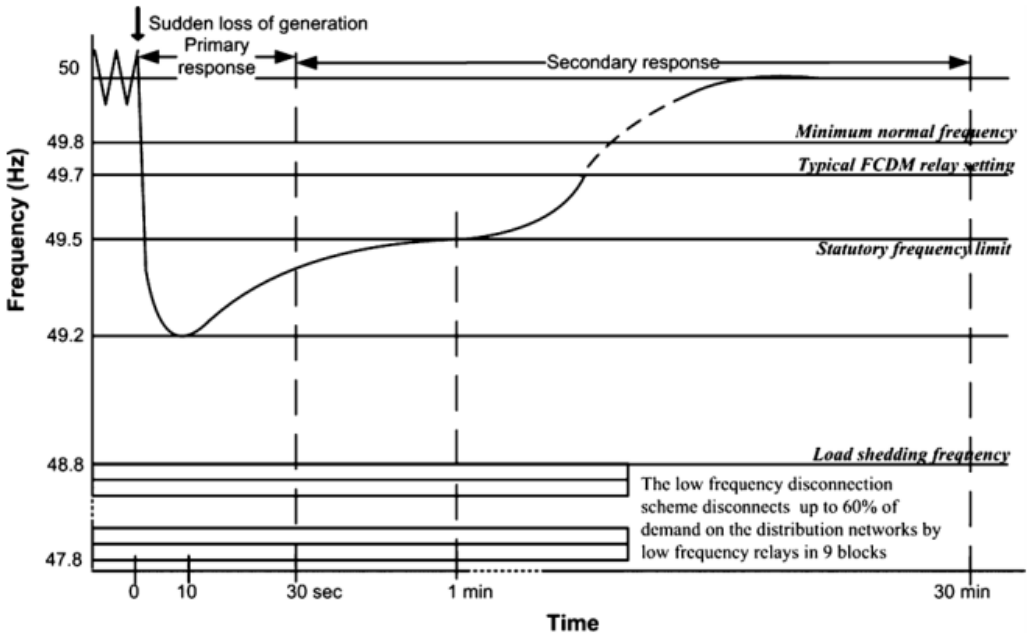

Figure 1.1: The frequency response requirements of the main utility grid of the Great Britain [1]

After an occurrence of a loss of generation, which is indicated by a change in frequency under the resistance of inertia, all Transmission System Operators (TSO) abide by the grid-code to provide primary frequency support for a period of 30 seconds. Once the PFC starts bringing up the frequency, the new power set-point will increase the power generation in order to raise the frequency to the nominal equilibrium (50 Hz). A half hour is allowed for the system operators to perform this task called the Secondary Frequency Response (SFC). The SFC is undertaken by the Automatic Generation Control (AGC) of

the power system. Usually, PFC has a droop controlling mechanism that raises the frequency to a level less than the nominal. Also, the SFC finally corrects any remaining steady state errors in frequency by manual dispatch of further generation, hence generally slower than the PFC [1]. As illustrated in the figure, if the disturbance causes the frequency to fall below 48.8 Hz, load shedding is activated to prevent further worsening of frequency.

Essentially, in a stiff grid, TSO have readily available operating reserves a.k.a. contingency reserves, to counteract large disruptions of generation/load. In fact typical loading events of the power system are entirely resolved within the primary frequency level, by small increases and decreases of power output of participating generators [14]. A major frequency fall in a stiff grid is more likely with a loss of generation of a large power plant than with a heavy loading[15].

However, in their weak counterparts such as micro-grids with high renewable energy participation, the practical frequency regulation may essentially be different to that in the main utility. One reason for this is, lack of availability of controlled power sources/reserves that can provide inertial responses in addition to that of synchronous generator(s). Most renewable power sources such as solar power and wind power are not adequately capable of contributing towards inertia. The resultant is a micro-grid that lacks sufficient inertial properties compared to its power demand profile. Therefore, a typical load perturbation in a micro-grid can cause large frequency fluctuations due to the low inertia [16]. Hence, situations similar to a loss of generation in a strong grid are faced by a weak grid every time a comparable load change occurs. This calls for special consideration in frequency regulation in weak-grids/micro-grids. In that case, the techniques described in this thesis using energy storage would apply to provide additional support for frequency in micro-grids.

1.3 Thesis Objectives and Contributions

The main aim of this thesis is to develop a novel control technique to optimally supply active power from energy storage to support frequency in weak electrical grids, in addition to the traditional speed governing. The control technique uses state-of-the-art power system frequency detection to employ real time power system frequency as the main control input; hence, facilitating independent operation and automation of the energy storage from the host micro-grid. In achieving this, the following objectives are being addressed in

this thesis.

The first objective is to deliver a control algorithm to maintain continuous operation of the traditional speed governing unhindered, while supporting the frequency with energy storage. It also addresses how power frequency, which is a direct indication of the load-generation imbalance, can be effectively exploited in delivering a decoupled control of the energy storage.

In order to do so, a dedicated frequency detection technique was needed to be identified that is both suitable and optimised for the energy storage control application devised above. Hence, the second objective is to define frequency detection requirements of the application and compare candidate frequency detection techniques for the optimum performance of the energy storage control when applied specifically to weak grid conditions.

In developing the proposed energy storage control technique, a niche was found in the literature for a complete weak-grid simulation model. Therefore, the third objective is to develop such a model based on an experimental weak grid facility. The model contributes as the major simulation platform to perform all developmental and analytical tasks presented in this thesis.

The work is further complemented with an experimental validation to confirm the presented techniques as the fourth objective of the work.

In order to use the energy storage practically, one would want to find out the optimal capacity of the energy storage, tuning parameters of the control strategy, the level of decoupling of the energy storage, etc. These questions will be answered in this work, as the fifth objective of devising "general design rules" of the energy storage control application for frequency support.

1.4 Thesis Outline

The content of this thesis is organized as follows. This introductory chapter is followed by a survey of current literature in Chapter 2, on techniques used for frequency support. It also briefly discusses available weak-grid simulation models and frequency detection techniques. Chapter 3 then introduces a complete simulation model of a weak electrical grid representing the practical operations of a prototype experimental weak-grid. Chapter 4 then describes the design and the development of the proposed energy storage control technique. The characteristics of the control strategy is described in the same chapter. In

addition, requirements for a frequency detection technique for effective operation of the system, is also laid out in this chapter. Chapter 5 presents a comparative analysis on candidate frequency detection techniques that were identified as suitable methods to extract frequency information from the 3-phase voltage of a weak-grid. Chapter 6 presents the experimental validation of the proposed energy storage control and demonstrates its effectiveness in frequency support. Chapter 7 explores the possibility of applying the proposed control technique to multiple energy storage. Chapter 8 concludes the thesis by suggesting extensions of the current work that needs further investigation in the future.

As a whole, this work demonstrates a novel technique to support frequency in weak electrical grids, discovers how independent control of energy storage using detected frequency can be achieved, and validates the benefits of the technique experimentally.

CHAPTER 2

Literature Review

Energy storage systems are increasingly considered as an important integral part of the electric power systems due to the broad spectrum of benefits they can bring in to the utility, the end-users and to the society as a whole. The primary benefit of energy storage to the electric supply is to store energy when its price/value is low, so that the stored energy can be utilised when the price/value is high. The contribution of energy storage as an enabling technology for integrating intermittent RES at the distribution level has been significant in the recent times. In this case, energy storage are beneficial to counteract the variable nature of the RE power generation both short and long term. Also, the usability of energy storage has been extended to provide ancillary services such as voltage and frequency regulation, to reduce the risk of blackouts and to improve power quality. In fact using energy storage for ancillary services can offer faster responsive regulation with less wear and tear compared to using conventional generation for the same. In addition, it can bring environmental and economic advantages to the electric grid if utilised properly [17, 18].

2.1 Energy Storage Technologies

The suitability of an energy storage technology for a given application depends mainly on the following characteristics [17].

- Energy density - Measure of the amount of energy that the storage system can provide
- Power density - Measure of the rate at which energy can be provided as well as capacity.

- Discharge duration - Measure of the time the energy storage can supply at the rated power

Depending on the above criteria, energy storage technologies can be classified into three categories [2, 17]. They are;

- Short-term energy storage (a few seconds - minutes)
- Long-term energy storage (minutes - hours)
- Very long-term energy storage (many hours - days)

Technologies with higher power densities and short response times fall into the short-term category. These technologies are more suitable for providing primary frequency regulation, maintaining stability during voltage transients and improving overall power quality [19–21]. Long-term energy storage technologies that can absorb and dispatch electrical energy for a few minutes to hours are suitable for energy management (e.g. peak shaving/valley filling) and secondary/tertiary frequency regulation. Very long-term energy storage technologies can be employed to match demand-supply over 24 hours or longer [2, 22]. Fig.2.1 summarises various types of energy technologies that fall under different classes using a charge/discharge characteristics called a Ragone plot [2, 23].

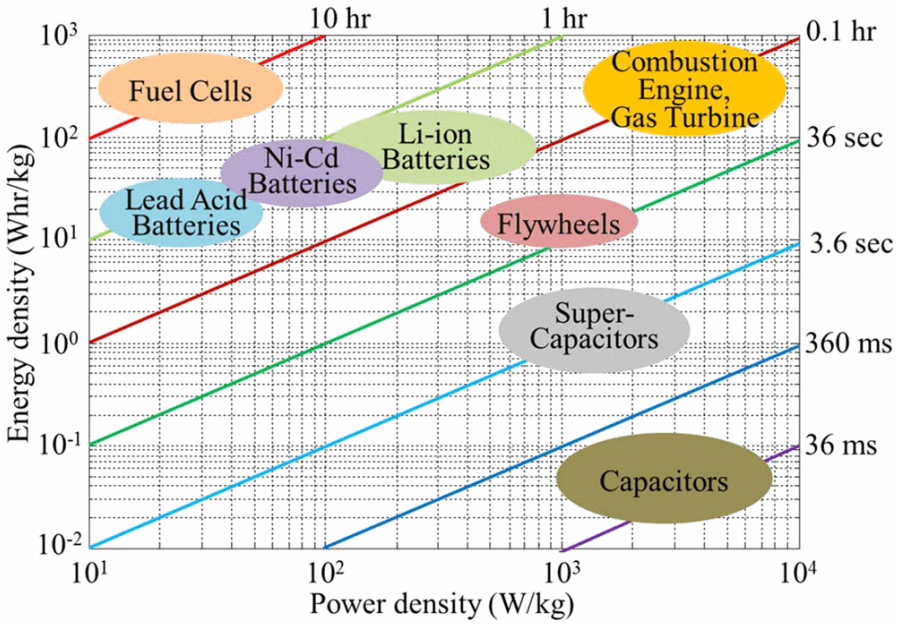

Figure 2.1: Classification of energy storage technologies [2]

As can be seen, battery energy storage [16, 24–27] , flywheels [28, 29], super capacitors [30, 31], super conducting magnetic energy storage technologies [32]

are suitable for short term grid applications such as Primary Frequency Regulation, smoothing renewable power supply and emulating inertia [33–35]. On the other hand, fuel cells [2, 36], lead acid batteries [37, 38] work well in long-term applications.

Although not shown in Fig.2.1, pumped hydro storage (PHS) and compressed air energy storage (CAES) are two other important energy storage technologies. While PHS is a mature technology, both PHS and CAES require large volume facilities for storage. Both feature medium to long discharge times, high power densities but low energy densities. PHS is the only currently feasible large-capacity energy storage technology with medium discharge times and high power capabilities; however, CAES is also expected to emerge in this area with future research developments. Heat thermal storage is another energy storage technology that stores available heat in an insulated repository for later use. It is currently used in various industrial and residential applications, such as space heating/cooling, hot water production and electricity generation. It can also be used to overcome the mismatch between demand and supply of local thermal energy requirements, which is important in the integration of RES [39].

In this thesis, a control technique to supply active power independently from an energy store to support of frequency in a weak grid is described. In doing so, the control technique has been developed based on an agnostic energy storage technology, which is presumed to fall into the short-term energy storage category. The literature review presented in this chapter explores control algorithms proposed in the same context irrespective of the energy storage technology used. In addition, frequency detection and weak grid modelling have given an especial focus in realising the proposed control technique. Therefore, this chapter presents an overview on the following topics.

- Energy Storage control strategies for frequency stability
- Frequency detection techniques in weak electrical grids
- Modelling weak electrical grids for frequency response

2.2 Energy Storage Control Strategies for Frequency Stability

Decreased inertia present in grids with RE generation causes frequency instability issues [4, 30, 40]. When frequency deviations occur as a result of demand-generation imbalances, traditional inertial response and speed governing takes a significant time to perform frequency compensation. During this time, large variations of frequency can occur instantaneously, as poor inertial response causes higher ROCOFs. To avoid violation of regulations imposed by grid-codes and other standards, supplying power from an auxiliary source such as energy storage can be proposed [2, 41].

As a mechanism to support/regulate frequency in all scales of power systems, several studies have been published by enlisting various energy storage technologies to perform short-term fast regulation [2, 12, 16, 24, 24, 26, 27, 30, 42–44]. As briefly introduced, a short-term fast responding energy storage technology with high power density is suitable for frequency support during load transients. Essentially, the energy storage should be able to supply active power immediately after a load disturbance to provide support during the time frame of the primary frequency control. Battery energy storage systems (BESS), Flywheels, super-capacitors and Superconducting Magnets (SMES) qualify under these conditions [14, 20, 45, 46]. Li-ion has both a high energy density and high power density, which explains the broad range of applications where Li-ion is currently deployed. Among these, according to the contemporary literature, Li-ion battery energy storage has been a popular choice for short-term frequency stability services [12, 24, 39, 47]. High efficiency in the range of 95%-98% and quick discharge time make it a reliable and flexible universal storage technology. Even though the share of Li-ion batteries in the portable and mobile market is high, it still faces challenges in the development in large scale applications. One of the main obstacles is the high cost for special packaging and internal overcharge protection circuits in such applications. However, it must also be emphasised that the experimental validation of the proposed control technique will use a Li-ion battery later in this work [39].

Generally speaking, the research trends can be identified as having two main paths;

- Techniques for optimising the size of energy storage for primary frequency

control;

- Techniques for integrating and controlling energy storage to provide primary frequency control

For both paths, it is common to recognise the energy storage as a reserve as well as a load. In other words, all techniques discharge energy when the frequency is below the nominal and absorb energy when the frequency is above the nominal. Various disparate parameters related to the technical performance, the life cycle cost/value, the size and the durability of energy storage have been optimised in [16, 24, 48]. The research on control techniques describe how to integrate energy storage to the power system electrically. This includes power processing structures, power conversion topologies and control systems that are needed when embedding energy storage in power systems [20, 27, 49, 50]. Apart from these two significant trends mentioned, there are a few studies conducted as techno-economic assessments of using energy storage for frequency stabilisation purposes [12, 24].

One of the earliest studies on using a battery energy storage for frequency regulation in a large island power system was published by Kottick et al. in 1993 [16]. This study was conducted for the National power system of Israel, which at that time had a peak demand of 3800 MW. A large BESS of 25 MWh was suggested to improve the reliability in case a large in-feed loss occurs. The BESS was modelled as a first order lag and the active power was supplied proportional to the frequency deviation. It was found that the battery discharges quickly when operated in an open loop. Thus, a high pass filter was added to the control signal in order to maintain its State of Charge (SOC). The maximum sizing of the battery energy storage is determined such that it is able to sustain a loss of 30 MW for a period of 15 minutes. Conclusions of the study state that with the BESS facility the frequency deviations resulting from sudden demand variations could be reduced drastically.

Another study proposed by Liang et al. [27], delivers a control method to provide a frequency regulation service. The method is proposed for a large power system with one or more interconnected areas. The traditional Automatic Generation Control (AGC) loop of the power system was modified with a controlled BESS. Therefore, the average power imbalance was considered as the control input signal to the BESS. The BESS control method models the battery charging loop and the effect of the DC/AC converter as first order lags. The BESS control was able to reduce frequency fluctuations caused by wind generators to less

than 10% of its original value. However, the amount of energy storage required for such frequency regulation was not addressed.

In [14], an interesting study on using an energy storage for frequency regulation in the main utility grid is presented by Leitermann. In this study, Leitermann emphasises that using the same thermal generators supplying the bulk of power to perform frequency regulation is inefficient. It reports that using energy stores on their own for frequency regulation would require large amounts of energy storage. Hence, the optimum size for the energy storage was evaluated by using duration curves for the energy capacity and instantaneous ramp rates after load disturbances. The traditional frequency regulation signal is then filtered to separate the fast and slowly varying components. The former was suitable to be controlled by energy storage, while the later was used in the regulation offered by conventional governing of thermal generators. This work can be considered as a case-study conducted on the utility grid of USA, which is one of the largest power networks. However, the findings cannot be generalised as benefits of using energy storage for frequency regulation may vary due to the size and geographical differences in other utility grids.

So far all studies discussed have been designed for large power systems and the energy storage control was mainly based on the average load current signal or on the traditional frequency regulation signal. This has essentially coupled the respective energy stores to the power systems they are connected to.

Frequency control in a small scale micro-grid of 11 kW, using energy storage is reported in a more recent study by Agbedahunsi et al. in [30]. The study introduces a closed-loop control of a STATCOM with super-capacitor energy storage, in order to prevent the normal frequency response of the generator during loading. The optimum control technique coordinates the control of both the energy storage and the governor and sends the speed governor to saturation as soon as a load disturbance is detected, by means of a throttle control. As a consequence, the engine torque is increased at its maximum rate to reach the torque disturbance of the load. By injecting an equal amount of energy from the STATCOM+Supercapacitor storage, the frequency deviation is kept minimal during the load transient. The control system is triggered by a change in the load current and the rotational speed acquired directly from the machine is regulated in a modified speed-governing loop [4, 50].

Using power frequency as a main trigger in energy storage control has been considered in [51] for a power system of 220 KW. The control system monitors

the grid-frequency using a PLL and activates an inverter to either charge or discharge a capacitor bank. When the frequency is above/below the nominal (60 Hz), frequency deviations are arrested by absorbing/injecting active power proportional to the difference between the grid frequency and the nominal. In this case the effectiveness of using an energy storage for frequency stabilisation was tested against a step change in the motor speed instead of the typical speed response during loading. Moreover, the article does not explain the effects of grid frequency estimation such as delay and harmonic content.

A more closely related study to this work was published by Serban et al. [20] in 2013. The article analyses the integration impact of BESS on short term frequency control in a $100kW$ micro-grid using a BESS rated at 50 kW. The power system with loads and BESS was modelled using small signal aggregated units representing the frequency response. Two main control inputs to the BESS controller are the frequency estimated by a PLL and the SOC of the BESS. The PLL is tuned to have a 100 ms delay and the estimated frequency is further filtered to reduce harmonic content. The study has found that the added delay in the frequency estimation causes a delayed response in BESS, weakening the stability; hence a compromise on the bandwidth of the frequency measurement system has to be agreed based on the speed of required response and on the level of the power oscillations. The output of the BES is determined by proportional derivative (PD) control. The proportional gain represents the BESS droop that delivers active power in steady state after the frequency disturbance, while the derivative component acts as a virtual inertia to reduce the ROCOF. This energy storage control was able to recover frequency to a droop-level, while decreasing the ROCOF, compared to the original case. The stability of the control system is limited by the noise amplified by the PD control and the delay imposed by the frequency estimation. The optimum sizing of the energy storage with respect to power system parameters was not discussed in this study.

The literature survey on using energy storage for short-term frequency support clearly elaborates the path of evolution of research interests from primary optimisation techniques to advanced control strategies to improve standalone control and plug-and-play capabilities of energy storage applications. It has also been learnt that the power system frequency has been used as the control signal in some recent research. As reported, stability has been an issue depending on the control systems used (PD-control) and on the delaying effects of frequency estimation. In addition, none of the methods report an in-detail analysis to choose a better frequency detection technique other than the conventional PLL.

Also, most of the methods were developed based on lumped grid models or small-signal models, but not on a realistic grid model, considering holistic effects of electrical power systems.

This indicates a need for further investigation on control strategies and frequency detection techniques suitable for the effective control of energy storage, with reasonable independence, while maintaining the stability of the overall system. This opens up the literature review to the later parts that explore more on frequency detection techniques specific to weak electrical grids and modelling weak grids, complementary to the work carried out in this thesis.

2.3 Frequency Detection Techniques in Weak Electrical Grids

Accurate power system frequency estimation is an essential requirement of all electrical grids, in order to ensure correct operation of interconnected devices. Under-frequency load shedding, ROCOF relay applications and grid connection of distributed energy resources (DER) including energy stores constantly consult the measured grid frequency to maintain healthy utility conditions.

Power system frequency is usually measured by processing the network voltage through a dedicated frequency detection method . The frequency measurement is sensitive to distortions and various forms of noise present in the voltage waveform [6, 52]. As will be experimentally observed in Chapter 3, the typical weak-grid voltage waveform is not only highly distorted with harmonics, but also contains glitches due to comparable source impedance. In addition, due to low inertia and slow frequency regulation, even small load perturbations in a weak grid cause considerable variations on the network frequency [16]. As the system inertia in a weak grid is small, frequency changes occur much more quickly than those illustrated for a strong grid in Fig.1.1. Therefore, frequency detection techniques suitable for weak-grids can be largely different to that for strong-grids, where above effects are mitigated due to large generation capacity and strict regulation of frequency and voltage. Hence, if the frequency is to be used as the control signal of the energy storage control, a robust frequency detection method needs to be incorporated to rapidly and accurately estimate frequency by processing a relatively complex voltage waveform of a weak-grid.

Akke specifies three criteria that a frequency detection technique has to satisfy

in a given application [53]. These criteria when combined with further suggestions by Thomas and Woolfson given in [52], one is able to come up with a set of essential properties of a frequency detection technique designed for a particular application.

- Short time to convergence
- High accuracy of frequency estimation
- Robustness to noise
- Acceptable delay between the estimated frequency and the actual frequency
- Ability to perform in the presence of voltage unbalances and faults

Frequency detection techniques in power systems have evolved through many different branches such as zero crossing [52], phase-locked loops (PLL) [54–56], Discrete Fourier Transform (DFT) based methods [57, 58], adaptive filtering techniques [59–61], Kalman filter based methods [62] and numerical optimisation techniques [52, 53].

Zero-crossing has been a popular method in protection and control. The method determines the time interval between two zero-crossings of the signal, thereby estimating the frequency [52]. The original zero-crossing algorithm can be inaccurate and unreliable in distorted conditions. Therefore, Begovic et al. [63] suggests a modified zero-crossing technique with added curve-fitting to suppress noise, that can deliver good tracking performance particularly in the presence of significant harmonics. However, the noise rejection could not be improved using the modifications. Therefore, for the estimation of dynamic frequency response in power systems with harmonics and noise, zero-crossing methods may be inadequate. The evaluation by Rodríguez and Holmes [64] of zero-crossing techniques confirms this further.

Three-phase PLLs are extensively used in grid-synchronisation and are directly associated with phase-detection rather than frequency-detection. However, since frequency is the time-derivative of phase, frequency can be derived instantaneously as a by product of phase detection. The PLL is a feedback system comprising of three stages, namely the phase-detector, the loop filter and the voltage controlled oscillator (VCO) as shown in Fig.2.2. The VCO creates an

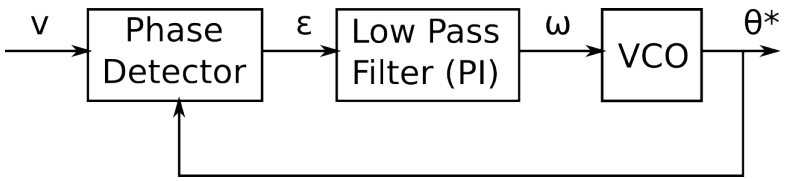

Figure 2.2: A block diagram of a the SRF-PLL

oscillatory output based on the detected phase, until the loop filter minimises the error between the VCO output and the input to the phase detector.

The most common PLL used in power systems is the conventional synchronous reference frame PLL (SRF-PLL) [65]. Due to the basic loop-filtering used, the SRF-PLL only performs well under ideal grid conditions. Under non-ideal conditions, the SRF-PLL becomes highly frequency sensitive and susceptible to harmonics and unbalances [66]. Moreover, in this method, improving the settling time would degrade the harmonic rejection properties due to mutually opposing effect of transient and steady state responses of a PLL. [6, 56, 67]. A complete analysis of the performance of the SRF-PLL can be found in section 5.3 in Chapter 5.

As mentioned, the main problem with conventional three-phase PLLs is their sensitivity to unbalance and harmonic-distortion in the voltage. The solutions to improve PLLs evolved through the path of finding ways to separate the unbalanced/distorted voltage as a combination of balanced components. The phase-detector stage is modified to generate two sets of balanced in-quadrature waveforms as inputs to the loop filter [54, 68–70]. The various approaches of realising the above have given rise to more advanced three-phase PLL structures such as double decoupled synchronous reference frame PLL (DDSRF-PLL) [71], enhanced PLL (EPLL) [60], quadrature PLL (QPLL) [61] and double second order generalised integrator PLL (DSOGI-PLL)[6].

The DDSRF-PLL has been designed with two rotating frames instead of the one in the SRF-PLL [6, 56]. This method represents an unbalanced voltage vector as a positive-sequence component and a negative-sequence component in two rotating $d-q$ frames, by proper use of transformations, prior to the loop filter. The amplitude and the phase of the positive component is estimated by removing the effects of the estimated negative component and low pass filtering the results. The negative component is similarly estimated by using the knowledge of the positive component estimated. Thus, the phase and the amplitude of the

positive sequence voltage, are used to calculate the instantaneous frequency of the voltage [71, 72].

The quadrature signal generation was implemented using two second-order generalised integrators (SOGI) in the DSOGI-PLL. The pair of SOGI-based adaptive filters generate two pair of orthogonal signals in a stationary reference frame $\alpha - \beta$. These quadrature signals are then passed into a positive-negative sequence calculation block that transforms them in to the $d - q$ rotating frame to produce the conventional d-q components that are input to the loop filter. The ability of SOGI to produce clean orthogonal signals which are pre-filtered, improves the quality of the phase/frequency estimation under faulty grid conditions [6, 73]. In addition, the frequency adaptability of SOGI can be used to directly estimate the frequency using a frequency-locked loop (FLL). This structure is then called a DSOGI-FLL. In this modification, the SOGI is tuned in such a way that it resonates when the grid frequency is equal to the natural frequency of the SOGI. The FLL is tuned to lock in to the frequency of the voltage, so that the SOGI resonates. This way, fast and accurate estimation of frequency is possible under unbalanced and distorted conditions. A more detailed explanation of the DSOGI-FLL can be found in section 5.5 in Chapter 5.

The enhanced PLL (EPLL) [60] and the quadrature PLL (QPLL) [61] use more advanced structures for phase detection. The EPLL has an adaptive notch filter (ANF) with a conventional PLL. This particular phase detector does not need additional transformations or subsystems to generate quadrature signals. Also the output exhibits superior harmonic and noise rejection capabilities. In addition to that, it gives more information such as amplitude and phase angle [60, 73]. The QPLL is a variation of the EPLL and can estimate the in-phase and the quadrature phase amplitude of the fundamental component of the input voltage. Unlike in the EPLL, the amplitude and the phase angle in the QPLL are not obtained directly, but are calculated indirectly. The QPLL shows better noise and harmonic rejection and more robustness to large and abrupt variations of frequency with its high filtering capabilities [74].

Another popular method of frequency detection is the DFT [57, 75, 76]. The DFT is a spectral analysis method for efficient estimation of components in the grid voltage. A commonly used DFT technique called the recursive DFT reduces the computational complexity as reported in [77, 78]. A modified DFT technique for real time frequency detection is presented in [57]. A method that uses DFT based SOGI technique is published in [76]. This literature survey revealed that

DFT techniques have not yet been particularly applied for frequency detection purposes in weak-grids. Generalisation of the modified DFT method presented by Lobos and Rezmer [57] applied to frequency detection in weak-grids, can be found in section 5.4 in Chapter 5.

Other methods of frequency detection techniques include Kalman Filters [77, 79, 80], numerical methods such as least square estimation (LSE) [81] and linear estimation of phase [82] and Prony estimation [57]. All these methods are computationally heavy and the implementations can be too complex to be used in real time three-phase systems [52].

In order to identify suitable frequency detection techniques for the energy storage control, a comparison of existing methods should be performed. While comparison studies amongst different methods can be found in references [52, 66, 68–70, 77, 83, 84], the need for a new comparison is indicated due to following problems. Different studies use various criteria for testing performance such as various levels of unbalance and arbitrary levels of harmonic distortion. Aptitude of these methods are mainly tested for step and ramp changes in frequency, under distorted conditions.

Generally speaking, the literature survey on frequency detection techniques in weak grid context revealed the following valuable insights. Firstly, the comparison studies presented so far may be inadequate to decide the best technique for a weak-grid environment. One reason for this is that even though the input voltage waveform exhibits a higher harmonic content and larger unbalance or was in a strong-grid situation, it may not necessarily represent a worst-case weak grid, covering all important variations including effects of source impedance and AVR that can affect the frequency detection. Secondly, this research strictly needs to estimate the frequency trend after a load disturbance rather than estimating a step or a ramp change in frequency. Another point of emphasis is the unavailability of an unbiased criteria for comparison among frequency detection methods of different theoretical backgrounds. Therefore, a niche has been identified for the requirement of a proper comparison study among frequency detection techniques specifically for weak grid conditions using an unbiased criteria. This requirement will be fulfilled in Chapter 5 of this thesis.

2.4 Weak Grid Simulation Models

Weak electrical grids are usually found towards the medium or low voltage feeders of conventional grids. Some of these weak grids are supported by distributed generation resources (DGR) consisting of renewable energy sources (RES) and energy storage facilities. Compared to strong grids, weak grids feature lower inertia and higher impedance, in addition to their typical low power ratings typically in the order of 100 kW [85]. System inertia of 1 kgm^2 or less can cause significant fluctuations in power system frequency for relatively low variations in loading. Also, the source impedance enforces significant effects on the voltage during loading and shedding of loads, DGRs and energy storage at the PCC. These manifest as distortions and unbalances at the PCC such as voltage dips and voltage glitches. This means that both the magnitude and the phase of the voltage in a weak grid is not as uniform as in a strong grid. Moreover, in a weak grid with only a few single synchronous generators, switching regulators cause high harmonic contamination in the voltage. This is also a concern in this study, as it directly affects frequency detection.

Having understood the need for an impartial comparison of frequency detection techniques in weak grids, the necessity to create a simulation model/platform which can mimic a worst-case weak grid can be justified. Such a model has to account for all important frequency and voltage dynamics in a weak-grid replicating the voltage and frequency characteristics appropriately and adequately for further design and development of the techniques. This includes the design, development and comparing of frequency detection techniques and the development and testing of the proposed energy storage control system. In order to satisfactorily perform the above, the model should ideally comprise of;

- The frequency dynamics of the power system, representing the inertial response and the governor controlled primary frequency control response
- The Automatic Voltage Regulation (AVR) characteristics
- Harmonics and unbalances typically found in a weak-grid
- The Effects of Supply impedance
- Connection of loads

Therefore, a survey has been conducted to identify suitable power system simulation models in the existing literature, that may be able to replicate a weak-grid.

Kundur et al. in [85] presents generic control system models of active power control for frequency regulation in power systems. The models are derived for large thermal power systems of large inertias that can supply a significant proportion of the national power generation. According to Kundur et al., there are two speed governing mechanisms practised in power systems to recover the immediate inertial response; i.e,

- Isochronous governors
- Governors with speed-droop characteristics

When a load disturbance occurs, isochronous governors can bring the decreasing frequency back to the nominal value, while a governor with speed-droop characteristics can restore the frequency to a set-point below the nominal. The use of isochronous governing is applicable, when a single generator is appointed for the speed regulation. However, when two or more generation units with speed regulation capabilities are present in a system, droop control has to be used to share the load among the generators at the steady state without conflict. The participating generators in that case are provided with a speed droop to settle in a steady state [85].

Anderson and Mirheydar in [3] published a low-order system frequency response (SFR) model for large power systems. The main aim of this model was to showcase only the essential dynamics, so that a droop frequency control is replicated using per-unit values of the inertia constant (H), the reheat time constant (T_R) and the droop gain ($\frac{1}{R}$) as the most dominant time constants. Other factors included are the damping factor (D), the fraction of the power generated by the high power turbine (F_H) and the mechanical power gain factor (K_m). See Fig.2.3 for an illustration of the SFR model. The SFR model shown regulates the power deficit equivalent to the load disturbance causing a deviation in the angular frequency, which is the output of the model. To realise the model to demonstrate frequency control, the knowledge of the dominant thermal time constants is necessary.

A more recent study by Costabeber in [4] introduces another speed-governing model based on the angular speed ω; so that, instead of active power, torque is considered in the loop. The engine is defined as a first order lag, and the

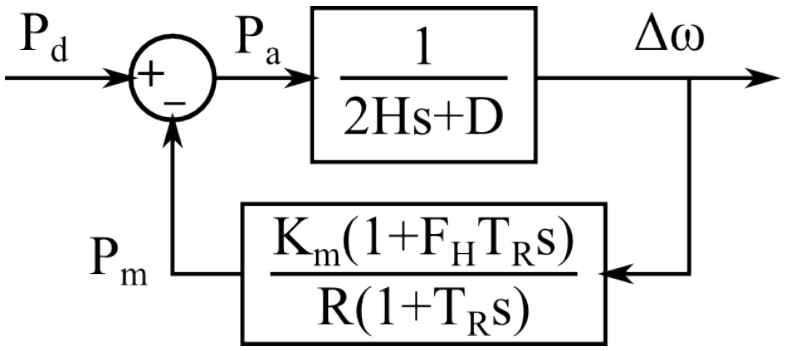

Figure 2.3: System Frequency Response model by Anderson and Mirheydar [3]

generator is modelled using actual inertia $J(Kgm^2)$, which are the dominant time constants of the overall system. The speed governor is a PI controller that is tuned to deliver the desired speed dynamics. As shown in Fig.2.4, the angular frequency error occurring as a result of the load torque disturbance is regulated by the speed governor at the nominal. Instead of the speed difference, this system provides the angular speed at the output of the loop.

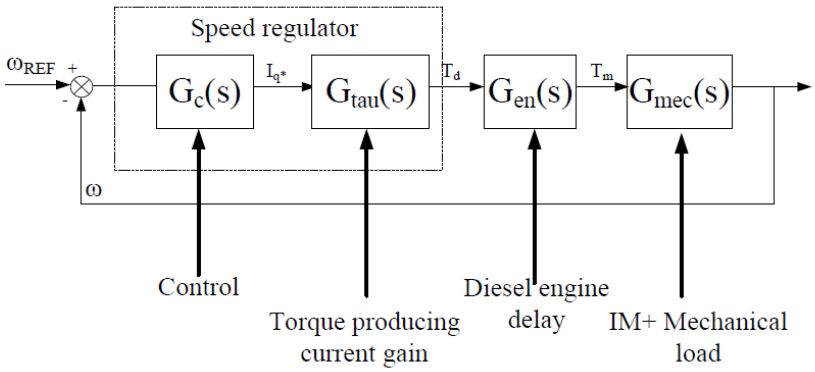

Figure 2.4: Speed governor loop by Costabeber [4]

Having considered several power system models for frequency control, the last model proposed by Costabeber was understood as the most suitable model for this work, due to its properties. The emulation of the diesel engine is achieved by representing the engine/prime mover as a first order lag and the generator is represented by its inertia. Note that the torque producing current gain was linearised and included in the PI control speed loop gain. This configuration delivers a simplified representation of the swing equation that can sufficiently indicate the speed change occurring as a result of the load torque disturbance. In a weak-grid, the speed control is usually performed by a single unit and

due to low inertia, the ROCOF following a load change can be very high (e.g. $-50Hz/s$) [41]. Also, the angular frequency makes provision to use angle θ to generate sinusoidal signals, which create the electrical network. These characteristics are fulfilled by the low order isochronous speed-control model presented in [4]. Nonetheless, the model needs to be updated with the inclusion of automatic voltage regulation and a supply impedance to adequately replicate the voltage of a weak-grid. The harmonic distortion can also be added manually to the voltage. The process of modifying Costabeber's model with the new additions can be found in Chapter 3, where a complete weak-grid simulation model is presented.

2.5 Summary

A Literature Survey was conducted in three major areas of the scope of this research. They are a) control and optimisation techniques of using energy storage for frequency regulation/support in electrical grids; b) frequency detection methods suitable for weak-grids; c) weak-grid simulation models. The survey revealed that the research theme of energy storage control for short-term frequency stability has taken different control and optimisation approaches. Some methods were proposed to supply the whole of active power demand during the disturbance, while others were controlled between tight frequency margins. Only a few studies used the power frequency in their energy storage control algorithms as a trigger, but not necessarily with the intention of gaining independent control. Due to primitive and non-optimal frequency estimation techniques used in those, the algorithms could not reap the full benefits of using frequency, which is a direct indication of the load-demand imbalance. This called for adequate comparison studies between candidate frequency detection techniques for weak-grids. In order to develop energy storage control and to perform a comparative analysis on frequency detection methods, a complete weak-grid simulation model with important voltage and frequency characteristics is also required. The rest of the thesis attempts at providing some solutions to the problems identified here.

CHAPTER 3

Model of A Weak Electrical Grid

3.1 Introduction

The experimental investigation carried out to observe the properties of a prototype weak-grid under test, and their effective replication on a simulation platform are discussed in this chapter. From this, a set of worst-case weak-grid conditions is declared, under which the designed system must operate. The findings of this chapter are to be used in the design and development of the proposed energy storage control, discussed in the next chapter. In addition, the selection of the most suitable frequency detection technique for the proposed energy storage control depends mainly on the worst-case weak-grid characteristics and on the weak-grid model derived in this chapter. The developed weak grid simulation model contains a speed-governor controlled generation system and a representation of the automatic voltage regulator (AVR) present in the synchronous generator under test. The weak-grid simulation will also include source impedance to represent voltage glitches and dips, in addition to the harmonic distortion. A comparison between the results obtained from the simulation and the experiments is included followed by conclusions.

3.2 Weak-Grid: An Experimental Investigation

This section describes the experimental technique and qualitatively discusses the voltage and frequency variations observed during the experiment. The experimental set-up represents a rudimentary low voltage weak-grid with a single generation source. The weak-grid is powered by an 8 kW synchronous

generator attached to a 16 kW induction motor acting as the prime mover. The prime mover is controlled by a vector drive with a speed governor. The load demand of the grid is defined by a 3-phase 3 kW resistive load. Both the generator and the load are Y-connected. Using this experimental facility, we can observe,

1. The variation of the voltage and the speed of the generator during loading/shedding of the resistive load.
2. The effects of source impedance on 3-phase voltage profile during loading/shedding
3. The effects of the AVR of the generator on the voltage, during loading/shedding.
4. The typical harmonic content of the 3-phase voltage generated by a synchronous generator.

3.2.1 Experimental Setup

The overall layout of the experimental weak-grid is shown in Fig.3.1. As shown, the microgrid is constructed using a Leroy Somer® 4-pole alternator, labelled as the synchronous generator [9], a Magnetic 4-pole induction motor [86] and a three phase resistive load. The vector controlled induction motor is used to emulate a diesel engine with governor control, which represent the prime mover in a conventional power system [85]. Prime mover is connected to the synchronous generator to form the weak microgrid. Even though the induction motor is powered by the grid via the vector drive, the micro-grid is isolated and operates independently to demonstrate the weak-grid characteristics. The development of the diesel engine emulation and its simulation model were reported in detail in two related research projects conducted in the PEMC group at the University of Nottingham. Further information can be found in PhD thesis [4] by Costabeber and [50] by Agbedahunsi.

The generator equivalent impedance is shown as X_s in series with the synchronous machine. During normal operation, the generator operates at the rated speed. The synchronous generator supplies the resistive load connected to the PCC via breaker C. When there is a load change, both speed and the voltage undergo a sudden variation. The synchronous generator uses an AVR to regulate the voltage and the IM drive uses a speed control to regulate the speed

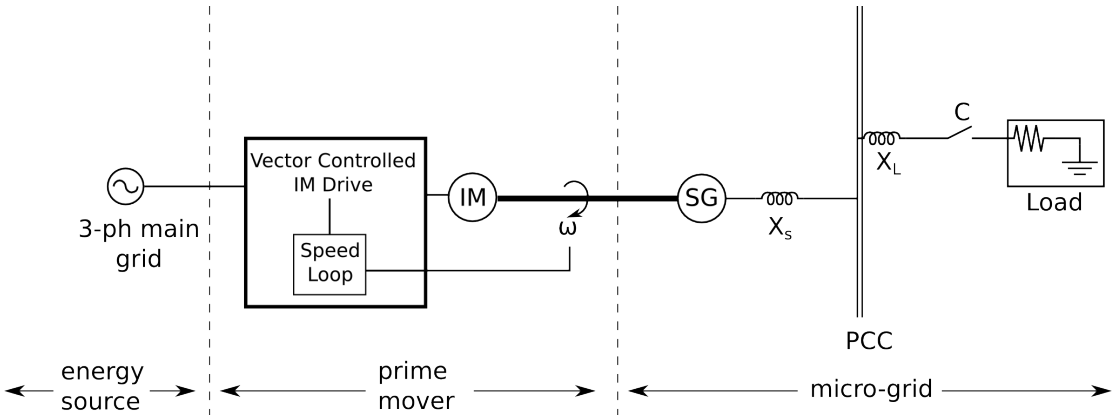

Figure 3.1: Schematic of the experimental rig

of the prime mover and emulate a governor. The selection criteria of the control dynamics of AVR and speed governor is explained in sections 3.3.4 and 3.3.1. The connection impedance of the resistive load was neglected.

The speed control in the IM drive is a PI controller with a proportional gain (K_p) and an integral time constant (T_i). These parameters can be set via the induction motor drive using its user interface [8].The speed loop was tuned in such a way that the speed governor has slow dynamics so that the frequency experiences a higher ROCOF and a longer settling time. This could be achieved with $K_p = 1$ and $T_i = 200ms$ which gives a ROCOF of $-86.23Hz/s$ and a settling time of $\approx 3s$ for the rated load disturbance. The respective parameters of the experimental grid are shown in Table 3.1.

Parameter	**Value**
Synchronous Generator	$8\,kW/10\,kVA$ at $\cos\phi = 0.8$
Synchronous Generator pole pairs	2
Synchronous generator voltage	$400\,V\ (RMS)$ line-line
Induction motor	$16\,kW$
Induction motor pole pairs	2
Motor voltage (V)	$390\,V$
Motor current rating	$34\,A\ (RMS)$
Induction motor drive	$22kW$
IM drive speed loop prop. gain (K_p)	1
IM drive speed loop int. time (T_i)	$200\,ms$
IM drive rated speed	$1500\,rpm$
IM drive max. speed	$2000\,rpm$
Resistive Load	$57\,\Omega$ per-phase
Load step	$2.78\,kW$

Table 3.1: Experimental rig parameters

3.2.2 Experimental Results

The speed of the prime mover can be accessed via the control terminals of the IM drive as a voltage signal proportional to the speed. The calibration procedure and the determination of the resolution of the speed acquisition is described in detail in appendix A. From this the frequency resolution was identified as 0.27 Hz ($\pm 0.135 Hz$). The 3-phase voltage at the PCC was also logged synchronised to the speed response. In the following sections the experimental results obtained for the frequency (calculated using (A.0.3) in Appendix A) and the voltage at the PCC will be studied.

3.2.2.1 Speed of the Synchronous Generator During Loading

At first, the speed of the synchronous generator was observed when a 3-phase resistive load $R = 57\Omega$ is connected by closing the breaker C. Fig.3.2a shows the power frequency variation during loading. Note that the governor speed loop was set with the parameters reported in Table 3.1.

As can be seen in Fig.3.2a, the power frequency drops critically during loading. The active power demand during loading is equivalent to 2.78 kW at 230V rms. Considering the generator rating of 8 kW, this represents a loading of 37.5% of the rated load. This has caused a severe dip of nearly 4.5 Hz, in frequency, which is well below the normal operation limit of 1% of the 50 Hz nominal ($= 49.5$ Hz) as stated in the grid-code. The drop of frequency during loading can be explained by the classic swing equation.

$$J\frac{d\omega}{dt} = T_m - T_e \tag{3.2.1}$$

where the total inertia J (kgm^2) of the system is the sum of individual inertia component on the same shaft, $d\omega/dt$ is the acceleration/deceleration caused by the imbalanced torque (i.e. loading/load-shedding), T_m is the mechanical torque and the T_e is the electrical torque.

In steady state operation, the mechanical torque is equal to the electrical torque (equivalent to electrical power spent). When there is sudden loading (i.e. sudden increase in T_e), the prime-mover and the governor act to match T_m to T_e. However, this reaction is relatively slowly. During such an incident, the deficit energy is supplied by the rotational kinetic energy; thus, the electrical torque demand causes a drop in the mechanical speed (or a deceleration), which also

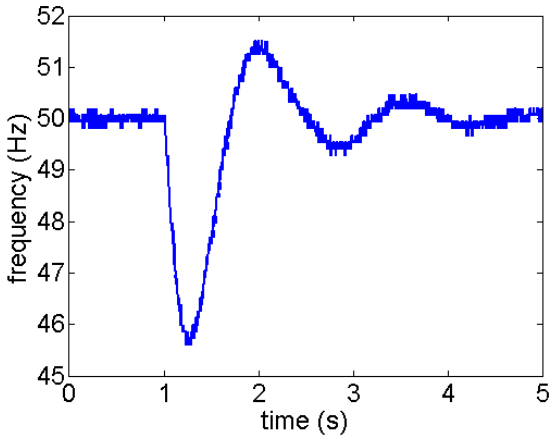

(a) Loading

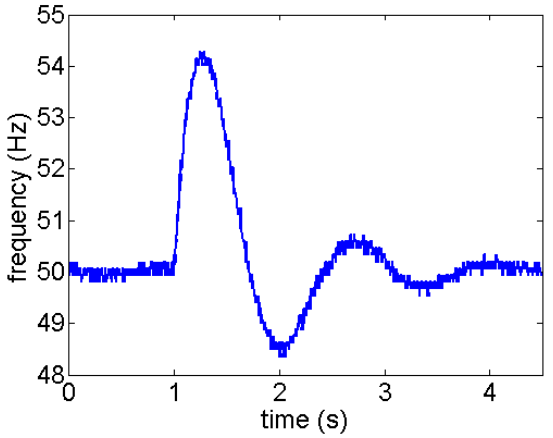

(b) Load shedding

Figure 3.2: Frequency response obtained experimentally with governor settings $K_p = 1$,$T_i = 200ms$, for a) loading and b)load shedding of a 2.78 kW step-load at $t = 1\ s$

manifests as a drop in the frequency of the generated voltage.

This initial drop in the frequency is determined by the inertia of the system and the applied load. Then the speed governor activates and actuates the prime mover to supply the additional torque. Therefore, the settling time is defined by the speed loop dynamics. The combined effect of the inertia of the power system, the loading and the speed-loop dynamics determine the maximum frequency drop. A mathematical discussion on this is presented in section 3.3.1.

3.2.2.2 Voltage at the PCC During Loading

The 3-phase voltage at the PCC was observed simultaneous to the speed signal during loading as illustrated in Fig.3.3a. One can see that loading has caused a

dip in voltage magnitude. To explore and understand these effects more clearly, an envelope of the voltage is generated. Fig.3.3b shows the envelope of the voltage dip section calculated by passing the 3-phase voltage through a simulated full-bridge rectifier and a first-order smoothing filter with a time constant of $10ms$. Note that this envelope does not take harmonics into account, thus, has a lower voltage than the apparent envelope.

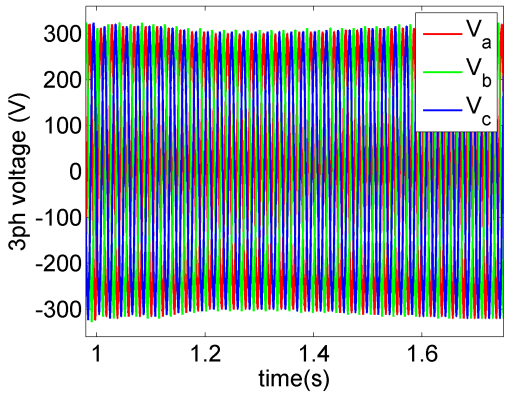

(a) Full voltage profile

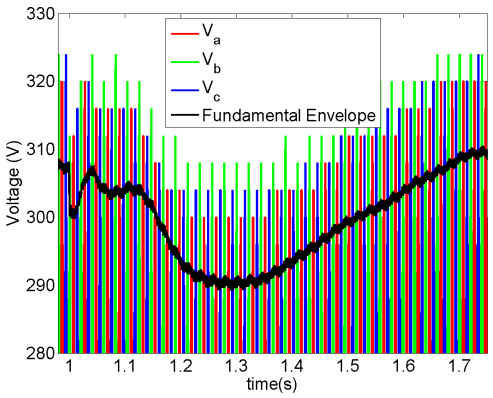

(b) The envelope of the fundamental

Figure 3.3: 3-phase voltage during a loading of 57Ω

The voltage envelope is zoomed-in in Fig.3.3b to view the balanced amplitude dip in the PCC voltage, occurring immediately after the load is switched on due to the presence of source impedance. However, when the terminal voltage at the generator undergoes a change from its nominal value, the AVR activates and restores the voltage to its rated value within 50 *ms* of applying the load. According to Fig.3.3b however, a more prominent prolonged dip can be seen which is an effect of the AVR response as explained below.

The AVR used in this synchronous generator is a custom built Leroy Somer® *R* 220 shunt-type AVR. A transient voltage drop at the terminal is recovered

during a load impact in a specific voltage-frequency profile, which is determined by the drop of the generator rated speed (i.e. frequency of the voltage). The voltage recovery profile taken from the R 220 AVR data-sheet [5] is shown in Fig.3.4. The voltage response of the experimental system is represented by the U/f curve without the Load Acceptance Module (LAM). According to the figure, if the speed drop is within 48 Hz and 50 Hz, the voltage is restored in a fast AVR response. If the speed drops below 48 Hz, the voltage follows the speed response, thereby reducing the load to allow the prime mover to restore the speed more easily [5].

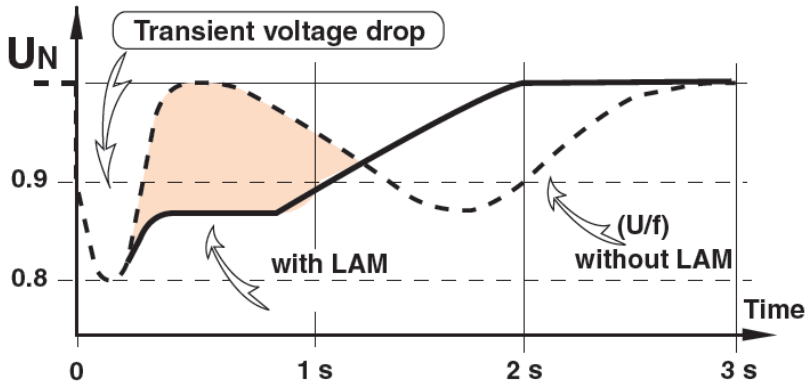

Figure 3.4: Leroy Somer ® *R* 220 AVR Response [5]

From Fig.3.3b, it can be seen that the envelope of the actual experimental 3-phase voltage follows the anticipated response shown in Fig.3.4 as given in the data sheet [5]. By comparing the shape of the frequency response below 48 *Hz* in Fig.3.2a, one can confirm that the voltage profile approximately fits the data-sheet description.

Further investigation in to the voltage dip caused by the load disturbance reveals that all three phases exhibit a sudden glitch in voltage for about 1 *ms* as soon as the load is switched on as shown in a further zoomed figure of the voltage waveform in Fig.3.5a. The load current flow during the load disturbance is shown in Fig.3.5b.

A circuit diagram illustrating the elements is given in Fig.3.6. When the switch in the circuitry is closed, the resistive load draws a current completely determined by its terminal voltage. The current through the inductor increases slowly for 1 *ms*. Thus the load voltage (PCC voltage) increases slowly from a

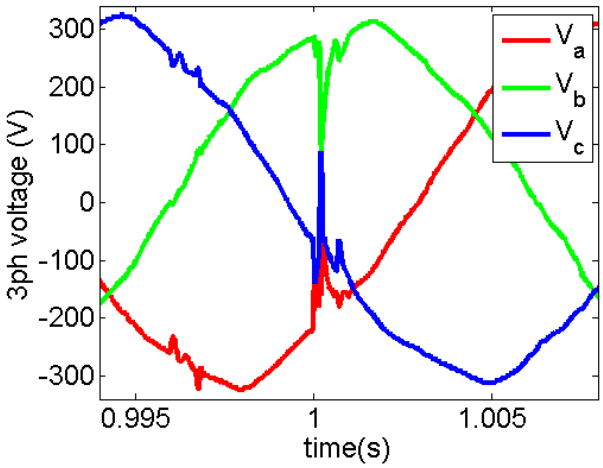

(a) Voltage

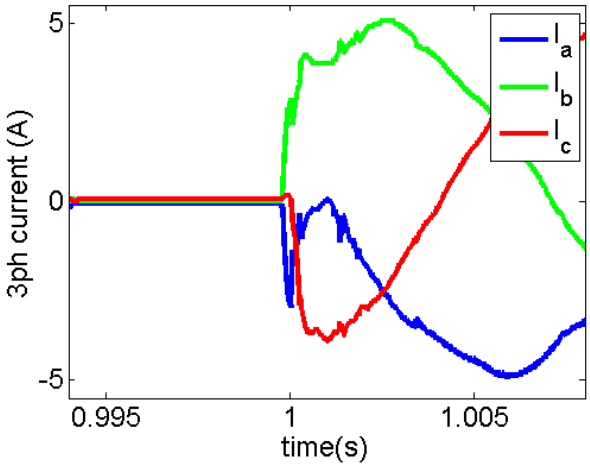

(b) Current

Figure 3.5: Three phase voltage and current during loading, zoomed to show the glitch.

very small value for all three phases. This duration is determined by the L/R time constant $\tau_{L/R} = L_s/(R_s + R_L)$.

3.2.2.3 Harmonic Distortion

Having examined the temporal properties of the voltage at the PCC during loading, the next important property of the voltage to consider is the harmonic distortion at steady state.

The weak grid voltage profile presented in Fig.3.7 can give a brief idea of the harmonic distortion present in the voltage. In order to discover more about the

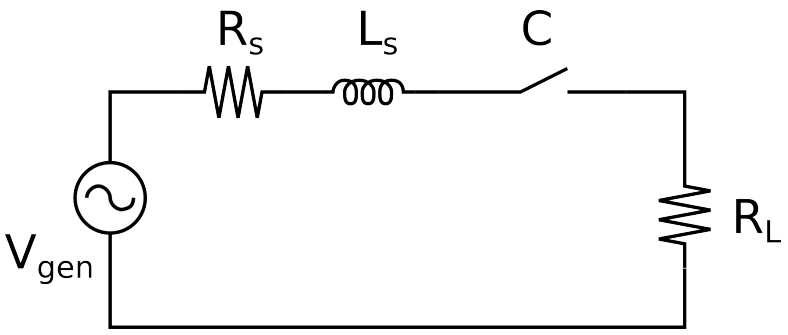

Figure 3.6: Circuit elements during loading

harmonic content in the voltage signal, an FFT analysis was carried out.

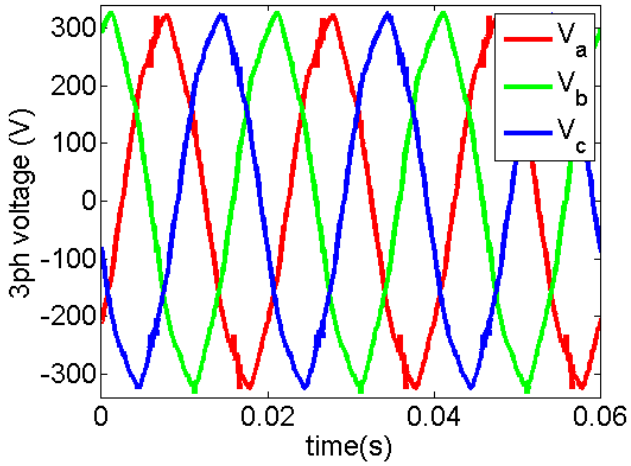

Figure 3.7: 3-phase voltage of the microgrid showing the harmonic distortion present

The 3-phase voltage v_{abc} was converted to $v_{\alpha\beta}$ using Park transform. An FFT was taken after forming the complex signal $v_\alpha + jv_\beta$. The magnitude of the FFT normalised to the fundamental is shown in Fig.3.8. As can be seen, the most prominent harmonic is the 7^{th} harmonic (i.e. $350Hz$), which has a 4.63% content compared to the fundamental. The other significant harmonics include the negative and the positive components of the 5^{th} ($250Hz$) with 3.90% and 0.33% of the fundamental respectively.

The phase values relative to the fundamental components are shown in Table 3.2.

$$THD\% = \sqrt{\sum_j A_j} = 6.07\%$$

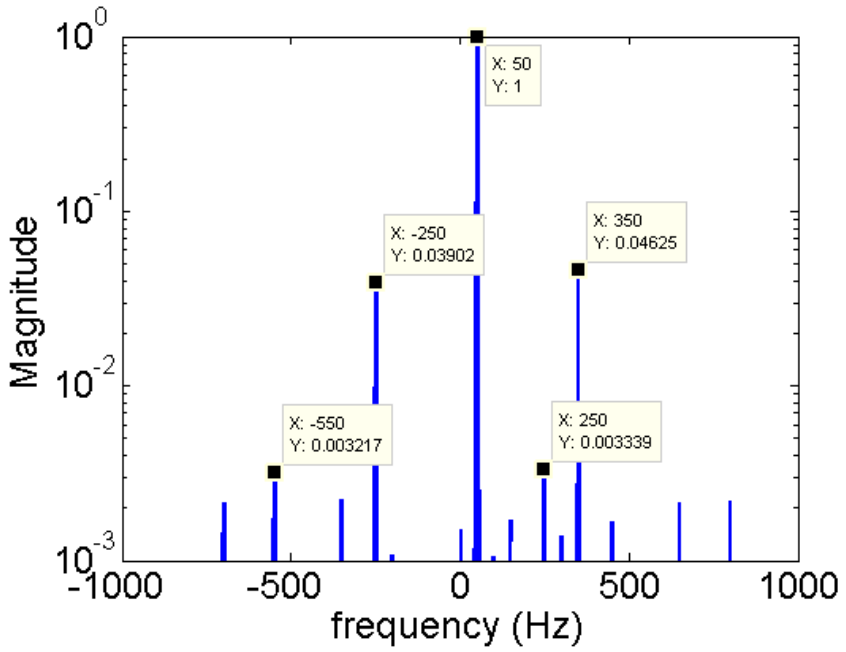

Figure 3.8: FFT of the 3-phase voltage during loading showing the level of harmonic distortion

where A_j are the magnitude of j_th harmonic as a percentage of the magnitude of the fundamental.

Harmonic	Percentage	Phase (rad)
7^{th}	4.63 %	-1.6862
-5^{th}	3.90 %	0.8375
5^{th}	0.33 %	-1.1995
-11^{th}	0.32 %	-2.4344

Table 3.2: Harmonic content in the experimental weak-grid voltage signal

3.3 Weak Grid: A Modelling Study

This section explains the overall design procedure of the weak grid simulation platform. The speed characteristics will be used in designing the speed governor. The voltage characteristics will be replicated by the AVR design and will be used to determine the electrical composition of the weak grid. As part of this exercise, the simulated results for the speed and the voltage will be compared with the experimental results.

3.3.1 Speed Regulation

As briefly introduced in section 3.2.2, the induction motor and drive in the experimental rig is used to emulate a diesel engine. The typical prime mover speed regulation is carried out by a PI control. Fig.3.9 illustrates the speed loop of a typical prime mover diesel engine. The linearisation of the speed loop is based on the angular speed and the torque. The power $P(W)$ is related to torque τ and the angular speed ω as,

$$P = \tau\omega \tag{3.3.1}$$

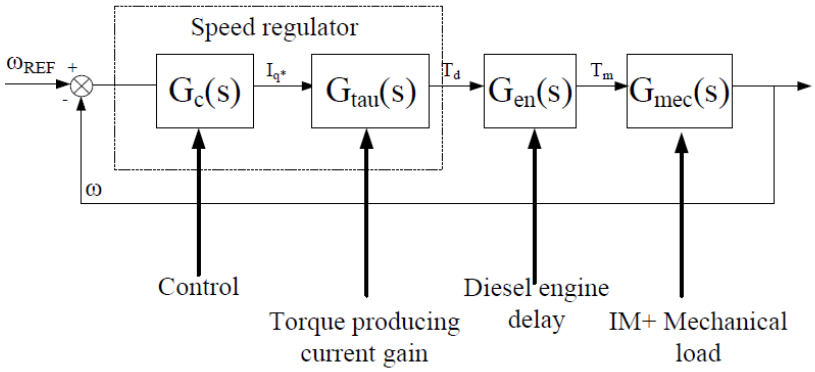

Figure 3.9: Block diagram of the speed governor loop by Costabeber [4]

The prime mover energy conversion from the energy source is modelled by the engine transfer function $G_{en}(s)$, which is responsible for delivering the torque demand τ_d. $G_{en}(s)$ was modelled as a first-order delay with a time constant of T_{en}. According to the actuation set by the speed governor, $G_{\omega PI}(s)$, the torque producing current gain $G_{\tau}(s)$, assumed here as a constant gain, sets the throttle demand to the prime mover. Then the resultant torque will restore the generator's speed to the nominal. The speed loop model developed to replicate the diesel engine emulation by Costabeber [4] and Agbedahunsi [50] of the PEMC group at the University of Nottingham was used in this thesis. The Matlab/Simulink block diagram of this model is shown in Fig.3.10. The torque producing current gain that amplifies the speed actuation that increments the required current to produce the torque by the engine is combined in the proportional gain K_p of the PI speed governor inn this model. Essentially the entire speed loop is linearised around the torque representing the conventional swing equation (3.2.1).

The transfer functions of the speed loop ($G_{\omega PI}(s)$), the engine ($G_{en}(s)$) and the

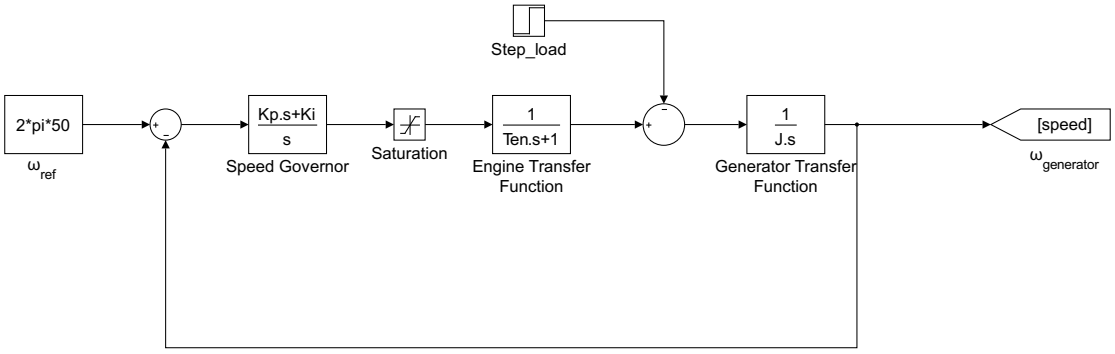

Figure 3.10: Simulink block diagram of the speed governor

generator ($G_{mech}(s)$) are shown in (3.3.2). The governor transfer function represents a typical PI transfer function with proportional gain K_p and integral gain K_i, the generator transfer function was obtained by s-domain representation of the swing equation (3.2.1).

$$\begin{aligned} G_{\omega PI}(s) &= K_{p\omega} + \frac{K_{I\omega}}{s} \\ G_{en}(s) &= \frac{1}{1 + T_{en}s} \\ G_{mech}(s) &= \frac{1}{B + Js} \end{aligned} \tag{3.3.2}$$

The Speed Governor

The transfer functions presented in (3.3.2) linearise the system using speed of the generator. This allows the power generated by the engine (P_{en}) and the active power required by electrical (resistive) loads (P_L) to be represented as equivalent torques.

The closed loop transfer function of the speed loop can be written as,

$$G_{CL}(s) = \frac{\omega(s)}{T_L(s)} = \frac{G_{mech}(s)}{1 + G_{mech}(s)G_{en}(s)G_{\omega PI}(s)} \tag{3.3.3}$$

By substituting for $G_{en}(s)$, $G_{\omega PI}(s)$ and $G_{mech}(s)$,

$$G_{CL}(s) = \frac{(T_{en}s + 1)s}{JT_{en}s^3 + (J + BT_{en})s^2 + (K_p + B)s + K_i} \tag{3.3.4}$$

Therefore, the characteristic equation of the speed loop is a third-order equation given by,

$$s^3 + \frac{(J + BT_{en})}{JT_{en}}s^2 + \frac{(K_p + B)}{JT_{en}}s + \frac{K_i}{JT_{en}} = 0 \tag{3.3.5}$$

As of now, the combined inertia of the system (J) and the combined windage constant (B) are unknown. Costabeber in [4] and Agbedahunsi in [50] have assumed a value of 31.8 ms for T_{en} in their thesis regarding the same induction motor. However, in realistic conditions, this value can be much larger [85]. Even though, K_p is set in the IM drive as 1.0, the torque current gain is unknown and should be included in K_p per current design. Therefore, a regression analysis was conducted on four parameters, K_p, T_{en}, J, B to match the experimental frequency response to the simulated frequency response using Matlab function *fmincon*. Note that during this analysis, it is assumed that the load is a step torque, whereas in reality it depends on the frequency and the AVR action due to frequency drop.

The fitted curve is presented in Fig.3.11 along with the experimental frequency response. The respective values of fitting parameters are listed in Table 3.3.

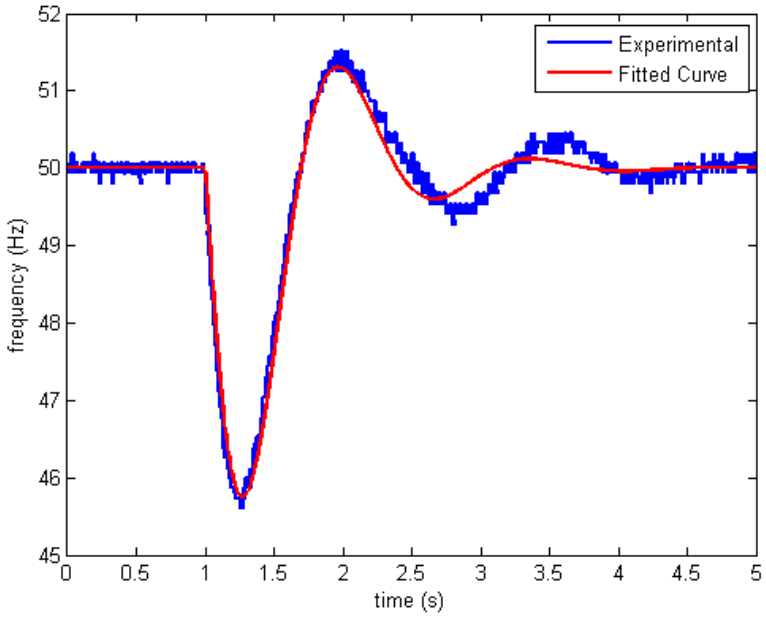

Figure 3.11: The curve fitting for the experimentally obtained frequency response.

Since the windage constant (B) is small, it is ignored in the subsequent models, representing the generator by $1/Js$. This means that the generator and the engine has no damping and represents a worst-case weak grid. Such conditions are beneficial in validating the main work proposed in this research (i.e. the

Parameter	Value
J	$0.0447 kgm^2$
H	$0.22s$
B	$0.0002 kgm^2 rad^{-1}$
T_{en}	$38.1\ ms$
K_p	0.1942
$K_i = 5K_p$	0.9709

Table 3.3: Parameters obtained from curve fitting the experimental speed response

frequency stabilisation algorithm).

The engine time constant (T_{en}) was found to be 38.1 ms which is close to the value used by Costabeber[4] and Agbedahunsi[50]. Because K_p value used in the IM drive is 1.0, the torque current gain of the drive can be inferred as 0.1942. The Bode Plot of the complete system given in (3.3.4) is shown in Fig.3.12. Hence, one can find that the speed loop with the above PI governor has a bandwidth of 8.61 $rads^{-1}$ and a phase margin of 34.5°. The phase margin, according to the control theory is a rough estimation of the damping factor (i.e. $phase\ margin \approx 10\zeta$) [87]. This provides an insight in to the relatively low damped speed response. On the other hand, after the second oscillation, there is a slight mismatch between the fitted and the experimental frequency response waveforms. This can be mainly attributed to the non-linear behaviour of the IM control such as the simplification of the torque loop of the IM drive in the simulation. Yet, the ROCOF at the beginning of the frequency drop, is the same suggesting that the estimation of J is valid and the initial drop confirms that the values K_p, T_{en} are also valid. Hence, it can be assumed that this linearisation model with the given parameters closely resembles the experimental speed loop characteristics.

The values listed in Table 3.3 will be used in the simulated speed-loop through out this thesis. Fig.3.13 illustrates the speed response of the simulated governor for loading and shedding of a load step of 2.78 kW compared with the experimentally obtained speed response. The simulated and the experimental speed responses exhibit significant approximation in the initial ROCOF and settling times in the entire transient.

Using (3.3.4), with the identified speed loop parameters, the system response from various aspects can be observed, such as the effect of inertia, the engine time constant and the speed loop bandwidth on the frequency variation for a change in load. These effects are discussed next partly because they provide an

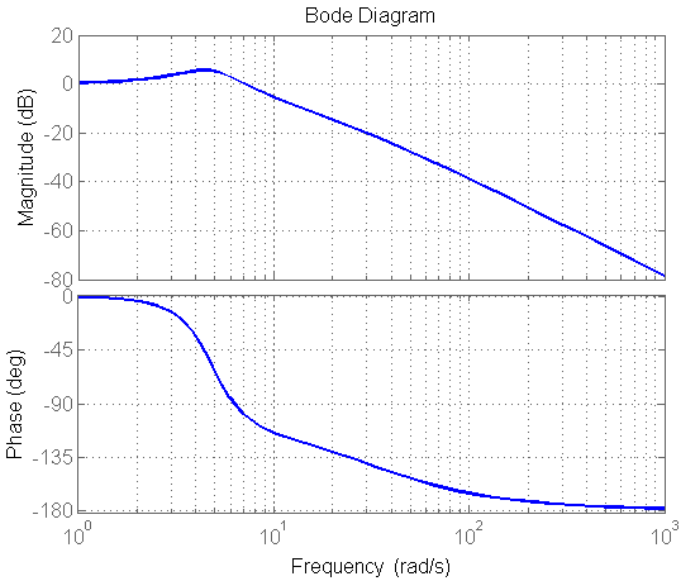

Figure 3.12: Bode plot of the closed speed-loop

insight into the system and also because these concepts are revisited later in the thesis.

Effect of Inertia

The inertia of a system is a measure of its resistance to changing velocity. When a load disturbance occurs, the inertia of the power system acts as a resistance to changing speed of the rotor, before the governor reacts. Therefore, the initial ROCOF soon after the load disturbance is defined by the system inertia. In other words, the higher the inertia of a power system, the speed fall resulting from load disturbances is more resisted, and the less steep is the ROCOF experienced. This is the typical case of a strong grid, where the combined system inertia is high, whereas for a weak grid, the ROCOF is higher due to lower combined inertia.

The influence of inertia on the initial ROCOF can be observed by simulating the system for different inertia for the same load step change. Fig.3.14 shows the speed variations observed for different inertia values, around the original inertia value. Note that the speed loop parameters (Kp, Ti) were kept the same. The torque load step used for the simulation is equivalent to the active power change that occurs in connecting a 3-phase 57Ω resistive load to the experimental system. This can be obtained using (3.3.1).

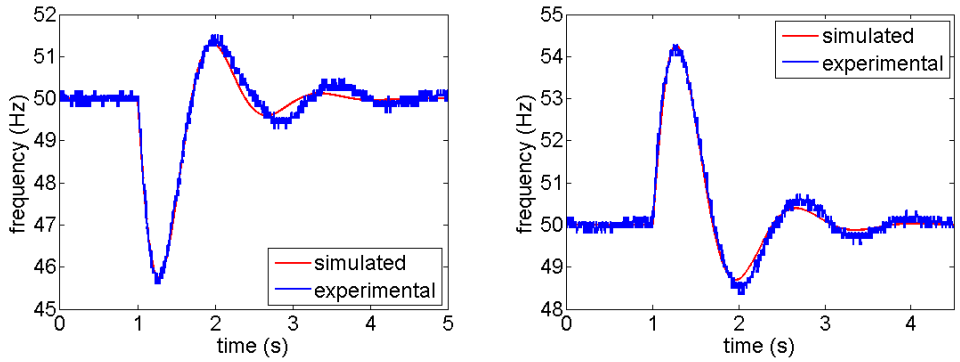

(a) Loading **(b)** Load shedding

Figure 3.13: Frequency response of the designed governor for a 2.78 kW step load change at $t = 1\ s$

.

Even though angular speed ω changes in $P = \tau\omega$ throughout the load transient in reality, for the purpose of this investigation, ω was chosen as the nominal angular frequency (i.e. $100 * \pi\ rad/s$) ignoring any effect of changing ω on the resultant torque. This was considered to generate an ideal step load torque to mainly observe the effect of inertia.

From the results, the effect of inertia can be seen in the initial slope after the occurrence of the load change. Also, it has a significant effect on the peak drop and the time of peak drop. However, the inertia has not influenced the steady state frequency due to the PI control.

Revisiting the swing equation in (3.2.1), the relationship between the system inertia and the change of speed for a change of load can be identified (angular speed is directly proportional to the frequency). To estimate the relationship between ROCOF and the inertia, the classic swing equation can be rearranged as follows. The rotational energy of the engine rotor $E(J)$ can be written as a function of the rotational speed $\omega(rad\ s^{-}1)$ and the combined moment of inertia of the prime mover and the generator $J(kgm^2)$,

$$E = \frac{1}{2}J\omega^2 \tag{3.3.6}$$

When the power system operates at its nominal speed ω_0, (3.3.6) becomes,

$$E_0 = \frac{1}{2}J\omega_0^2 \tag{3.3.7}$$

When a sudden load disturbance occurs, the engine must supply the load with

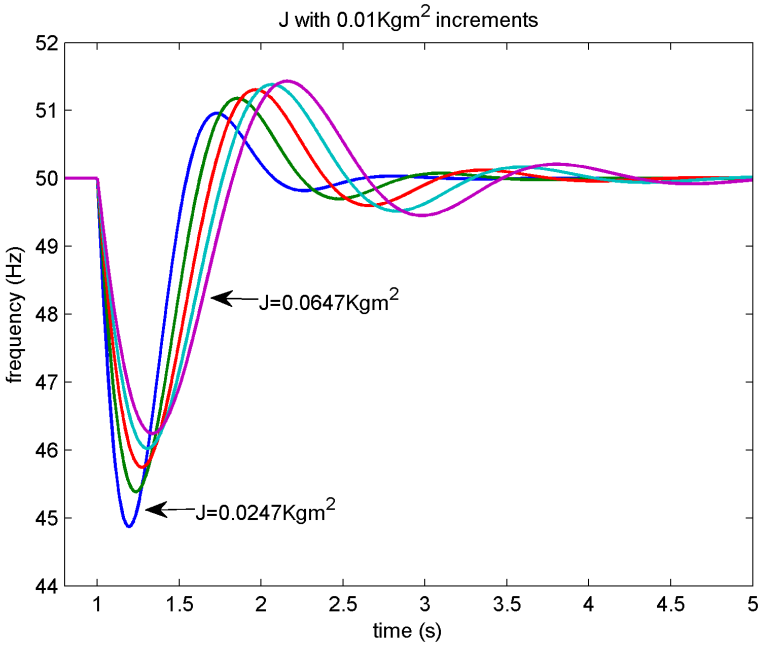

Figure 3.14: Frequency response of the synchronous generator for various system inertia

its existing rotational energy until the governor action takes over.

By differentiating (3.3.6), following is deduced;

$$\frac{dE}{dt} = J\omega\frac{d\omega}{dt} \tag{3.3.8}$$

Just after the application of the load disturbance, the rotor speed is close to the nominal value i.e. $\omega \approx \omega_0$; thus, (3.3.8) becomes,

$$\frac{dE}{dt} \approx J\omega_0\frac{d\omega}{dt} \tag{3.3.9}$$

After rearranging,

$$\Rightarrow \frac{d\omega}{dt} = \frac{1}{J\omega_o}P_d \tag{3.3.10}$$

where $P_d = dE/dt$ is the active power required by the load disturbance.

By substituting $\omega = 2\pi f$, and $\omega_0 = 2\pi f_0$ one can obtain,

$$\frac{df}{dt} = \frac{1}{4\pi^2 f_0}\frac{P_d}{J} \tag{3.3.11}$$

The above equation describes the relationship between the ROCOF and the load

disturbance. For a given load change the ROCOF is inversely proportional to the system inertia. The same can be confirmed in the results shown in Fig.3.14, where the ROCOF decreases with increased inertia. The values of ROCOF calculated according to the (3.3.11) are shown in Table 3.4. The ROCOF values calculated match with the ROCOF graphically observed in Fig.3.14. As can be seen, the calculated ROCOF values shows a good approximation to the ROCOF values that were observed from the graph.

J (kgm^2)	**ROCOF calculated** (Hz/s)	**ROCOF observed from Fig.3.14** (Hz/s)
0.0247	57.02	56.2
0.0347	40.59	40.0
0.0447	31.51	30.8
0.0547	25.75	25.3
0.0647	21.77	21.3

Table 3.4: Calculated ROCOFs for different inertia (J kgm^2) for a load of 2.78 kW compared with the values observed from Fig.3.14

Effect of Engine Time Constant

The transfer function of the engine was chosen to be a first-order system to simplify the engine transfer function. From the regression analysis, the value of the engine time constant was found to be $T_{en} = 38.1\ ms$. The impact of this pole can be better understood in the root-locus diagram of the complete speed feedback system, shown in Fig.3.15, for the forward path transfer function $G_{\omega PI}(s)G_{gen}(s)G_{mech}(s)$.

The most influential roots (the dominant poles) belong to the PI speed controller and the generator. The fast engine pole has a little effect on the transient according to control theory [87].

3.3.2 Creating the Voltage Waveform

Having modelled the speed loop with acceptable accuracy, next the voltage can be generated from the frequency response to replicate the experimental voltage. This is important for frequency detection later in the study.

The angle of rotation is related to the rotational speed of the generator by the relationship,

$$\theta(\tau) = \int_0^\tau \omega(t)dt \tag{3.3.12}$$

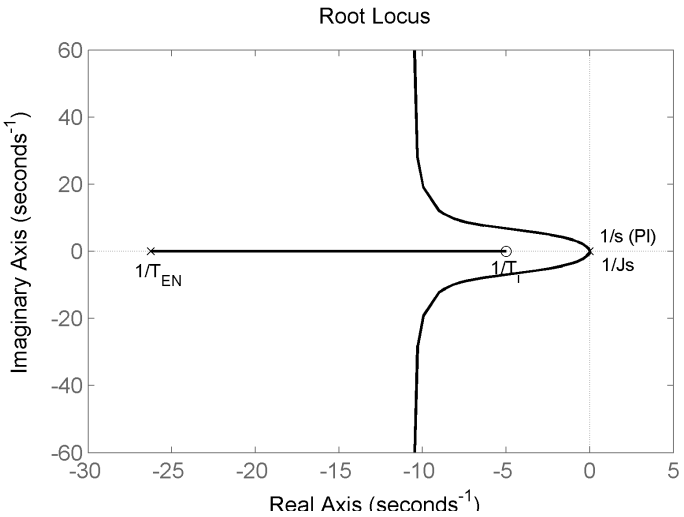

Figure 3.15: Root locus of the speed-loop

θ can be used to create a quadrature voltage $V_{\alpha\beta}$ as,

$$v_{\alpha\beta} = V_{pk} exp(j\theta) \tag{3.3.13}$$

where $v_{\alpha\beta} = v_\alpha + jv_\beta$, V_{pk} is the voltage amplitude.

This in-quadrature $v_{\alpha\beta}$ can be transformed in to a balanced 3-phase voltage v_{abc} using an inverse Clarke transform given by,

$$\begin{bmatrix} v_a \\ v_b \\ v_c \end{bmatrix} = \begin{bmatrix} 1 & 0 \\ -\frac{1}{2} & \frac{\sqrt{3}}{2} \\ -\frac{1}{2} & -\frac{\sqrt{3}}{2} \end{bmatrix} \begin{bmatrix} v_\alpha \\ v_\beta \end{bmatrix} \tag{3.3.14}$$

The block diagram that was used to generate the 3-phase voltage is illustrated in Fig.3.16. Thus, a balanced and undistorted 3-phase voltage is created, of which the amplitude is 325 V and the fundamental frequency is 50 Hz.

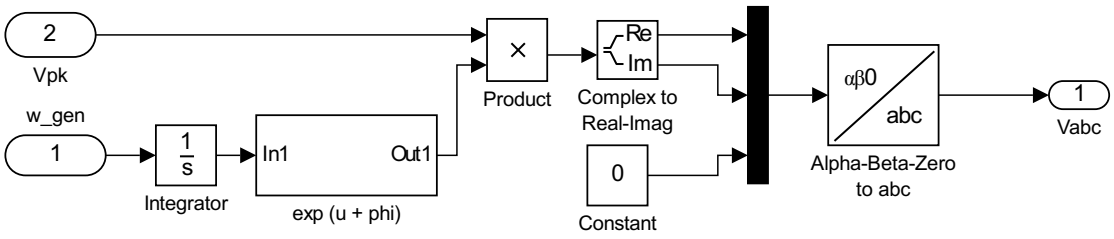

Figure 3.16: Transformation of the 3-phase sinusoidal waveforms using the speed signal of the generator

Since the actual weak grid voltage to be reproduced has considerable harmonic

contamination, a similar distortion needs to be added to the clean voltage waveform generated in simulation. Using the magnitude and the phase values relative to that of the fundamental as listed in Table 3.2, the quadrature harmonic waveforms in the $\alpha - \beta$ frame $v^n_{\alpha\beta}$ on the original waveform given in (3.3.13) were superimposed before transforming to v_{abc}.

The quadrature nth harmonic in the $\alpha - \beta$ frame is given by,

$$v^n_{\alpha\beta} = V_{pk}\{V_n exp(n\theta + \phi_n)\} \tag{3.3.15}$$

where V_n and ϕ_n are the magnitude and the phase relative to that of the fundamental.

The block diagram in Fig.3.17 augments this system to add four more harmonic components.

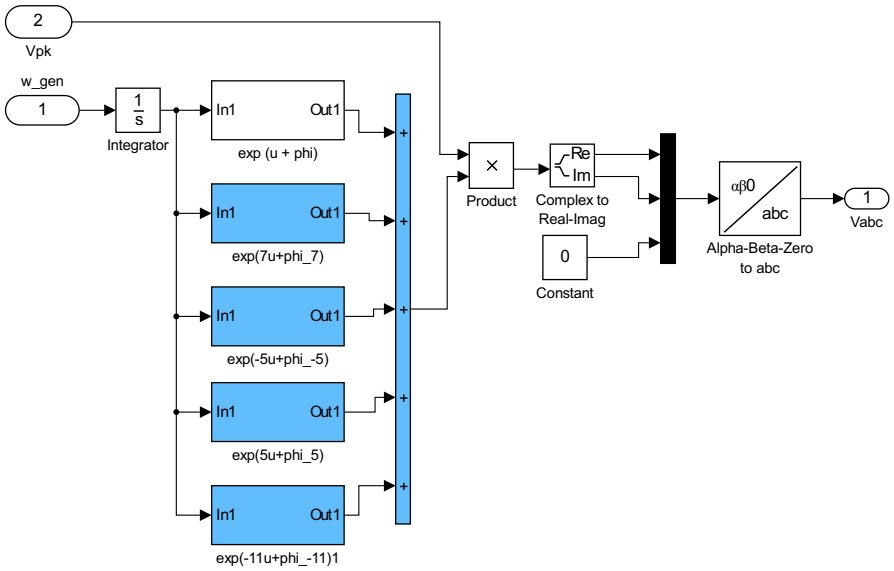

Figure 3.17: Procedure to add harmonics to the 3-phase voltage signal

The 3-phase voltage waveform created with harmonic distortion is shown in Fig.3.18.

3.3.3 Source Impedance

The source impedance is significant compared to the load-side in a weak grid. Thus, the effect of the source impedance can be seen during connection (disconnection) of loads. As discussed earlier, it causes an abrupt voltage glitch (due to inductive reactance) followed by an overall voltage dip (due to impedance)

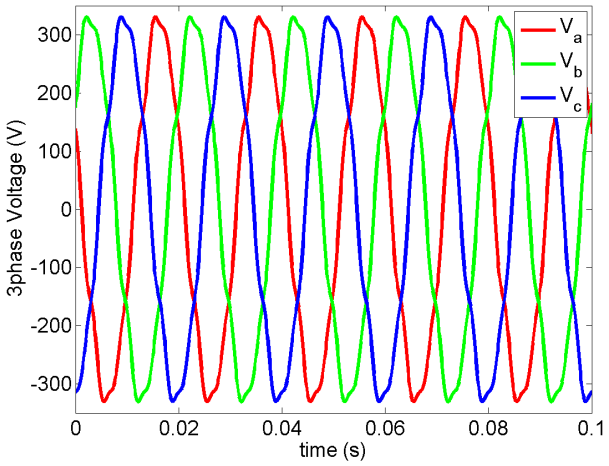

Figure 3.18: 3-phase voltage simulated with harmonics

during loading. During load shedding, a voltage surge occurs (due to inductive reactance). In this section, these properties are mathematically modelled in order to estimate the source impedance.

It is assumed that the source-side impedance is represented by an equivalent inductance of L_s and an equivalent resistance of R_s as illustrated in the generator equivalent circuit diagram drawn with the load-side resistance of R_L in Fig.3.6. When the resistive load is switched on, the resulting voltage transient provides some information regarding the ratio of $L_s/(R_s + R_L)$. However, this information was particularly difficult to extract since one cannot clearly observe the rise of the voltage in the sinusoidally varying 3-phase voltage waveform. Therefore, the current waveform during shedding of the load is considered, two phases of which are shown in Fig.3.19.

As shown in Fig.3.19, when the load is switched off, the current decreases gradually. This is because the current through the inductance can only decay gradually via the path through R_s. If the initial current just before switching off is I_0, the current waveform is given by an exponential decay,

$$I(t) = I_0 exp(-t/\tau) \tag{3.3.16}$$

where τ is the time constant of an RL circuit given by L_s/R_s. By definition, τ is also the time taken for the current to decay down to 36.8% of the initial value I_0. This time can be estimated from Fig.3.19 for both phases as $\tau = 25\ ms$.

Hence, the relationship can be deduced,

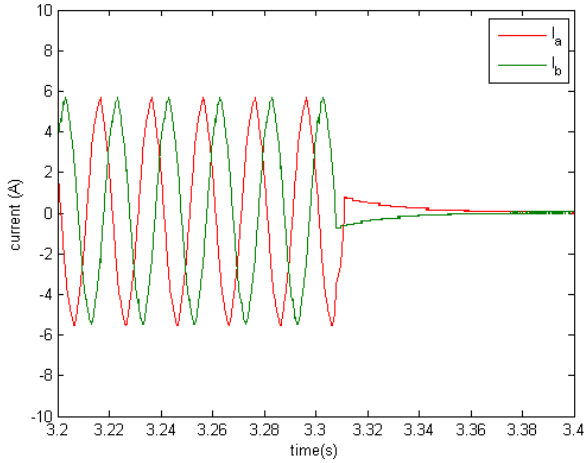

(a)

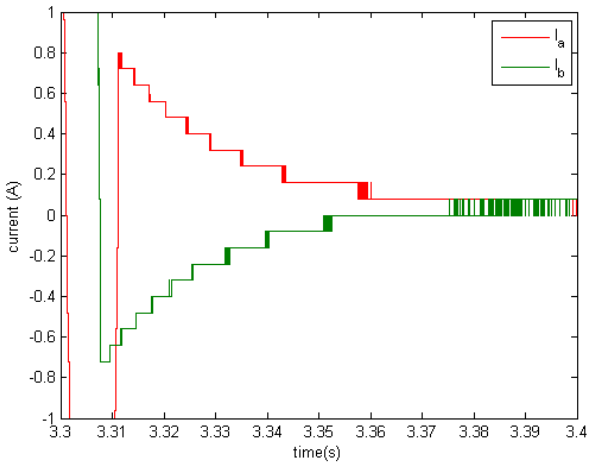

(b) zoomed (a)

Figure 3.19: Two phase currents during shedding of 2.78 kW step load

.

$$L_s = \tau R_s = 25 \times 10^{-3} R_s \tag{3.3.17}$$

Earlier it was shown experimentally in Fig.3.5 that a voltage glitch occurs at the beginning of the load transient, which corresponds to point A in Fig.3.20. As soon as the glitch is recovered, the V_{PCC} attains a steady state level due to the fast action of the AVR at point B. However, since the frequency drops below $48Hz$, the frequency responsive AVR action commences to reinstate the voltage amplitude to the nominal at point C. At the intermediate steady state (point B), a voltage divider is formed between the voltages seen at the generator (V_{GEN}) and at the PCC (V_{PCC}) as given in (3.3.18),

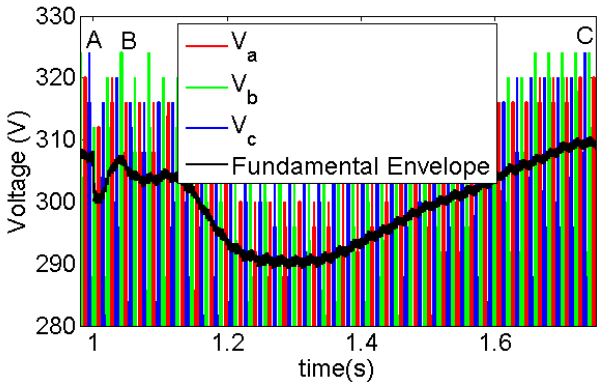

Figure 3.20: Experimental PCC Voltage for a load change of 2.78kW

$$\left|\frac{V_{PCC}}{V_{gen}}\right| = \frac{R_L}{|R_L + R_S + j\omega L_S|} \tag{3.3.18}$$

The voltage variation at the PCC for the loading of 57Ω resistive load observed experimentally was displayed in Figs.3.5 and 3.3b (envelope). From the figures the values of V_{GEN} and V_{PCC} for the fundamental were obtained as 307.5 V and 300.5 V respectively. Also, from (3.3.18),

$$(R_L + R_s)^2 + \omega^2 L_s^2 = R_L^2 \left(\frac{V_{gen}}{V_{PCC}}\right)^2$$

By substituting (3.3.17),

$$R_s^2(1 + \omega^2\tau^2) + 2R_L R_s - R_L^2 \left(\left(\frac{V_{GEN}}{V_{PCC}}\right)^2 - 1\right) = 0$$

and

$$R_s = \frac{R_L\sqrt{1 + (1 + \omega^2\tau^2)\left(\left(\frac{V_{GEN}}{V_{PCC}}\right)^2 - 1\right)} - R_L}{1 + \omega^2\tau^2} \tag{3.3.19}$$

the values of R_s and L_s can be found and are listed in Table 3.5.

R_S	0.9Ω
L_S	$22.5mH$

Table 3.5: Calculated values of source resistance and inductance using experimental results

The calculated values of R_s and L_s will be adopted in developing the weak

electrical grid simulation. The impact of adding source impedance, is replicated in the simulation and the corresponding voltage envelope is shown in Fig.3.21 and the zoomed in voltage glitch is shown in Fig.3.22.

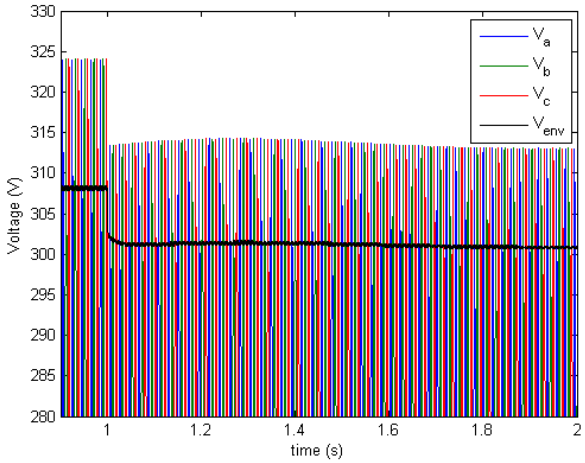

Figure 3.21: Simulated voltage after introducing source impedance

As can be seen, the voltage glitch and the overall voltage dip is now created during loading as a result of the presence of the source impedance. It can be confirmed by comparing Figs.3.3b and 3.21 regarding the voltage dip and Figs.3.5 and 3.22 regarding the glitch duration, that the source impedance is adequately modelled. Note that the simulated voltage in Fig.3.21 does not regain the nominal value as the AVR is not yet included in the design at this stage. The design of the AVR is explained in the following section.

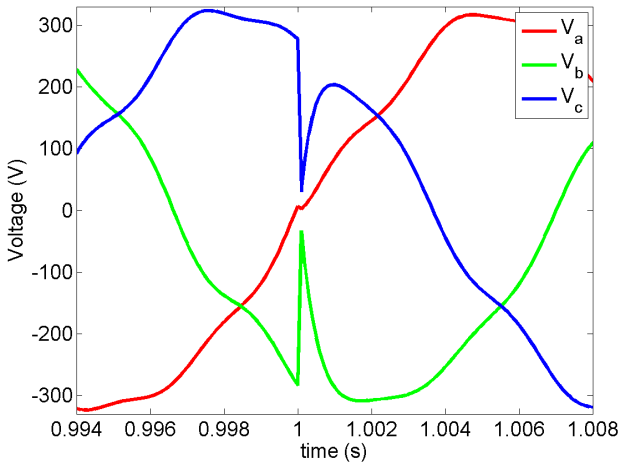

Figure 3.22: Simulated voltage glitch after introducing source impedance

3.3.4 The Effect of Automatic Voltage Regulation

During a voltage drop due to source impedance, the AVR activates in order to regulate the terminal voltage at the nominal. In this section, the replication of a response similar to that shown in Fig.3.5 is attempted in the simulation by modelling the AVR.

In section 3.2.2.2 it was realised that the activation of the AVR is fully frequency dependent. This means that the reference voltage is defined as a function of the instantaneous frequency of the voltage below 48 Hz. When the frequency is above 48 Hz, the *rms* reference voltage is 230 V (V_{rated}). Once the frequency falls below 48 Hz, the *rms* reference voltage is determined by the constant U/f, where U and f are the instantaneous *rms* voltage and the instantaneous frequency. Then the instantaneous *rms* voltage reference, V_{ref} can be calculated as,

$$V_{ref} = \begin{cases} V_{rated} & f \geq 48 \\ \frac{V_{rated} f}{48} & f \leq 48 \end{cases} \tag{3.3.20}$$

which is activation mechanism of the AVR. Using this, the designing of an AVR that brings the voltage to the reference voltage is considered. In this research, the aim is to replicate the AVR response with the simplest model possible. Fig.3.23 shows the block diagram of the AVR, as stated in the data-sheet [10]. The R 220 AVR has a shunt excitation system that consists of a 3-phase full-bridge rectifier, an exciter and a generator field. The AVR is a PID controller which regulates the amplitude of the instantaneous 3-phase voltage obtained via the rectifier.

For a design of the fast PID controlled AVR, the shunt excitation system is represented as a control block diagram as illustrated in Fig.3.24. The parameters used in the control blocks can be found in the Leroy Somer ® LSV40 generator data sheet [9] and are presented in Table 3.6.

Parameter	Symbol	Value
Smoothing time constant	$\tau_{s(AVR)}$	20ms
Exciter time constant	$\tau_{e(AVR)}$	11ms
Generator field time constant	$\tau_{g(AVR)}$	780ms
Line Voltage	V_{LL}	400V

Table 3.6: Control block parameters of the AVR as reported in data sheets [9],[10]

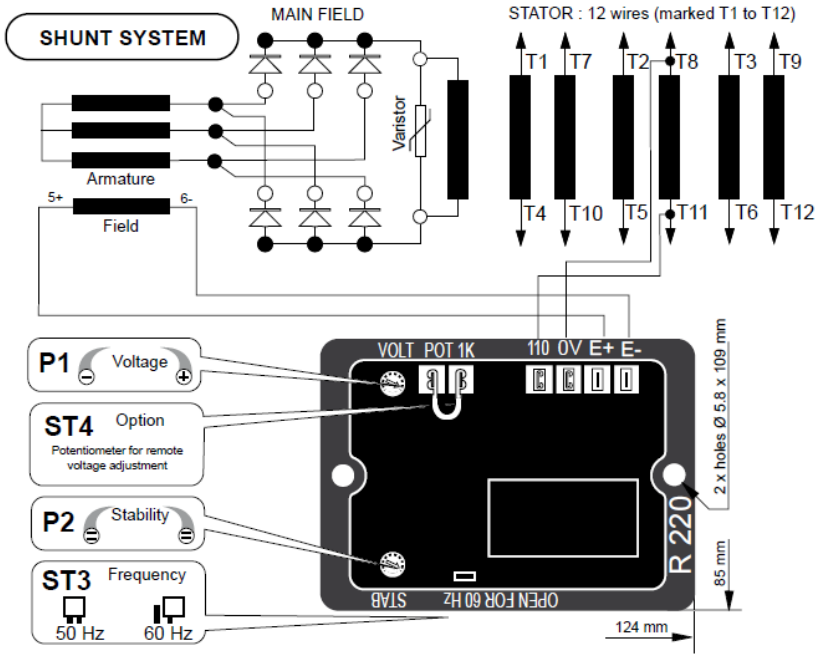

Figure 3.23: Block diagram of a classic AVR [5]

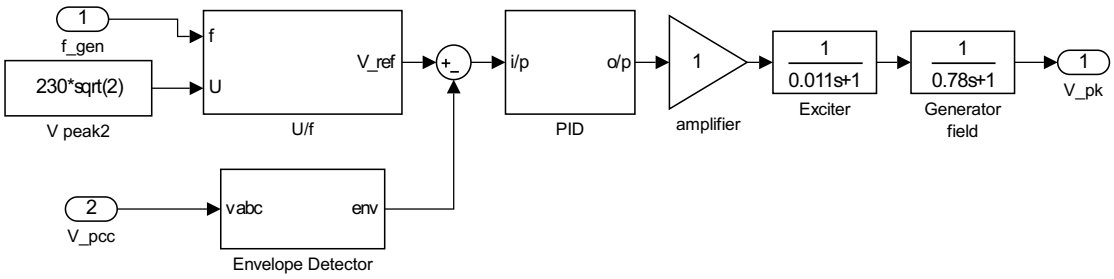

Figure 3.24: Control block diagram of a classic AVR

The rise time of the AVR was assumed based on the observations made experimentally in voltage from Fig.3.3b. The rise time of the AVR response is estimated to be $50ms$. As a rule of thumb in control theory, the rise time (t_r) and the bandwidth (BW) are related by,

$$BW \approx \frac{0.35}{t_r}$$

This provides a bandwidth of $7.0Hz$ for the AVR. The phase-margin of 65° was chosen to represent a damping factor $\zeta \approx 0.707$. Using the Matlab PID tuning tool, the parameters K_p, K_i and K_d of the PID controller were derived for the above bandwidth and the phase margin. All the control design parameters used in the AVR design including the PID gains are recorded in Table 3.7.

phase margin PM_{AVR}	65°
rise time $t_{r(AVR)}$	50ms
ζ_{AVR}	0.707
$K_{p(PID)}$	39.1
$K_{i(PID)}$	142
$K_{d(PID)}$	1.59

Table 3.7: PID controller gains in the AVR design

The envelope of the simulated voltage with the designed AVR along with the experimental counterpart is shown in Fig.3.25. The two voltage envelopes exhibit a reasonable closeness, noting the lack of information of the AVR internal operation. However, the designed AVR is capable of delivering a good platform to recreate the characteristics of weak grids.

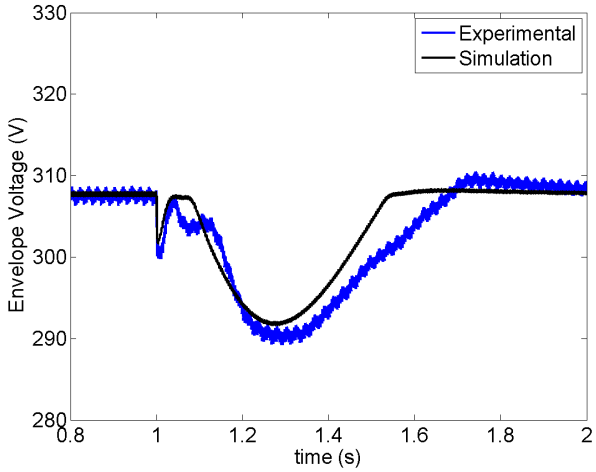

Figure 3.25: Voltage envelope: a comparison between simulation and experiment

3.3.5 The Complete Weak-Grid Simulation

The complete weak electrical grid model developed in Matlab/Simulink is shown in Fig.3.26. This model is capable of sufficiently replicating the effects present in an actual low voltage weak-grid powered by a single synchronous generator, as it has been developed consulting an actual weak grid emulation conducted in an experimental setup.

Next, the developed model was validated for various loads including the rated load listed in Table 3.8.

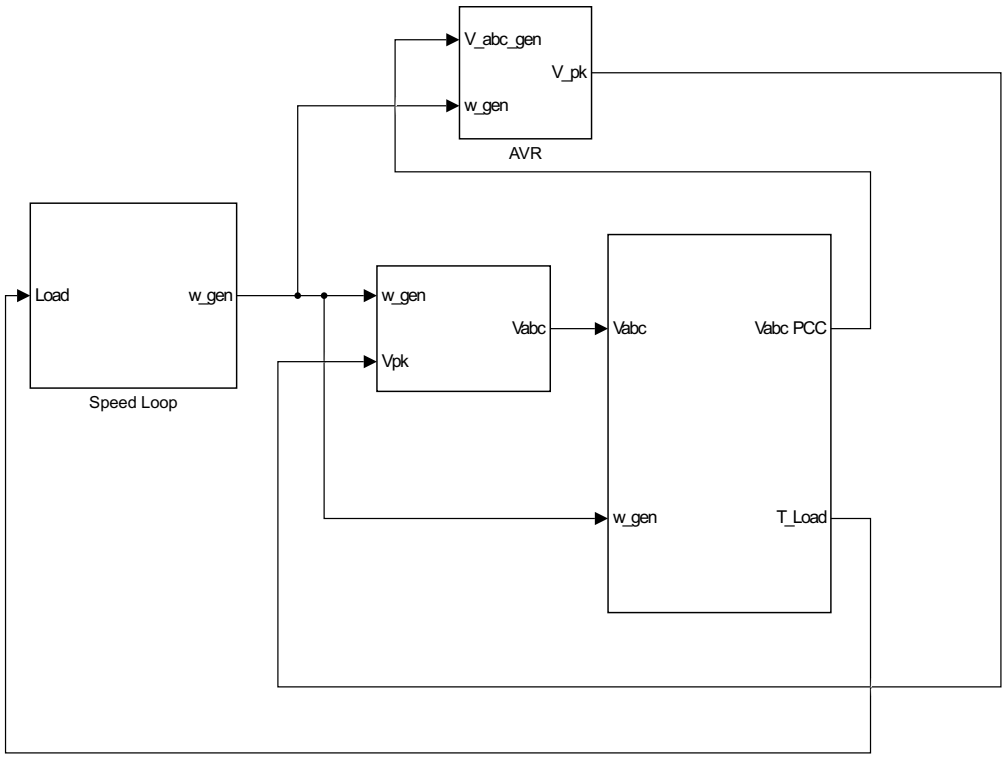

Figure 3.26: The complete weak-grid model

case	per-phase resistive load	3-phase load
case 1	57Ω	2.78kW
case 2	27.5Ω	5.77kW
case 3	20Ω (rated load)	8kW

Table 3.8: Per-phase resistive loads considered for validating the weak grid simulation model

The respective voltage and frequency variations will be observed. All the design parameters used in the simulation are now listed in the Table 3.9. These parameters will be used throughout the simulation studies in this thesis unless otherwise stated.

The simulated weak grid was loaded with 3-phase resistive loads of 57Ω and 27.5Ω. In Fig.3.27, the experimental frequency response due to loading of 57Ω and 27.5Ω are shown along with the corresponding simulated frequency responses. As can be seen from the results, the simulated system shows a sufficient approximation of the actual weak grid considered. The results confirm that the inertia of the two systems matches well in both cases, which is exclusively responsible for the initial rate of change of frequency. A higher drop in frequency is experienced when the load was increased. Moreover the system shows its integrity for different loads by settling around the same time. How-

Parameter	Value
Synchronous Generator	$8kW/10kVA$
Synchronous generator voltage	$230V_{RMS}$ line-line
Generator Equivalent Inductance	$22.5mH$
Generator Equivalent Resistance	0.9Ω
Inertia	$0.0447kgm^2$
Engine Time Constant	$38.1\ ms$
Governor speed loop prop. gain	$K_p = 1$
Governor speed loop int. time	$T_i = 200ms$
AVR $K_{p(PID)}$	39.1
AVR $K_{i(PID)}$	142
AVR $K_{d(PID)}$	1.59

Table 3.9: Simulated weak grid model parameters

ever, a slight mismatch after the second overshoot can be seen. This may be due to unaccounted non-linearities in the experimental system, especially in the IM vector drive, due to the limited disclosure of the internal parameters by the manufacturers.

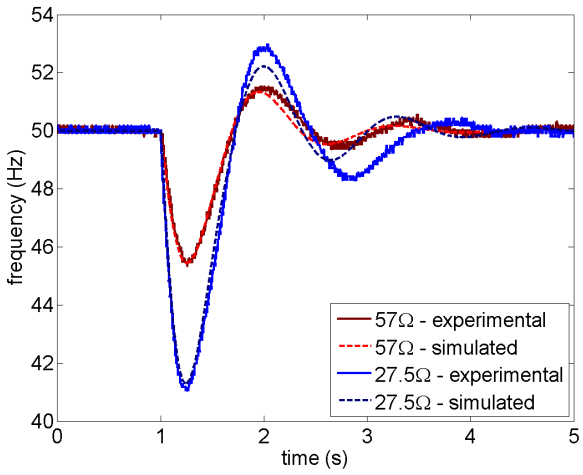

Figure 3.27: Speed response for loading case 1,2

In Fig.3.28, the envelopes of two voltage waveforms observed experimentally and simulated for loads case 1 and case 2 are shown. For 57Ω, the simulated and the experimental voltage envelopes exhibit a reasonable likeness. The application of the actual AVR mechanism in the simulation (as explained in section 3.3.4) has produced a similar effect to that observed in the experiments, confirming the frequency responsive voltage regulation. However, when the load resistance is roughly halved i.e. 27.5Ω (active power doubled) the experimental voltage follows a significantly different envelope after the load appli-

cation (from $t \approx 1.5\ s$) as shown in Fig.3.28. This AVR behaviour may be due to the activation of the LAM module of the AVR as given in the data sheet [10], occurring as a result of rapid and excessive drop of the frequency. However, the restoration of voltage and its dynamics under the LAM module were not disclosed in documentation.

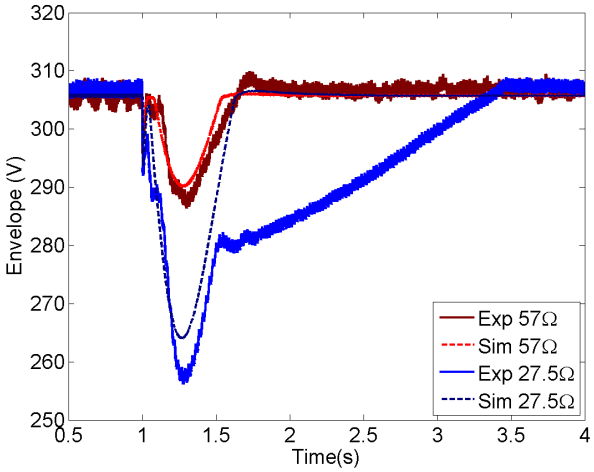

Figure 3.28: Voltage response for loading case 1,2

In the frequency response during load shedding as shown in Figs.3.29 and 3.30, the simulated and the experimental results have maintained the validity of the deduced inertia , as that in the case of loading. Other characteristics explained for loading are also true in this case. However, the subsequent oscillations in the speed response shows a visible discrepancy, especially for the higher load.

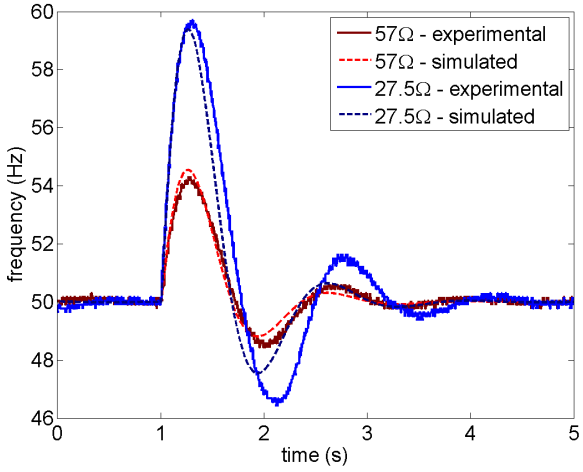

Figure 3.29: Speed response - shedding of loads for case 1,2

The disclosed behaviour of the IM drive in experiments does not suggest that

the vector control mechanism behaves differently in loading and load shedding. The developed simulation model is sufficient to effectively model load shedding in a practical weak-grid, even though the result is not as good as for the case of loading.

The voltage envelope during load shedding as presented in Fig.3.30 also shows considerable approximation for 57Ω load and a partly unexplained response for 27.5Ω. In the latter case, the frequency drops below 48 Hz in the second oscillation, the time and the amplitude of which differ in the simulation. In addition, the envelope detection algorithm does not cope well during load shedding as lots of voltage spikes and harmonics are generated due to the sudden change in current through the source inductance, in both simulation and experiment. Within these limits and in the absence of LAM in simulation, it can be concluded that the simulated model resembles the experimental system satisfactorily.

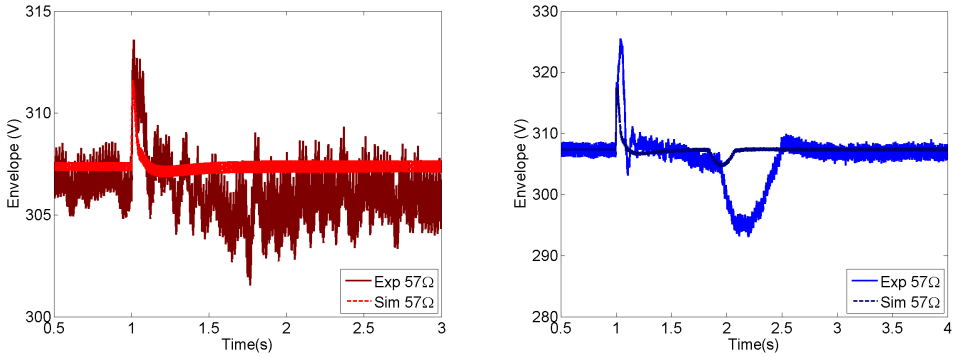

(a) $R = 57\Omega$ **(b)** $R = 27.5\Omega$

Figure 3.30: Voltage response - shedding of the loads for case 1,2

It has been suggested that such irregular voltage regulation in weak grids during load disturbances can be alleviated with the introduction of the proposed energy storage methods. Since frequency dips can be significant in weak-grids, the use of energy storage to limit off-nominal frequency deviations can directly minimise frequency dependant automatic voltage regulation as observed in the case of this weak-grid. The application of such method will be explained in detail in Chapter 4.

As an additional exercise the model was also simulated for the rated load to observe the validity in the extreme case. The rated load of 8 kW is equivalent to a per-phase resistance of 20Ω in a 230 V/400 V system. During loading and load shedding, the frequency response is shown in Fig.3.31.

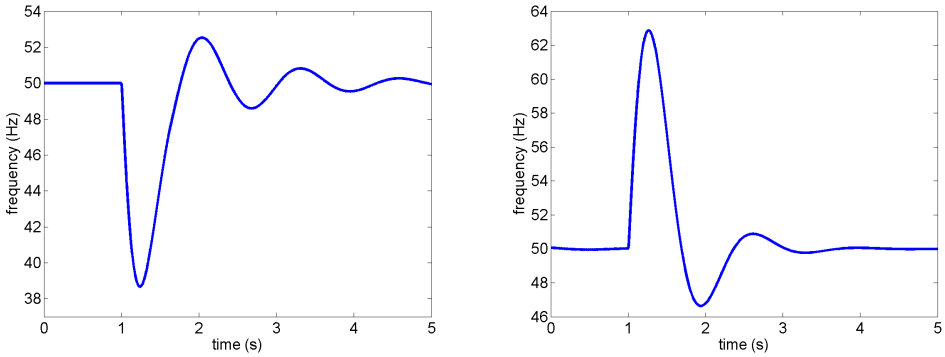

(a) Loading **(b)** Load shedding

Figure 3.31: Speed Response for loading and shedding of the rated load (case 3)

The rated load experiences the maximum frequency drop of $\approx 11Hz$. This is slightly less than the load shedding overshoot of $\approx 13\ Hz$, which is mainly due to the apparent load reduction provided by the AVR during loading. The corresponding frequency response for the rated load disturbance was not observed experimentally for the safety reasons.

3.4 Conclusion

In this chapter, a complete simulation model has been created using Matlab/Simulink in order to replicate a weak electrical grid powered by a synchronous generator. The development of the model was aided by an example 8 kW generation facility. The experimental results observed for speed and voltage during loading and shedding of various resistive loads were used to estimate the parameter values of the approximate model. The model includes a speed governor, an AVR and source impedances. The simulated model was validated for two resistive loads and has shown an adequate level of approximation between the experimental results and the simulated results. Further, the model displays capability to handle higher loads up to the equivalent rated load in simulation.

In the upcoming chapters, the simulated weak grid model will serve as the basis for the design and the development of the energy storage control and for comparison of associative frequency detection techniques, by providing a more realistic and accurate simulation environment compared to other simulation models presented in the literature.

CHAPTER 4

Frequency Stabilisation In Weak Grids Using Independent Energy Storage

4.1 Introduction

Frequency instability during load transients is a common power quality issue present in the weak electrical grids with distributed generators [19, 20, 30, 88]. The origin of frequency instability can be accounted by the low inertia and slow dynamics of the generation side as experimentally observed in Chapter 3. Improving frequency stability in low voltage weak grids may help prevent islanding, cascading failures in the main utility and consequential power disruptions to the consumers.

A novel energy management scheme is proposed in this chapter to utilize an energy storage for frequency stabilisation by fast injection of active power, while keeping the application independent from the host micro-grid. The decoupling of the energy storage (ES) control was made possible by using detected power system frequency as the main control signal. The power frequency is a direct indication of the real-time generation-demand imbalance and can be extracted from the voltage signal at any point in the grid. This obviates the need for load torque/current measurements to detect load changes, improving the plug-and-play capability of the proposed method. The proposed ES control technique is able to constrain the frequency within $\pm 1Hz$ limits, during load transients, yet maintain a finite speed error so that the generator's own speed governor can work unhindered to take over the load demand at the steady state. Also, the

control system facilitates efficient use of the energy available by making provisions for automatic activation and deactivation of the ES based on real time frequency, supplying only when frequency support is required.

In this chapter, the overall topology of the control scheme will be introduced first. Next, achieving independent control by using detected power frequency is explained. In support of this, application-wise frequency detection requirements will be discussed. Then, an approximated s-domain model representing each component of the control system is developed to examine the stability margin and to conduct off-line tuning. The complete control system is then validated under various tests, using the simulated weak-grid model developed in Chapter 3. Finally, some conclusions will be drawn followed by suggestions for further developments.

4.2 The Proposed Control Technique

As discussed in chapter 3, a large frequency drop occurs due to the inertial response of the power system in response to sudden load disturbances. The dynamic frequency response to the rated load disturbance in the 8 kW power system is shown in Fig.4.1a. The speed governing activates almost immediately to reverse the frequency drop by increasing the prime mover supply to the generator. This is known as the primary frequency response (PFR). According to the UK grid-code, DNOs are bound to provide PFR within 30 s from the occurrence of a disturbance [13].

An ES providing short-term active power could be used to prevent/mitigate such sudden frequency drops during PFR. Initially, the ES system is assumed to have the same rating as that of the power system and is connected in parallel with the load and the generator at the point of common coupling (PCC) of the grid. The amount of additional active power required to completely prevent the frequency from dropping is theoretically equivalent to the power derived using the time varying generator torque shown in Fig.4.1b. This also assumes that the speed governor increases the mechanical power as if there was a speed-error shown in Fig.4.1a. If the ES supplies active power to balance out frequency variations, the speed governor would see a null-error preventing the governor action. This means that when the frequency settles at the nominal without the help of the governor, the load is unsupported by the generator. In such a case, continuous support of the ES is essential until the shedding of load, for unin-

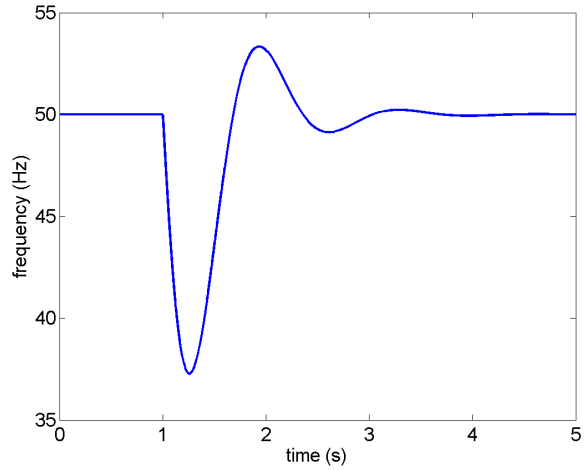

(a) Frequency response

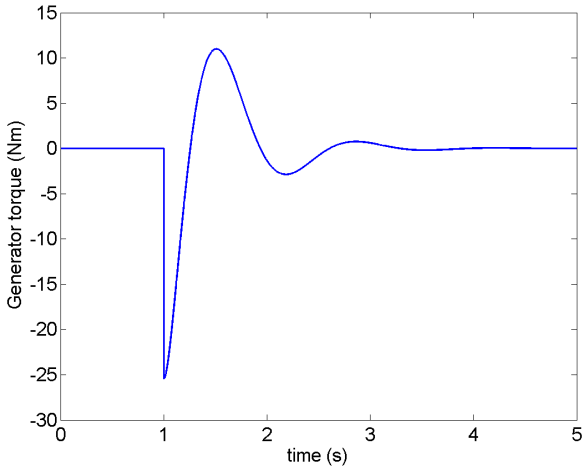

(b) The torque deficit as seen by the generator.

Figure 4.1: Simulated Frequency response and generator torque during the rated step load change (without ES support)

terrupted supply. Secondly, if the governor is made sensitive so that the prime mover is sent to saturation as in [50] even for minute speed errors, the governor and generator will be exposed to excessive wear and tear [14]. Therefore, a method is required to both increase the engine power via the governor with a non-null speed error and also to supply active power to balance the frequency fluctuations within constraints.

As briefly mentioned, the proposed ES control strategy is developed around the power system frequency, recognising its ability to indicate real time generation-demand imbalance of the grid. Also power frequency can be monitored throughout and it can eliminate the need for intercommunication between the governor

and the ES control, offering plug-and-play capability to the ES control. The deviation of the frequency from the nominal value (which indicates the load demand) is used as the actuation signal to the energy injection function. The two frequency bounds that the ES control is activated and deactivated are named as the lower frequency threshold ($f_{TH}^{l} = 49\ Hz$) and the upper frequency threshold ($f_{TH}^{h} = 51\ Hz$). The ES provides active power to the grid, when the frequency falls below the lower threshold 49 Hz and charges the ES from the grid when the frequency rises above the upper threshold of 51 Hz; thus controlling the frequency within a $\pm 1\ Hz$ limit.

At first, instead of using the detected frequency, the instantaneous frequency derived from the rotational speed of the generator was considered as the ideal input signal for the primary development of the control technique. This is purposely adapted to understand and appreciate the properties of the control system. The ideal frequency signal will later be replaced by the non-ideal detected frequency signal in the latter sections of this chapter.

Fig.4.2 shows a schematic diagram of a typical speed governor controlled power generation system as introduced in section 3.3.1 in chapter 3, with the proposed ES control. The ES is controlled in such a way that it supplements active power during periods when the frequency drops below the predefined threshold frequency.

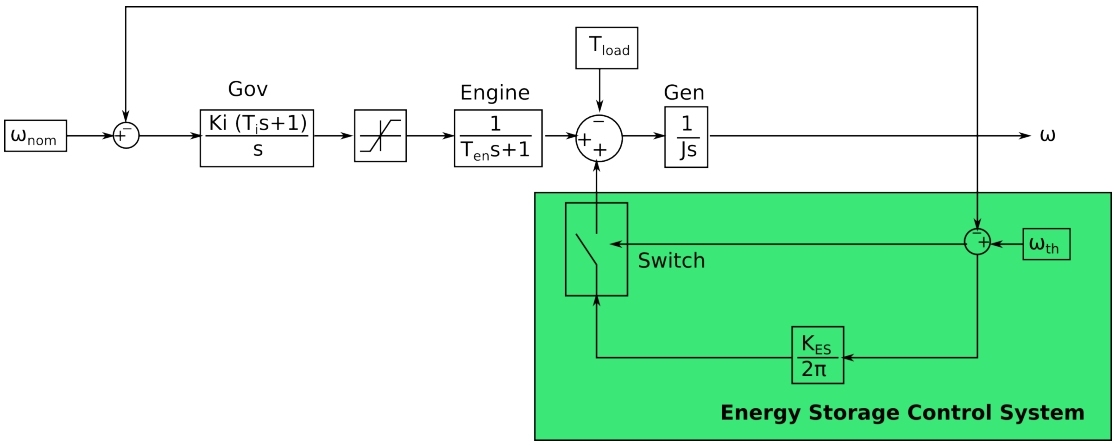

Figure 4.2: The control block diagram of the proposed ES control system within governor controlled power system.

Fig.4.3 shows how the frequency response without ES is improved by the proposed control technique. The proportional gain K_{ES} was set to 30 for this simulation (Note that the determination of the value of K_{ES} is explained in sec-

tion 4.7 of this chapter). When the frequency crosses the lower threshold of 49 Hz, the ES control activates and supplies active power proportional to the instantaneous frequency deviation from the threshold, so that the frequency is recovered at 49 Hz. Throughout the duration of the load transient, the speed governor acts until it reclaims the full speed regulation. Once the frequency is above the threshold, the ES control is deactivated.

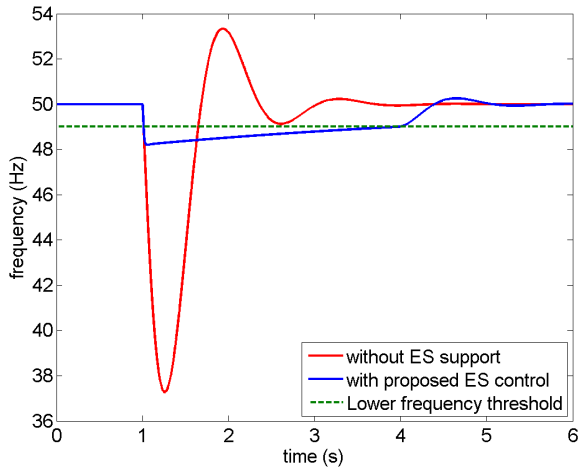

Figure 4.3: Frequency control improvement with the proposed method

As shown in Fig.4.3, the energy is supplied in the form of a torque T_{ES} to supplement the prime mover torque. This technique can now be expressed mathematically using a proportional gain of K_{ES} as;

$$T_{ES} = K_{ES} \begin{cases} f_{TH}^{l} - f & f < f_{TH}^{l} \\ 0 & f_{TH}^{l} < f < f_{TH}^{h} \\ f - f_{TH}^{h} & f > f_{TH}^{h} \end{cases} \tag{4.2.1}$$

The torque generated by the proportional actuation of the instantaneous frequency deficit is shown in Fig.4.4b. As shown, the ES is activated at 11 ms after the load disturbance, when the frequency crosses the threshold. While the active power supply from the ES is occurring, the governor action creates a gradual increase in the prime mover torque as shown in Fig.4.4c. This is only possible due to the sufficient finite frequency error left as a consequence of the ES effort to bring the frequency up to the threshold.

The proportionally controlled active power injection maintains a finite error of at least 1 Hz until the active power supplied by the prime mover surplus the power required to bring the frequency above 49 Hz. At this point, the ES sees

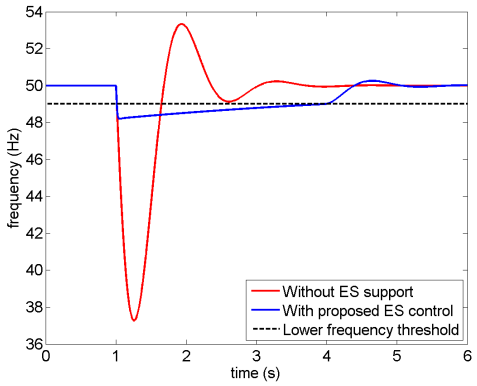

(a) The frequency response with ES control, without ES control

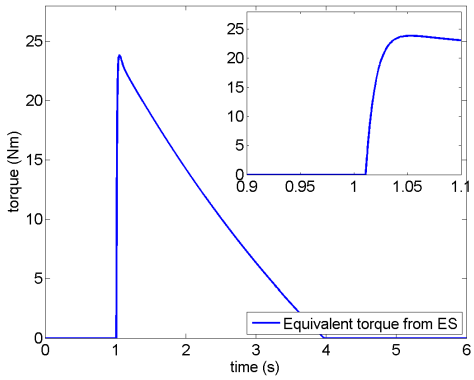

(b) The equivalent torque supplied by the ES control

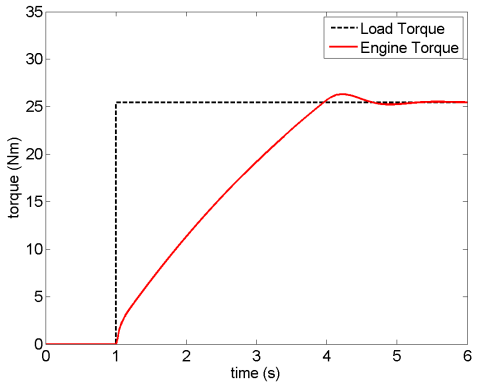

(c) The engine torque

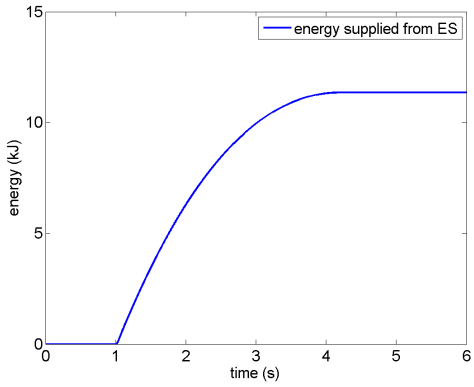

(d) The total energy supplied by the ES

Figure 4.4: The frequency response, ES control torque, the engine torque and the energy supply with the proposed ES control during the rated step load change at $t = 1s$,($K_{ES} = 30$)

no frequency error relative to the threshold; thus, automatically switches off. At the same time, the frequency regulation is fully handed over to the speed governor with a starting frequency error of 1 Hz. The rest of the frequency regulation occurs in a shape similar to the ordinary governor response, but with less overshoot in frequency as shown in Fig.4.4a.

According to Fig.4.4b, the torque profile suggests that the maximum torque is approximately equal to the rated load torque applied. This amount decreases gradually both due to the continuous proportional control action on the decreasing frequency deficit and the increasing prime mover power, and reaches zero resulting in an automatic switch-off. The triangular shape of this curve exhibits the gradual handover of responsibility from the quick acting ES buffer to the slow acting governor-prime mover.

As shown in Fig.4.4c, the engine accelerates gradually during the time period,

in which the ES is activated, as the frequency error is maintained at a near constant value. After this period, the engine torque undergoes a temporary overshoot, before settling at the steady state, due to the typical dynamics of the governor.

When comparing the torque response of the engine with ES support with the torque response without ES support as shown in Fig.4.5, the abrupt response of the governor and prime mover action seems to be damped in the presence of the ES control. The reason for this is associated with the modified governor action with the ES support. The speed governor is now acting upon a minute decreasing portion of speed error, in addition to the finite 1 Hz error left by the design, which in total is much smaller than the abrupt speed error imposed without ES support. Thus, the engine torque experiences a gradual acceleration and smooth transition at the equilibrium. This is also reflected in frequency as can be seen in Fig.4.4a.

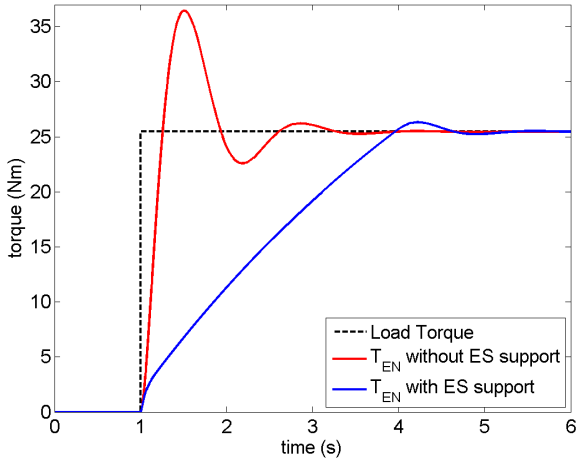

Figure 4.5: The engine torque with and without ES support

The total energy used by the ES can be calculated by integrating the torque profile multiplied by the speed in $rads^{-1}$ as shown in Fig.4.4d over time. This value for a rated load is an indication of the size of the ES required to supplement the worst-case load disturbance.

4.2.1 More Proportional Control Properties

Another property observable from the frequency response shown in Fig.4.4a is that the time taken for the overall frequency to reach the steady state is longer

with the ES support. During the ES active time, the time taken for the engine torque to reach the required torque is determined by the speed of the PI controlled governor. This is because the speed governor has a slower bandwidth than that of the proportional ES control. As explained earlier, the ES keeps the frequency error of the power system nearly a constant at about 1 Hz. When zoomed in, the shape of the frequency error becomes trapezoidal. By slowing down the ES controller, one can expect to lengthen the first edge of the trapezoid, increasing the frequency error and thereby shortening the governor response time.

In order to slow down the ES controller, the proportional gain K_{ES} needs to be lowered. Fig.4.6 shows the frequency response for systems with different K_{ES}, while keeping the same governor. A smaller proportional gain means there is more frequency error available to the governor. The larger the frequency error, the faster the governor response becomes, relatively reducing the total time taken to achieve the steady state. On the other hand, smaller K_{ES} increases the frequency drop. Thus, one would want to keep K_{ES} as large as possible to limit the frequency, but only large enough that it does not lengthen the settling time beyond the requirements i.e. $\leq 30\ s$ to fulfil frequency support during PFR.

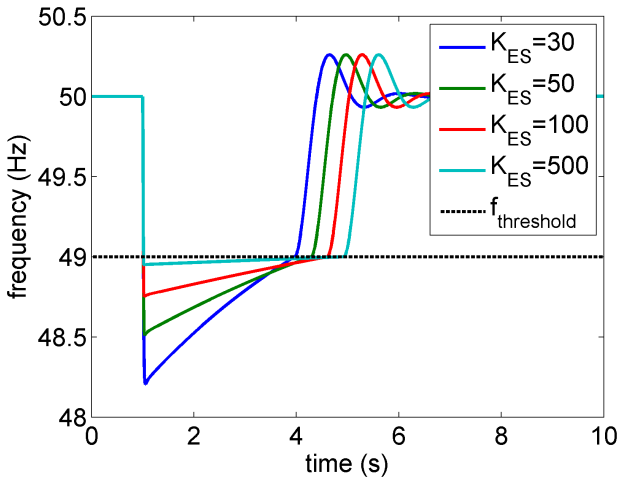

Figure 4.6: Frequency responses for a rated step load disturbance of a power system with ES controllers with different K_{ES}

Subsequently, the nominal steady state frequency is reached in equal time intervals from the instant the frequency arrives at 49 Hz, after completing the active power support. If a faster governor is used, the time to reach the steady state can be reduced. Since the project aims to deal with weak grid conditions with slow dynamics, the governor was kept as it is.

Having discussed the effects of K_{ES} value of the ES control on the overall frequency improvement, the next step is to explore the limits of K_{ES}. In order to discuss this, a control theory approach was used. The proposed ES controller is inherently non-linear due to the switching action at 49 Hz. During the ES active time the system can be considered linear time invariant. Hence, the switch was ignored in the control system analysis. This approximation is exact if the ES is switched on/off only once during a load disturbance, which is the condition in this ideal system (using ideal power frequency).

The open-loop transfer function of the generator + ES control system is given by;

$$\frac{\omega(s)}{T_{EN}(s)} = \frac{\frac{1}{Js}}{1 + \frac{K_{ES}}{2\pi Js}} \tag{4.2.2}$$

In Fig.4.7, the root locus of the speed governor + ES control system is drawn for varying K_{ES}. According to the evaluation of the open loop transfer function, it can be said that the complete system is stable irrespective of the value of the proportional gain K_{ES}. Therefore, for this ideal system, it is unable to define a limit for K_{ES} and the previously mentioned statement about K_{ES} still stands (i.e. increase K_{ES} as far as the settling time does not surpass 30 s).

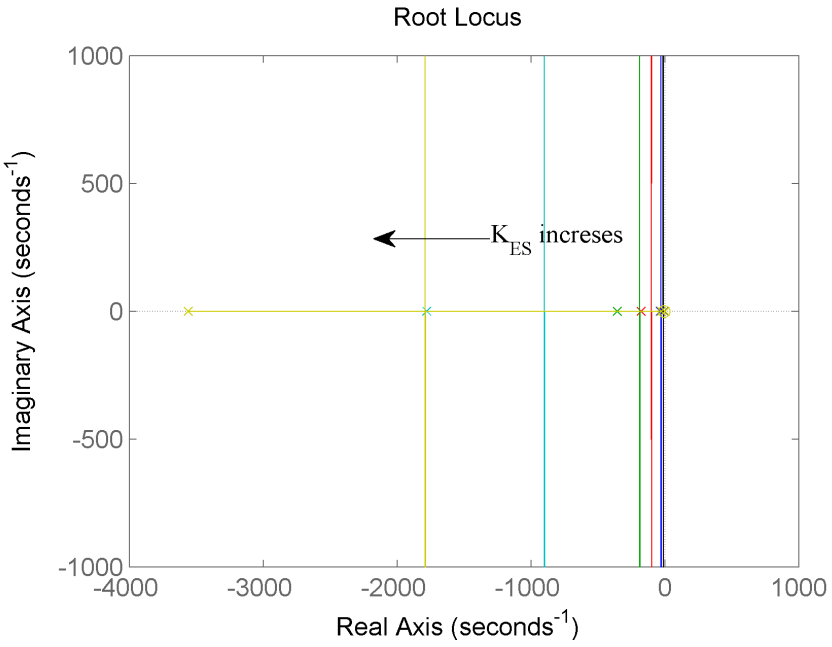

Figure 4.7: The root locus of the ideal ES control system for different K_{ES}

4.3 Frequency Detection Requirements

Up to now, the control of the ES was achieved using the instantaneous ideal frequency signal (i.e. the speed signal from the generator) of the power system. To improve the control system ideal frequency will be replaced by detected frequency. Therefore, it is necessary to introduce non-ideal conditions and test the control technique against them. Practically, the power system frequency cannot be obtained instantaneously. In real world applications, the frequency has to be estimated via a dedicated frequency detection method. Usually, the frequency is estimated by processing the voltage waveform. Because the proposed control technique and its properties depend on the power system frequency, this section is dedicated to observing the effects of using a detected frequency signal on the control system.

The grid environment considered in this research is a weak grid powered by a synchronous generator. The typical 3 phase voltage signal generated by a synchronous generator in a weak grid was experimentally observed in Chapter 3. The voltage was not only distorted with harmonics but also contained effects of AVR and supply impedance as various forms of unbalances. While the frequency detection methods were thoroughly investigated for performance in highly distorted weak-grid conditions in Chapter 5, this section mainly concentrates on the effects of having a generic frequency estimation method in place of the ideal frequency signal in the ES control application.

When the voltage is processed by a frequency detection method, the following two characteristics are embedded in the estimated frequency. They are,

- The transient time delay (transient response)
- The steady state ripple (steady state response)

The transient and the steady state responses are specific to the frequency detection method used. The transient delay is a combined result of the voltage signal processing method of the frequency detection method, which usually incorporates filtering of the distorted voltage waveform. It is also a measure of the time taken to accurately detect changes in the frequency. The steady state ripple is the residual of the harmonic rejection mechanism of the frequency detection method. The larger the harmonic content in the input voltage signal, the higher the steady state ripple and the less precise the detected frequency is

[6, 54–56, 68]. An improvement in the transient response degrades the steady state response (i.e. a transient response with a smaller delay in the measured frequency results in an increased ripple in the steady state and vice versa). This is due to the interdependence of the two responses on the same process, such as filtering. The requirements of a generic frequency detection technique is presented next to identify the best compromise of the transient and the steady state responses for the application of the ES control for frequency support.

4.3.1 The Effect of Frequency Detection Time Delay

In order to observe the effects of time delay in frequency detection, the ideal frequency signal was modified with varying time delays. A time delay can be approximated by a first order lag according to control theory [87]. The modified control block diagram is shown in Fig.4.8. As can be seen, the first order lag of T_d (frequency detection delay) is placed before the proportional ES controller to impose the effect of the frequency detection delay at the most appropriate point.

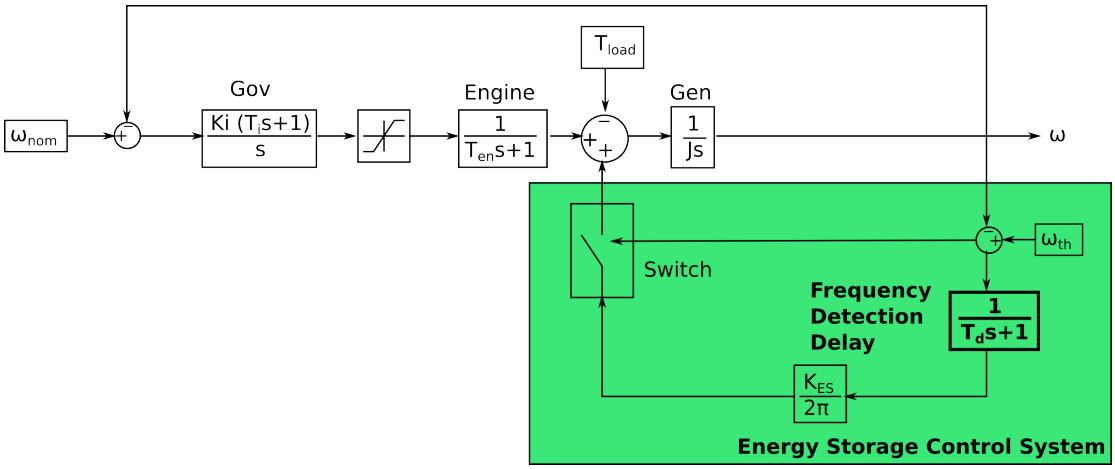

Figure 4.8: Block diagram of the proposed ES control system with frequency detection delay

Delay in frequency detection causes a delay in activating the ES. This condition directly influences the way the active power is supplied. The ideal frequency signal in the ES control is now replaced by the delayed signal, allowing the effect of the delay T_d to be seen in the frequency recovery. The frequency recovery achieved during rated load disturbance with the ES support for varying frequency detection delays of $10ms$, $20ms$ and $40ms$ are shown in Fig.4.9a. These values represent typical delays associated with common frequency de-

tection methods [6, 57, 59, 68, 70]. Fig.4.9a also shows a reference frequency recovery with no frequency detection delay. The active power supplied from the ES, corresponding to the delays considered is shown in Fig.4.9b.

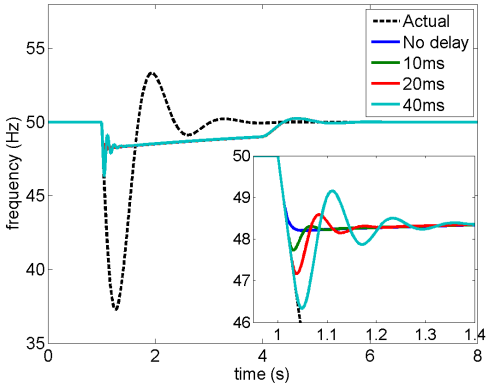

(a) Frequency recovery

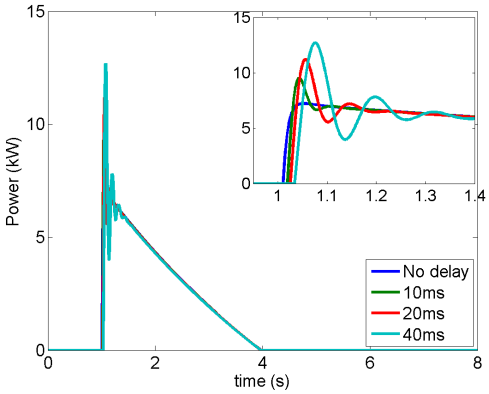

(b) Active power

Figure 4.9: The effect of frequency detection delay T_d (ms) on frequency recovery and active power supplied by the ES control during the rated load disturbance, $K_{ES} = 30$

The Figs.4.9a and 4.9b show the consequences of having a frequency detection delay on the recovered frequency and the ES usage. According to Fig.4.9a, when the delay is increased, the recovered frequency experiences more under damped oscillations with larger initial oscillations. However, the time taken for the frequency to settle at the final steady state is approximately the same. Therefore, it can be concluded that the first order delay decreases the damping factor of the system for a fixed proportional gain K_{ES}. The reason for the appearance of oscillations can be explained as follows.

A delay in the detected frequency delays the detection of crossing the frequency threshold. During this delay, the actual frequency drops further. Therefore, the ES supplies power trying to catch up. During this time, due to the supplied en-

ergy, the frequency reduces its drop rate down to zero. Yet, the ES still supplies power. During the next phase, the frequency starts to rise due to extra energy. After realising this, the ES reduces the supplied power during which time, the frequency stops rising and starts decreasing again but to a lesser extent creating exponentially damped oscillations in the frequency response. This scenario is illustrated in zoomed images of Figs.4.9a and 4.9b.

This phenomenon can also be viewed in a different perspective. The oscillations occur due to the high rate of injecting energy (i.e. injected power) proportional to the frequency drop. If the constant of proportionality K_{ES} is decreased, one might be able to reduce the oscillations. Therefore, when the frequency detection delay is increased, K_{ES} needs to be limited to mitigate frequency oscillations. In extreme cases where K_{ES} is too high, the ES may switch on and off rapidly. On the other hand, understandably, the maximum frequency drop in the recovered frequency increases with increased frequency detection delay as shown in Fig.4.10d. This may be of concern that a larger initial frequency dip crossing 47.5 Hz may start load-shedding, hence, reducing the effectiveness of the frequency support technique.

In Fig.4.10a, the peak active power response from the ES is seen to be increasing with respect to the time delay. Due to the exponential damping of the frequency oscillations, the initial peak active power is significantly high. Moreover, the damped oscillations in the frequency and the active power supplied has a coupled effect on each other ($P = \tau\omega = \frac{K_{ES}\delta\omega.\omega}{2\pi}$). The energy supplied during the frequency oscillations aids in damping the frequency oscillations, while the frequency triggers the ES to supply active power demand.

Another important characteristic measure of the ES control system is the total energy supplied during the frequency support period (the period during which the frequency falls below the threshold). The integrated power over the time of the load disturbance transient, calculated for various frequency detection delays are shown in Fig.4.10b. As seen in the figure, the time delay has a negligible effect on the total energy supplied. In fact, with increasing time delay, the total energy spent decreases slightly.

This result can be explained with the peak active power supplied and the time taken for ES control to bring the system above the threshold. According to the results, longer frequency detection delays were found to be associated with larger initial peaks and shorter settling times. This means that the frequency recovery is over assisted as a result of the frequency oscillations; thus, is able to

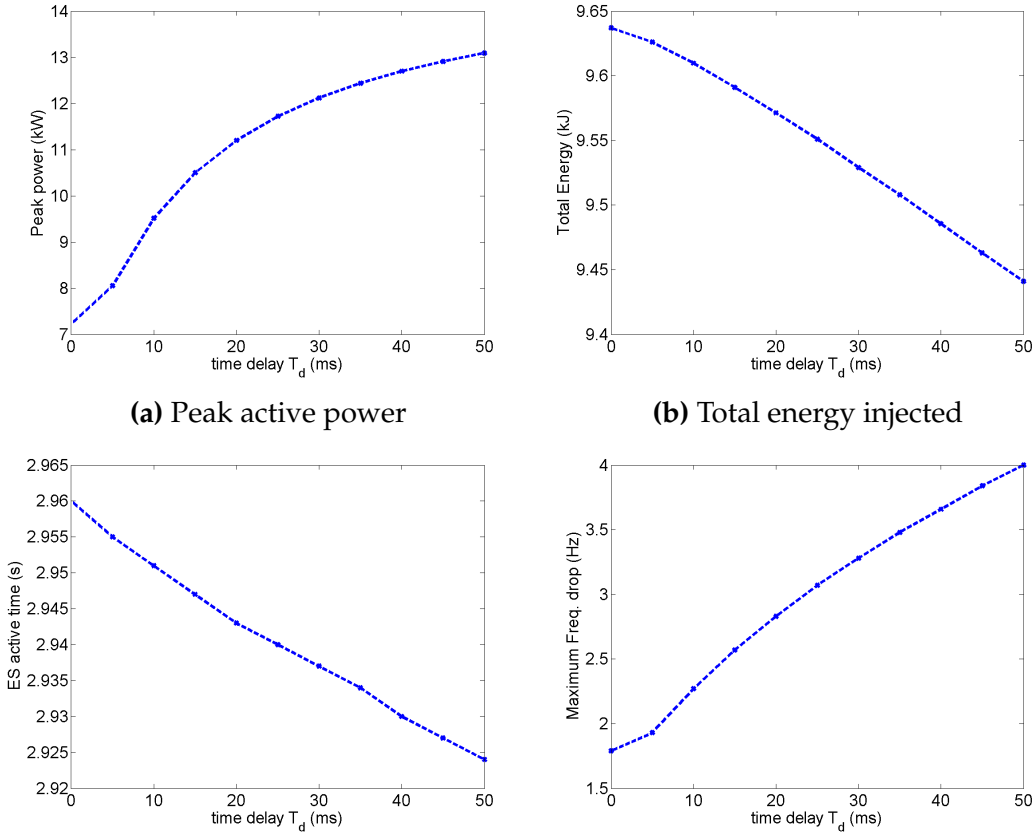

(a) Peak active power

(b) Total energy injected

(c) ES active time

(d) Maximum initial frequency drop

Figure 4.10: ES usage with different frequency detection delays T_d (for the rated load disturbance, $K_{ES} = 30$)

achieve the threshold with a subsequently shorter time, resulting in a marginal reduction in total energy supplied. Also, the ES active times of delivering active power support are relatively consistent under increasing detection delays as can be seen in Fig.4.10c.

4.3.2 Effects of Steady State Ripple of Frequency Detection

The steady state response of the detected frequency contains a ripple as a residual of the harmonics present in the input voltage signal. The amplitude of this ripple directly affects how the ES is used during the frequency recovery. This section will investigate the possible impacts of the ripple on the frequency response, in addition to the peak power and the total energy required from the ES.

In Chapter 3, the 3 phase voltage generated in the experimental weak grid was shown to prominently consist of the 5^{th}, 7^{th} and the negative 5^{th} harmonics of

the fundamental 50 Hz. The effects of harmonic distortion is present in almost all frequency detection methods as a residual ripple at the steady state. Frequency mixing occurring in most frequency detection techniques contributes towards this ripple. This especially creates a double frequency component of the fundamental. In order to eliminate the double frequency component a filtering technique is usually employed. The main task of the filtering is to extract the fundamental (50 Hz), while attenuating other remaining components.

In order to keep this section generic, the ripple frequency was assumed to be 100 Hz for this application as it is the most common occurrence in frequency estimation techniques [6, 55]. Higher ripple frequencies are usually attenuated by frequency detection techniques and their effects will be further attenuated by current controllers later used in the ES control system. In general, ripple is expected to switch the ES control on and off at the ripple frequency, but the extent of this switching is determined by the ripple amplitude. Thus, the key parameter considered in superimposing the ripple is the ripple amplitude. The modified frequency signal is fed into the ES controller. Fig.4.11 shows the frequency response for varying ripple amplitudes. Due to the ripple, the ES first switch-on frequency value has not changed, but the final switch-off frequency value has increased by the amount of ripple amplitude. That is, in the presence of harmonics the ES helps the engine above the threshold and has much smoother transfer indicated by the smaller frequency overshoot of the power system. As a result of this, the settling times are increased with the increasing ripple amplitude as well. However, note that in doing so, the ES system switches on and off frequently (at the frequency of the ripple). This also assumes that the ES can supply energy instantaneously.

The peak active power, the total energy spent, the time period of ES support were plotted against the ripple amplitude in Fig.4.12. Fig.4.12a shows that the peak active power increases linearly with increasing ripple amplitude. Figs.4.12b and 4.12c show that the total energy spent and the total time for recovery increases exponentially with increasing ripple amplitude. All of this suggest that, increasing ripple amplitude increases energy and power requirements of the ES. Taking all these into account, one can conclude that the increasing ripple requires larger ES and converters, but may provide smoother but longer frequency responses due to sustained oscillations at the 49 Hz threshold.

Further, the ripple in the detected frequency will toggle the supply, whenever the ripple superimposed on the signal crosses the frequency threshold. The

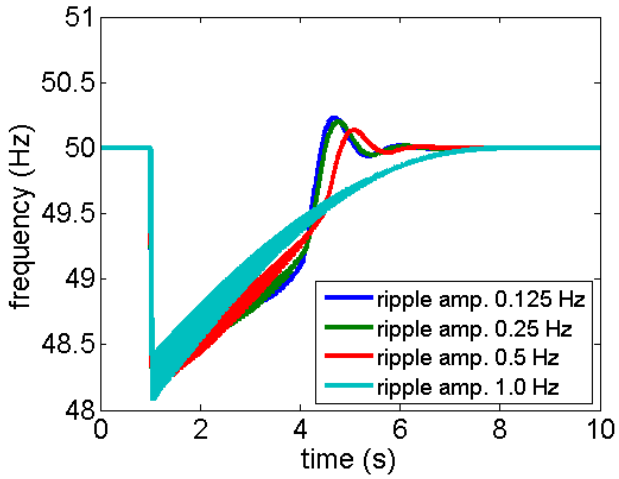

Figure 4.11: Frequency recovered for various ripple amplitudes (rated load, $K_{ES} = 30$)

amount of power delivered may depend upon the instant and the rate at which the frequency crosses the threshold. Therefore, it is possible that the peak power and the energy injected, to depend on the phase angle of the ripple. With this in mind, the next simulation study was carried out by switching the ES by a frequency signal with a ripple of constant amplitude of 0.25 Hz, but varying the phase angle. The observations made are shown in Fig.4.13.

The results presented show that the phase angle of the ripple at the point of trigger has no significant effect on both peak power supplied and the total energy injected as shown in Figs.4.13a and 4.13b. This is further supported by the ES active times shown in Fig.4.13c that have taken approximately the same amount of time for the frequency to reach steady state.

A study on effects of the frequency detection on the proposed ES control was carried out to identify specific requirements for frequency detection techniques suitable for independent ES control. The results based on the transient delay strongly suggest that a small delay results in efficient ES usage and better frequency recovery, while the results from the steady state ripple insist that a larger amplitude of the ripple requires more energy and power from the ES.

Therefore, it can be concluded that the candidate frequency detection technique has to be capable of,

- Fast transient response to minimise oscillations in the frequency recovery, in terms of magnitude and the frequency of occurrence.
- Less ripple amplitude for smaller energy and power requirements of the

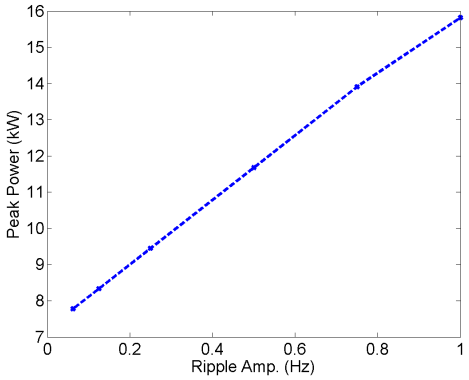

(a) Peak active power

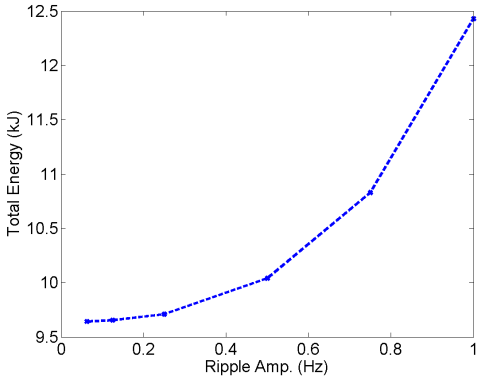

(b) Total energy injected

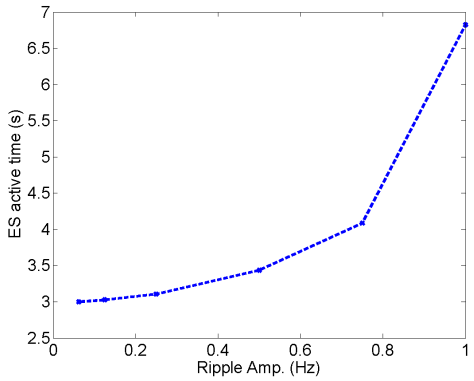

(c) ES active time

Figure 4.12: ES usage when the ideal frequency signal is superimposed by a 100 Hz ripple of varying amplitudes (for rated load disturbance and $K_{ES} = 30$)

storage.

Referring back to Fig.4.10a, one can see that the peak power nearly doubles beyond a frequency detection delay of 50 ms. Hence, for this application, one would consider 50 ms as the transient response requirement. A longer delay inadvertently requires one to financially invest more for a larger power converter as well.

The discussion on the ripple amplitude suggests that even though it is theoretically possible to allow for ripple to be as large as 1 Hz (more than 1 Hz would never switch ES control off), one would want to keep the size of the power converter to a minimum. Hence, 0.5 Hz was taken as the requirement considering that using a 50 ms frequency detection delay would double the size of the units already.

After consulting various possible frequency detection techniques in Chapter 5 for optimum transient and steady state responses, a Double Second Order Gen-

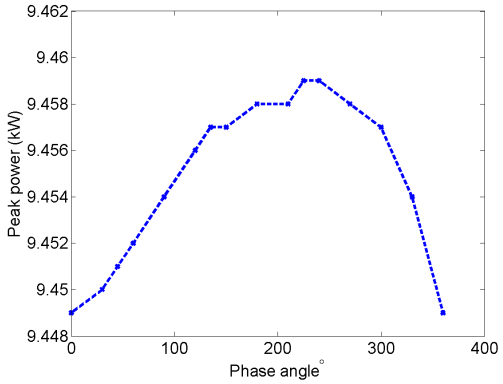

(a) Peak active power

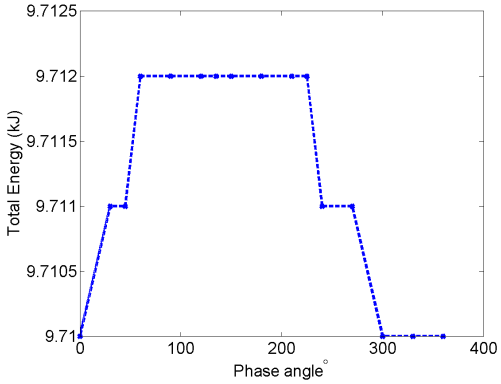

(b) Total energy injected

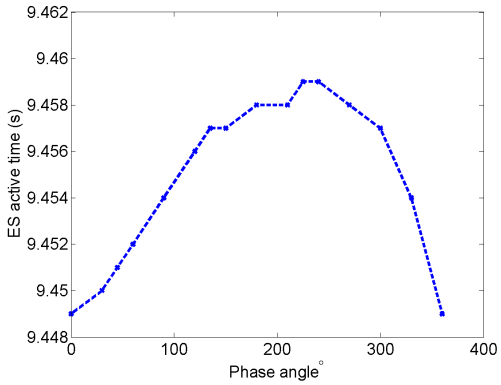

(c) ES active time

Figure 4.13: ES usage when switch-on occurs on different phase angle positions with rippled frequency input of 0.25 Hz (for rated load disturbance and $K_{ES} = 30$)

eralised Integrator based Frequency Locked Loop (DSOGI-FLL) was concluded to be the best technique to be used in independent ES control for frequency stability improvement in a weak grid. The selected optimum DSOGI-FLL with its tuning parameter $\Gamma = 125$ settles within 40 ms and has a ripple amplitude of ≤ 0.2 Hz for the given harmonic content. Further details of the decision process of selecting and optimising the DSOGI-FLL can be found in section 5.5 in Chapter 5.

4.4 The Energy Storage Control System With Frequency Detection

In the previous section, the frequency detection in general was represented as a first order lag. However, a detailed analysis to identify the best frequency

detection technique was carried out in chapter 5 of this thesis. This analysis concluded that the DSOGI-FLL based frequency detection is the most suitable method to estimate the frequency and it was understood that the frequency detection time lag must be represented as a second order transfer function for the DSOGI-FLL used in this work. This is explained fully in the section 5.5 in chapter 5. An LTI approximation of the DSOGI-FLL can be performed to analyse the stability by means of a simplified system and to validate the feasibility of the independent control of the ES by tuning the parameters prior to application on the grid. This section contains validating studies performed based on the approximation with the corresponding electrical system.

The approximated DSOGI-FLL system equation derived in section 5.5 in chapter 5 is given in (4.4.1),

$$G_{DSOGI}(s) = \frac{1}{s^2 + 183.5s + 23.69 \times 10^3} \tag{4.4.1}$$

It is necessary to validate the DSOGI-FLL approximation further by including it in the main ES control system. In order to do so, two systems were considered in the following discussion. System 1 generates a 3-phase voltage signal at the frequency of the generator and is distorted with harmonics found in the experimental voltage (as listed in 3.2). This will then be input to the DSOGI-FLL. The DSOGI-FLL detects the frequency deviation occurring due to the load disturbance and the resultant detected frequency signal becomes the input to the ES control. The ES control then injects the necessary active power as a torque equivalent at the PCC, thereby recovering the frequency change. A schematic of the system 1 is shown in Fig.4.14a. System 2 in Fig.4.14b replaces the DSOGI-FLL of System 1 with the approximated second order system, while keeping other control blocks the same with the properties defined in the previous section.

The two systems described above were simulated under different load disturbances. Fig.4.15 presents the respective frequency responses for varying step load disturbances. The frequency response of the ES control with the second order approximation of the DSOGI-FLL follows that of the ES control with the actual DSOGI-FLL well for different load conditions. This confirms the viability of using a second order approximation in the control system to represent the corresponding effects of frequency detection by a DSOGI-FLL.

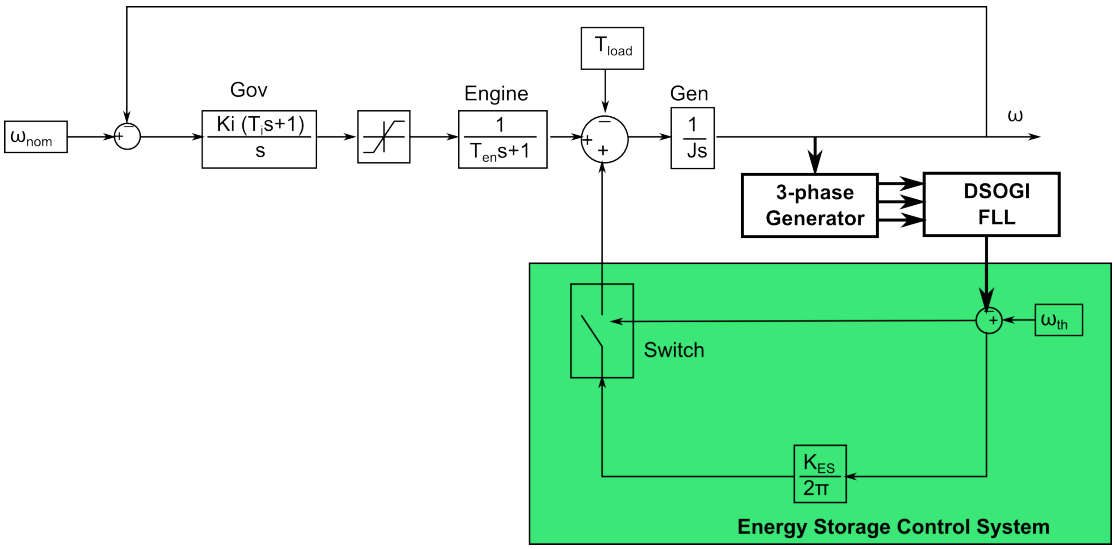

(a) System 1: Partially electrical system

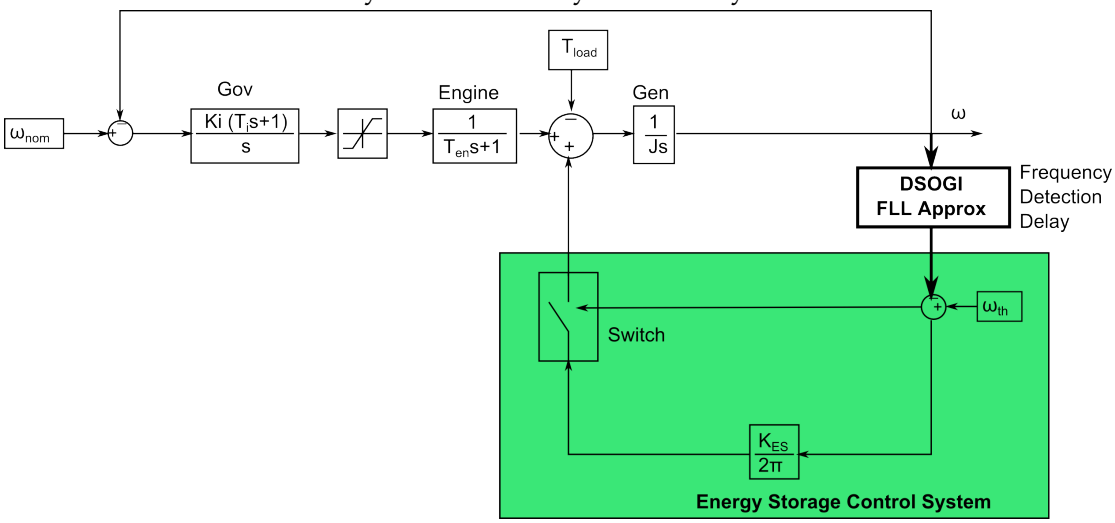

(b) System 2: LTI equivalent

Figure 4.14: The partially electrical system with DSOGI-FLL and its control system approximation

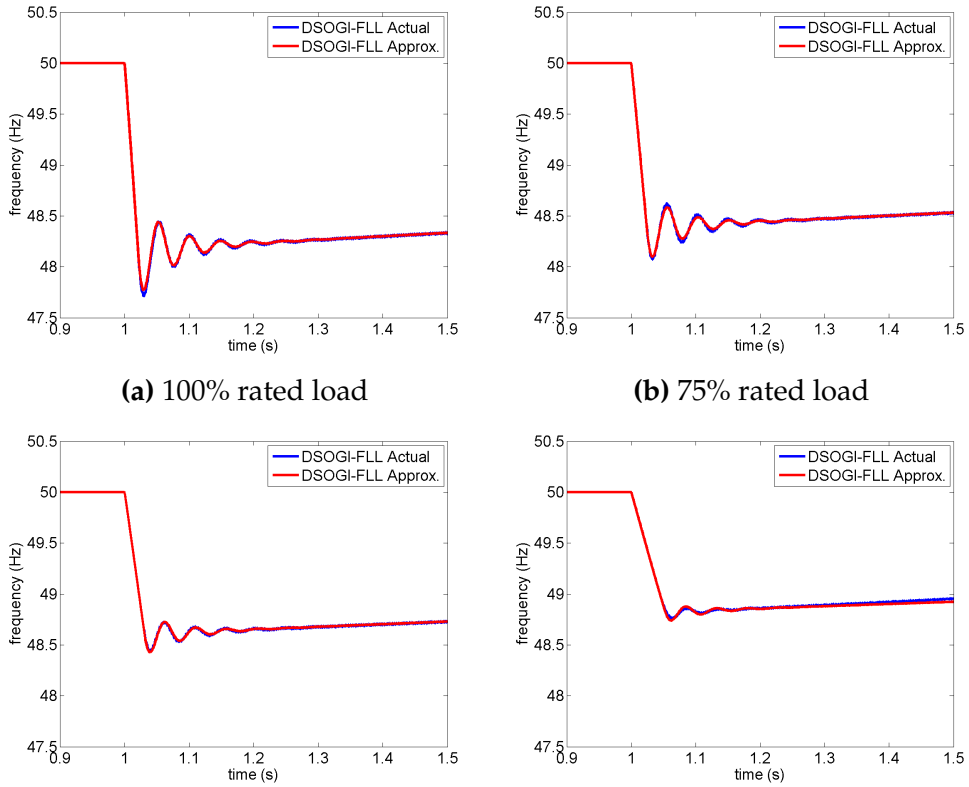

(a) 100% rated load

(b) 75% rated load

(c) 50 % rated load

(d) 25% rated load

Figure 4.15: Validation of the control systems approximation of the partially electrical system with DSOGI-FLL ($\Gamma = 125$), for different load disturbances ($K_{ES} = 30$)

4.5 Validation of The ES Control in a Simulated Electrical Grid

In the previous section, the approximation of the non-ideal ES control with the DSOGI-FLL, with an ideal 3 phase voltage source was validated. In this section, more non ideal conditions that affect the ES control in a real world application are investigated using more non ideal electrical components in the system. The approximated system is also tested for its validity for control and tuning purposes. The following non ideal properties that are mainly associated with weak electrical grids are to be considered.

- Application of electrical loads (only resistive loads were considered in this thesis),
- Effects of source impedance,
- The generator automatic voltage regulator (AVR) response,

- The power conversion delays associated with vector control.

As the first step, the load torque will be replaced by an equivalent resistive load. This load was connected to the 3 phase grid model developed in Chapter 3. The details of adding the 3 phase resistive load, calculation of power consumed in each phase, the total power consumption, hence, obtaining the equivalent torque as discussed in Chapter 3. Due to the pulsating nature of the load power and the dependence on the engine speed, the load torque now contains small variations in time, compared to a ideal step load torque. The load torque calculated is also fed into the approximated system in order to make an unbiased comparison. At this point, the voltage waveform includes the effects of the AVR and the source impedance described in Chapter 3.

In the presence of source inductance, the voltage experiences a sudden dip when a load disturbance occurs, since the current through the inductor cannot increase instantaneously. The sudden transient only lasts less than a cycle as was observed in the experimental weak grid studied in chapter 3. However, when the PCC voltage with the voltage glitch is processed through the DSOGI-FLL, an initial erroneous frequency dip occurs in the estimated frequency. This can falsely switch the ES control on and supply active power inaccurately. A detailed discussion on this is presented in section 5.7 in chapter 5, including a remedial method. A hybrid filter was used to mitigate the spurious frequency dip by means of combining a slow and a fast filter. Its effect can essentially be considered as equivalent to the effect of a fast filter, which can be represented as a first order transfer function with a time constant of 1 *ms* given in (4.5.1).

$$Fs(s) = \frac{1}{0.001s + 1} \tag{4.5.1}$$

The block diagrams of the electrical system and the approximated system with the modified elements are shown in Fig. 4.16.

The two systems are then simulated using a DSOGI-FLL with $\Gamma = 125$ for rated load disturbance and ES control gain $K_{ES} = 30$. The frequency recovery obtained by the electrical system and the approximated system are presented in Fig.4.17. The consistency in the performances of the two systems can be appreciated; hence, it can be concluded that the non-ideal parameters have been modelled in the approximated system appropriately.

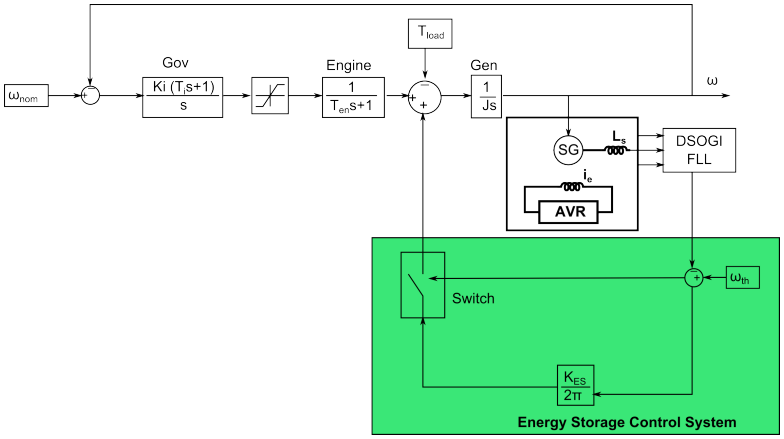

(a) System 1: Partially Electrical System

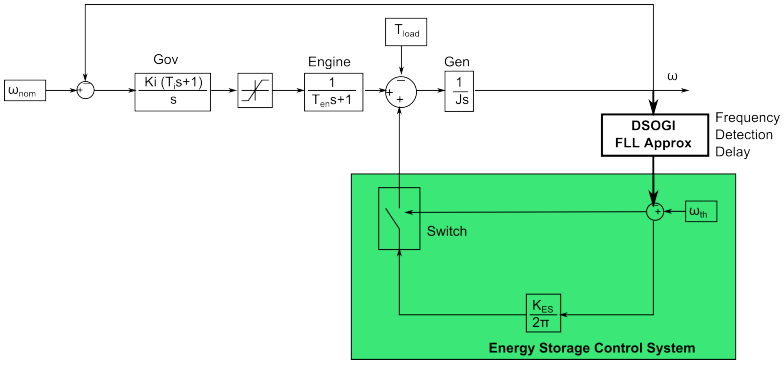

(b) System 2: LTI equivalent

Figure 4.16: Block diagram of the electrical system complete with AVR source impedance and DSOGI-FLL along with the system

4.6 The Complete System With Current Injection

Up to now, the proposed ES control was tested with the assumption that the ES is supplying a torque equivalent of the required active power support at the PCC. In reality, the ES is connected to the PCC via a DC/AC converter that is synchronised with the 3-phase voltage at the PCC. The inclusion of this power conversion in the electrical system and its equivalent approximated control system will be discussed in this section.

4.6.1 The Complete Electrical System

The active power requirement needs to be supplied through a DC/AC inverter, because the ES is usually a DC battery. Due to internal resistance and dependence on the state of charge, the battery voltage changes in short term and in long term respectively, when drawing current from the battery. Hence, in the most common configurations, the battery is connected to a DC bus via a

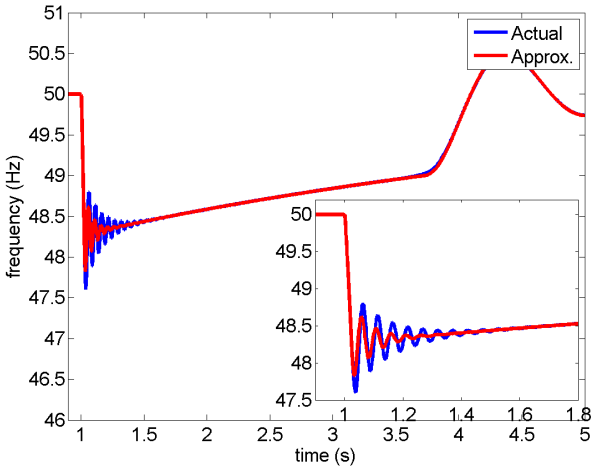

Figure 4.17: Frequency recovered by the ES control : In the electrical system (blue), and in the approximated system (red), (rated load, $K_{ES} = 30$

DC/DC converter. The DC/DC converter attempts to keep the DC bus at a respecified voltage by drawing current from the battery at the varying battery voltage. The DC bus is then connected to the 3 phase PCC via a DC/AC converter. This configuration allows the energy to flow both ways as required in this application. Both DC/DC and DC/AC converters are PWM controllers that switch at frequencies typically above 10 kHz.

In order to include the DC/DC and DC/AC converters by a simple model, a current controller (a current source inverter) was selected to inject power at the PCC. Since frequency support is the theme of this study, the converter was set to supply only active power. The required active power was injected as a d-axis current assuming that the required q-axis current is zero. The required d-axis current can be calculated using (4.6.1);

$$I_d = \frac{2\pi\, f_{DSOGI}\, T_{ES}}{V_d} \tag{4.6.1}$$

where I_d and V_d are the d-axis current required and the d-axis voltage at the PCC, f_{DSOGI} is the frequency measured from the PCC voltage.

The d-axis voltage V_d is calculated by the Park-transformation using the phase of the 3-phase voltage estimated by the DSOGI-FLL as detailed in chapter 5. Once the required current I_d is calculated, the per-phase currents are determined by the inverse Park-transformation using the same technique. The resultant current is directly injected at the PCC.

Typically, power converters, incur a relatively small delay both due to micro-processing and due to the control strategy. In chapter 6, the total delay of the power injection was identified as approximately 11 *ms*, from the experiments. This was accomplished by comparing the required power and the actual power delivered at the PCC. Hence, a delay of 11 *ms* was included as a first order lag to model the total delay including the vector control response between the ES and the PCC, as given in (4.6.2).

$$Vs(s) = \frac{1}{T_v s + 1} \tag{4.6.2}$$

where T_v is the total delay between the ES and the PCC including the vector control delay. The complete electrical diagram of the weak-grid supported by the ES is shown in Fig.4.18.

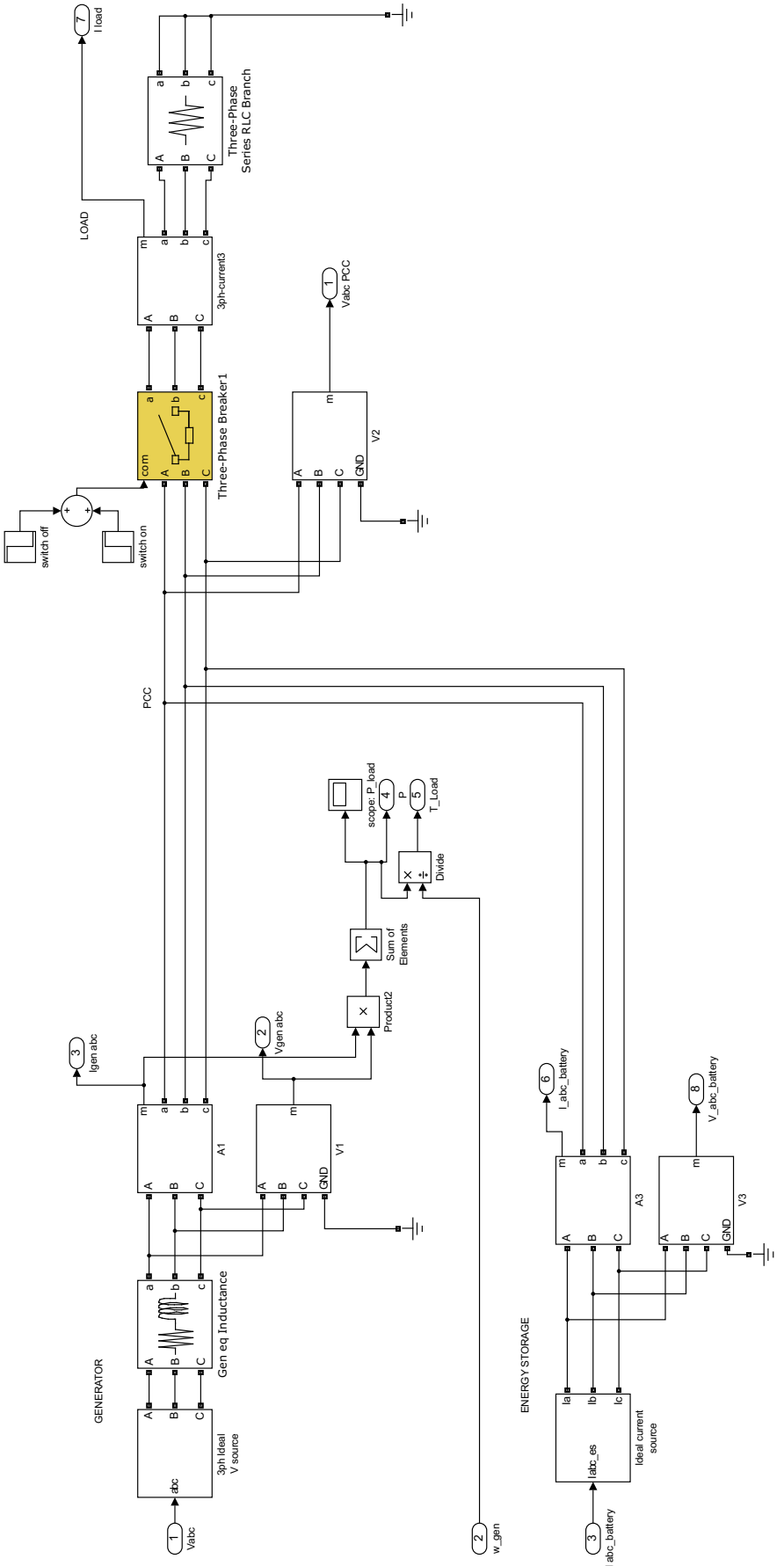

Figure 4.18: The complete electrical system in Simulink

4.6.2 The Complete Control Approximation

The complete electrical system has introduced many non-linear components in to the system. This includes the d-axis voltage determination, the active power calculation, the d-axis current calculation and the 3-phase current injection. At each point, the control system depends non-linearly on both instantaneous voltage and instantaneous frequency rendering them rather difficult to model.

While keeping the power conversion delay as a first order lag of 11 ms in the system, the other effects are lumped together as an unknown pole-zero pair. In order to determine the pole-zero pair, the equivalent load torque of the load power in the electrical system was fed into the approximated system with the pole-zero pair $\frac{T_b s+1}{T_c s+1}$ placed before supplying the ES torque (T_{ES}) to the grid. By using a regression analysis, the torque equivalent of the injected power of the electrical system was matched with T_{ES} of the approximated system after the pole-zero pair. The resulting T_b, T_c was found to be $T_b = 0.0264\ s$ and $T_c = 0.114\ s$.

The pole-zero pair determined this way is only valid for the specified impedance at the PCC, and the AVR of the generator. Even though these are characteristics of the host grid, they can be determined by an automated regression analysis as mentioned above to obtain an equivalent lumped LTI system transfer function. Therefore, this does not necessarily reduce the plug-and-play capabilities of the proposed ES control.

The final approximated control system is shown in Fig.4.19.

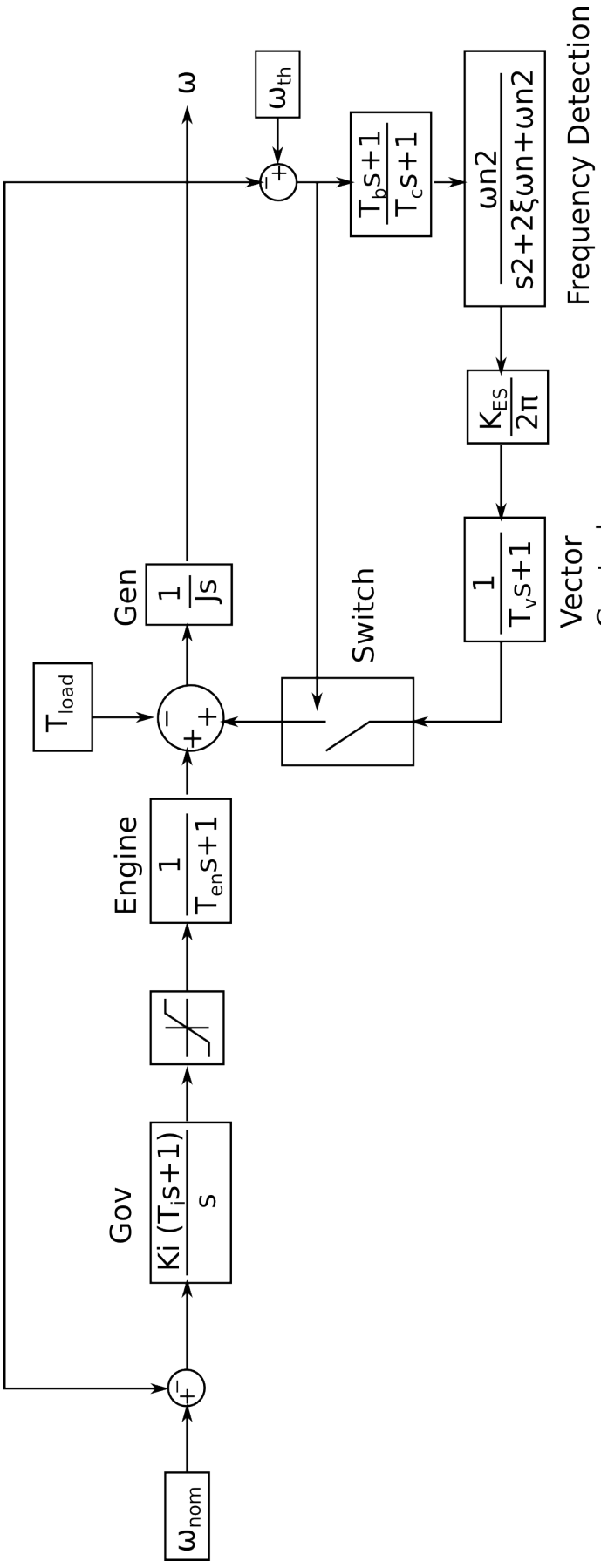

Figure 4.19: The complete approximated control system

4.6.3 A Comparison Between The Approximated & The Electrical Systems

The electrical system and the approximated system were simulated with an ES control gain $K_{ES} = 30$. The resulting frequency responses of both systems are shown in Fig.4.20 for rated and half-rated load conditions.

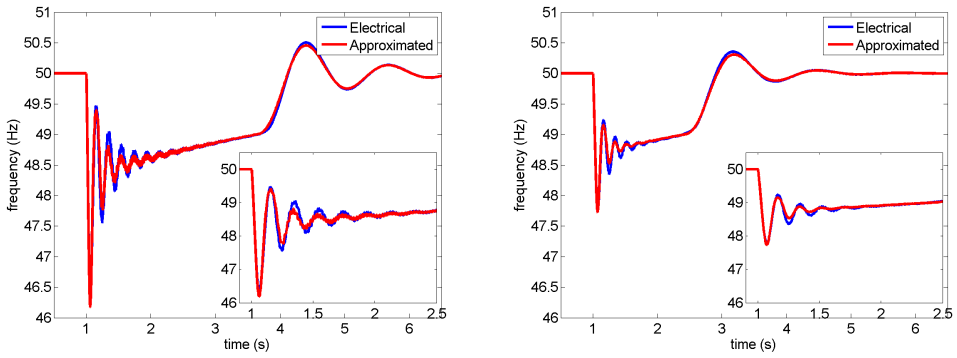

(a) Rated load **(b)** Half rated load

Figure 4.20: Frequency recovery using the complete approximated system (red) and the electrical system (blue) for rated and half rated loads ($K_{ES} = 30$)

From the results, one can see that the pattern of the frequency recovery under both load conditions are almost equal. Most importantly, the exponential damping of the rapid initial oscillations are the same, which is essential for control system analysis.

4.7 The Stability Analysis of The Proposed ES Control System

In the past sections, the complete control system was developed step by step. The complete control approximation system was illustrated in Fig.4.19. A stability study of the proposed ES control technique and a subsequent study on the tuning of the key parameters of the control system will be carried out in this section.

The stability of the system is one of the key factors that define the limitations of the system. Such an analysis reveals the parameters on which the stability of the system depends on, and their respective influence on the dynamic response. To do so, a root locus analysis was conducted considering the approximated

control system.

First, consider the approximated control system as two subsystems as shown in Fig.4.21. The inner loop subsystem consists of the generator and the ES feed back, whereas the outer loop subsystem includes the speed regulation in addition to the inner loop subsystem. Understandably, the inner control loop is faster than the outer loop so that the inner loop can deliver the desired quick frequency recovery. Therefore, the stability margin of the inner loop may become a deterministic factor of the stability margin of the overall system.

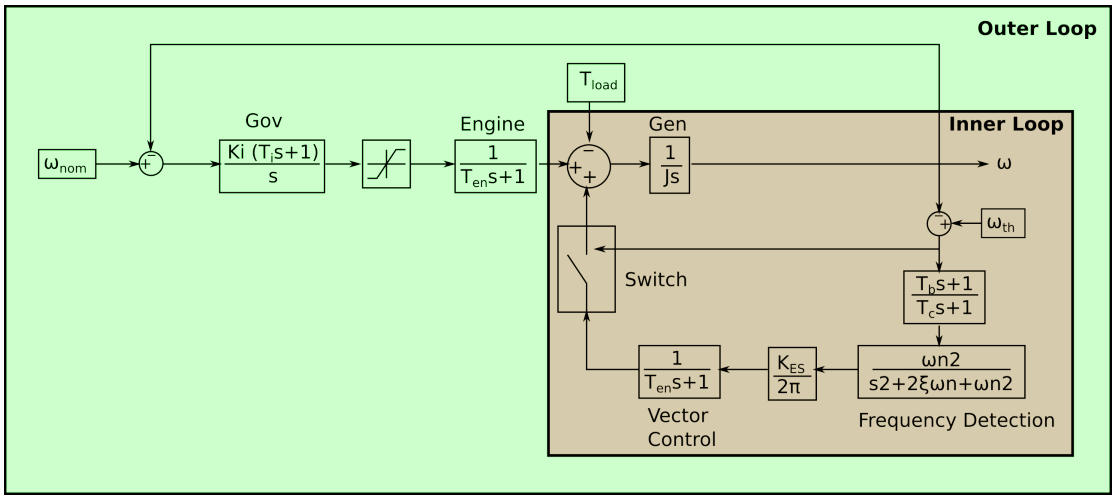

Figure 4.21: The complete approximated system showing the two major subsystems boxed

The forward control path and the feedback control path of the inner loop can be derived as given in (4.7.1) and (4.7.2).

$$\omega(s) = \frac{1}{Js}(T_{EN}(s) - T_{ES}(s)) \tag{4.7.1}$$

$$T_{ES}(s) = \frac{K_{ES}}{2\pi}\left(\frac{\omega_n^2}{s^2+2\zeta\omega_n+\omega_n^2}\right)\left(\frac{T_b s+1}{T_c s+1}\right)\left(\frac{1}{T_v s+1}\right)\left(\frac{1}{0.001s+1}\right) \tag{4.7.2}$$

The root locus of the inner loop for the open loop transfer function of $\frac{\omega(s)}{T_{EN}(s)}$ is shown in Fig.4.22. The two complex poles in the inner loop belong to the DSOGI-FLL. The most dominant poles start from the lumped pole and the pole at the origin belonging to the generator, as shown in Fig.4.22. Yet, the positions of the dominant poles crossing the imaginary axis are dependent on the location of the complex poles of the DSOGI-FLL.

The branches cross to the positive half of the real axis at $Gain \approx 70$. Revisiting

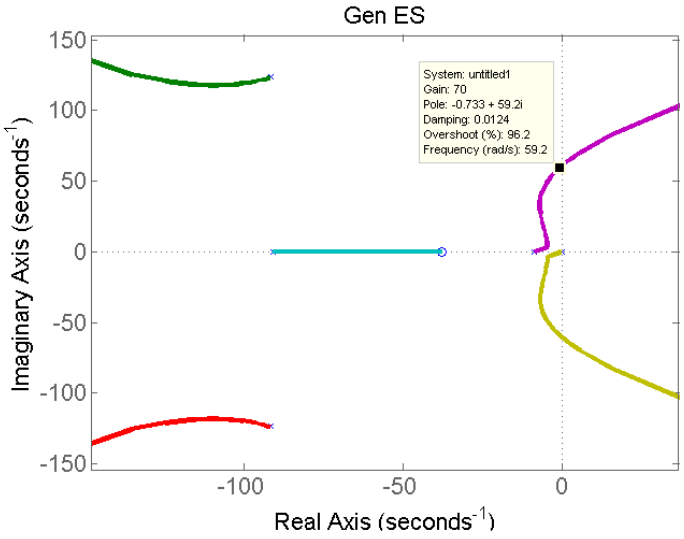

Figure 4.22: The root locus of the generator and the ES controller

the open loop transfer functions given in (4.7.1) and (4.7.2), one can see that the *Gain* in the loop, directly corresponds to the proportional gain K_{ES} of the ES control. This means specifically that the stability margin for the overall system can be defined using the proportional gain K_{ES}.

Now consider the overall system transfer function, including the PI speed governor and the engine transfer function.

$$T_{EN}(s) = \frac{K_p}{s}\left(s + \frac{K_i}{K_p}\right)\left(\frac{a}{1+a}\right)\left(\omega_{ref} - \omega(s)\right) \tag{4.7.3}$$

To acknowledge the above findings regarding the proportional gain K_{ES} at the stability margin, the root locus depicting the closed loop response of the overall system was considered as shown in Fig.4.23, for when $K_{ES} = 70$, i.e. K_{ES} corresponding to the stability margin of the inner loop. In the root locus shown in Fig.4.23, the system is not unconditionally stable as some of its branches cross over to the right half of the real plane.

If the root locus is drawn for when $K_{ES} = 60$ as shown in Fig.4.24, one can clearly see that the latter is marginally and conditionally stable. Hence, one can obtain the stability criterion for the overall system as $K_{ES} < 60$.

The recovered frequency obtained using the approximated system for different K_{ES} values can be used to further validate the point. The Fig.4.25 shows frequency recovery responses carried out for a rated load disturbance for $K_{ES} = 60,\ 70$. The frequency recovery for a K_{ES} that satisfies the above stability crite-

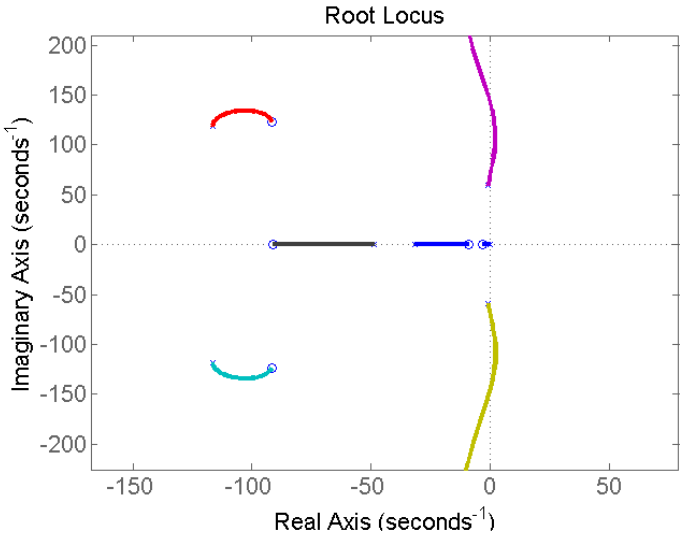

Figure 4.23: The root locus of the complete system including the governor and the ES control ($K_{ES} = 70$)

ria shows an exponential damping in the frequency oscillations, which corroborates with the proposed ES control design. On the contrary, when marginally unstable i.e. $K_{ES} = 70$, the recovered frequency experiences sustained oscillations throughout the period the ES support is active. Seeing that, one can deduce that the sustained yet converging oscillations are a result of the non-linear switching of the ES. Moreover, this means that even when the stability margin is violated, the ES can supply energy to constrain the power frequency within the limits.

In an approximated system such stipulation may be acceptable; however, it may not be the case in a practical grid where an unstable gain in the connected ES control can produce voltages and currents that can jeopardize the normal operation of the grid. Therefore, it is necessary to test whether the same stability criteria can be applied in a non-ideal weak grid with ES support.

In addition, to find out any direct dependences of K_{ES} on power system parameters, the closed loop transfer function of the inner loop was considered. From the inner loop system, one can write the characteristic equation as,

$$s(0.001s+1)(T_v s+1)(T_c s+1)(s^2+2\zeta\omega_n s+\omega_n^2)+\frac{K_{ES}\omega_n^2}{2\pi J}(T_b s+1)=0 \tag{4.7.4}$$

Thus, at the stability margin, the factor $K_{ES}/(2\pi J)$ will have a specific value depending on all other parameters $\omega_n, \zeta, T_v, T_c, T_b$. Out of these parameters,

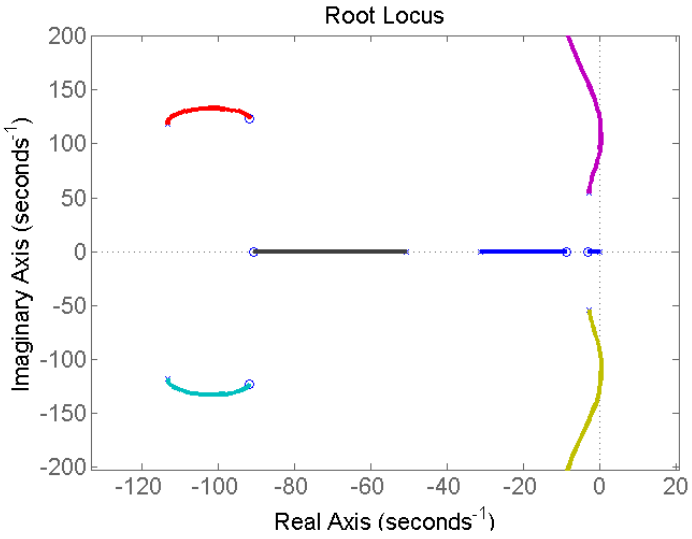

Figure 4.24: The root locus of the Complete system including the governor and the ES control ($K_{ES} = 60$)

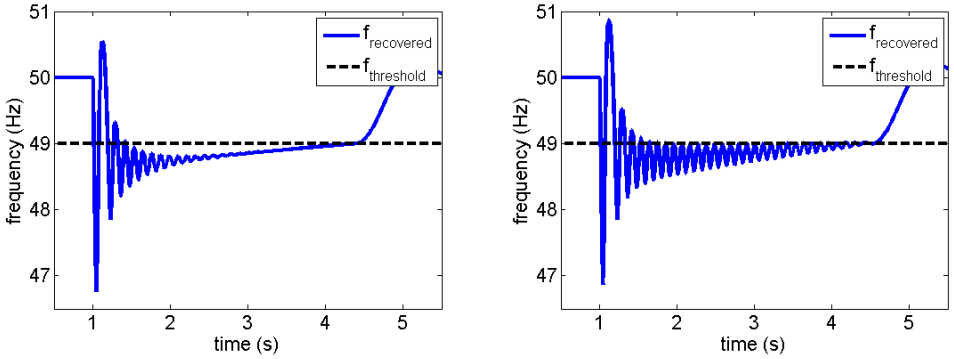

(a) $K_{ES} = 60$ **(b)** $K_{ES} = 70$

Figure 4.25: Stability of the approximated system: Observed in the frequency recovery for $K_{ES} = 60, 70$

ω_n, ζ depends on the frequency detection technique, T_v depends on the vector control, and T_c, T_b depend on the electrical impedance and AVR effects in the system. When these parameters are fixed, K_{ES} is directly proportional to system inertia J. That is, a system with higher inertia would let one use higher proportional gain K_{ES} for the ES controller.

4.7.1 Stability Analysis of The Proposed ES Control: Non-ideal Electrical Grid

Having demonstrated the stability criterion for the proposed ES control using the approximated system, the same criteria is now checked against a practical

weak grid. The response of the frequency recovery was observed for different K_{ES} using the complete weak electrical grid model shown in Fig.4.26.

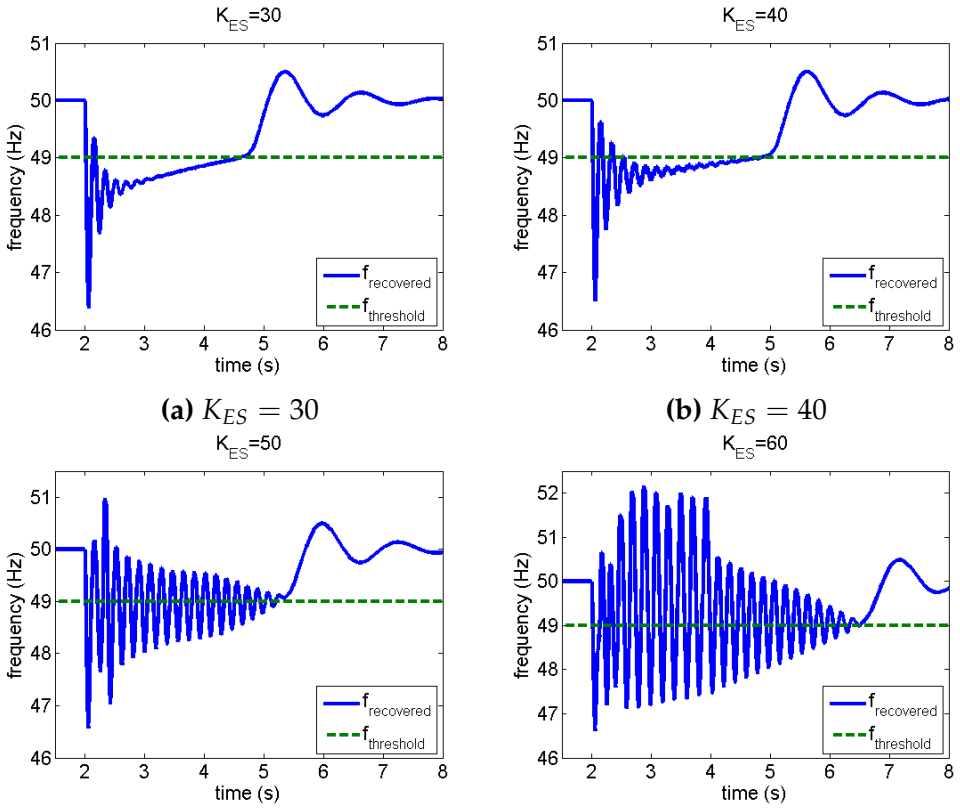

(a) $K_{ES} = 30$ **(b)** $K_{ES} = 40$

(c) $K_{ES} = 50$ **(d)** $K_{ES} = 60$

Figure 4.26: Stability of the electrical system: Observed in the frequency recovery for $K_{ES} = 30, 40, 50, 60$

The results presented in Fig.4.26 show that the stability criterion defined for the approximated system is still valid for the ES control in the simulated weak grid, which shows instability at $K_{ES} \approx 60$. The frequency recovery corresponding to $K_{ES} = 60$ in Fig.4.26d shows how the instability is manifested in the frequency in a practical situation. The prevalence of such oscillations will result in a similar oscillatory speed response in the prime-mover. On the other hand, this means the rapid connection and disconnection of the ES. An analysis based on the hybrid system theory may benefit in understanding the stability of the ES control in detail. However, such an analysis is out of the scope of this work; thus, may be suggested as future work.

The effect of larger K_{ES} can also be observed from the voltage at the PCC, when the ES is activated during a load disturbance. The voltage at the PCC when the ES control is active for different K_{ES} are shown in Fig.4.27. For smaller K_{ES} (i.e. more stable) the voltage at the PCC has been improved during the load

transient by not allowing the frequency to fall too low so that the AVR does not modify the voltage drastically. (See Fig.3.3 for the V_{PCC} without ES support during the rated load disturbance). Nevertheless, V_{PCC} under unstable conditions as shown in Fig.4.26d, becomes unbalanced in the three phases and contains a high harmonic content. Therein lies the answer to the decreased stability observed for the electrical system. Because the signal gets distorted, the load torque gets distorted and hence the frequency. It can be further explained by the current injected from the ES and the d-axis current injected to the grid. The corresponding results are presented in Figs.4.28 and 4.29. As can be seen, the peak current increases slightly with increasing K_{ES}, except when K_{ES} increases from 50 to 60 resulting in a significant increase of current to a value over $40A$. Hence, for $K_{ES} = 60$, the peak current of 40 A results in a peak power injection of 9.2 kW, which is higher than the power capability of the prime mover used in the study.

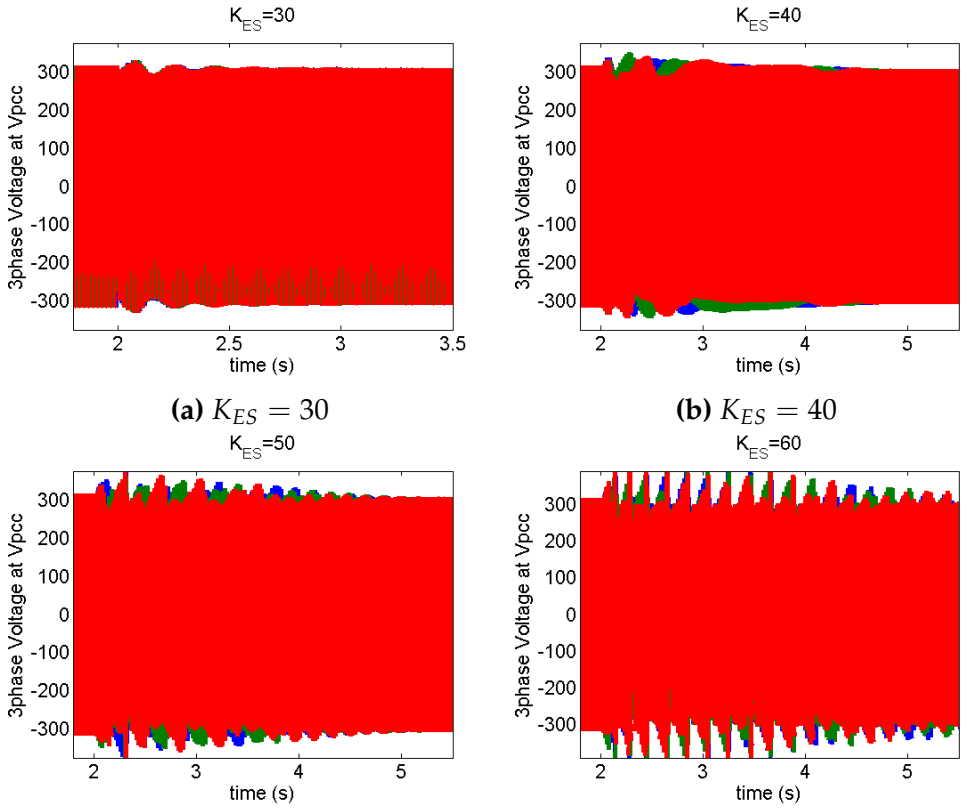

(a) $K_{ES} = 30$ **(b)** $K_{ES} = 40$

(c) $K_{ES} = 50$ **(d)** $K_{ES} = 60$

Figure 4.27: Stability of the electrical system: Observed in the 3-phase voltage at the PCC for $K_{ES} = 30, 40, 50, 60$

The reason is that, up to now in this simulation study, no restriction has been placed upon the amount of current (or power) that can be injected. In practice, the current is naturally limited by the power converter used. Nonetheless, it

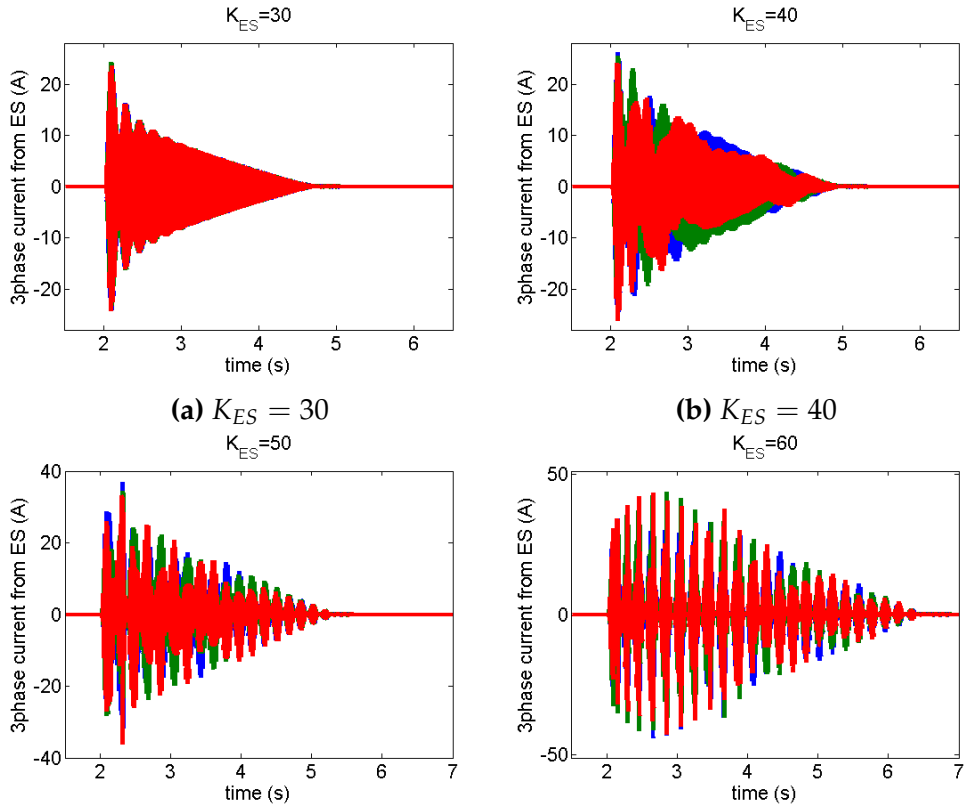

(a) $K_{ES} = 30$ **(b)** $K_{ES} = 40$

(c) $K_{ES} = 50$ **(d)** $K_{ES} = 60$

Figure 4.28: Stability of the electrical system: Observed in the 3-phase current supplied by the ES at the PCC for $K_{ES} = 30, 40, 50, 60$

should not provide more power than the prime mover itself. Imposing these restrictions are being discussed later. In conclusion, it can be said that even though the power frequency converges both in the approximated system and in the electrical system, K_{ES} value should be kept well below the stability margin.

4.8 Simulated Results

The analysis presented in this section is dedicated to appreciate the robustness of the proposed ES control in frequency stabilisation in a weak grid. The value of the proportional gain K_{ES} was chosen to be 30 for the simulation studies. Using the complete weak grid with ES support, the following simulations were conducted to observe the frequency.

- Loading of the rated and 50% rated load
- Shedding of the rated and 50% rated load

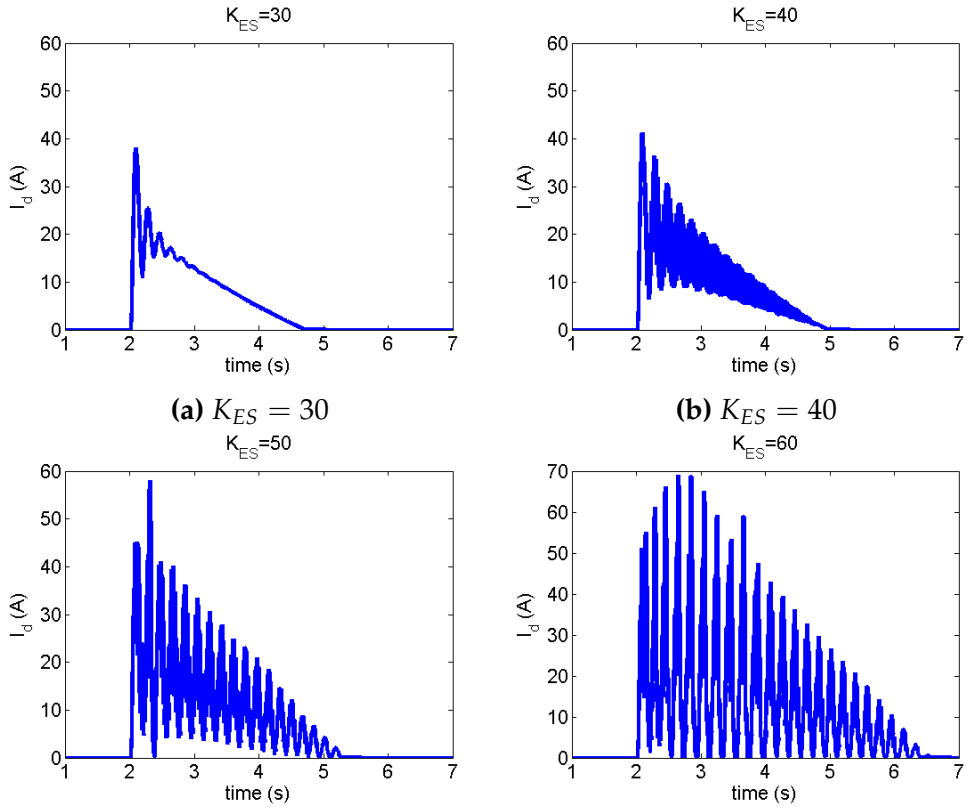

(a) $K_{ES} = 30$ **(b)** $K_{ES} = 40$

(c) $K_{ES} = 50$ **(d)** $K_{ES} = 60$

Figure 4.29: Stability of the electrical system: Observed in the d-axis current extracted from the grid at the PCC for $K_{ES} = 30, 40, 50, 60$

In addition to the frequency response, the relevant 3 phase voltages and currents at the PCC and the active power injected by the ES are also studied for each case.

4.8.1 Performance of the ES Control During Loading

The Fig.4.30 illustrates the improvements in frequency recovery using the proposed technique. To appreciate this, the results are presented with the frequency response in the absence of the proposed technique. When there is no ES support, the frequency drops drastically and reaches a level less than 40 Hz for a rated-load disturbance, warranting disconnection of the DG unit from the main utility according to the grid code [13, 89]. Comparatively, the frequency for a half-rated load, falls to a level less severe; yet, well out of the normal operational limits. When the new ES control was applied, the frequency refrains from falling to critical levels and settles within the set threshold within a few seconds. With the proposed method, the frequency during worst case load dis-

turbance i.e. rated, was recovered above 48 Hz within half a second, and the overall frequency was regained within the 1 Hz limit in 4 s.

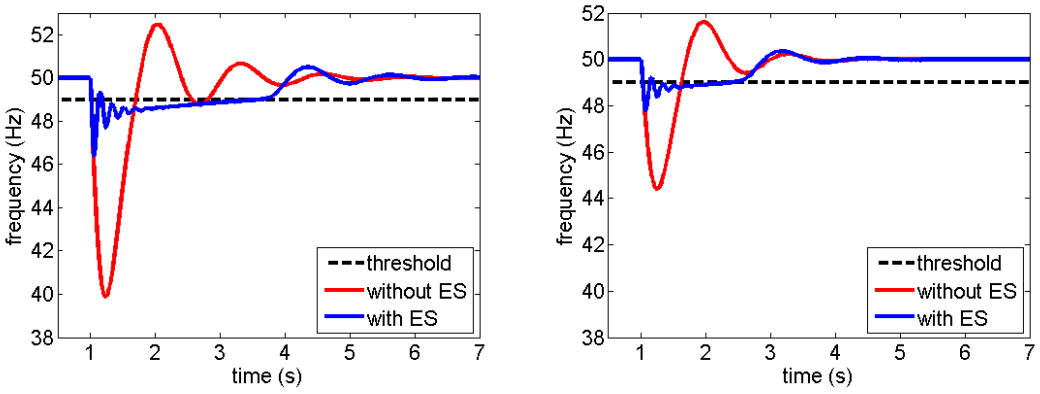

(a) rated load **(b)** 50% rated load

Figure 4.30: The frequency response with and without ES support for different load disturbances at $t = 1\ s$ ($K_{ES} = 30$)

The effect of the frequency recovery is also reflected on the voltage at the PCC. Fig.4.31 shows how the voltage is affected during the rated and the half rated load disturbances respectively. The effects of the AVR response is visible in the voltage at the PCC, which follows the shape of the frequency response as soon as the frequency falls below 48Hz as seen in Figs.4.31a and 4.31c. This response has been significantly improved by the ES support as can be seen in Figs.4.31b and 4.31d, understandably, due to the respective improvement in frequency.

The 3-phase current supplemented at the PCC by the ES control is shown in Fig.4.32. When there is a rated load disturbance, the maximum current that has to be injected was around 20 A, for the system under test and this was halved when the half rated load was applied. As the amount of power required gets halved, the required current also is halved, since the PCC voltage does not vary much. The triangular shape of the current waveforms corroborates with the concept of the ES support, which starts injecting at the required current and slowly passing the control over to the governor by decreasing linearly until the frequency reaches the threshold. The ES in this case completely hands over the control within 4 s and 2 s from the occurrence of the disturbance for rated and half rated loads respectively. In particular, these properties show the consistency and robustness of the ES support for different load conditions. A similar behaviour can be observed in the discharging ES current i.e. the d-axis current shown in Fig.4.33.

Having studied the electrical parameters, it is worthwhile looking at the changes

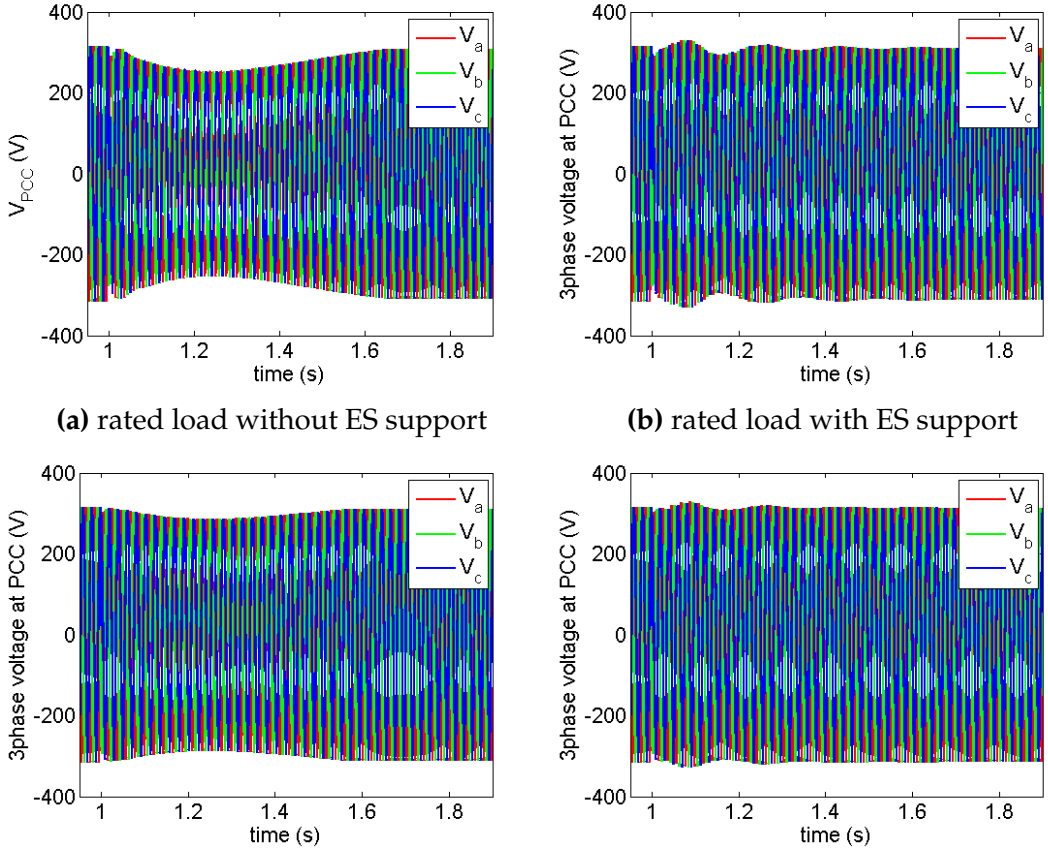

(a) rated load without ES support

(b) rated load with ES support

(c) half rated load without ES support

(d) half rated load with ES support

Figure 4.31: 3 phase voltage at the PCC with and without ES control during rated and half rated load disturbances a $t = 1s$),($K_{ES} = 30$)

taking place in the electro-mechanical relationship of the synchronous generator subsequent to the ES support. This area can be explored by observing the engine torque and the total torque seen at the generator, both when active power support is available and when it is not available.

The engine torque increases gradually with the ES support as shown in Fig.4.34 as opposed to the rapid increase in the engine torque in the absence of the ES support. As shown in Fig.4.35, the generator suffers a rapid oscillatory response in the rotor due to the initial response of the ES, occurring as a result of associated delays in energy injection. Yet, these oscillatory variations in torque occur for less than a quarter of a second compared to the significant acceleration and deceleration torques occurring for a couple of seconds when there is no ES support. Further, the synchronous generator model used in the simulated weak grid was designed as a worst case representation by avoiding rotor losses and frictional damping that are usually present in practice. Therefore, a further damping of these oscillations can be expected in practical circumstances, which

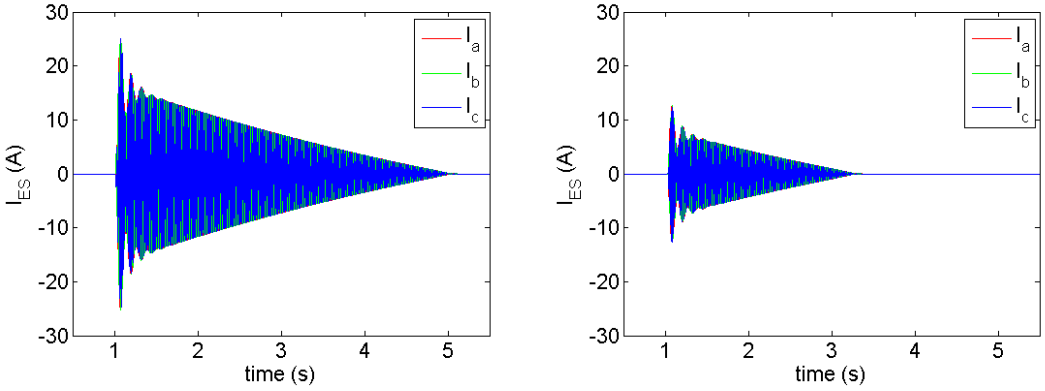

(a) rated load **(b)** 50% rated load

Figure 4.32: The 3 phase current supplied by the ES at the PCC during different load disturbances at $t = 1\ s$ ($K_{ES} = 30$)

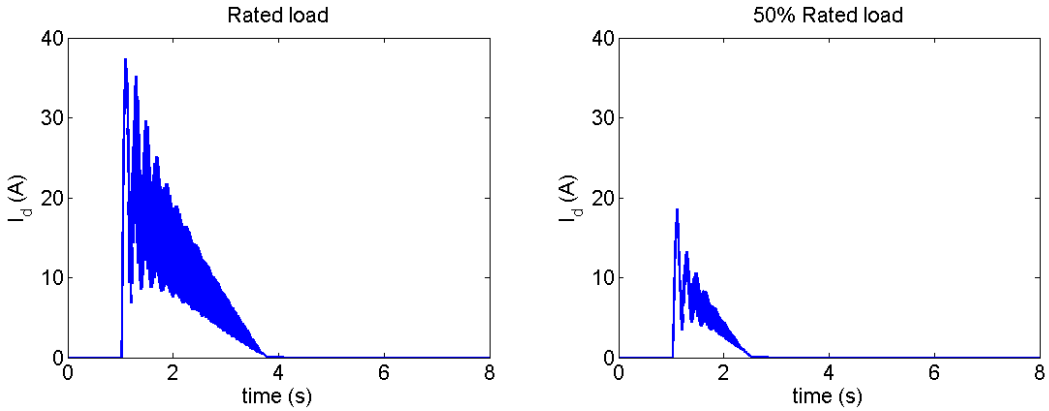

(a) rated load **(b)** 50% rated load

Figure 4.33: d-axis current injected by the ES at the PCC during different load disturbances at $t = 1\ s$ ($K_{ES} = 30$)

might also provide additional stability.

4.8.2 Performance of The ES Control During Load Shedding

Following the approach taken in the previous section, load shedding effects are to be observed in this section for rated and half-rated load disturbances. An upper frequency threshold of 51 Hz was used to adapt to the over-frequency variation. While this only affects the switching of the ES, the rest of the configuration was kept the same. Also, it is important to note that that, bi-directional power flows were assumed to direct current from the grid to the ES via the current controller and charge the ES, mitigating the load shedding effects on the frequency. Therefore, during load shedding the power system is able to maintain an equal and opposite response in frequency, compared to that dur-

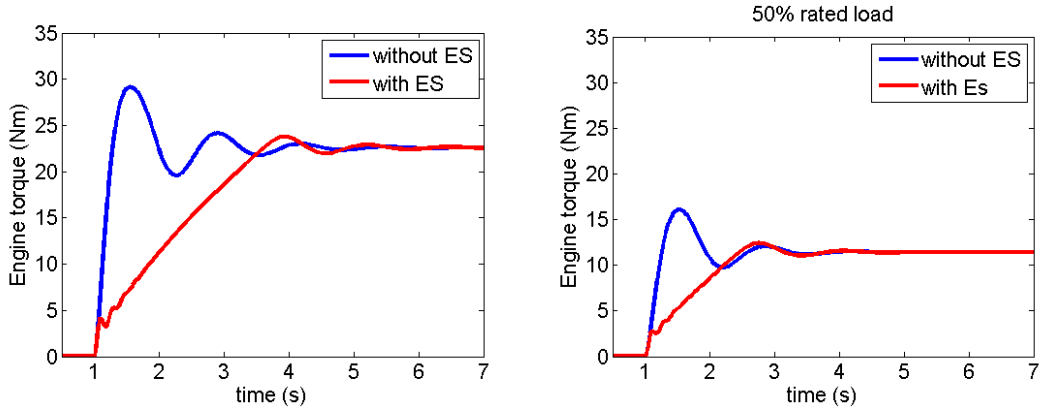

(a) rated load **(b)** 50% rated load

Figure 4.34: The torque supplied by the engine during load disturbances at $t = 1\ s$),$K_{ES} = 30$

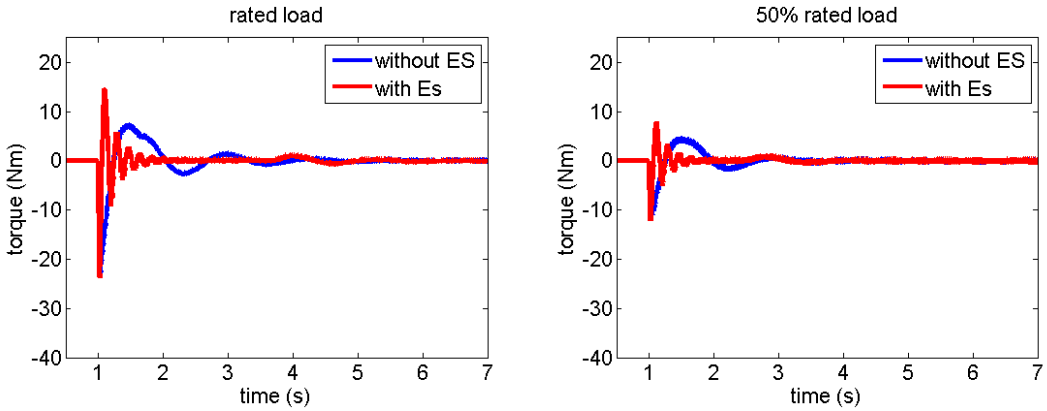

(a) rated load **(b)** 50% rated load

Figure 4.35: The torque seen at the generator during different load disturbances at $t = 1\ s$),$K_{ES} = 30$

ing loading as shown in Fig.4.36.

Even though the frequency response was the equal and opposite for both loading and shedding, the voltage observed at the PCC behaves differently. According to Fig.4.37, there is no significant improvement in the voltage due to the ES support. In fact, the voltage waveforms have worsened slightly during load shedding. In a typical electrical grid, the frequency regulation is coupled with active power, whereas the voltage regulation is coupled with reactive power. The proposed ES control only supplies active power; thus can only be expected to aid in the frequency recovery. In other words, if the grid was provided with reactive power support at the same time during load shedding, the voltage at the PCC might have been improved. Such investigation can be noted down as a suggestion for future work.

As the ES absorbs the surplus power that needs to be utilised, the current flow

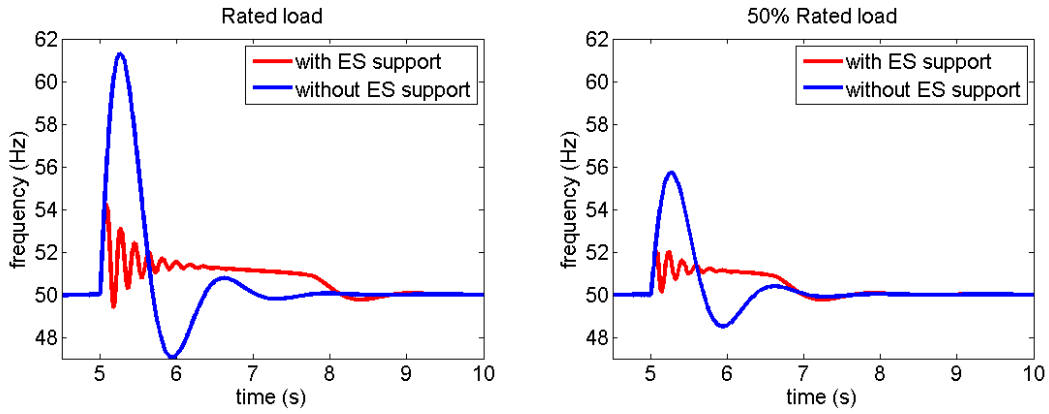

(a) rated load **(b)** half rated load

Figure 4.36: The frequency response with and without ES support for load shedding at $t = 5s$ when ($K_{ES} = 30$)

to the ES gets reversed (i.e. ES is charging), as shown in Fig.4.38, thereby preventing the frequency from rising above the upper threshold. The 3-phase ES currents are shown in Fig.4.39.

The mechanical response of the synchronous generator during load shedding mirrors that was observed during loading. For instance, as shown in Fig.4.40, with the ES support the engine torque decreases gradually. The rapid initial oscillations are present in the net generator torque as shown in Fig.4.41, analogous to the effects of loading.

4.9 Effect of The Current Limits

Up to now, the ES was assumed to be of the same size as the synchronous generator. Also, there has been no imposed limit on the maximum current the ES can supply. However, in a practical situation, the size of the ES is a deterministic factor as to how well the frequency can be recovered.

In this step, limits are imposed on the current, hence on the peak power to replicate real world limitations. The maximum ES current will be limited either by the maximum battery current or by the maximum converter current. The Li-ion battery ES available in the Flexelec laboratory at the University of Nottingham was taken as an illustration. The maximum ES current was limited at $\pm 25A$ at a battery terminal voltage of 350 V, hence the equivalent d-axis current was limited at ± 27 A ($V_d = 325$ V) in the simulation. The d-axis current was calculated using the battery voltage and the d-axis voltage. The frequency recovery,

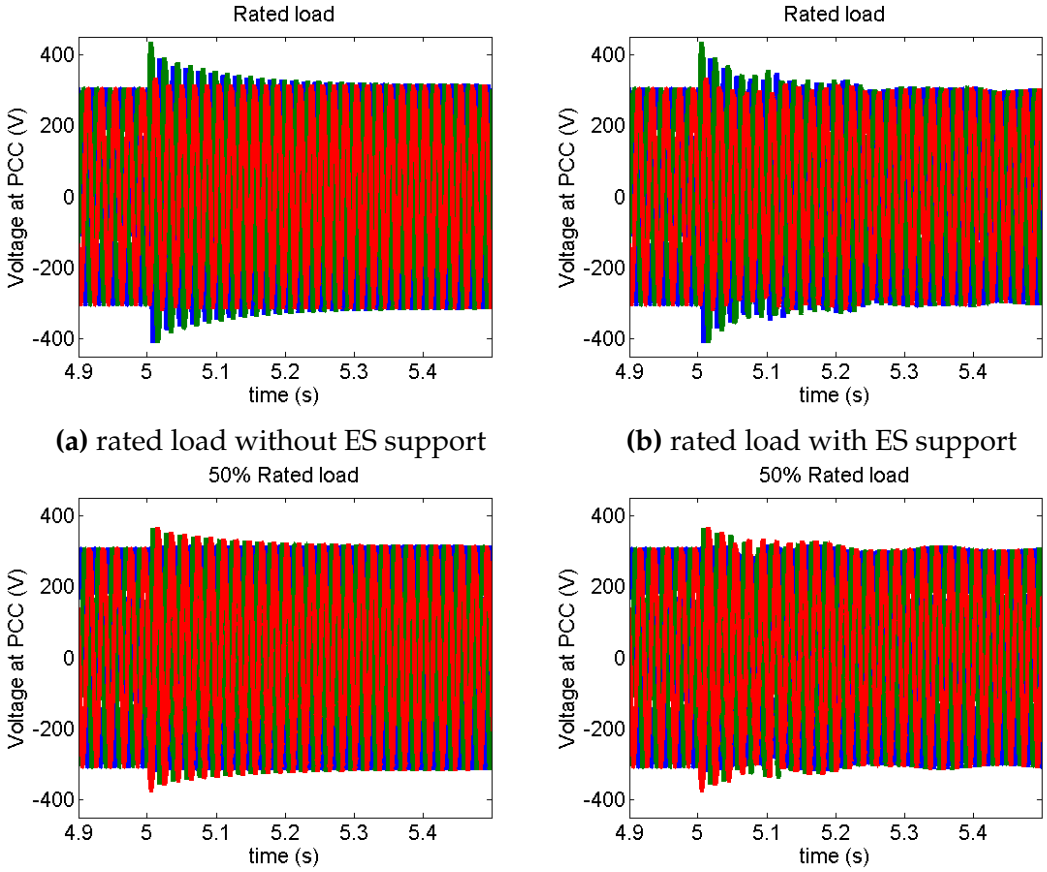

(a) rated load without ES support

(b) rated load with ES support

(c) half rated load without ES support

(d) half rated load with ES support

Figure 4.37: 3phase voltage at the PCC during load shedding at $t = 5s$, ($K_{ES} = 30$)

and the d-axis current injected are shown in Figs.4.42 and 4.43.

With saturation, one can see that injected d-axis current is curtailed at 27 A in Fig.4.43, whereas in the case with no saturation limits, the current goes up to 38 A. When the load was halved, systems with both with and without saturation limits produce a current of about 19 A. For the smaller load, the current required is well within the limitations and is not affected by the saturation limits.

The current injection for two frequency responses presented in Fig.4.43 for rated and half rated load disturbances respectively confirm that the current limitation affects only the rated load. Since the ES current is curtailed at the maximum, the naturally exponentially damped fluctuations in the frequency is dampened further by the saturation limit after the first oscillation. This in fact is a positive effect that effectively withholds gain K_{ES} temporarily for larger loads, stabilising the system. When the maximum output power does not reach the limits, frequency recovery is unaffected.

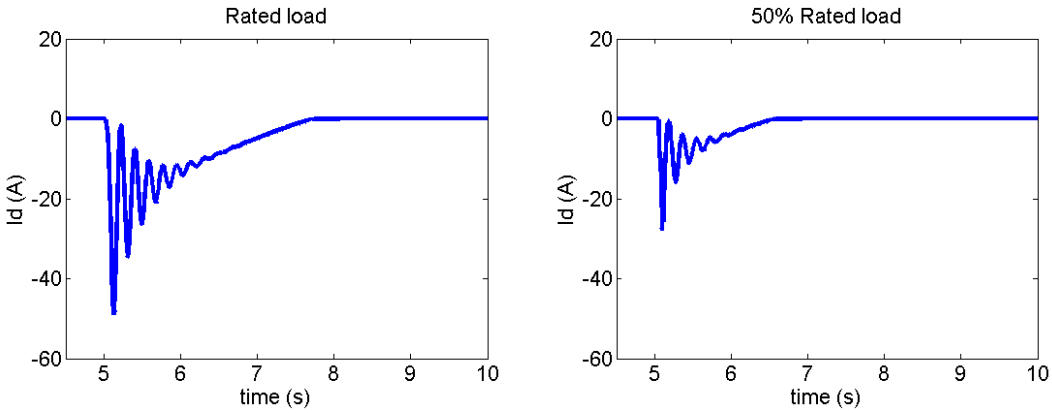

(a) rated load **(b)** 50% rated load

Figure 4.38: The d-axis current absorbed by the ES at the PCC during load shedding at $t = 5\ s$, ($K_{ES} = 30$)

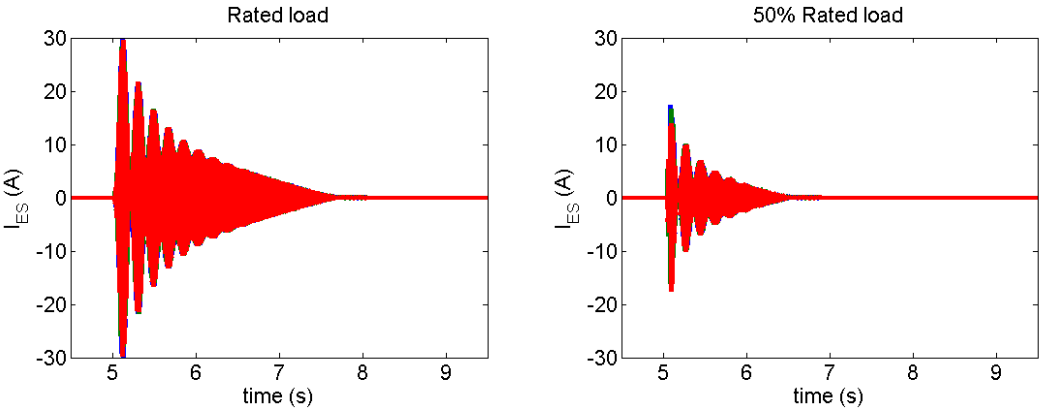

(a) rated load **(b)** 50% rated load

Figure 4.39: The 3 phase current absorbed by the ES at the PCC during load shedding at $t = 5\ s$, ($K_{ES} = 30$)

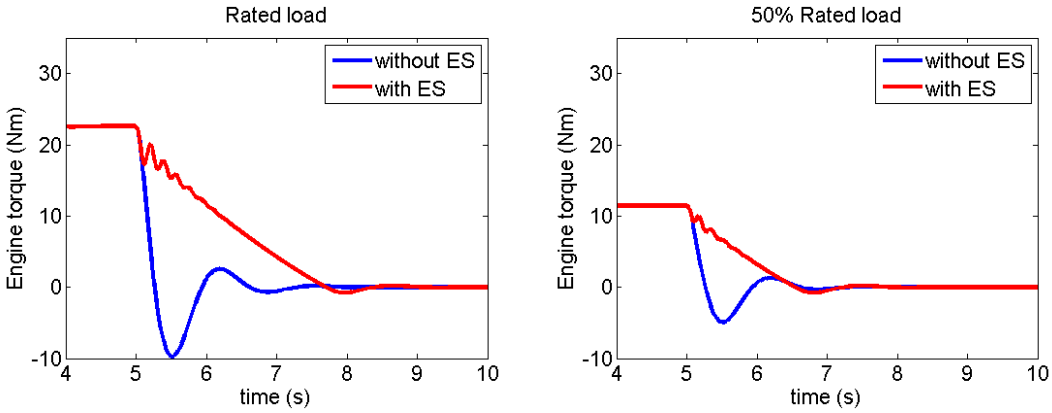

(a) rated load **(b)** 50% rated load

Figure 4.40: The engine torque released by the engine during load shedding at $t = 5\ s$ ($K_{ES} = 30$)

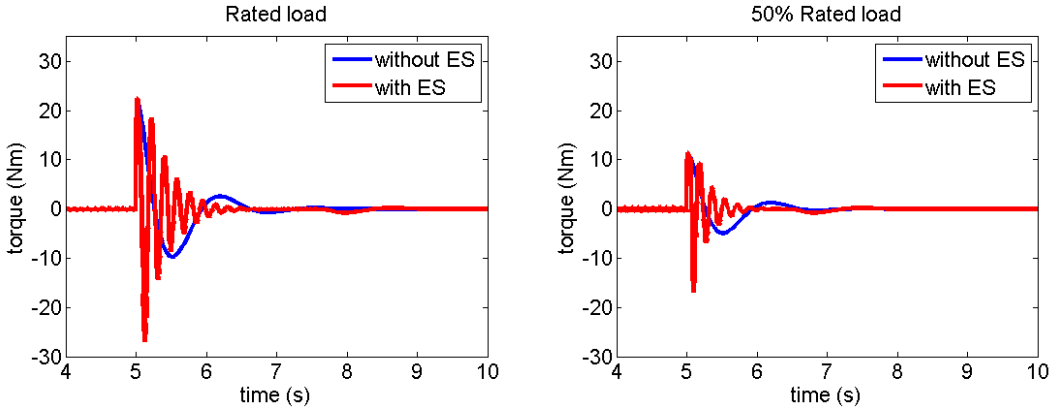

(a) rated load **(b)** 50% rated load

Figure 4.41: Torque error seen at the generator during load shedding at $t = 5s$, ($K_{ES} = 30$)

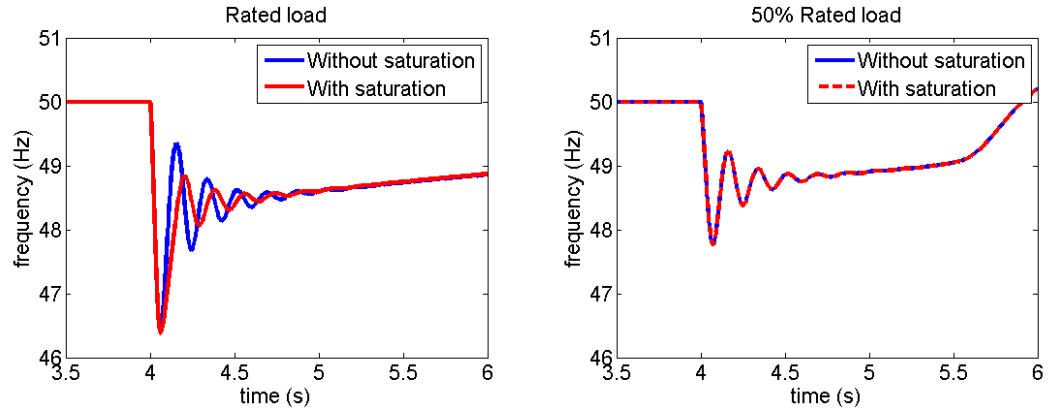

(a) rated load disturbance **(b)** 50 % rated load disturbance

Figure 4.42: The frequency response with and without saturation limits, for different load disturbances at $t = 4s$ ($K_{ES} = 30$)

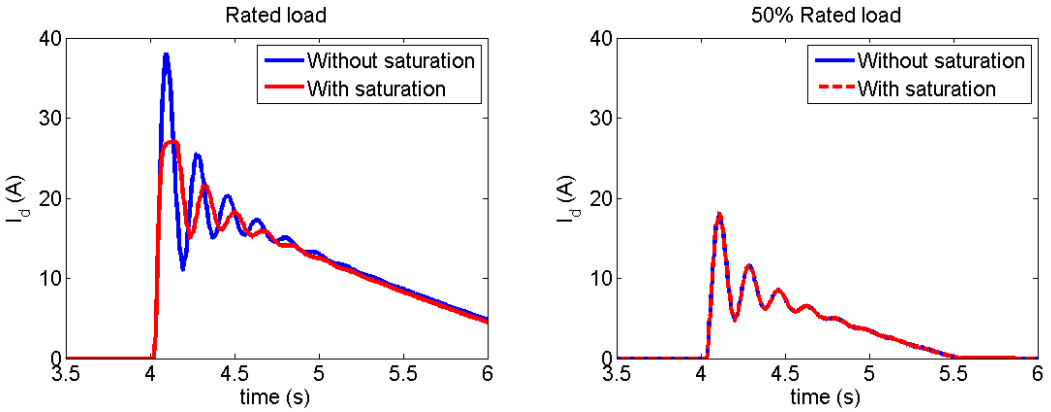

(a) rated load **(b)** 50% rated load

Figure 4.43: The d-axis current supplied by the ES at the PCC during a load disturbance at $t = 4s$, with and without current limits ($K_{ES} = 30$)

In order to further observe the increase in stability with current limiting, the frequency recovery for high proportional gains $K_{ES} = 50, 60$ for the current limited and unlimited cases are shown in Fig.4.44.

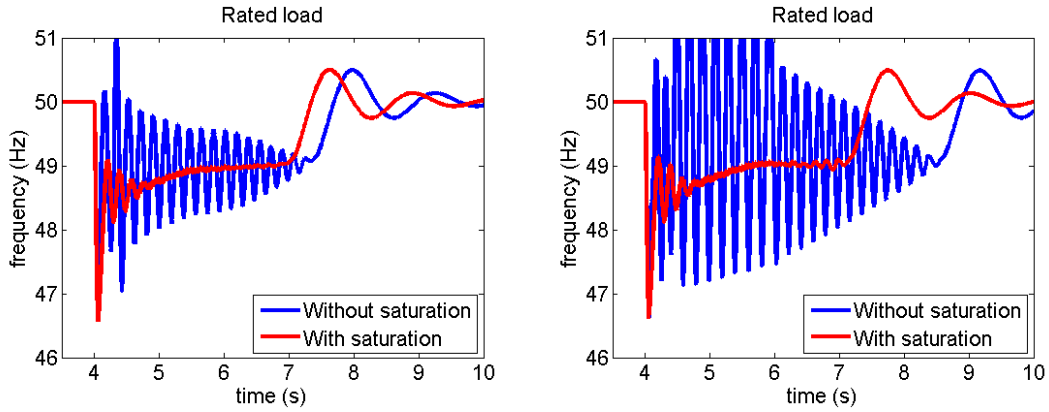

(a) K_{ES}=50 **(b)** K_{ES}=60

Figure 4.44: The frequency response with and without saturation limits, for the rated load disturbances at $t = 4s$ for higher gain values of K_{ES}

According to Fig.4.44, the stability has clearly increased as one can now observe the exponential damping of the initial oscillations, which is a characteristic of a stable system. However, when $K_{ES} = 60$, which is the stability margin predicted from the control system analysis, in Fig.4.44b the frequency response at the tail end just before reaching the threshold of 49 Hz, there is a slight building up of non converging oscillations. Therefore, one should still consider the stability limit of $K_{ES} < 60$ for the system considered in the study.

4.10 Characterisation of The Proposed ES Control Technique For Varying K_{ES}

The main parameter of the ES control as witnessed is the proportional gain K_{ES}. Up to now K_{ES} has been a deterministic factor in stability, and it was understood that for best frequency recovery K_{ES} needs to be as high as possible. However, this is valid when there is no restriction on the size of the ES or the rating of the power converter. In order to determine an optimum K_{ES}, a study is now conducted to observe the power and energy usage when K_{ES} is varied.

The power rating of the ES corresponds to the maximum active power required (P_{MAX} (kW)), while the energy capacity corresponds to the total energy supplied (E_{total} (kJ)). Hence,the peak active power and the total energy spent were

recorded for varying K_{ES}, while imposing a current limit of 27 A on the d-axis current to perceive the size requirements.

As one can see in Fig.4.45a, P_{MAX} increases when K_{ES} is increased, for both rated and half rated load disturbances. For the rated load, the peak power does not increase much with K_{ES} as the current limit affects the maximum peak power. For the half-rated load, the peak power increases significantly for smaller K_{ES}, but levels off for $K_{ES} > 50$ as a consequence of reducing frequency drop. Nonetheless, one can select any power converter and limit the current accordingly, while selecting a high K_{ES} below the stability margin.

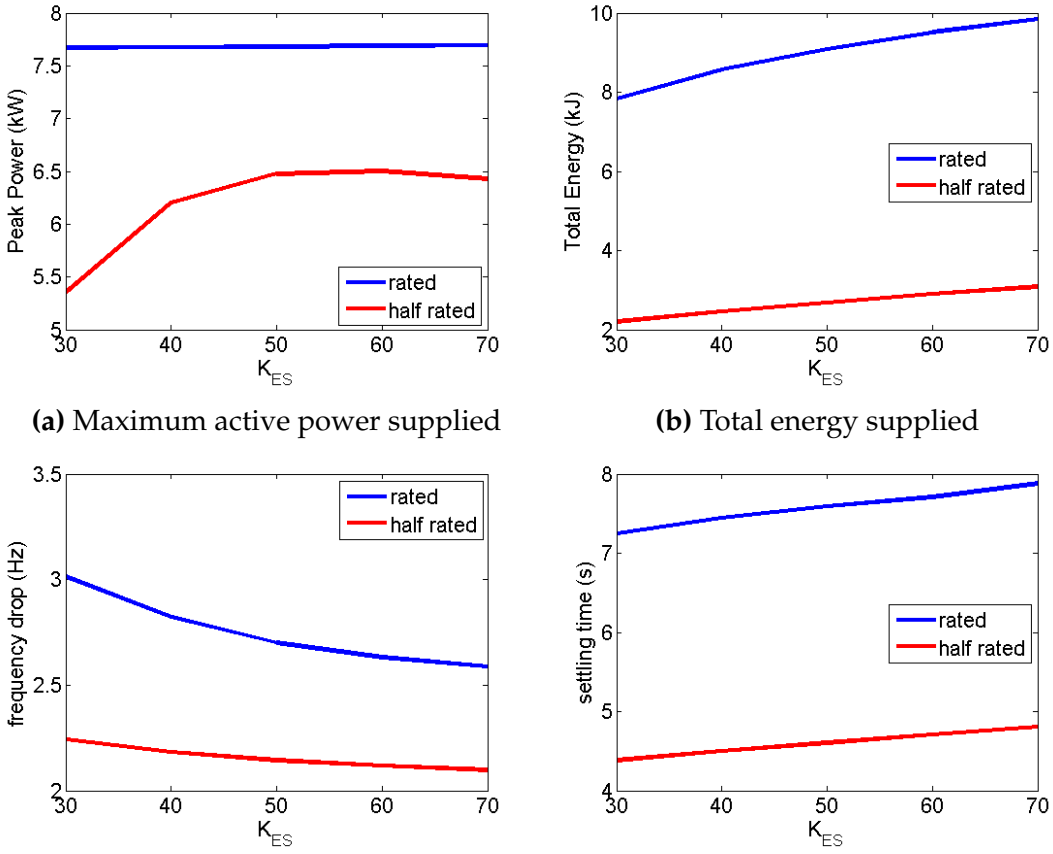

(a) Maximum active power supplied

(b) Total energy supplied

(c) Maximum frequency drop

(d) Settling Time

Figure 4.45: ES performance against various K_{ES}, for rated and half rated loads

The size requirement of the ES can be determined from the total energy spent in delivering the required frequency response. As shown in Fig.4.45b the total energy supplied increases with K_{ES} as expected. The total energy used has a stronger dependence on K_{ES} as the capacity should increase by nearly 20% when K_{ES} is increased from 30 to 70. Therefore, K_{ES} has to be determined according to the available capacity of the ES.

Consequently, higher K_{ES} produces lower initial frequency drops as displayed in Fig.4.45c. Even though for higher K_{ES}, the initial peak power is limited at a constant value, for higher K_{ES}, the ES provides energy longer at this high peak power, reducing the actual frequency drop. The settling times, as shown in Fig.4.45d increase with K_{ES}. When using higher K_{ES}, the frequency error seen by the governor becomes slightly smaller, lengthening the time taken for the governor to increase the engine torque up to the required torque.

In conclusion, in selecting a K_{ES} value, one must consider both the stability margin and the energy capacity. If one has a large enough ES, K_{ES} should be as high as possible without violating the stability margin to decrease the frequency drop.

4.11 Conclusion

In a weak electrical grid, due to low inertia, frequency drops are eminent during load disturbances. The slow dynamics of typical speed governors exacerbate the response and usually produce frequency responses outside of the desired regulatory limits levied by the grid code. This situation may be disadvantageous to emerging distributed power generation, as failure to abide by the frequency regulations of the main utility may result in islanding and cascading disconnection of weak counterparts of the grid, causing undesirable blackouts.

As a solution, this research proposes a novel technique to independently control an ES, for the specific purpose of frequency stabilisation in weak electrical grids. It was successfully achieved by employing power system frequency as the key control input. In brief, the proposed technique compares the instantaneous power frequency with a set frequency threshold and as soon as the frequency falls below this threshold, the ES is automatically activated. The resultant frequency deficit proportionally actuates the ES to generate additional active power required to restore the power frequency above the threshold.

In this way, a non-zero frequency error is maintained throughout the load disturbance; thereby, not interfering with the power system's usual speed governing, while supplementing active power. The prime mover (engine) experiences a gradual torque increment compared to the rigorous action required without ES support, as a combined result of the proposed ES control and speed governing. Once the power frequency reaches the threshold, the ES is deactivated

and smoothly hands over the rest of the power frequency control to the speed governor, meaning the prime mover continues to supply the added load demand in steady state without further support. This indicates and assures the rest of the grid that the DG is self sufficient to accommodate the new demand. An equal and opposite scenario was also observed during load shedding. Using detected frequency completely eliminated the need for communication between the speed governor and the ES.

In a practical situation, detected frequency is associated with inevitable transient delays and steady state ripple. It was also revealed that a delay in frequency detection causes an oscillatory response in the recovered power frequency. On this basis, a smaller delay and a higher attenuation of the steady state ripple were declared as desirable for the proposed technique. Such criteria in frequency detection could be realised using a DSOGI-FLL.

To explore the properties of the new control technique, application of the ES with the proposed method in a weak grid was approximated in the s-domain using control systems analysis. The stability criteria for the proposed control was derived using the complete approximated system, which implies that the stability of the method depends on the inertia and the impedance of the power system it is coupled with. In other words, a higher value of K_{ES} may be desired for larger power systems.

The ES support was represented as a controlled current source, which injects d-axis current in order to supply the additional active power as calculated by the ES control. This simulated environment was used to examine and validate frequency recovery in more practical situations.

The purpose of frequency recovery for both loading and load-shedding was validated using the simulated electrical system. Consistent performance could be observed for different load conditions. The proposed ES control was successfully able to restore frequency within the $\pm 1\ Hz$ in $4s$ for the loading and shedding of the rated load and in $2s$ for the half the rated load. The method was successfully able to maintain the d-axis voltage, V_d nearly a constant, given that no reactive power control is specified.

The investigation of power and energy usage showed that the choice of K_{ES} depends on the power and energy rating of the ES, provided that the stability margins are maintained.

A saturation limit on the current defines the maximum power injection possible

under practical conditions. The simulated results suggest that having saturation limits only affects the responses with respect to larger load disturbances, which commands the ES current to exceed the nominal limits. This was found to have a positive effect on the recovered frequency by further damping the initial oscillatory response for larger loads.

Since the proposed method works by supplementing the active power, the most significant improvement was seen in terms of frequency. While the frequency following AVR effect on the PCC voltage was eased during loading, drawing power at the PCC slightly disturbed the voltage during load shedding. Since the voltage control is associated with reactive power, an analogues control technique may be suggested to control reactive power at the PCC as a future study.

On the whole, compared with the conventional governor controlled frequency regulation, the proposed ES control technique was successfully able to deliver a much better frequency regulation in a worst case weak grid, by independently controlling an ES that uses detected frequency as the main control input and trigger. The proposed technique improves the viability of weaker parts of the grid, subsequently aiding in sustaining a safe and assured DG power supply in places where the strong grid is unable to reach.

CHAPTER 5

Comparison of Methods For Accurate Frequency Trend Estimation Following Load Transients in Weak Electrical Grids

5.1 Introduction

Estimating the frequency trend following a load disturbance accurately is of utmost importance in the scope of this research, which proposes using energy storage for frequency support in weak grids. The particular energy storage control technique presented in Chapter 4 exploits the detected frequency signal as the main control input, thereby calling for unique frequency detection requirements, as discussed in the section 4.3. In support of this, Chapter 5 investigates selected frequency detection techniques with the aim of discovering the best suited method(s) for the energy storage control applied specifically to weak electrical grids.

In this chapter, three candidate frequency detection methods were chosen for comparison, from different technical backgrounds; namely, a phase locked loop (PLL) based Synchronous Reference Frame PLL (SRF-PLL), a Discrete Fourier Transform(DFT) based Generalised Modified DFT and an adaptive filtering technique called Double Second-Order Generalised Integrator Frequency-Locked Loop (DSOGI-FLL). The methods will be first investigated individually against a set of specifications for frequency detection requirements derived specific to weak grids. Then, the three methods will be compared on an unbiased criteria

based on bandwidth-matching. After declaring suitable method(s) to be used in the energy storage control strategy, a further optimisation technique to avoid spurious frequency variations in the estimation due to abrupt changes in voltage will be presented. Then, the comparison of methods are validated using experimentally acquired voltage data from the weak-grid facility presented in Chapter 3. Finally, conclusions are drawn.

5.2 Classification of Requirements

In Chapter 3, a characteristic worst-case weak-grid scenario was developed. There a typical voltage waveform generated in a weak grid with AVR effects and a comparable source impedance was observed experimentally and was replicated in a simulation environment. This sets the context for comparison of frequency detection methods.

In order to optimise the frequency detection methods for this application, the following required properties and boundaries in the context of operation can be considered.

- Maximum frequency range
- Maximum rate of change of frequency (ROCOF)
- Required speed of convergence
- Required accuracy (relates to harmonic attenuation)

Hence, the discussion on frequency detection techniques will take the above into account with respect to the weak-grid condition presented in Chapter 3 and the energy storage control proposed in Chapter 4.

5.2.1 Frequency Range and Maximum Rate of Change of Frequency

The frequency range corresponding to the worst-case load disturbance i.e. loading and shedding of the rated load torque (see Fig.3.31 in chapter 3)sets the maximum allowable range of frequency as $40Hz - 60Hz$.

According to (3.3.11) in chapter 3 that relates ROCOF, system inertia and applied load, the maximum ROCOF can be calculated by considering the maximum possible load disturbance. In most cases this is equivalent to the power

system rating which in the case of the practical system is $8kW$. Therefore, the maximum ROCOF value that the power system under study can experience for rated loading is,

$$\left.\frac{df}{dt}\right|_{max} = -86.23Hz/s \tag{5.2.1}$$

The ROCOF detected using the frequency detection technique must not under-estimate or over-estimate the ROCOF so that the rate of energy supply from the energy storage is neither too low nor too high. If the detected ROCOF is too low, the rate of energy supply will be too low and the recovery will be slow. On the other hand, if it is too high, the rate of energy supply will be too high causing oscillatory effects in the system. For the correct operation, it is acceptable to set a $\pm$15% bound on the ROCOF error. In order to cover a broader range of weak grids, the maximum followable ROCOF was set to 100 Hz/s.

5.2.2 Requirements For Speed of Convergence

The proposed energy storage control aims to prevent the frequency from falling below 49 Hz. This frequency level is reached at -86.23 Hz/s within 12 ms (assuming frequency was nominal before the disturbance). If this is to be detected properly, the frequency detection method needs to settle in 12 ms to ensure an accurate control signal is sent to the energy storage.

However, this is quite a challenging requirement to achieve using any frequency detection method, as it is less than a full cycle length (20 ms). In addition, steady state ripple that increases with decreasing settling time must be considered. Therefore, a settling time range of 10 $ms < t_{delay} < 50$ ms (i.e. between 0.5 to 2.5 cycles) was defined, so that the steady state requirements can be met.

This requirement has also been discussed in the context of energy storage control in section 4.3. The transient delay needs to be minimised for effective energy storage control. Therefore, the aim is to find a settling time for each frequency detection method such that it minimises the time delay, while meeting the steady state requirement.

5.2.3 Steady State Requirements

The harmonic contamination in the voltage at the PCC is mainly responsible for the ripple on the steady state detected frequency. In addition, most of the frequency detection methods, including PLLs, generate a double frequency component of the fundamental, as a result of essential frequency mixing occurring at the phase-detector stage [73, 83, 84]. Both these factors cause ripple in the steady state frequency, which affect the accuracy (error in frequency detection) of the estimation. The attenuation of such components depends on the bandwidth and the high-frequency roll-off of the frequency detection system, factors which also govern the settling time.

The measured worst-case voltage profile from the experimental system was found to contain a total harmonic distortion of 6.07% of the fundamental. In section 4.3.2 of chapter 4, the maximum allowable ripple content was discussed with regard to the energy storage control. The ripple content was found to have a lower effect than the transient delay, on the effective operation of the energy storage. However, if the ripple amplitude is more than 0.5 Hz, the peak power, the energy spent by the energy storage and the time taken to settle increase significantly. Hence, the requirement for the accuracy at steady state may be defined as $\Delta f \leq \pm 0.5Hz$, where $2\Delta f$ is the $peak - peak$ steady state ripple.

The Table 5.1 presents an overall summary of frequency detection requirements.

Parameter	Requirement
frequency	$40Hz - 60Hz$
$\text{ROCOF}_{\text{max}}$	$100Hz/s$
transient delay	$10ms \leq t_{delay} \leq 50ms$
accuracy	$\Delta f \leq \pm 0.5Hz$

Table 5.1: Frequency detection requirements for ES control

5.3 Synchronous-Reference-Frame Phase-Locked Loops

The most commonly used grid synchronisation technique in 3 phase power converters is the synchronous-reference-frame Phase-locked loop (SRF-PLL) [6, 67]. The simplicity in design, application and tuning has made SRF-PLL a popular choice.

A diagram of a SRF-PLL is shown in Fig.5.1, which summarises the function of phase-locking. As can be seen, conventionally the 3-phase input voltage

signal is transformed in to $d-q$ rotating reference frame, by employing Park's Transformation. If the rotating $d-q$ axis is synchronised and aligned to the d-axis, the q-axis voltage will be zero. Therefore, the q-component of the resulting $d-q$ axis voltage is considered the error signal, which is minimised by the feedback loop. By doing so, the d-axis voltage will represent the amplitude of the fundamental input voltage signal. The only modification required to obtain the voltage signal amplitude is to reverse the scaling factor of $3/2$ introduced in the Park-Transformation.

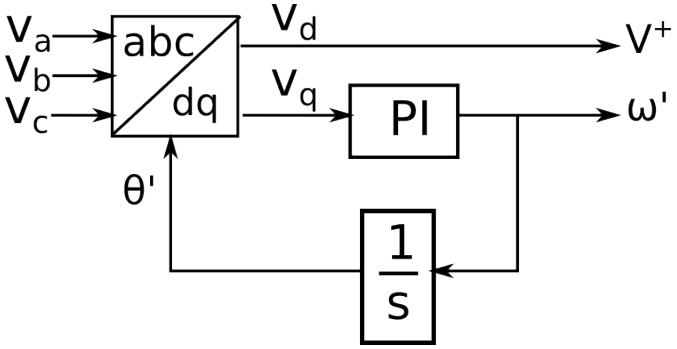

Figure 5.1: The model of an SRF-PLL

In the following mathematical discussion, the input voltage is assumed to be normalised, so that the amplitude of each phase is unity. The open-loop transfer function can be written using estimated θ' as,

$$G_{OL}(s) = \frac{\theta'}{V_q} = \left(K_p + \frac{K_i}{s}\right)\frac{1}{s} \tag{5.3.1}$$

Hence, the closed-loop phase transfer functions,

$$G_{\theta}(s) = \frac{\theta'}{\theta} = \frac{K_p s + K_i}{s^2 + K_p s + K_i} \tag{5.3.2}$$

Since $\theta' = \frac{\omega'}{s}$ and $\theta = \frac{\omega}{s}$, the closed-loop frequency transfer function is also the same as (5.3.2) , from which the second-order characteristic equation can be derived,

$$s^2 + K_p s + K_i = 0 \tag{5.3.3}$$

By equating coefficients with a characteristic second-order system of a damping factor, ζ and a natural frequency, ω_n;

$$s^2 + K_p s + K_i \equiv s^2 + 2\zeta\omega_n s + \omega_n^2 \tag{5.3.4}$$

the tuning criteria for K_p and K_i for a normalised PLL can be obtained as,

$$K_p = 2\zeta\omega_n \tag{5.3.5}$$

$$K_i = \omega_n^2 \tag{5.3.6}$$

Also, from control theory [6, 87], the settling time, t_s of a second-order system can be approximated as,

$$t_s \approx \frac{3.9}{\zeta\omega_n} \tag{5.3.7}$$

By substitution and rearrangement, K_p, K_i in (5.3.5) can be obtained, using the approximated function of settling time t_s as shown below,

$$K_p \approx \frac{7.8}{t_s} \tag{5.3.8}$$

$$K_i \approx \left(\frac{3.9}{t_s\zeta}\right)^2 \tag{5.3.9}$$

Another key parameter that needs considering in tuning a PLL is the lock range. The lock range is defined as the frequency range within which the PLL is able to stay locked. (5.3.10) gives an approximation for the lock range $\Delta\omega_L$, based on the design parameters ζ and ω [6].

$$\Delta\omega_L \approx 2\zeta\omega_n \approx K_p \approx \frac{7.8}{t_s} \tag{5.3.10}$$

From the restriction of $\Delta\omega_L > 20Hz$ (from frequency range requirement), a restriction for the settling time can be set as $t_s < 390\ ms$. This requirement must be met, otherwise SRF-PLL would not be able to function.

5.3.1 SRF-PLL Response to Step Change

The response of SRF-PLL for a balanced and undistorted signal undergoing a step frequency variation is considered in this section. The PLL was tuned for various settling times t_s, while keeping the damping factor, ζ at 0.707 for fast detection with minimal oscillations - see Fig.5.2a. For each designed settling time t_s, the actual settling time (i.e. within 2%) measured from the graph is shown in Fig.5.2b.

According to Fig.5.2b, one can see that for smaller settling times, the measured is close to the designed settling times. It differs slightly for longer settling times,

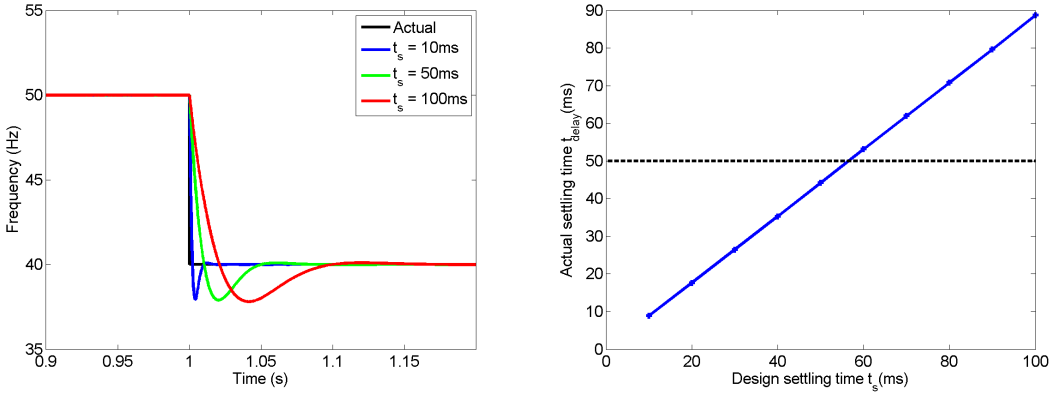

(a) Frequency step down **(b)** Measured Settling Time

Figure 5.2: Frequency responses to step frequency change and measured settling times for varying design settling times

but the measured settling time and the design settling time has a linear relationship. The exact reason for the difference in two settling times is the effect of the zero in the closed-loop transfer function. The approximation of the design settling time given by (5.3.7) is for an ideal second-order system with no zeros. From the results, the design settling time parameter can be restricted such that $t_s < 56\ ms$ in order to adhere to the requirements.

5.3.2 SRF-PLL Response to Ramp Change

The next frequency variation considered is a ramp of $100Hz/s$. The input voltage signal remains clean and balanced, while the ramp frequency variation was applied. For each design settling time t_s, the derivative of the ramp frequency response was calculated to obtain the rate of change of frequency. The maximum ROCOF obtained in each case was recorded against the design settling time as shown in Fig.5.3b. In order to illustrate the settling for a ramp, the frequency response for three settling times are shown in Fig.5.3a.

According to Fig.5.3a, the SRF-PLL converges to the ramp at about its settling time. This naturally will make the estimated ROCOF at some point higher than the actual value. The longer the settling time, the smaller the overestimation of ROCOF as can be seen in Fig.5.3b. According to Fig.5.3b, the settling time needs to be at least 200 ms, in order for SRF-PLL to not overestimate ROCOF by more than a 15%.

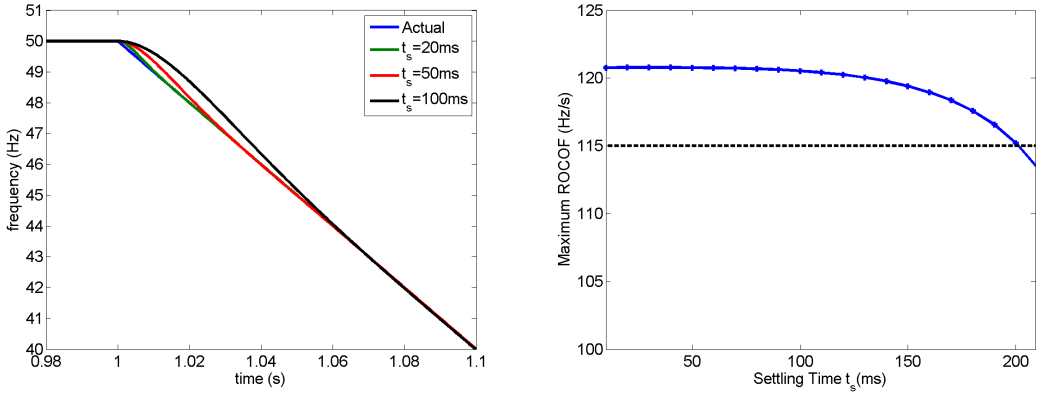

(a) Frequency ramp **(b)** Measured maximum ROCOF

Figure 5.3: Frequency responses to ramp frequency change of 100 Hz and measured maximum rocof for varying design settling times

5.3.3 SRF-PLL Response to Harmonics and Unbalance

In a weak grid, the voltage waveform is usually contaminated by harmonics especially when connected to a grid with switching power converters. Recall that the experimentally measured harmonic content was $THD = 6.07\%$. Compared to the undistorted case, the SRF-PLL clearly shows a rippled response in detected frequency when the input signal is distorted, even though, there has not been a frequency change as shown in Fig.5.4a. Therefore, the average value of the ripple frequency matches the expected value. This means that additional filtering can attenuate the ripple further by tuning the loop-filter with a higher settling time, at a cost of longer delay. Moreover, from Fig.5.4a, the ripple frequency could be seen as approximately 300 Hz. The formation of $300Hz$ can be accounted to the mixing of 7^{th} harmonic (350 Hz) and the fundamental as well as mixing of -5^{th} harmonic ($-250Hz$) and the fundamental.

An unbalance in the voltage input is caused by a sudden dip in the amplitude(s) of one or two phases. Even though the main concern does not include dealing with severe unbalance, the selected method must be able to tolerate relatively small unbalances. Hence, an unbalance of 5% was assumed by reducing phase-A by 5%. When the voltage experiences a 5% dip in one of the phases, the detected frequency becomes oscillatory with a double frequency ripple as shown in Fig.5.4b. The figure shows the response for three different settling times. This is caused by the frequency mixing effect of the Park transformation. Hence, the q-axis voltage contains a double frequency component caused by the frequency summation in addition to the error component (frequency difference) already present in the q-axis voltage. Since, the PLL is designed to minimise the error

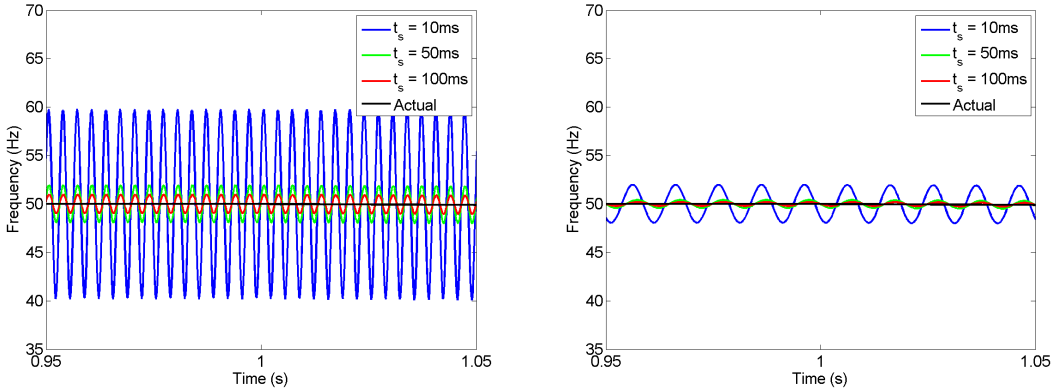

(a) Frequency Response with Harmonics **(b)** Frequency Response with Unbalance

Figure 5.4: Frequency responses of a constant frequency with a) added harmonics to replicate the weak grid voltage and b) unbalance.

in the q-axis voltage by minimising the phase difference, the double frequency component appears as a double frequency ripple in the detected frequency [6].

In order to obtain a measure of error in estimated frequency due to ripple caused by both harmonics and voltage unbalance, the ramp response was observed from 60 Hz to 40 Hz with 2 Hz/s. This slow ramp rate was chosen in order to capture the ripple at all frequencies in a single simulation. The error at each point in time relative to the actual frequency is recorded. By doing so, one can find the maximum error throughout the entire frequency range, if there exists any variation in ripple due to variations in the fundamental frequency. The maximum error at each design settling time provides a measure of uncertainty in the context of the weak grid facility. The maximum error is recorded for several SRF-PLLs with varying settling times and is shown in Fig.5.5a, where frequency estimation error due to harmonics and unbalance are shown separately and in Fig.5.5b, where a combined error is shown.

According to Fig.5.5a, one can see that the error due to 5^{th} and 7^{th} harmonics dominate the error due to the 5% unbalance. As expected, longer settling times attenuate the ripple better. Also, Fig.5.5b shows that the design settling time must at least be 230 ms in order for the steady state error to be less than 0.5 Hz as per the requirements. Note that this is for the specific harmonics and unbalance present in the weak grid considered. A higher harmonic distortion and a larger unbalance in the voltage would require one to increase the settling time further.

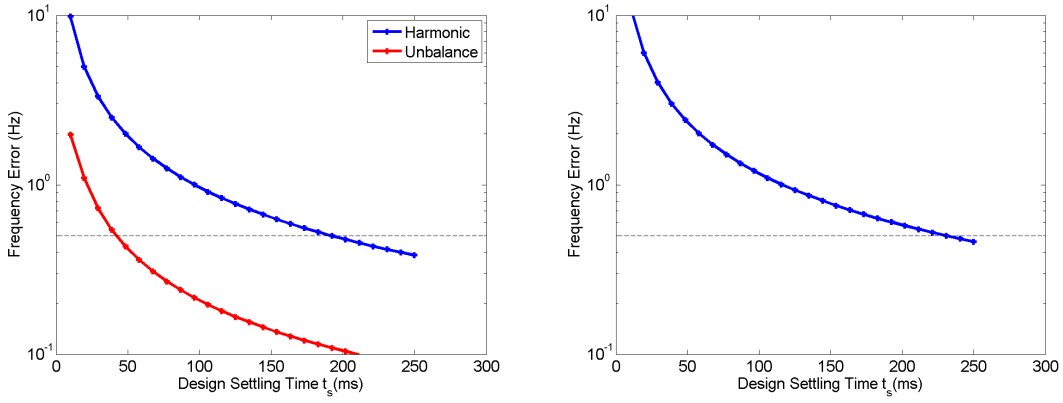

(a) Error due to harmonics and unbalance **(b)** Combined error

Figure 5.5: Error in the frequency measurement due to ripples in the steady state due to harmonics and voltage unbalance.

5.3.4 SRF Bandwidth Considerations

In the previous sections, the main design parameter of the SRF-PLL was the settling time (t_s), which is the traditional technique followed [6]. However, the linearised transfer function given in (5.3.2) shows that there is a zero in the closed loop system. Usually, a closed-loop zero quickens the response, while lessening the damping (i.e. more overshoot) [87]. Therefore, one can expect to see a difference between the SRF-PLL response and a typical second-order system response with no zeros. The bandwidth of the SRF-PLL can be derived by evaluating the transfer function (5.3.2) in the frequency-domain as follows,

Using $s = j\omega$, (5.3.2) becomes,

$$G_\theta(j\omega) = \frac{2\zeta\omega_n j\omega + \omega^2}{-\omega^2 + 2\zeta\omega_n j\omega + \omega_n^2} \tag{5.3.11}$$

The magnitude of this is,

$$|G_\theta(j\omega)| = \left[\frac{(\omega_n^2)^2 + (2\zeta\omega_n\omega)^2}{(\omega_n^2 - \omega^2)^2 + (2\zeta\omega_n\omega)^2}\right]^{\frac{1}{2}} \tag{5.3.12}$$

The bandwidth of the system is defined as the frequency at which the magnitude response crosses over $-3dB$. Therefore, at the bandwidth frequency the magnitude is,

$$|G_\theta(j\omega_{-3dB})| = \frac{1}{\sqrt{2}} \tag{5.3.13}$$

By solving for the resulting quadratic equation in $(\omega_{-3dB})^2$ and taking its posi-

tive square root, the bandwidth of the SRF-PLL can be derived as,

$$\omega_{-3dB} = \omega_n \left[1 + 2\zeta^2 + \sqrt{(1+2\zeta)^2 + 1}\right]^{1/2} \tag{5.3.14}$$

Because $\zeta = 0.707$, and $\omega_n \approx 3.9/\zeta t_s$, the bandwidth is given by,

$$\omega_{-3dB} \approx \frac{1.185}{t_s} \tag{5.3.15}$$

This confirms that the bandwidth is inversely proportional to the settling time as expected. This relationship is graphically shown in Fig. 5.6, which is to be used in section 5.6 to compare all three frequency detection techniques with the same bandwidth.

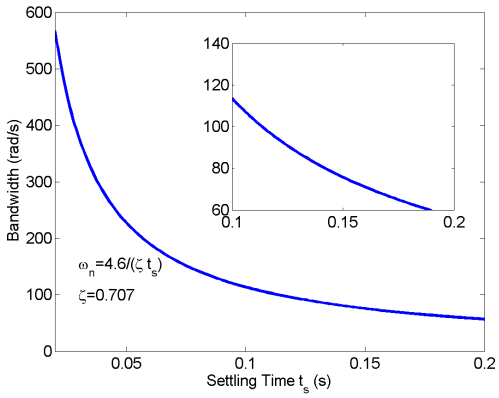

Figure 5.6: Bandwidth of SRF-PLL for varying settling times.

5.3.5 Optimum SRF-PLL Parameters For Energy Storage Control

The Table 5.2 summarises the requirements of the application (Energy storage control) and the design parameter t_s restrictions that must be adhered to, if one should satisfy the requirements.

Parameter	Requirement	Restriction
frequency range	$40Hz - 60Hz$	$t_s < 390\ ms$
$\text{ROCOF}_{\text{max}}$	$100Hz/s$	$t_s > 200\ ms$
transient delay	$10ms \leq t_{delay} \leq 50ms$	$t_s < 56\ ms$
accuracy	$\Delta f \leq \pm 0.5Hz$	$t_s > 230\ ms$

Table 5.2: SRF-PLL Design Parameter Restrictions

Immediately, from Table 5.2, it can be seen that a SRF-PLL is unable to satisfy all the requirements together. Out of all the requirements, only the frequency

range and the accuracy requirements are mandatory, so that both the SRF-PLL and the ES control can function. (The others increase the performance of the ES control and are thus essential.) Therefore, a design settling time of $t_s = 230\ ms$ has to be selected, in order to satisfy the mandatory requirements.

5.3.6 Summary

So far, the effective use of SRF-PLL for frequency detection purposes in a weak grid was demonstrated. The SRF-PLL tuning is relatively straight forward, because the equivalent second-order system allows tuning based on the required settling time. As observed, the transient response and the steady state response are coupled and one can tune the PLL to obtain a compromise for the desired outcome. Even though the SRF-PLL can be tuned to achieve individual requirements, not all the requirements can be met at the same time. Therefore, its use in a weak grid, where voltage unbalances and high harmonic distortion is commonplace, is not recommended.

5.4 The Generalised Modified DFT

In this section, a Discrete Fourier Transform based frequency detection technique by Lobos and Rezmer presented in [57] has been studied. The method which has been originally published as a modified DFT with a window length equivalent to one cycle (20 *ms*) was further generalised supported by a mathematical investigation. The contributions in this section improved the method's application in real time frequency determination to use different window lengths and components.

Discrete Fourier Transform (DFT) based frequency detection can primarily be expected to yield discrete frequency components with frequency resolution corresponding to the DFT's time interval. The classic DFT formula of a sinusoidal signal is given by,

$$X_k = \sum_{i=1}^{N} v_i e^{-j2\pi k \frac{i}{N}} \tag{5.4.1}$$

where X_k is the k^{th} frequency component that are multiples of the fundamental frequency f_0, v_i is the i^{th} instantaneous voltage value, N is the total number

of samples within the window. The time length of the window $T = N\Delta t = 1/f_0$. Since the equation does not contain any terms concerning f_0 or T, it is normalised.

For example, if the fundamental component of the power system frequency is $50Hz$, a typical voltage waveform after discrete Fourier transformation results in a series of frequency components at $50Hz$, $100Hz$, $150Hz$, $200Hz$, etc., when the window length is 20 ms (one-cycle) [58]. There are two tangled uncertainties associated with the DFT; namely the temporal uncertainty and the frequency uncertainty. This is in fact a property associated not only with the DFT, but with functions related by a Fourier transform and is known as Heisenberg uncertainty principle. Because the results of the DFT depends on past values within the sampling window, there is an inherent maximum temporal delay equal to the window's time length. The uncertainty in frequency (or frequency resolution) is equal to the reciprocal of the window's time length. Hence, in order to improve frequency resolution, one must increase the window's time length; but increasing the window's time length would proportionally increase the time delay.

Power system frequency in low voltage feeders (weak-grid) usually varies within a few Hz (i.e. ± 10 Hz) around the nominal frequency ($50Hz$). Therefore, a resolution higher than $50Hz$ is required from a DFT based frequency detection technique. Thus, the DFT needs to be modified to find instantaneous frequencies at various levels apart from the discrete repetitions of $50Hz$, while keeping the same time-delay of 20 ms (i.e. one cycle). The method presented by Lobos and Rezmer in the literature uses angular velocity of the fundamental rotating voltage phasor to measure the instantaneous frequency in [57]. This is explained in the following section.

5.4.1 Modified DFT Technique: Theoretical Investigation

Lobos and Rezmer in [57] present a real time frequency detection technique that involves DFT and a windowing technique to extract the fundamental component of the voltage instantaneously. This has been realised by means of calculating the angular velocity of the rotating voltage phasor, which can be defined as the instantaneous frequency. This method was specifically used in a single-phase environment in [57].

It has been considered for a complex voltage waveform with amplitude A and

frequency f of the form,

$$y(t) = Ae^{j(2\pi ft+\phi)} \tag{5.4.2}$$

where ϕ is a constant phase shift. In a balanced three phase system, such a waveform can be obtained from the Clarke transform ($\alpha\beta$ transform), by representing the real part by v_α and imaginary part by v_β.

The k^{th} component in the frequency domain can be obtained using the Fourier series for the continuous signal within the window $(0, T)$. This assumes that the signal within the window is repetitive with a period equal to the window length T. This is common to both the Fourier series and the DFT presented in (5.4.1). The only difference is that the DFT time signal is discrete, while the Fourier series time signal is continuous.

In addition, in the method presented by Lobos and Rezmer, a running DFT is conducted that modifies (5.4.1), such that at each time step, the DFT of the past N values is calculated. Hence, the modified DFT equation can be presented as follows.

$$X_k[n] = \sum_{i=1}^{N} v_{i+n-N} e^{-j2\pi k \frac{i}{N}} \tag{5.4.3}$$

Similarly in the continuous domain, another time variable τ is considered as the current time. Then, in the Fourier series, the time (t) window is the range $(\tau - T, \tau)$. When t varies in this range, the time value in the Fourier series exponent should vary from 0 to T. Therefore, it can be identified that the time in the exponent of the Fourier series should change to $t - \tau + T$. Therefore, the k^{th} component of a running Fourier series at time τ can be obtained as

$$C_k(\tau) = \frac{2}{T} \int_{\tau-T}^{\tau} y(t) e^{\frac{-j2\pi k(t-\tau+T)}{T}} dt \tag{5.4.4}$$

Note that the fundamental frequency is defined as $f_0 = \frac{1}{T}$.

By substituting for $y(t)$ and simplifying,

$$C_k(\tau) = \frac{2Ae^{j\phi}}{T} e^{j2\pi f\tau} e^{-j\pi(f+kf_0)T} \left[\frac{sin(\pi(f-kf_0)T)}{\pi(f-kf_0)}\right]$$

Since normalised $\text{sinc}(\theta)$ is defined as $\frac{\sin(\pi\theta)}{\pi\theta}$, the following can be obtained,

$$C_k(\tau) = 2A\,\mathrm{sinc}((f - kf_0)T)e^{j\phi}e^{j2\pi f\tau}e^{-j\pi(f+kf_0)T} \tag{5.4.5}$$

The phase angle of the k^{th} component w.r.t. τ is,

$$\angle C_k(\tau) = \phi + 2\pi f\tau - \pi(f + kf_0)T \tag{5.4.6}$$

The derivative of the angle of the k^{th} component is,

$$\frac{d\angle C_k(\tau)}{d\tau} = 2\pi f \tag{5.4.7}$$

This shows that the frequency of a balanced 3-phase signal can be obtained using a running DFT from the derivative of the phase angle of any frequency component. The magnitude of the component is a sinc function dependent on f and is largest when the frequency of the k^{th} component is closest to f. Of course one should select the component with the maximum magnitude in order for the phase to be resilient to noise.

Compared to a classic DFT, which can only extract frequencies at harmonics of the fundamental, the modified version can detect any frequency around the fundamental with only a delay equivalent to the time length of the DFT-window. However, in practice, there are other parameters limiting the frequency resolution of the frequency detection, such as ripple due to harmonic content and imbalance in the voltage.

Another interesting fact about this method is that the magnitude of the complex envelope is defined as a sinc function. According to the graphical illustration of a sinc function as shown in Fig.5.7, the function reaches zero at even multiples of f_0 around kf_0. If $f_0 = 50\ Hz$ and $k = 1$, this means that the detected frequency will produce a null response at $0Hz$, $\pm 50Hz$, $\pm 100Hz$,$\pm 150Hz$, $\pm 200Hz$, $\pm 250Hz$, $\pm 300Hz$ ... Since the frequency range of interest is $40Hz \leq f \leq 60Hz$, this is not an issue for $f_0 = 50Hz$. However, if $f_0 < 10\ Hz$ (i.e. $T > 100\ ms$), for any selected k, one or more magnitude nulls will occur within the frequency range of interest. Hence, some very narrow frequency ranges will become unmeasurable. The solution is to modify the magnitude function to not contain frequency nulls, by applying a window function.

Now that the method has been demonstrated in ideal circumstances, it is interesting to see how the method changes mathematically in the presence of har-

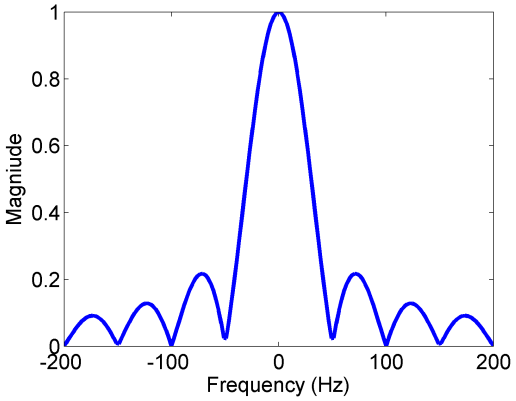

Figure 5.7: The magnitude of a sinc function

monics and/or unbalances.

In order to theoretically investigate the effectiveness of the DFT in the presence of harmonics, consider the input signal,

$$y_{nh}(t) = A\left(e^{j(2\pi ft+\phi_1)} + \alpha e^{j(2\pi nft+\phi_2)}\right) \tag{5.4.8}$$

where $n \neq 1$ is the integer harmonic component.

The k^{th} component now changes to include the extra harmonic component.

$$\begin{aligned} C_k^h(\tau) = {} & 2A\,\text{sinc}((f-kf_0)T)e^{j\phi_1}e^{j2\pi f\tau}e^{-j\pi(f+kf_0)T} \\ & + 2A\alpha\,\text{sinc}((nf-kf_0)T)e^{j\phi_2}e^{j2\pi nf\tau}e^{-j\pi(nf+kf_0)T} \end{aligned} \tag{5.4.9}$$

In general, the above equation can be written as,

$$C_k'(\tau) = Be^{j\gamma}\left(e^{j2\pi f\tau} + \beta e^{j\delta}e^{j2\pi nf\tau}\right) \tag{5.4.10}$$

where $B = 2A\,\text{sinc}((f-kf_0)T)$, $\gamma = \phi_1 - \pi(f+kf_0)T$, $\beta = \alpha\frac{\text{sinc}((nf-kf_0)T)}{\text{sinc}((f-kf_0)T)}$ and $\delta = \phi_2 - \phi_1 - \pi(n-1)fT$.

The phase angle of $C_k^h(\tau)$ can be written as

$$\angle C_k^h(\tau) = \gamma + \tan^{-1}\left(\frac{\sin 2\pi f\tau + \beta\sin(\delta+2\pi nf\tau)}{\cos 2\pi f\tau + \beta\cos(\delta+2\pi nf\tau)}\right) \tag{5.4.11}$$

The derivative w.r.t τ can now be written as,

$$\frac{d\angle C_k'(\tau)}{d\tau} = 2\pi f\frac{(1+n\beta^2)+\beta(n+1)\left[\cos(\delta+2\pi(n-1)f\tau)\right]}{1+\beta^2+2\beta\cos(\delta+2\pi(n-1)f)} \tag{5.4.12}$$

According to (5.4.12), the presence of the n^{th} component creates a ripple of $(n-1)^{\text{th}}$ harmonic. In the experimental weak grid, the most prominent components of 350 Hz and -250 Hz will create a ripple of 300 Hz and -300 Hz respectively.

A voltage unbalance can also be thought of as harmonic contamination due to the negative fundamental (i.e. $n = -1$).

Hence, the derivative w.r.t τ can be written as,

$$\frac{d\angle C_k'(\tau)}{d\tau} = \frac{2\pi f(1-\beta^2)}{1+\beta^2+2\beta cos(\delta+4\pi f\tau)} \tag{5.4.13}$$

(5.4.13) reduces to (5.4.7) when $\beta = 0$. The derivative of the phase angle now oscillates between $2\pi f\frac{1-\beta}{1+\beta}$ and $2\pi f\frac{1+\beta}{1-\beta}$ at a frequency of $2f$. This oscillation around $2\pi f$ reduces the accuracy of the detected frequency.

Lobos and Rezmer suggest filtering out the negative component using windowing techniques such as Hamming or Blackman windows. This will decrease β and improve the accuracy. This is not only effective against unbalance, which creates a double frequency component, but also effective against higher order negative and positive harmonics.

Spectral leakage influences the steady state response for a given window length. In order to improve the filtering qualities of the modified DFT, Lobos and Rezmer suggest using a smoothing window, that is usually used in the traditional DFT. Two common window-functions, Hamming and Blackman are considered in their study and are representative of most available window functions. The Hamming window (5.4.14) is optimised to minimise the first side-lobe, whereas the Blackman window (5.4.15) has a flatter top at the centre and a good overall attenuation beyond the first side-lobe. The window functions in the frequency domain are illustrated in Fig.5.8.

$$\omega_{Hamming} = 0.54 - 0.46\cos\frac{2\pi n}{N-1} \tag{5.4.14}$$

$$\omega_{Blackman} = 0.42 - 0.5\cos\frac{2\pi n}{N-1} + 0.08\cos\frac{4\pi n}{N-1} \tag{5.4.15}$$

According to Fig.5.8a, it can be seen that the magnitude response is significant at all frequencies between $-2f_0$ and $2f_0$ (in the figure $f_0 = 50$ Hz) for both Hamming and Blackman windows. Due to the windows, the window length can now be increased by twice the limit of the standard DFT. In this case, the

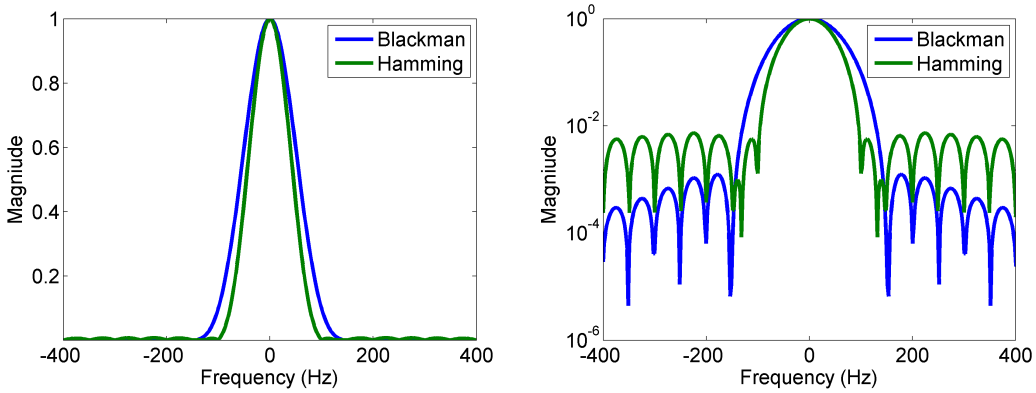

(a) Linear Scale **(b)** Log scale

Figure 5.8: The frequency domain of the Hamming and the Blackman windows for a window length of $T = 20\ ms$ in linear and log scale.

window length is limited by $T < 100\ ms$. Beyond this, some frequency bands will be unmeasurable between $40Hz$ and $60Hz$. Mathematically, this requirement can be generalised as,

$$f_0 > \frac{1}{4}\Delta f_{range} \tag{5.4.16}$$

A block diagram of the Modified DFT method is shown in Fig.5.9.

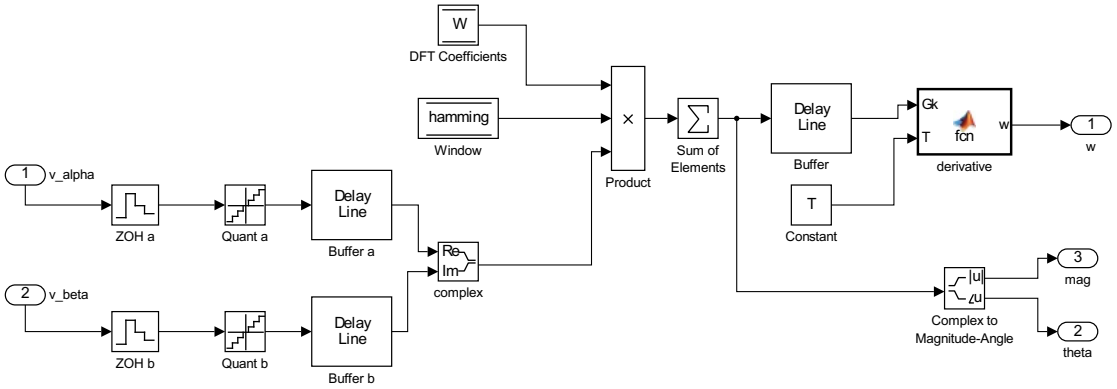

Figure 5.9: A block diagram of the modified DFT method

In Lobos and Rezmer's method, the window length was fixed as the time period of the nominal fundamental (i.e. 20 ms for 50 Hz). However, with the generalisation, the window length can be allowed to vary and the choice of specific component is free. In this thesis, the component closest to the nominal fundamental was selected. But in theory, it should be the component that provides the largest magnitude for a given frequency. For most window lengths, the former is the same as latter.

In a DFT, the two prominent characteristics that can vary are the length of the

window(T) and the number of samples (N_s) in a window. Since the frequency of the fundamental is f_0, the number of samples (N_s) can be obtained by

$$N_s = \frac{f_s}{f_0} \tag{5.4.17}$$

where f_s is the sampling frequency.

Using a sampling frequency larger than twice the highest component of harmonics present in the input, can avoid the aliasing effect. In this case, it has already been found out that the highest harmonic dealt with is $550Hz$. Hence, theoretically, any sampling frequency higher than $1100Hz$ can be used in the DFT. Varying the sampling frequency within valid limits (i.e. > 1100 Hz) showed no significant improvement in the detected frequency. The sampling frequency is 8 kHz in the experimental facility and was kept at 10 kHz in the simulation. Both fulfil the Nyquist requirement and provide integer number of samples per millisecond so that the window length can be varied with millisecond precision.

In the following sections, the optimum design parameters (i.e. window length) of the DFT that satisfies all the requirements of the ES control application, will be investigated.

5.4.2 Generalised Modified DFT Response to Step Frequency

A frequency step change test is conducted in this section, under undistorted and balanced voltage conditions. However, windowing functions are applied, as they are used in the presence of harmonic distortion and unbalance in later sections. This gives an opportunity to vary the window length (T) and observe the settling of the generalised modified DFT.

Fig.5.10a shows the detected frequency for three window lengths 10 ms, 20 ms and 40 ms. The settling time to settle within 2% is measured and plotted for various window lengths in Fig.5.10b.

According to Fig.5.10a, DFT detected frequency always settles within the window length (T). As can be seen, the rise times are different between the Hamming windowed DFT and the Blackman windowed DFT, indicating that the two have different bandwidths. From both Figs.5.10a and 5.10b, the Blackman windowed DFT is seen to be slightly faster. The discontinuities present in the settling time graph are when the component is changed from $k = 1$ to $k = 2$ at 30 ms and from $k = 2$ to $k = 3$ at 50 ms and also due to the stepwise nature

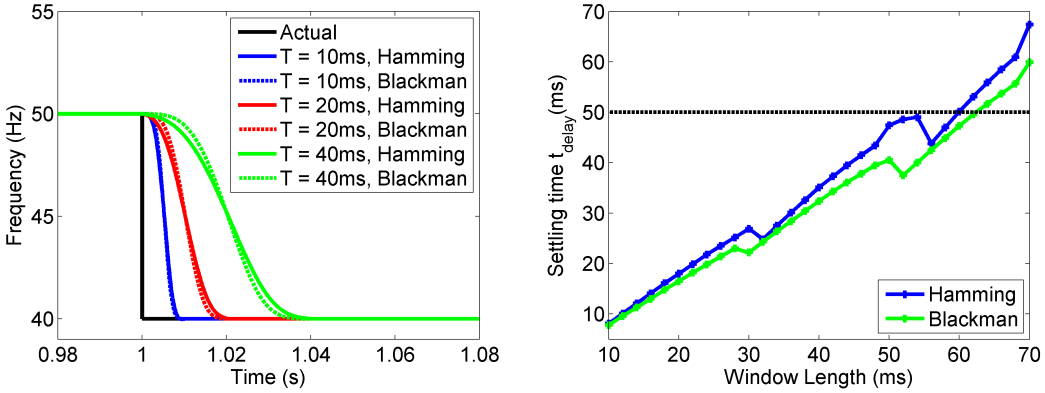

(a) Detected step frequency **(b)** Settling time of the DFT

Figure 5.10: Illustration of DFT frequency detection for three illustrative window lengths and the settling times for varying window lengths with with Hamming and Blackman windows.

of settling time measurement. From Fig.5.10b, one can infer that the window length $T < 60\ ms$ for the Hamming windowed DFT and $T < 62\ ms$ for the Blackman windowed DFT, satisfy the delay requirement. However, as a rule of thumb, it is safer to restrict the window length $T < 50\ ms$ of the generalised modified DFT so that it satisfies the settling time requirement for any window type.

5.4.3 Generalised Modified DFT Response to Ramp Frequency

A ramp frequency variation of 100 Hz/s was applied to the clean balanced 3-phase voltage signal. The detected frequency for three different window lengths are shown in Fig.5.11a for illustration. Even though the steady state error of the step response is null, for the ramp response it is finite. This error has been caused by the finite delay in frequency detection, which is defined by the window-length of the DFT. This steady state error of the ramp response cannot be eliminated, since the DFT is not a closed-loop system. This may be a drawback compared to the SRF-PLL as the SRF-PLL has zero steady state error for both step and ramp responses.

However, it is interesting to note that the detected frequency of the DFT does not experience a transient over-shoot as seen with the SRF-PLL. That indicates that the DFT does not overestimate the ROCOF too much for these window lengths.

As with the SRF-PLL, the ROCOF from the derivative of the detected frequency

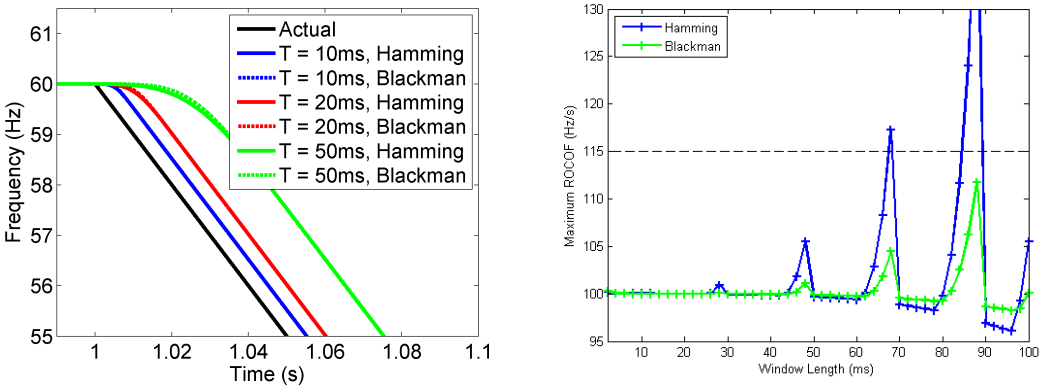

(a) Detected Ramp frequency

(b) Maximum ROCOF estimated by the DFT

Figure 5.11: The illustration of DFT frequency detection for three illustrative window lengths and the maximum ROCOF for varying window lengths with Hamming and Blackman windows.

was measured. The maximum ROCOF for varying window lengths are shown in Fig.5.11b. From this figure, it is evident that the ROCOF is never overestimated if the window length $T < 26$ ms. This characteristic opens up the DFT for applications based on ROCOF limiters. In terms of energy storage control, the only restriction is that $T < 68$ ms so that the estimated ROCOF is within 15% of the actual value. Similar to that witnessed in the settling time figure, irregular values could be observed just before a change in the component k used to calculate phase. In addition, when $T > 40$ ms, the DFT in general underestimates the ROCOF. Therefore, it is best to keep a smaller window length, that will both minimise the frequency error and ROCOF underestimation.

With the same ramp input, another test was conducted. Fig.5.11a shows that there is a finite delay between the actual and the detected ramps. This delay was calculated and observed that it increases with time, by a small amount for shorter window lengths and by a relatively large amount (≈ 6 ms for $T = 90$ ms) for longer window lengths. This behaviour can also be confirmed by the detected ROCOF being slightly less than 100 Hz/s for longer window lengths. The maximum ramp delay for each window length was recorded and is shown in Fig.5.12.

According to Fig.5.12, the ramp delay is almost linearly proportional to the window length. This delay value is less than the settling times shown in Fig.5.10b. In fact, one can see that the relationship between the window length and the

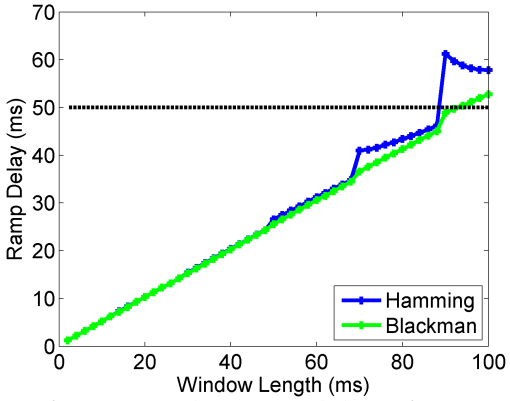

Figure 5.12: The DFT frequency detection delay of a 100 Hz/s ramp for varying window lengths

ramp delay time to be,

$$t_{delay(ramp)} \approx \frac{1}{2}T \tag{5.4.18}$$

For the application of energy storage control, both of these delays need to be minimised. In comparing two frequency detection methods, one must take both delays into account.

5.4.4 Generalised Modified-DFT Response to Harmonics and Unbalance

In this section, the variations in the detected frequency when harmonics and unbalance are present in the input signal are observed. The voltage signal was contaminated by the harmonic content listed in Table 3.2, similar to the signals used in section 5.3.3. An unbalance of 5% of a single phase was created. A ramp frequency variation of 2 Hz/s was imposed and the input signal was processed through DFTs of different window-lengths. The detected frequency ramp in the presence of harmonics and unbalances are shown separately for three different window lengths in Figs.5.13a and 5.13b respectively.

From Figs.5.13a and 5.13b, one can see that increasing the window length decreases the ripple content as expected. Yet, one can appreciate that the ripple content is significantly lower than that observed in the SRF-PLL. The ripple effect due to unbalance for the DFT with a window length of 10ms is significantly more than that observed for window lengths of 20ms and 40ms. In order to obtain a complete picture, the ripple amplitude against window length in the presence of harmonics, unbalance and both effects are shown in Figs.5.14a and

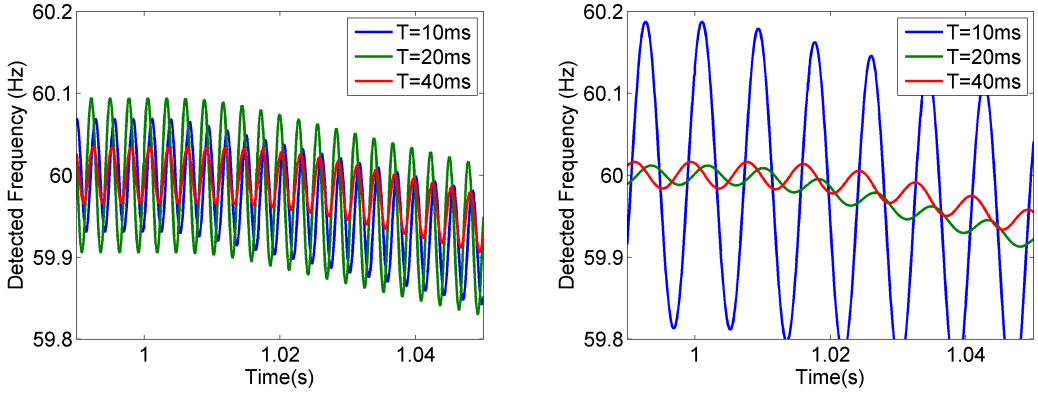

(a) With Harmonics **(b)** With Unbalance

Figure 5.13: Illustration of DFT detected frequency of a slow ramp with three different window lengths with Hamming window.

5.14b respectively.

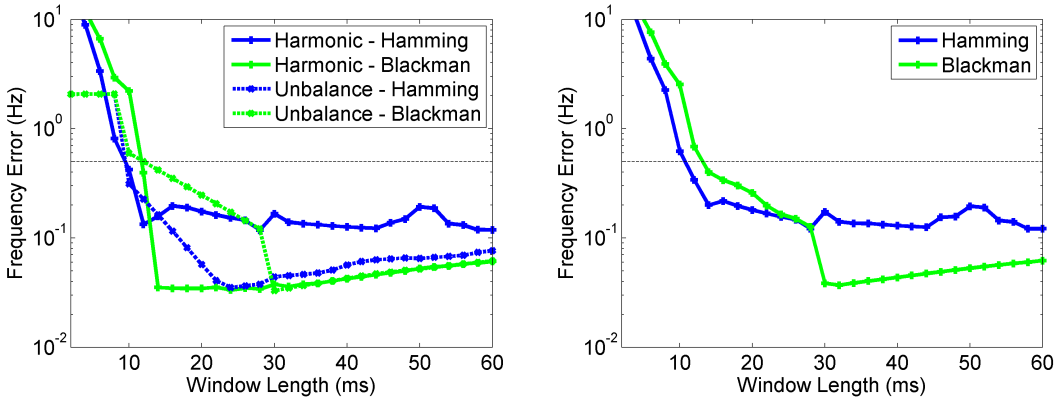

(a) Separate Error **(b)** Combined Error

Figure 5.14: Error in DFT detected frequency in the presence of harmonics and unbalance for varying window lengths.

From Fig.5.14a, one can observe that when using the Hamming window, the ripple due to harmonics and unbalance reduces quickly when $T > 12\ ms$. When using the Blackman window, the error due to harmonics drops around $T = 12\ ms$, while the error due to unbalance drops around $30\ ms$. This is because the Blackman window does not attenuate the double frequency as much as the Hamming window, even when $T = 20\ ms$ as can be seen from Fig.5.8b. The DFT with Blackman window attenuates when the main lobe is narrow enough to cut off the double frequency component beyond $T = 30\ ms$.

According to Fig.5.14b, the application requirement of energy storage control can be met for $T > 12\ ms$ when using the Hamming window and $T > 14\ ms$ when using the Blackman window.

5.4.5 DFT Bandwidth Considerations

The main tuning parameter of a DFT is its window length. The window length determines the settling time for a step change in frequency, and the steady state error for a ramp change in frequency. Also, in the presence of harmonics and unbalances in the input voltage, adjusting window length varies the filtering properties of the DFT, changing the magnitude of the ripple. In order to compare the DFT performance against other methods, the bandwidth of the DFT is defined similar to that defined for the SRF-PLL in section 5.3.4.

Unlike the second-order SRF-PLL, the DFT is an N^{th} order system. However, a simplified linearised approximation of the DFT to a second/ third/ fourth-order system can be suggested. For this, the response of the DFT to a step change in frequency for a clean and balanced input signal was considered and compared with the typical second/third/fourth order system responses given in (5.4.19), (5.4.20) and (5.4.21) respectively.

$$H_{DFT2}(s) = \frac{\omega_n^2}{(s^2 + 2\zeta\omega_n s + \omega_n^2)} \tag{5.4.19}$$

$$H_{DFT3}(s) = \frac{\alpha\omega_n^2}{(s+\alpha)(s^2 + 2\zeta\omega_n s + \omega_n^2)} \tag{5.4.20}$$

$$H_{DFT4}(s) = \frac{\omega_{n1}^2\omega_{n2}^2}{(s^2 + 2\zeta_1\omega_{n1} s + \omega_{n1}^2)(s^2 + 2\zeta_2\omega_{n2} s + \omega_{n2}^2)} \tag{5.4.21}$$

A regression analysis was then performed to estimate the parameters (i.e. ζ, ω, α, ζ_1, ζ_2, ω_{n1} and ω_{n2}) such that the difference between the approximated system response and the DFT response is minimised using the *fminsearch* utility in Matlab.

Figs.5.15a and 5.15b shows the DFT response with Hamming window and its approximated responses for window lengths of 10 *ms* and 40 *ms* respectively for illustration. According to the figures, one can see that the second order system is unable to approximate the DFT step response in terms of either the rise time or the settling time.

For $T = 40$ *ms* case, the third-order approximation shows a good proximity compared to that obtained by the second-order system. Not only the rising times are closer, but also the settling times are improved. Unlike in the second-order system the overshoot is reduced.

As can be understood, the modified DFT was better approximated when the

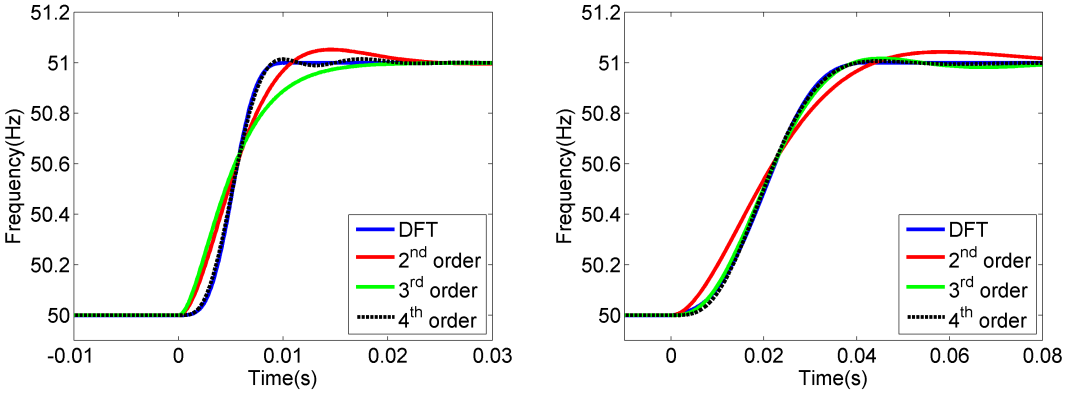

(a) Window length of 0.01s **(b)** Window length of 0.04s

Figure 5.15: Hamming DFT approximation with a $2^{nd}/3^{rd}/4^{th}$ order systems

order of the approximation was increased, since the DFT is inherently a higher order i.e. N^{th} order system. This is proven when a fourth-order approximation was carried out. Figs.5.15a and 5.15b display excellent approximation properties by a fourth-order system compared to the previous systems for both $T = 10\ ms$ and $T = 40\ ms$. Both the rise times and the settling times are well matched, while overshoots are significantly minimised. However, now the approximation consists of two second-order systems, resulting in a more complex design. Even though a third order system could approximate the DFT when $T = 40\ ms$, it is unable to do so for the shorter window length. This means that for the purpose of bandwidth comparison, a fourth-order approximation may be regarded as sufficient.

The bandwidth of a typical fourth order system can be calculated by the following equation by equating the magnitude of the frequency response to $1/\sqrt{2}$,

$$\{(\omega_{n1}^2 - \omega^2)^2 + 4\omega^2\zeta_1^2\omega_{n1}^2\}\{(\omega_{n2}^2 - \omega^2)^2 + 4\omega^2\zeta_2^2\omega_{n2}^2\} = 2\omega_{n1}^4\omega_{n2}^4 \tag{5.4.22}$$

where ω_{n1}, ζ_1 and ω_{n2}, ζ_2 are the natural frequency and damping factor of two respective second order systems that form the fourth order system.

The resulting bandwidths obtained for varying the window lengths of DFTs with both Hamming and Blackman windows are shown in Fig.5.16.

According to Fig.5.16, in general there is an inverse relationship between the window length (T) and the DFT bandwidth. The window lengths of exception are that close to the component (k) changing times (i.e. 30 ms and 50 ms). By a

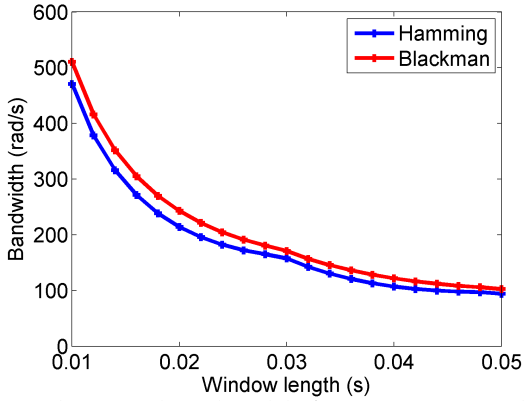

Figure 5.16: The DFT bandwidth for varying window lengths.

regression analysis one can find out that,

$$w_{3dB(Hamming)} \approx \frac{4.5}{T} \tag{5.4.23}$$

$$w_{3dB(Blackman)} \approx \frac{5.0}{T} \tag{5.4.24}$$

5.4.6 Optimum DFT parameters for Energy Storage Control

Table 5.3, shows the restriction on the window length from the results obtained so far in order to cater for the requirements of the energy storage control application.

Parameter	Requirement	Restriction	
		Hamming	Blackman
frequency range	$40Hz - 60Hz$	$T < 100\ ms$	$T < 140\ ms$
$\text{ROCOF}_{\text{max}}$	$100Hz/s$	$T < 67\ ms$	$T < 106\ ms$
transient delay	$10ms \leq t_{delay} \leq 50ms$	$T < 60\ ms$	$T < 62\ ms$
accuracy	$\Delta f \leq \pm 0.5Hz$	$T > 12\ ms$	$T > 14\ ms$

Table 5.3: DFT design parameter restrictions

According to Table5.3, any window length within $14\ ms \leq T \leq 60\ ms$ will adhere to the application requirements. Since the primary aim is to minimise the settling time, $T = 12\ ms$ and $T = 14\ ms$ were selected for Hamming and Blackman windowed DFTs respectively as optimum designs.

5.4.7 Summary

In this section, a generalisation of the modified DFT method for the purpose of frequency estimation in weak grids was presented. The frequency detection requirements are realisable in a DFT by tuning it to minimise the settling time, while adhering to other requirements, by changing the window-length of the DFT, which is the only tunable parameter. The fact that any window length and any frequency component can be used to extract the frequency was shown mathematically. Yet, practically, one would need to restrict the window length and select an optimum frequency component depending on the application. In addition, the existence of a limit to the window length similar to lock range in PLLs was also shown. The presence of harmonics in the input voltage generated an oscillatory steady state error, whereas unbalance in the voltage caused a double frequency ripple. With the addition of a window-function, the steady state response of the DFT could be improved vastly, without affecting the transient response. This also increased the allowable window length by a factor of two. Finally, an approximation of the modified DFT was conducted using control-theory. Since, the DFT represent an N^{th}order system, a higher order linearisation showed increasingly better approximation of the actual DFT. However, for the simplicity of the calculation of the DFT bandwidth for comparison purposes, a fourth-order approximation was declared sufficient and thus obtained the bandwidth.

5.5 Adaptive Filtering

In a three-phase PLL, one of the major draw backs is the inability to attenuate the double frequency component. In addition, when the voltage is contaminated with other higher harmonics, the measured frequency contains a significant ripple component. This is mainly because the conventional filter of a PLL can only be designed to attenuate a certain frequency range, for a defined time delay.

This has given rise to studies in adaptive filtering techniques, mainly to attenuate the double frequency component, which is the hardest to eliminate without significantly compromising the time delay. An adaptive filter has the ability to adjust its design (the parameters) automatically according to an optimisation algorithm. Also, the design does not necessarily require prior knowledge of the

signal to be filtered [90]. Usually the optimisation is based on a cost function, which sets the parameters of the filter in such a way that the filter coefficients are modified with respect to minimising a certain noise/harmonic component. The algorithm is optimised so that the cost of the next iteration is minimised [6, 90].

There have been a lot of studies of adaptive filter based techniques for single phase applications. Well known methods include Adaptive Notch Filter (ANF) based methods [59], Quadrature-PLL (QPLL) [61] and Enhanced-PLL (EPLL) [60]. All adaptive based techniques can be attributed to their robustness in estimating the power system frequency quickly and accurately, while being less-sensitive to noise and unbalance compared to conventional PLLs. However, many of these methods were developed in a single-phase environment and considering the high computational requirements of realising the methods, these methods were not added to the comparison section of this research. However, a few similar comparison studies [6, 54] showed that a special adaptive filtering based technique using the Double Second-Order Generalised Integrator (DSOGI) could be effective and was therefore included in this work. The method was specially chosen as it can be developed as a Frequency-locked loop (FLL) or as a PLL. Since the interest lies in methods for quick frequency estimation with good harmonic attenuation, the DSOGI technique is suitable for this study. The theory and the characteristics of the method will be discussed next, followed by simulated results to investigate the performance of the method.

5.5.1 DSOGI-FLL: A Theoretical Investigation

The SOGI structure consists of two generalised integrators as seen in Fig.5.17. The configuration of the SOGI has the following transfer function, given that the gain of the SOGI-loop is k,

$$SOGI(s) = \frac{v'}{k\varepsilon_v}(s) = \frac{\omega' s}{s^2 + \omega'^2} \tag{5.5.1}$$

From Fig.5.17, it can be seen that $qv'/v' = \omega'/s$, meaning if v' is a harmonic wave with an angular frequency ω, $qv'/v' = \omega'/j\omega$. If ω' is made equal to ω, qv' lags v' by $\pi/2$ and the two outputs are said to be in quadrature.

In a three-phase environment, two SOGI-QSGs are used separately on v_α and v_β to obtain two quadrature signals. These signals can be mathematically rear-

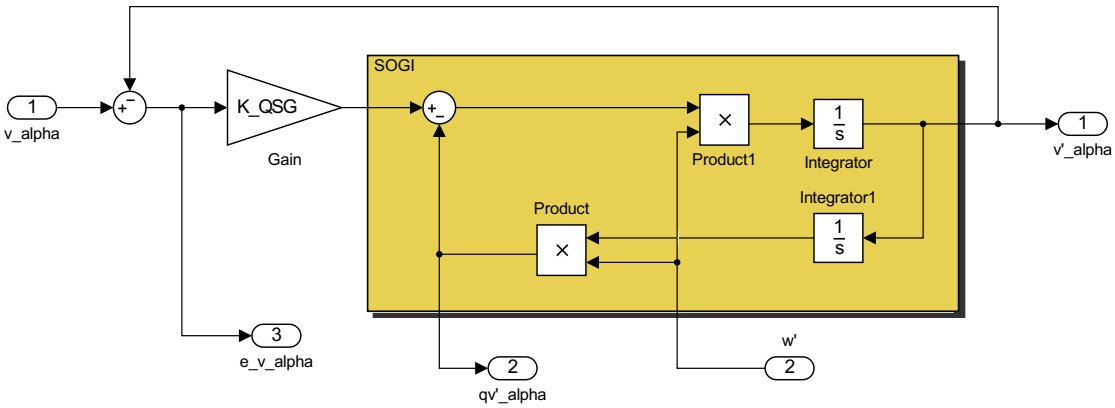

Figure 5.17: The SOGI-structure

ranged to obtain the positive and negative components of the original voltage.

$$v^{+}_{\alpha\beta} = \frac{1}{2}\begin{bmatrix} 1 & -q \\ q & 1 \end{bmatrix} v_{\alpha\beta} \tag{5.5.2}$$

$$v^{-}_{\alpha\beta} = \frac{1}{2}\begin{bmatrix} 1 & q \\ -q & 1 \end{bmatrix} v_{\alpha\beta} \tag{5.5.3}$$

where $q = e^{-j\frac{\pi}{2}}$ is a 90 deg phase-shifting operator which can be applied in the time-domain to obtain an quadrature representation of the input signal [6].

The closed loop transfer functions for the in-quadrature signals referring to Fig.5.17 are,

$$D(s) = \frac{v'}{v}(s) = \frac{k\omega' s}{s^2 + k\omega' s + \omega'^2} \tag{5.5.4}$$

$$Q(s) = \frac{qv'}{v}(s) = \frac{k\omega'^2}{s^2 + k\omega' s + \omega'^2} \tag{5.5.5}$$

Equations (5.5.4) and (5.5.5) represent the transfer functions of the in-quadrature signals in the s-domain. Hence, one can create an analogous to (5.5.2) in the s-domain,

$$v'_{\alpha\beta+} = \frac{1}{2}\begin{bmatrix} D(s) & -Q(s) \\ Q(s) & D(s) \end{bmatrix} v_{\alpha\beta} = \frac{1}{2}\frac{k\omega'}{s^2 + k\omega' s + \omega'^2}\begin{bmatrix} s & -\omega' \\ \omega' & s \end{bmatrix} v_{\alpha\beta} \tag{5.5.6}$$

A similar expression can be deduced using (5.5.3) or simply transposing the

matrix (5.5.6). From the theory of positive and negative components,

$$v^{+}_{\alpha\beta}(j\omega) = \begin{bmatrix} 1 & -j \end{bmatrix}^{T} v^{+}_{\alpha\beta}(j\omega) \tag{5.5.7}$$

$$v^{-}_{\alpha\beta}(j\omega) = \begin{bmatrix} 1 & j \end{bmatrix}^{T} v^{-}_{\alpha\beta}(j\omega) \tag{5.5.8}$$

$$\tag{5.5.9}$$

where $v^{+}_{\alpha\beta}, v^{-}_{\alpha\beta}$ are scalar values. By substituting $v^{+}_{\alpha\beta}$ and $v^{-}_{\alpha\beta}$ separately in place of $v_{\alpha\beta}$ in (5.5.6) and rearranging one can write the contributions of the positive ($v^{+}_{\alpha\beta}$) and the negative ($v^{-}_{\alpha\beta}$) components of the input signal to the recreated positive component ($v'_{\alpha\beta+}$) after the positive negative sequence combiner (PNSC).

$$\frac{v'_{\alpha\beta+}(j\omega)}{v^{+}_{\alpha\beta}(j\omega)} = \frac{1}{2}\frac{k\omega'(\omega'+\omega)}{k\omega'\omega + j(\omega^2 - \omega'^2)} \tag{5.5.10}$$

$$\frac{v'_{\alpha\beta+}(j\omega)}{v^{-}_{\alpha\beta}(j\omega)} = \frac{1}{2}\frac{k\omega'(\omega-\omega')}{k\omega'\omega + j(\omega^2 - \omega'^2)} \tag{5.5.11}$$

A Bode-diagram can be plotted as shown in Fig.5.18, for the two responses;

$$P(j\omega) = \frac{|v'_{\alpha\beta+}|}{|v^{+}_{\alpha\beta}|} \qquad N(j\omega) = \frac{|v'_{\alpha\beta+}|}{|v^{-}_{\alpha\beta}|} \tag{5.5.12}$$

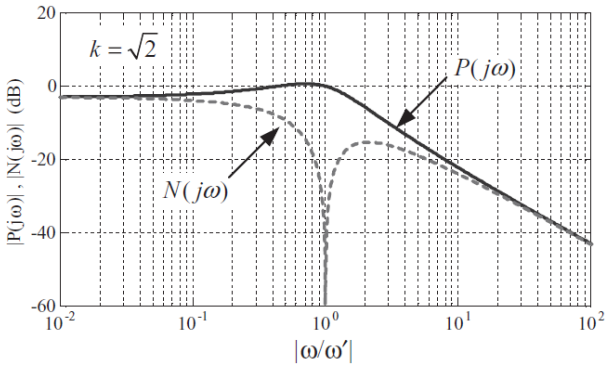

Figure 5.18: Frequency response of the DSOGI adaptive filter [6]

The Bode-diagram depicts some interesting characteristics of the DSOGI in the frequency domain. It shows that the DSOGI is able to act as a low-pass filter for the positive components and as a notch-filter for the fundamental negative component. Another key point is that the notch is achieved when the detected frequency of the signal is equal to the actual frequency of the input i.e. $\omega' = \omega$.

It is also evident in the transfer function of the SOGI in (5.5.1) that quadrature generation is only possible when the input frequency ω' of the SOGI is equivalent to the frequency of the input voltage ω. This calls for a mechanism to make $\omega' = \omega$ and a FLL is proposed for the above purpose in [6], which has far better combined characteristics than a PLL on the obtained positive component.

A single FLL is suggested in [6] combining the outputs of two SOGI filters for v_α and v_β, and the signal flow-diagram is shown in Fig.5.19.

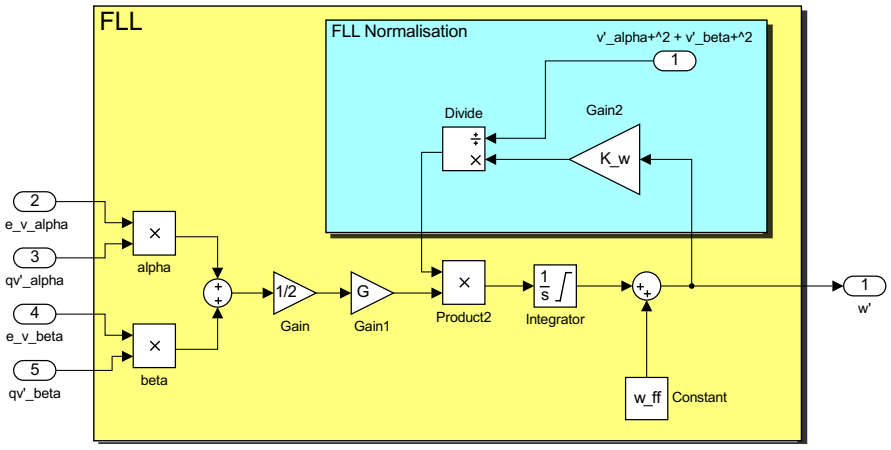

Figure 5.19: Structure of FLL for the DSOGI method

The frequency error signals generated by the QSG of the α and β inputs are combined in an average error signal as given by;

$$\varepsilon_f = \frac{\varepsilon_{f(\alpha)} + \varepsilon_{f(\beta)}}{2} = \frac{1}{2}(\varepsilon_\alpha q v'_\alpha + \varepsilon_\beta q v'_\beta) \tag{5.5.13}$$

However, for linearisation purposes,the FLL has to be normalised in the frequency adaptation loop, by dividing the detected frequency by the amplitude of the positive-sequence component $(v_\alpha^+)^2 + (v_\beta^+)^2$. The amplitude and the phase-angle of the sequence components estimated by the DSOGI-FLL can be calculated instantaneously as,

$$|v'| = \sqrt{(v'_\alpha)^2 + (v'_\beta)^2};\ \theta' = \tan^{-1}\frac{v'_\beta}{v'_\alpha} \tag{5.5.14}$$

5.5.2 Tuning A DSOGI-FLL

As already explained, the two major components of a DSOGI-FLL are the SOGI-QSG and the FLL. The two tunable parameters that determine the dynamic

response of a DSOGI-FLL are the gain K of the SOGI-QSG and the gain Γ of the FLL as shown in Fig.5.20. By considering the state-space equations of a direct FLL, the analysis presented in [6] reports the first order transfer function,

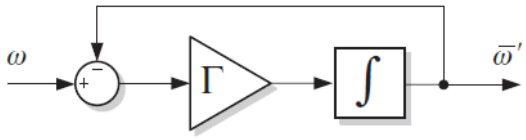

Figure 5.20: A classic linear-FLL [6]

$$\frac{\omega'}{\omega} = \frac{\Gamma}{s+\Gamma} \tag{5.5.15}$$

This allows one to use a typical first-order approximation for the settling time of the FLL system according to control theory [87],

$$t_s(FLL) \approx \frac{3.9}{\Gamma} \tag{5.5.16}$$

This approximation helps determine the optimum combination of K and Γ to achieve the desired performance of the frequency estimation. The gain K of QSG is set to $\sqrt{2}$ so that the transfer functions of the SOGI-QSG given in (5.5.4) and (5.5.5), will have a damping factor $\zeta = \sqrt{2}$, delivering a compromise between the settling time and the overshoot. Note that this analysis was conducted under the assumption that the input voltage only undergoes a frequency change. On the other hand, the dynamics of the QSG could be observed when there is an amplitude change while the frequency is invariant. According to Franklin et al. [91] the dynamics of the SOGI-QSG can be approximated by,

$$t_{s(SOGI)} = 3.9\tau, \; where \; \tau = \frac{2}{k\omega'} \tag{5.5.17}$$

This gives a settling time of 17.6ms for 50 Hz for the QSG. These two approximations were confirmed to be valid in [6]. When the voltage experiences a change in both the amplitude and the frequency, the settling times of the FLL and the QSG should maintain a relationship such that,

$$t_{s(FLL)} \geq 2\, t_{s(SOGI)} \tag{5.5.18}$$

in order for both subsystems to have sufficient time to react according to re-

spective variations in the voltage. In other words, the FLL dynamics needs to be slower than the dynamics of the QSG by at least two times. If the settling times get any closer, the dynamic response will be altered to a second-order system, as shown later in section 5.5.6. Through the study, the settling time of the QSG loop was kept constant at 17.6 *ms* by keeping $K = \sqrt{2}$.

5.5.3 DSOGI-FLL Response to Step Frequency

Similar to the previous methods, the frequency of a clean and balanced input voltage signal was varied in a step. The frequency of the voltage was estimated using DSOGI-FLL with different FLL gains Γ. The detected step frequency for three different Γ is shown in Fig.5.21a for illustration. The variation in 2% settling time was measured from the detected frequency for each Γ and is shown in Fig.5.21b.

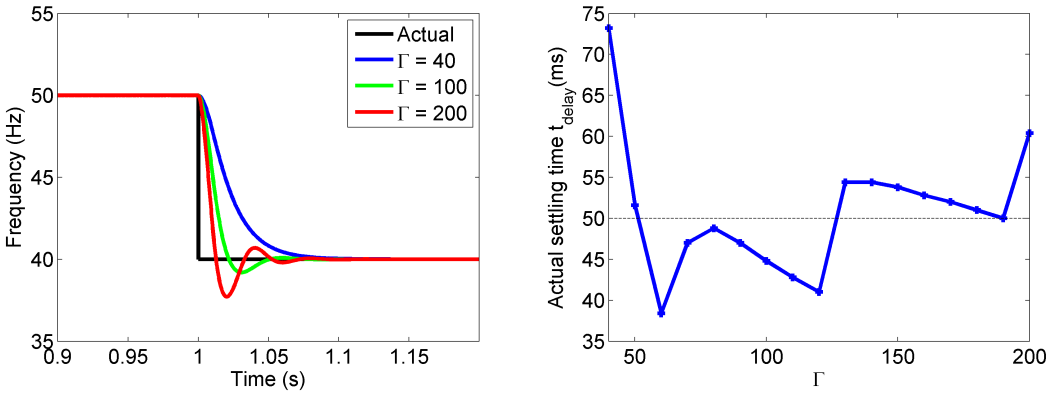

(a) Detected step frequency **(b)** Settling time of the DSOGI-FLL

Figure 5.21: Illustration of frequency detection for three illustrative Γ and the settling times for varying Γ in DSOGI-FLL.

In the previous section, Γ was said to be inversely proportional to the settling time according to the literature. According to Fig.5.21b, the settling time is around 40 *ms* − 60 *ms* for higher Γ. This is also confirmed in the illustration in Fig.5.21a. Because for higher Γ, the settling time is predominantly determined by the QSG settling time. Contrary to the common belief, increasing Γ does not necessarily decrease the settling time for a step change.

According to Fig.5.21b, one can restrict Γ so that the response is within the settling time requirement as $52 \leq \Gamma \leq 125$.

5.5.4 DSOGI-FLL Response to Ramp Frequency

When the frequency was changed as a ramp function, the DSOGI-FLL acted similar to a DFT, where the estimation of the frequency was achieved with a fixed delay and with a steady state error for a ramp. See Fig.5.22a for an illustration of detected frequency ramps for three different Γ. This steady state error can be explained using the FLL design. The FLL only consists of one integrator and is only designed to minimise the steady state error for a step disturbance in frequency.

The ROCOF of the ramp was obtained as in previous studies and the maximum detected ROCOF is shown against varying Γ in Fig.5.22b.

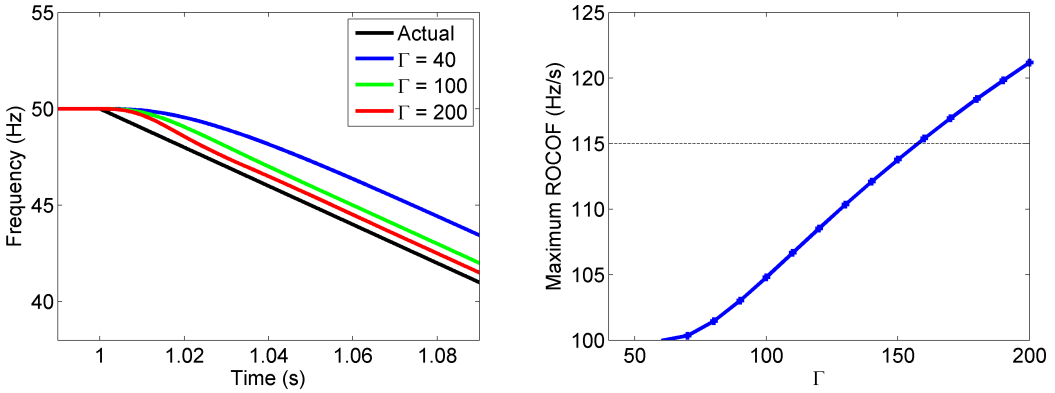

(a) Detected Ramp frequency

(b) Maximum ROCOF estimated by the DSOGI-FLL

Figure 5.22: Illustration of frequency detection for three illustrative Γ and the maximum ROCOF for varying Γ in DSOGI-FLL.

According to Fig.5.22b, the ROCOF is almost always overestimated unlike that of a DFT. Above $\Gamma > 60$, the maximum detected ROCOF seems to vary linearly with Γ. In order to satisfy the ROCOF detection requirement of being within 15% of the actual value, $\Gamma < 160$ was chosen as the constraint.

The ramp delay was also detected and unlike the DFT, the ramp delay did not vary much with frequency or with time beyond the initial transient. The ramp delay is shown in Fig.5.23 against Γ.

The ramp delay seems to have the inverse relationship between the settling time and Γ, sought for in step settling. This is because, by the time the ramp delay was measured, the QSG transients have settled. Hence, this is related to the true FLL settling time. From the figure, one can see that the relationship is

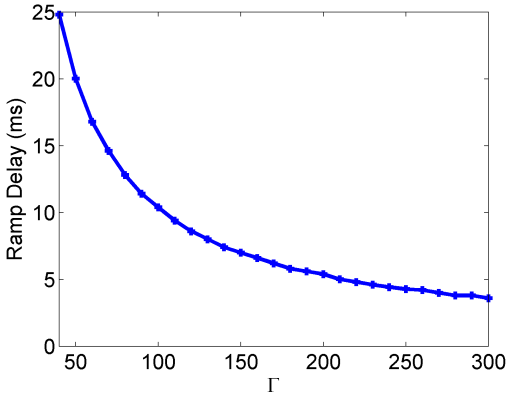

Figure 5.23: The detection delay of a 100 Hz/s ramp with varying Γ in DSOGI-FLL.

such that,

$$t_{s(ramp)} \approx \frac{1}{\Gamma} \tag{5.5.19}$$

According to this information, the settling time restriction for Γ should be $\Gamma < 20$.

5.5.5 DSOGI-FLL Response to Harmonics and Unbalance

The effect when the input voltage was polluted with 6.07% THD and 5% voltage unbalance on the frequency detection by DSOGI-FLL is considered next. The detected frequency in the presence of harmonics and unbalances for a frequency ramp of 2 Hz/s is shown in Fig.5.24a and 5.24b respectively for different Γ.

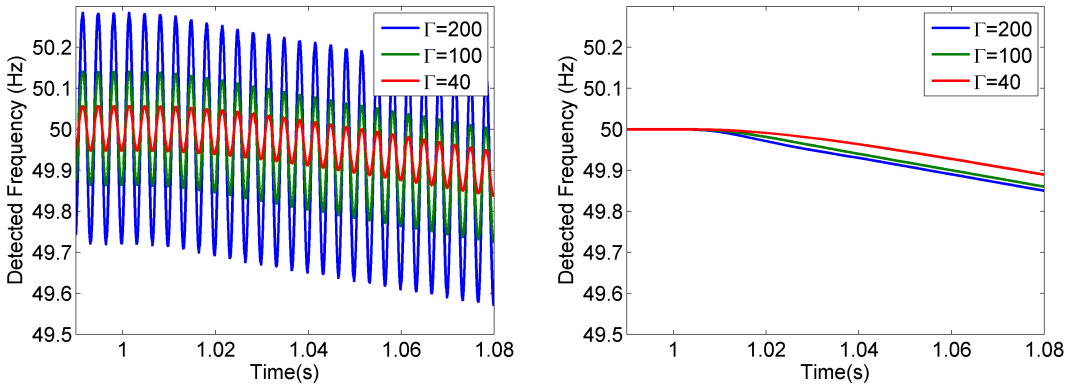

(a) With Harmonics **(b)** With Unbalance

Figure 5.24: The illustration of DSOGI-FLL detected frequency of a slow ramp with three different Γ.

From Fig.5.24a, one can see the amplitude of the ripple is better attenuated for lower values of Γ, which indicates a longer ramp delay. The improvement of steady state at the expense of poor transient response can be regarded analogous to the response of SRF-PLL and DFT, for when harmonic distortion was present in the input voltage.

When the steady state ripple was analysed through a FFT, it has been revealed that before the frequency ramp change i.e. frequency at $60Hz$, the estimated frequency contains a ripple of 360 Hz, clearly showing the association of the ripple with the 6^{th} harmonic, which can be explained as a constructive effect of the 5^{th} and the 7^{th} harmonics present in the input voltage.

For an imbalance in voltage, the frequency detection by the DSOGI-FLL is unimpeded as shown in Fig.5.24b. However, the Fig.5.24b also shows that the frequency detection experiences a bend in the beginning that is resolved within a fixed amount of time, which is roughly the same for all Γ. This can be explained by the dependency of the DSOGI-FLL design on the amplitude of the voltage envelope as detected by the QSG. In the FLL, the normalisation of the voltage magnitude is obtained by instantaneously detected voltage amplitudes v_α and v_β. Nevertheless, the frequency estimation is still free from oscillatory steady state error.

According to the frequency response of the DSOGI, the notch filter is tuned in order to cancel the double frequency. Therefore, irrespective of the severity of the unbalance, the frequency of a clean voltage waveform will be estimated without any steady state ripple. This property of the DSOGI-FLL stands out compared to the other two methods discussed in this chapter.

The error of the detected frequency for a 2 Hz/s ramp in the presence of harmonics and unbalances gives a measure of accuracy. Thus, the maximum error for the ramp between 40 Hz and 60 Hz for varying Γ is shown in Figs.5.25a and 5.25b due to individual effects of harmonics and unbalance and due to the combined effect respectively.

According to Fig.5.25a, there is a finite error in the presence of unbalance. This is only due to the inherent ramp error rather than the ripple due to unbalance. The ripple due to harmonics however is seen increased with increasing Γ as stated previously. From Fig.5.25b, one can see that the combined error is same as the error due to harmonics. Γ can now be restricted to $\Gamma < 320$ according to Fig.5.25b, so that the error (ripple) is smaller than $\pm 0.5Hz$.

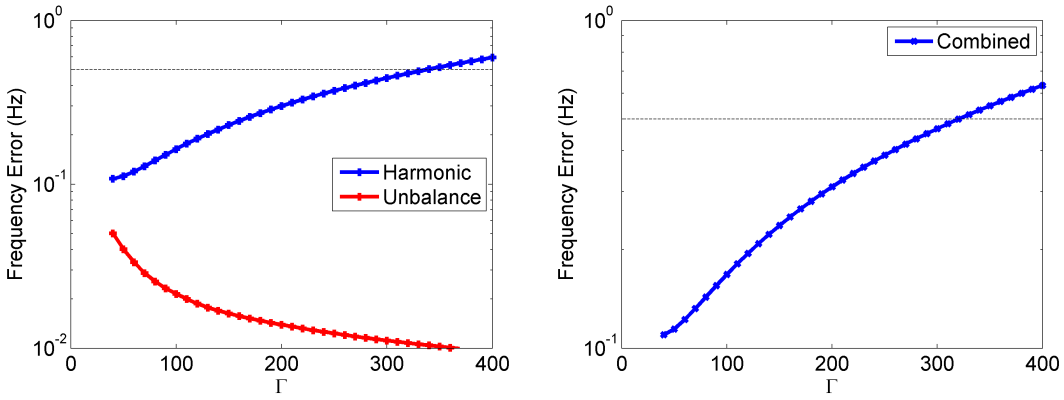

(a) Separate Error **(b)** Combined Error

Figure 5.25: The frequency error of DSOGI-FLL in the presence of harmonics and unbalance for varying Γ.

5.5.6 DSOGI-FLL Bandwidth Considerations

As conducted for previous methods, it is necessary to identify the bandwidth of a DSOGI-FLL for comparison of the three methods. Hence, in this section, a further analysis on the DSOGI-FLL properties is carried out. In section 5.5.2, it has been learnt that the key to optimum dynamic response of a DSOGI-FLL is the proper selection of the proportional gain K of the SOGI-QSG and the FLL gain Γ. Also, Teodorescu et al. in [6] suggested a first-order linearised frequency adaptive system to represent the DSOGI-FLL. Until now the tuning of the DSOGI-FLL was achieved by obeying (5.5.16), which has been derived assuming a first order approximation to the DSOGI-FLL following [6].

In order to validate the above linear approximation given in [6], a 3-phase balanced voltage signal without harmonic distortion or unbalance was considered. The step frequency response of the DSOGI-FLL was compared with a typical first order and a second order response. Using a regression analysis, the parameters of the most suitable first/second order system (a in first order, ζ, ω_n in second order) were selected. The DSOGI-FLL response and the obtained approximated systems' responses for $\Gamma = 40$ and $\Gamma = 200$ are shown in Figs.5.26a and 5.26b respectively.

The results clearly show a discrepancy between the approximation and the actual when using first order systems as the approximation. The inadequacy of the approximation of DSOGI-FLL by a first order transfer function can be especially seen in higher values Γ (i.e. 200) as shown in Fig.5.26b.

A point often overlooked is the effect of dynamic response of the SOGI with a

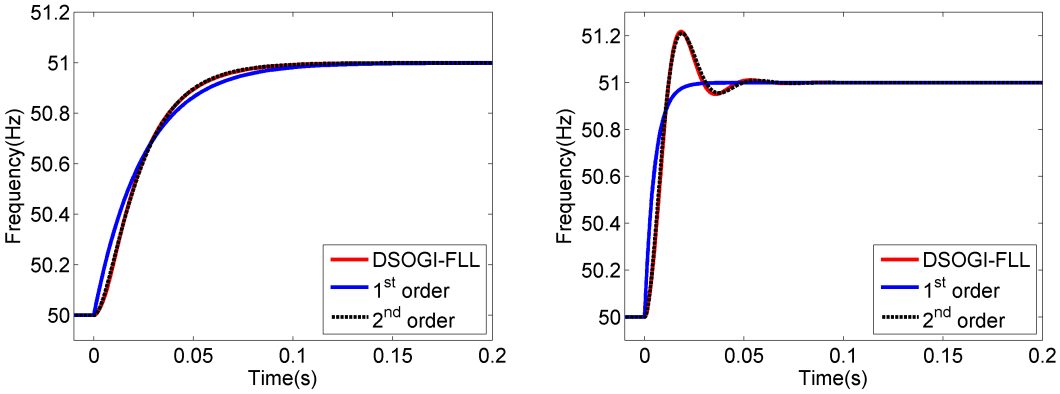

Figure 5.26: Approximation of the DSOGI-FLL using first and second order systems

relatively high Γ. In [6] the authors state that the first order approximation of DSOGI-FLL is only valid when the $t_{S(FLL)} \geq 2 * t_{S(SOGI)}$. According to (5.5.17), $t_{s(SOGI)}$ is unaffected by Γ and remains constant at 17.6 ms. From the settling times of FLL, $t_{s(FLL)}$ for different Γ, calculated using (5.5.16), listed in Table5.4, one can confirm that for higher Γ this rule is violated. This means that the dynamics of the FLL are no longer dominated singly by higher Γ that delivers faster detection.

Γ	$t_{s(FLL)}$ ms	$t_{s(SOGI)}$ ms
46	84.8	17.6
100	39.0	17.6
200	19.5	17.6

Table 5.4: FLL and SOGI setting times for different Γ

The graphical results presented in Figs.5.26a and 5.26b show that a second-order approximation of DSOGI-FLL is sufficiently able to represent the actual response of the DSOGI-FLL. The error between the actual and the second-order approximation is considerably smaller than that of the first-order approximation. Therefore, it can be concluded that fast DSOGI-FLL should be approximated by the corresponding second-order system. Hence the bandwidth of the DSOGI-FLL can be approximated by the following typical equation for bandwidth estimation of a second-order system.

$$\omega_{-3dB}(DSOGI-FLL) = \omega_n \left[1 - 2\zeta^2 + \sqrt{(2-4\zeta)^2 + 4\zeta^4}\right]^{1/2} \tag{5.5.20}$$

This is graphically shown in Fig.5.27 by finding the second order parameters ζ

and ω_n for each DOSGI-FLL Γ.

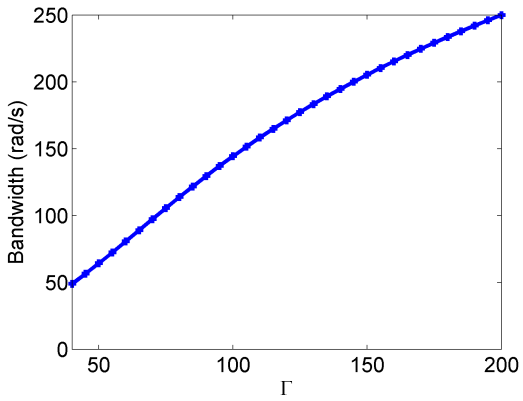

Figure 5.27: The DOSGI-FLL bandwidth for varying Gamma Γ.

It shows that the bandwidth increases almost linearly with increasing Γ. One can suggest the following relationship for the bandwidth of a DSOGI-FLL with $K = \sqrt{2}$.

$$\omega_{-3dB}(DSOGI - FLL) \approx 1.25\,\Gamma \tag{5.5.21}$$

This information is to be used later to compare the three frequency detection techniques with equivalent bandwidths.

5.5.7 Optimum DSOGI-FLL Parameters For Energy Storage Control

The restrictions obtained so far for Γ so that the DSOGI-FLL delivers the requirements are summarised in Table 5.5.

Parameter	Requirement	Restriction
frequency range	$40Hz - 60Hz$	No Restriction
$\text{ROCOF}_{\text{max}}$	$100Hz/s$	$\Gamma < 160$
transient delay	$10ms \leq t_{delay} \leq 50ms$	$52 \leq \Gamma \leq 125$
accuracy	$\Delta f \leq \pm 0.5Hz$	$\Gamma < 320$

Table 5.5: DSOGI-FLL design parameter restrictions

As with the DFT, the requirements are satisfied for a wide range of Γ ($52 \leq \Gamma \leq 125$). Since the optimum method should have minimum time delay, the Γ value corresponding to the minimum ramp delay was selected without violating other criteria. Therefore, the optimum value for Γ is 125.

5.5.8 Summary

In this section, it has been identified that the DSOGI-FLL achieves frequency locking by estimating the instantaneous voltage and its quadrature signals generated using SOGI-QSG, processed by an FLL to estimate the frequency. SOGI-QSG concentrates on eliminating the double frequency ripple in the steady state by means of its adaptive filtering properties, while the FLL concentrates on locking the frequency as fast as possible. This leads to a system with two different dynamics that are interconnected. The tuning of the two dynamic systems, SOGI and the FLL were discussed in detail, including an approximation to calculate bandwidth requirements.

The settling time only varied between $40\ ms - 60\ ms$ for a step, when Γ is varied between 60 and 200. However, for a ramp, the ramp delay had an inversely proportional relationship with Γ. The reason was that the QSG dominates the step settling time, while ramp delay involves only the FLL, which responds according to Γ.

It was also understood that the DSOGI-FLL almost always overestimates the ROCOF. The presence of unbalance did not affect the DSOGI-FLL frequency detection at the steady state, even though higher harmonics do as the DSOGI is only tuned to eliminate the double frequency component. At the same time, the bandwidth was found to vary almost linearly with Γ.

As for the DFT, a wide range of Γ values satisfied all the requirements for the energy storage control application and the best value was selected by considering the ramp delay time.

5.6 Comparison of Frequency Detection Techniques

The main purpose of understanding the properties of different frequency detection techniques and their tuning methods was to compare and analyse the methods in order to identify the best technique to detect frequency in a weak electrical grid. Essentially the chosen method has to adhere to the requirements of frequency detection declared in section 5.2.

As part of the theoretical investigation of each method, the bandwidth for varying design parameters were studied. In this section, all the frequency detection methods are compared so that they all share the same bandwidth, for an unbi-

ased comparison. Step and ramp frequency variations will be simulated using a voltage waveform with harmonic distortion. The frequency trending during loading will also be simulated using the weak grid model for cases with and without source impedance.

5.6.1 Test cases

For testing a set of four bandwidths corresponding to the optimum designs of the SRF-PLL, the DFT with Hamming window, the DFT with Blackman window and the DSOGI-FLL was considered. The bandwidths of the candidate frequency detection techniques were made equivalent as the basis of comparison. The bandwidths were calculated using (5.3.14), (5.4.22) and (5.5.20) for the SRF-PLL, the generalised modified DFT and the DSOGI-FLL respectively. The test cases and the design parameters for all methods for each case are listed in Table 5.6. These test cases will be evaluated for different frequency and voltage variations in the following sections. However, note that the SRF-PLL for very high bandwidths ($t_s < 50\ ms$) produces a large ripple rendering the significant ripple effects of other methods unobservable. Therefore, for the two higher bandwidths, SRF-PLL results were not included.

Case	**Bandwidth**	**SRF-PLL**		**DFT(Hamming)**	**DFT(Blackman)**	**DSOGI**
	rad/s	ms	rad/s	ms	ms	
		t_s	ω_n	t_w	t_w	Γ
1	49.4	230.0	23.98	55	57	40
2	177.4	64.0	86.2	25	29	125
3	351.9	*32.3*	*171.0*	13	14	360
4	378.6	*30.0*	*184.0*	12	13	397

Table 5.6: Test cases for the optimum design of each method along with other methods adjusted to the same bandwidth.

5.6.2 Comparison for a Step Change In Frequency

Firstly, the three methods are compared under the same bandwidth for a step change in frequency. Fig.5.28 presents the simulation results for the three frequency detection techniques discussed.

From the step response for each test case presented in Figs.5.28a to 5.28d, one can see that all methods have approximately the same rise time, confirming that their respective bandwidths are aligned for each test case. For all test cases,

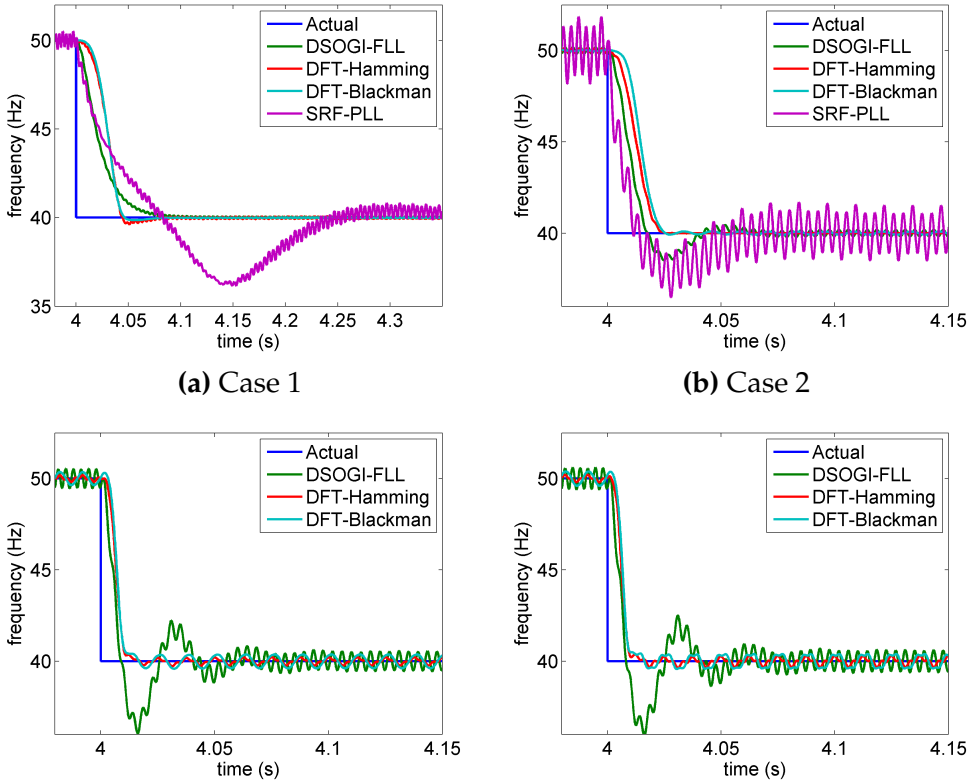

(a) Case 1 **(b)** Case 2

(c) Case 3 **(d)** Case 4

Figure 5.28: Comparison of frequency detection techniques for Case 1,2,3,4 for a step change in frequency

one can see that the DFT with either Hamming or Blackman window has the fastest settling time with the minimum steady state ripple. Between, the two windowing techniques, the DFT with Hamming is slightly faster. The DSOGI-FLL exhibits midway performance between the DFT and the SRF-PLL, with regards to both settling time and harmonic attenuation. Therefore, for a step change in frequency, the DFT displays superior qualities over the other two.

5.6.3 Comparison for a Ramp Change In Frequency

Next, all methods are compared with the same test cases for a ramp frequency variation. Fig.5.29 shows the simulation results obtained.

When the frequency variation is changed from a step to a ramp, the performance ordering of the methods change dramatically under the same bandwidth comparison. The SRF-PLL, which is a type II system that produces a zero steady state error for a ramp, always settles at the actual ramp during the given settling time. Also, the SRF-PLL overestimates the ramp (ROCOF) within the settling

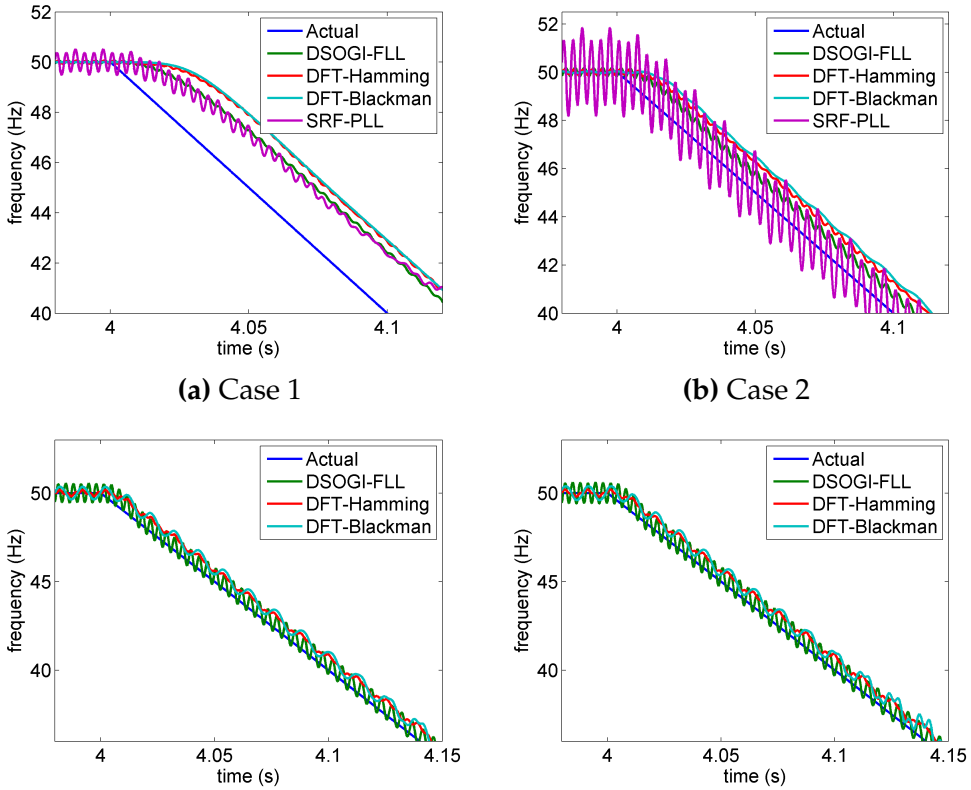

(a) Case 1 **(b)** Case 2

(c) Case 3 **(d)** Case 4

Figure 5.29: Comparison of frequency detection techniques for Case 1,2,3,4 for a ramp change in frequency

time. On the other hand, the increase in bandwidth (i.e. decrease in settling time) causes a larger ripple. The results confirm over and over again that the SRF-PLL is unable to fulfil the requirements of the proposed energy storage control system.

In the case of the DFT, the delay dependence on the window length is apparent in all test cases. Without any closed loop mechanism, the DFT techniques will always have a delay in estimating a ramp. Nevertheless, the error (due to ripple) of the ramp estimation is excellent with minimal steady state ripple.

The DSOGI-FLL for a given bandwidth is able to track the ramp with low error, while also being closer to the actual ramp than the other techniques. Although the FLL suffers from non-zero steady state error for a ramp, compared to the DFT, the corresponding steady state error is lower for all bandwidths. Hence, we can state that for the estimation of ramp changes frequency, the DSOGI-FLL displays better overall performance.

5.6.4 Comparison of Frequency Trending for Load Changes

Having compared the methods for step and ramp changes in frequency, the most important frequency variation in the context of this research is approached next. Our preliminary interest lies on estimating the frequency trend followed by changes in loading. The shape of a typical oscillatory speed trend occurring as a consequence of loading/shedding was explained in Chapter 3. Using the weak grid simulation model, a worst-case weak grid voltage profile was created, to be processed using the frequency detection techniques. This voltage contains the effects of the AVR, effects of the impedance in addition to the frequency variation. The methods are tested for two sets of cases i.e. when there is a comparable source impedance and when there is not, both in the presence of AVR effects.

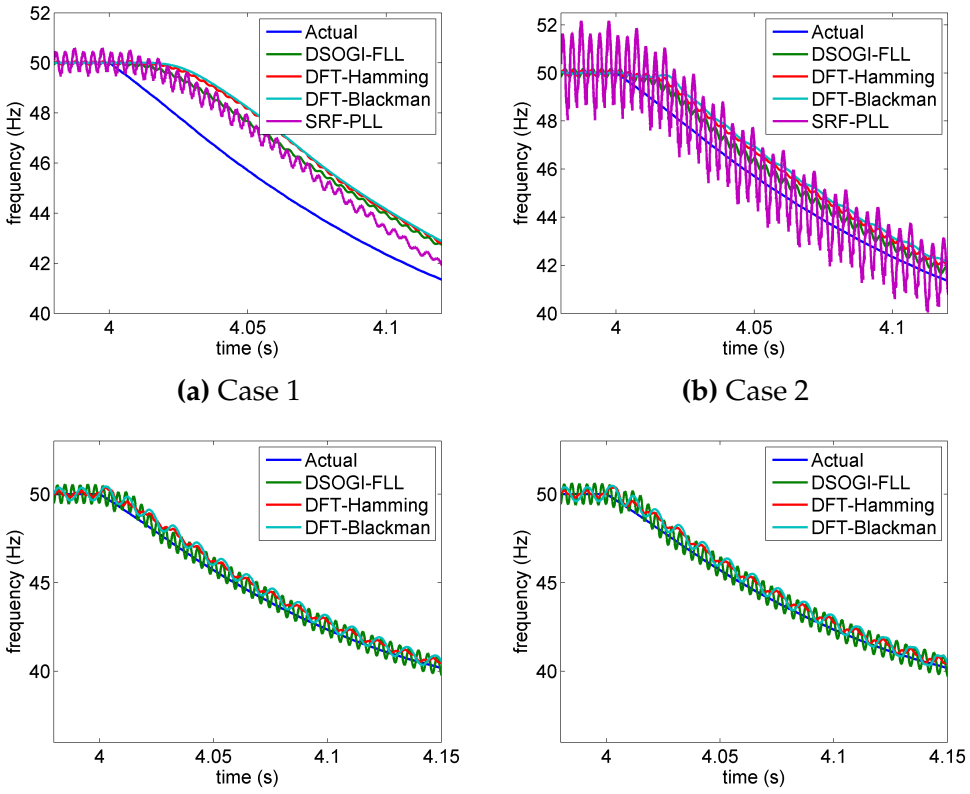

(a) Case 1 **(b)** Case 2

(c) Case 3 **(d)** Case 4

Figure 5.30: Comparison of frequency detection techniques for Case 1,2,3,4 for a load change frequency trend without source impedance

For the case without the source impedance, there exists no instantaneous voltage glitch, but the amplitude of the voltage is regulated by the AVR. A rated load (i.e. $R = 20\Omega$) is used to create the frequency drop. Fig.5.30 presents the simulation results that estimates the characteristic frequency trend after load-

ing.

The results obtained for the detected frequency closely resembles that observed for a ramp. The DSOGI-FLL provides a slightly better estimation with less overall delay that that of the DFTs. A DFT with a Hamming over a Blackman windowing can also be recommended for higher bandwidths to minimise delay.

Next, a source impedance was introduced to the weak grid simulation as found in section 3.3.3 in chapter 3 , i.e. $Ls = 22.5mH$ and $R_s = 0.9\Omega$. With the voltage waveform representing the complete worst-case weak grid voltage profile, the consequences of the instantaneous voltage glitch on frequency detection can now be observed. Fig.5.31 presents the results of the frequency estimation from the voltage profile. The results clearly exhibit an initial dip in the detected frequency, which was not present in the case without impedance in Fig.5.30.

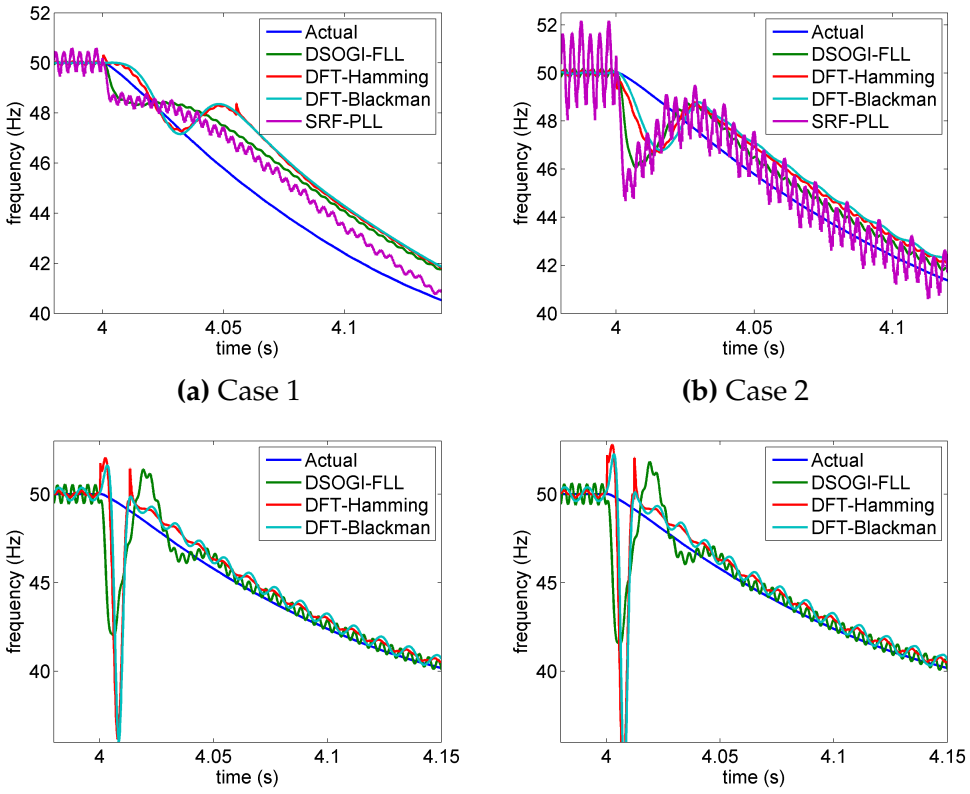

(a) Case 1 **(b)** Case 2

(c) Case 3 **(d)** Case 4

Figure 5.31: Comparison of frequency detection techniques for Case 1,2,3,4 for a load change frequency trend with source impedance

All frequency detection techniques tested experience the initial dip in the estimated frequency. This is both due to the sudden change in voltage amplitude and the sudden phase shift in the voltage. A phase shift necessarily creates a change in frequency during that cycle despite the method used. This directly

explains how the voltage glitch affects the DFT. The modified DFT processes the instantaneous phase difference in order to calculate the instantaneous frequency, meaning a phase jump directly affects the value calculated. While a similar manifestation of the phase jump occurs in the SRF-PLL and the DSOGI-FLL, these methods use the amplitude of the voltage in the frequency estimation algorithm. In SRF-PLL, it is replicated in the d-axis voltage prior to the loop-filter, whereas in the DSOGI-FLL, it is replicated in the QSG amplitude.

Since the voltage glitch/phase shift is self-recovering, the frequency dip in the estimation is self-recovering as can be seen in all test cases. The recovery time has a close relationship with the settling time chosen (i.e. bandwidth). For a given case, all four estimations recover the initial dip and follows the frequency trend. Hence, the recovery time is not helpful in distinguishing a better technique for the worst-case.

Consider the maximum dip experienced by the different techniques. The DSOGI-FLL dip is the smallest, whereas the SRF-PLL produces a similar dip if one examines closely ignoring the ripple. The DFT methods make a larger dip because the dip settles quickly in the DFT algorithm. According to the fundamentals, the area under the frequency curve is equal to the phase difference. However, the area of the dip is equal to the phase-shift and is the same across all methods. Hence, the dip height is inversely proportional to the dip duration.

Reviewing all methods for the worst-case voltage profile, one can see that none of the methods is capable of detecting the estimated frequency from the initial erratic dip. Technically, the spurious frequency dip can cause the energy storage control to falsely activate early as it exploits the real time frequency to trigger the energy storage control. All methods erratically crosses the threshold frequency i.e.49 Hz, before the actual frequency crosses the threshold for the rated load. In the worst case, the initial dip can mimic a non existent frequency drop that is not necessary to be recovered by the energy storage. Due to this, the energy storage may respond and supply active power unnecessarily.

5.6.5 Comparison of Methods for Frequency Trending Using Optimum Bandwidths

In addition to the same bandwidth comparison, this section presents all the methods with their best parameters. Fig.5.32 shows the frequency response for a rated loading using all methods with their best parameters.

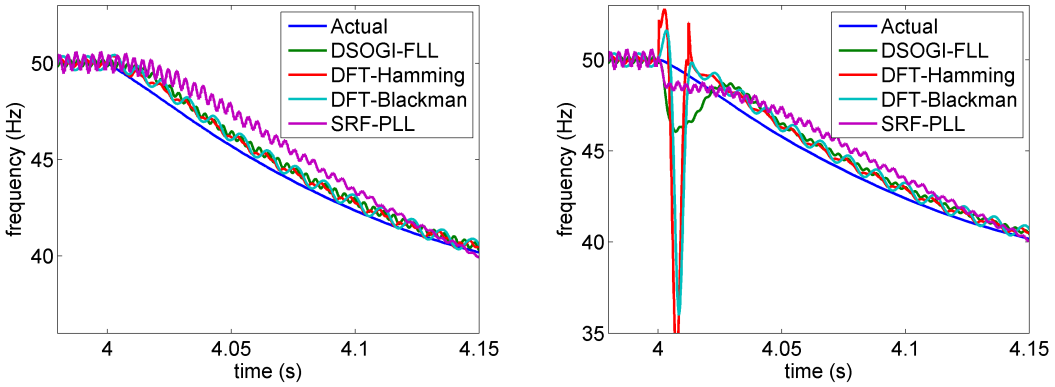

(a) Without Impedance **(b)** With Impedance

Figure 5.32: Comparison of frequency detection techniques with their optimum parameters, for a load change in frequency with and without source impedance

According to Figs.5.32a and 5.32b, one is unable to take advantage of the ramp settling provided by the SRF-PLL due to its long settling time. Both DSOGI-FLL and DFTs estimate the frequency with a similar delay with similar ripple amplitude. Hence, with their optimum parameters, both DSOGI-FLL and the DFTs provide similar performance. The difference between the DSOGI-FLL and the DFTs can only be seen in the presence of source impedance in Fig. 5.32b. The erratic dip of the DFT is three times as larger than that of the DSOGI-FLL.

In order to use the proposed energy storage control in weak grids, this erratic dip should either be eliminated or mitigated. A smoothing technique to flatten the dip is proposed in the next section.

5.7 Mitigating Spurious Frequency Dips

A smoothing technique to mitigate the effect of spurious frequency dip produced by frequency detection techniques is explained in this section. The initial frequency dips are a consequence of the source impedance as illustrated in Fig.5.33 for a DSOGI-FLL and a DFT with Hamming for the four test cases.

The proposed smoothing technique uses a combination of filters; the rapid frequency variation during the initial dip period is cut-off, while the slowly varying frequency is allowed through. It is of paramount importance not to delay the detected frequency too much after the initial dip. To achieve this, a heavy filter was incorporated throughout the duration of the initial erroneous dip. Immediately after recovering to the normal pattern of the frequency detection, a

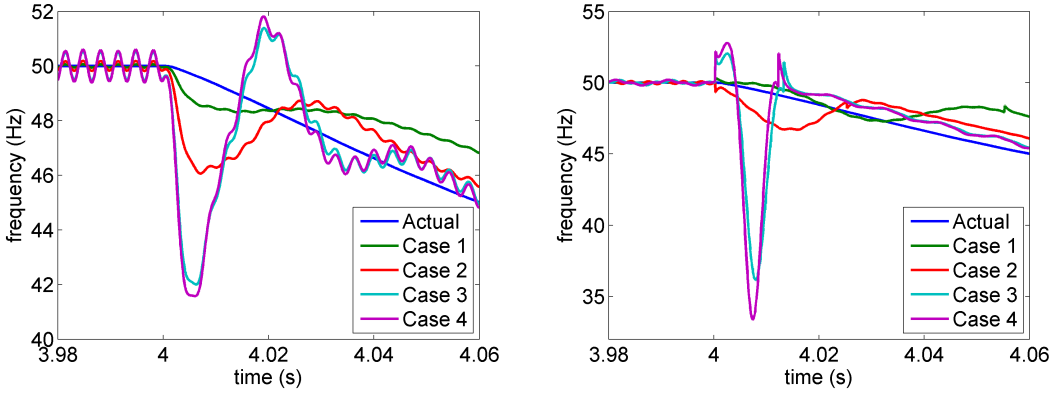

(a) DSOGI-FLL **(b)** DFT Hamming

Figure 5.33: Initial frequency dip produced by a DSOGI-FLL and a DFT with Hamming window

faster filter was appointed to let the correctly measured frequency pass through with minimal delay.

It is mandatory to identify a clear reliable trigger for the point at which the dip begins to form, in order to sustain the independence of the energy storage control. Since a voltage glitch essentially creates a rapid change in magnitude, the instantaneous time derivative of the magnitude of input voltage may be used as an accurate indication of the glitch occurrence. Figs.5.34b and 5.34c show the derivative of voltage magnitude calculated as a by product of the DSOGI-FLL and the DFT, for the rated load disturbance. One can see a clear fluctuation in the rate of change of magnitude of the DSOGI-FLL, corresponding to the instance of glitch shown in Fig.5.34a. However, the DFT does not show such rapid variation in the rate of change of magnitude.

In the DSOGI-FLL, the magnitude variation is immediately detected by the QSG and can be used as reliable trigger. But, in the DFT, the magnitude change can only be detected after at least half of the window length has passed. This is mainly because the Hamming and Blackman windows give prominence to the centre of the window. During this time, the magnitude drops slowly to its lowest value and rises again slowly. Therefore, an effect (i.e. glitch) that only lasts for 1 *ms* in the 3-phase voltage is spread out during a 12 *ms* period in the DFT magnitude output. Therefore, the derivative of the voltage magnitude calculated by the generalised DFT with Hamming windowing as shown in Fig.5.34, does not show distinguishable characteristics to that of the DSOGI-FLL, that is necessary if it is to be employed as a trigger. However the author would like to recommend the use of the generalised DFT in energy storage control, if other

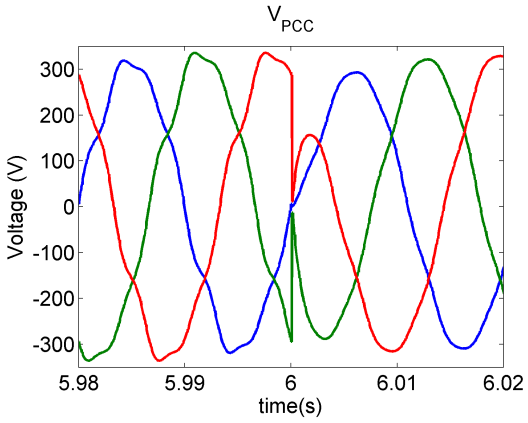

(a) V_{PCC}

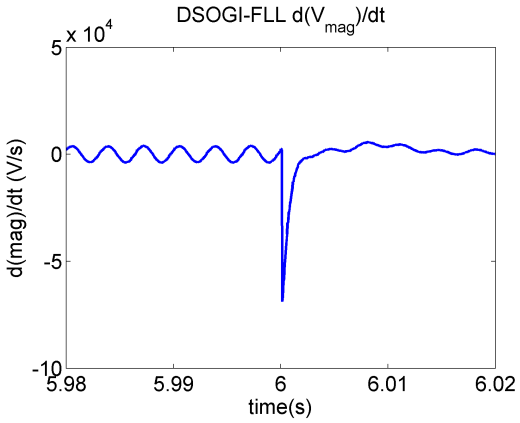

(b) DSOGI-FLL $d(V_{mag}/dt)$

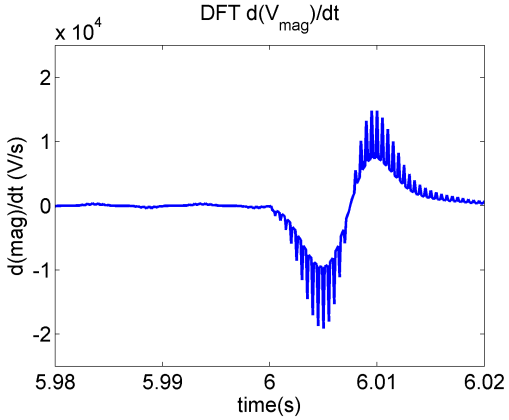

(c) DFT $d(V_{mag}/dt)$

Figure 5.34: Time derivative of the voltage magnitude obtained using DSOGI-FLL (middle); using DFT (bottom) for the rated load with the corresponding V_{PCC} (top)

suitable provisions can be made to avoid the spurious frequency dip.

Therefore, during this study, the DSOGI-FLL was chosen as the suitable technique to detect the frequency avoiding spurious frequency dips. This is justified as for the optimum parameters, both techniques perform similarly for the weak grid conditions defined in this study.

The significant variation in the rate of change of magnitude is set as the trigger of the smoothing technique. It is important to note that the rate of change of magnitude is independent of the load change - see Fig.5.35; and is fundamentally defined by the total source impedance, which is fixed for a particular power system. The smoothing technique triggering condition was set as,

$$\frac{d(V_{mag})}{dt} \geq 1 \times 10^4 \tag{5.7.1}$$

In this smoothing technique, the knowledge of the frequency dip duration is essential. This is crucial for a smooth variation of the output when the two filters are interchanged. The duration of the dip is largely dependant on the frequency detection method used and its tuning parameters. For a DSOGI-FLL, the initial dip was found to last a period slightly less than the settling time. In this case, the duration of the depth was set as $30ms$ considering the settling time of the optimum DSOGI-FLL.

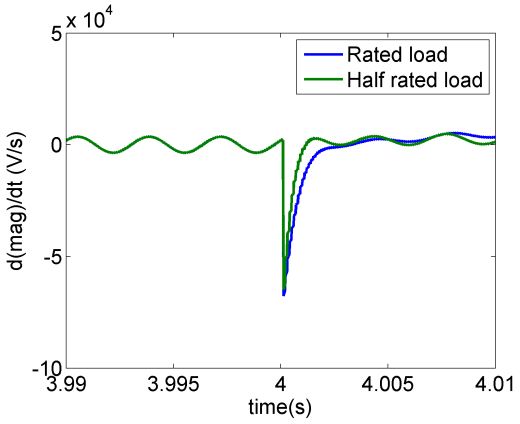

Figure 5.35: Time derivative of the voltage magnitude obtained using the DSOGI-FLL for rated and half rated loads

The heavy filter f_{sH} used immediately after the trigger indicating the glitch until the end of the dip is,

$$f_{sH}(s) = \frac{1}{0.033s + 1} \tag{5.7.2}$$

And the faster filter f_{sL} which was used before and after the initial dip duration is given by,

$$f_{sL}(s) = \frac{1}{0.001s + 1} \tag{5.7.3}$$

The value for the faster filter was chosen such that its time constant was insignificant ($< 10\%$) relative to the settling time. The time constant of the heavy filter was chosen by trial and error considering the frequency dip for a rated load.

Fig.5.36 shows the effective smoothing achieved by filtering for rated and half-rated loads. As can be seen, the smoothing technique has visibly alleviated the erratic initial dip. Considering the benefits of mitigating the inaccurate activation of energy storage over the slight delay($\approx 1\ ms$) caused by the fast filter, the proposed smoothing technique can be declared acceptable in the energy storage control algorithm.

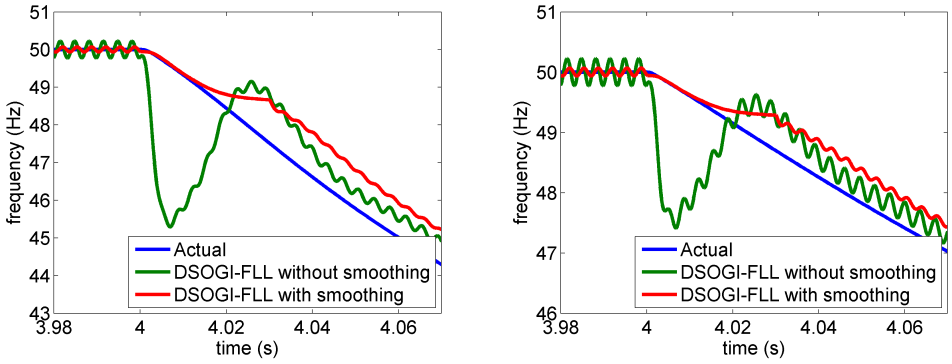

(a) rated load **(b)** half-rated load

Figure 5.36: DSOGI-FLL frequency detection with the smoothing technique

5.8 Experimental Validation

In support of the theoretical comparison conducted for the chosen candidate frequency detection technique based on simulation, a comparison based on experimental conditions is presented here, to ensure the practicability of the selected DSOGI-FLL method. The worst-case voltage profile recorded in the experiments explained in Chapter 3 is used as the input voltage and the frequency estimated from the methods are compared with the speed signal obtained simultaneously with the voltage signal using the data acquisition system of the IM drive. Note that the resistive load used in the experiment was 57Ω as opposed to the rated load of 20Ω used in the simulations. Fig.5.37 shows the

comparison of the candidate methods.

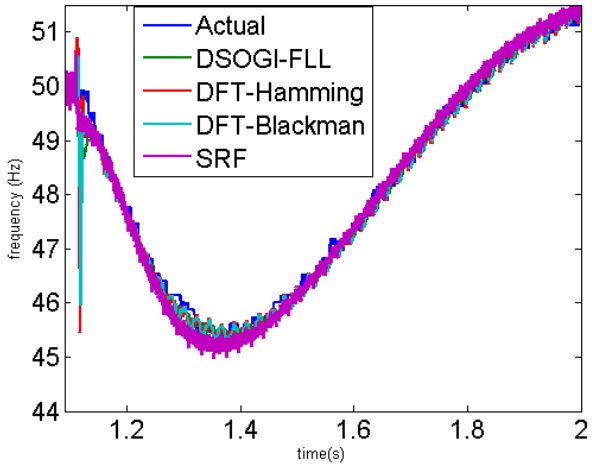

(a)

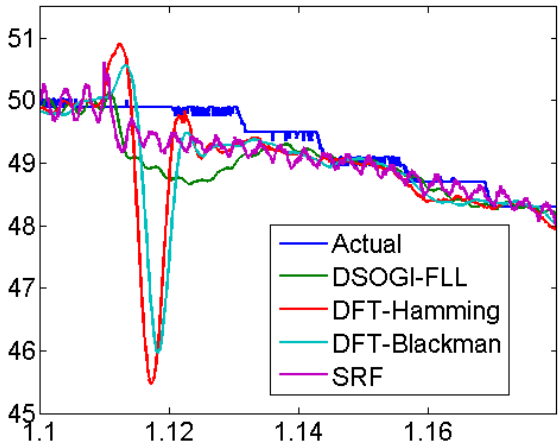

(b)

Figure 5.37: Experimental results for frequency detection techniques with optimum parameters ($R_{Load} = 57\Omega$)

One can observe a profile similar to that in the simulation results in terms of the transient settling time and the steady state ripple. Like in the simulation, the experimental results show the initial erratic dip in frequency in all methods. The smoothing technique was applied to DSOGI-FLL in order to flatten the initial dip, and the results presented in Fig.5.38 confirm the effective mitigation of the spurious dip. This enables the use of the DSOGI-FLL method in the application of energy storage control, specifically in a weak electrical grid.

On a side note, one can see that the detected frequency is just as fast as the speed signal detected from the IM driver interface, indicating that a delay in speed

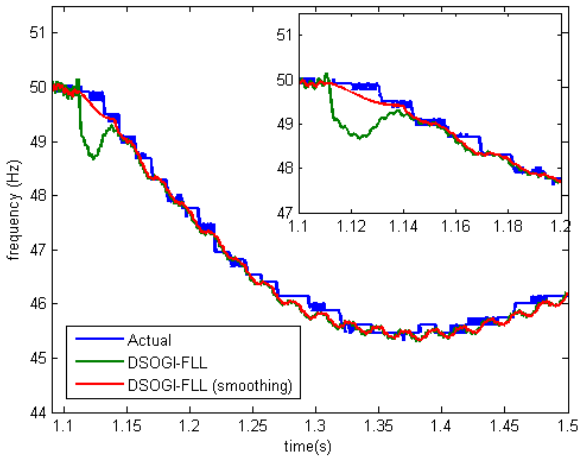

Figure 5.38: Experimental results for frequency detection techniques with the DSOGI-FLL with and without the smoothing filter ($R_{Load} = 57\Omega$)

signal acquisition relative to the voltage acquisition. On the positive side, this shows that there is no disadvantage in using the detected frequency compared to directly using the speed signal for control applications.

5.9 Conclusion

In this chapter, three candidate frequency techniques of different origin were discussed. They are the SRF-PLL, the generalised DFT and the DSOGI-FLL representing adaptive filtering based techniques. The design and the tuning of each method was explored and a bandwidth was defined for each method. The three methods were compared in worst-case weak electrical grid conditions under the same bandwidth in simulations. The assessment revealed that both the DSOGI-FLL and the DFT with windowing demonstrate competitive qualities that can be appreciated for frequency detection applications in weak grids. However, all three methods suffer an initial erratic frequency dip as a consequence of the source-impedance. Based on the existence of a reliable trigger to detect voltage glitches, occurring as a consequence of source-impedances, the DSOGI-FLL method was chosen over the generalised DFT as the most suitable frequency detection technique for applications in weak grids. A smoothing technique based on filtering was proposed to effectively mitigate the spurious frequency dip detected by the high rate of change of magnitude of the DSOGI-FLL. The effectiveness of using a DSOGI-FLL with the smoothing technique was further validated using an experimentally recorded worst-case volt-

age profile. Hence, the combined technique can be concluded to be successful in applications specific to weak electrical grids.

CHAPTER 6

Experimental Validation of Energy Storage Control

6.1 Introduction

The Energy Storage Control strategy developed using the weak grid simulation model is tested in an experimental 8kW micro-grid with Li-ion battery energy storage, in order to demonstrate its effectiveness on delivering frequency support during load disturbances. Experimental tests using various gain values and frequency thresholds in the energy storage control have been conducted on different loading and load-shedding levels to validate the simulation results presented in the Chapter 4.

This chapter consists of an overview of the prototype micro-grid with energy storage used as the experimental set-up, followed by a discussion on the experimental results obtained that are compared with the simulation results as well. Finally, conclusions are drawn.

6.2 Implementation of Energy Storage Control

The model of the energy storage control with frequency detection capabilities was implemented using a 15 kW Triphase® PM15F42C power module available in the Flexelec laboratory at the University of Nottingham. This power module allows bidirectional transfer of energy between an AC load/source and a DC load/source. It comprises of a state-of-the-art 3PExpress® platform to develop and test power converter algorithms efficiently in a Matlab/Simulink

environment [7]. This has facilitated rapid testing by plugging in the developed Matlab/Simulink model of the Energy storage control in to the Triphase platform for the experimental validation. The specifications of the Triphase® module are listed in Table 6.1.

Specification	Value
Rated power	$15kW$
Power supply voltage	$3\Phi\ 220 - 480\ V_{RMS(LL)}$
frequency	$50 - 60Hz$
Switching frequency	$8 - 16kHz$
AC output voltage	$0 - 480V_{RMS(LL)}$
AC output current $3\Phi + N$	$4 \times 16A_{RMS}$
DC Output voltage	$100 - 650\ V_{DC}$
DC Output current	$2 \times 16A$

Table 6.1: Specifications of the Triphase® PM15F42C Power Module [7]

6.2.1 Interfacing Triphase® PM15F42C Power Module

The Triphase PM15F42C power module is controlled by a dedicated Triphase PC. The program logic can be implemented in Simulink in a user PC using the block-set provided by the manufacturer. This Simulink model is then translated to C/C++, which the dedicated PC then compiles and builds as a real time target. The real time program itself can be controlled in real time via the Simulink interface in the user PC. The monitored data for Simulink scopes are sent to the user PC in real time via an Ethernet connection, which can also be used to send feedback to the real time program using Simulink switches. In addition, real time data logging is also available in the Triphase PC, which can be downloaded to the user PC after the emulation run via the Ethernet connection. The real time sampling frequency of all data is set as 8 kHz. Fig.6.1 shows a schematic diagram that describes the interface between the Triphase and the user.

From the hardware point of view, the Triphase power module consists of two three-leg IGBT converters. The converters are connected in a back-to-back configuration providing a three-phase AC interface with neutral and two DC channel interfaces as shown in the electrical schematic of the Triphase in Fig.6.2. As can be seen in the schematic, the AC side of the inverter 1 can be connected to a 3-phase grid, while the AC side of the inverter 2 is connected such that two legs are used as a dual channel interface to the energy storage. The remaining

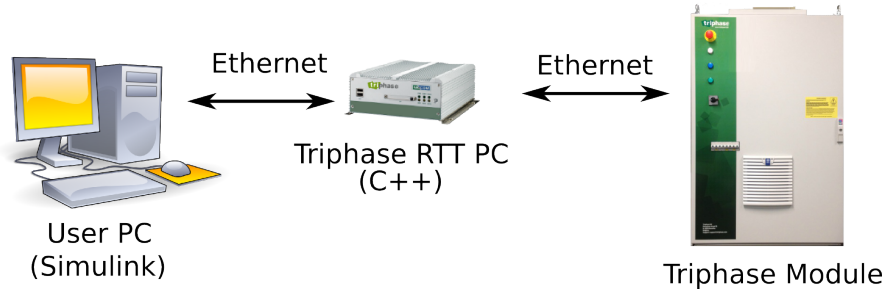

Figure 6.1: Schematic of the Triphase User-Interface [7]

leg can control the neutral line of the grid.

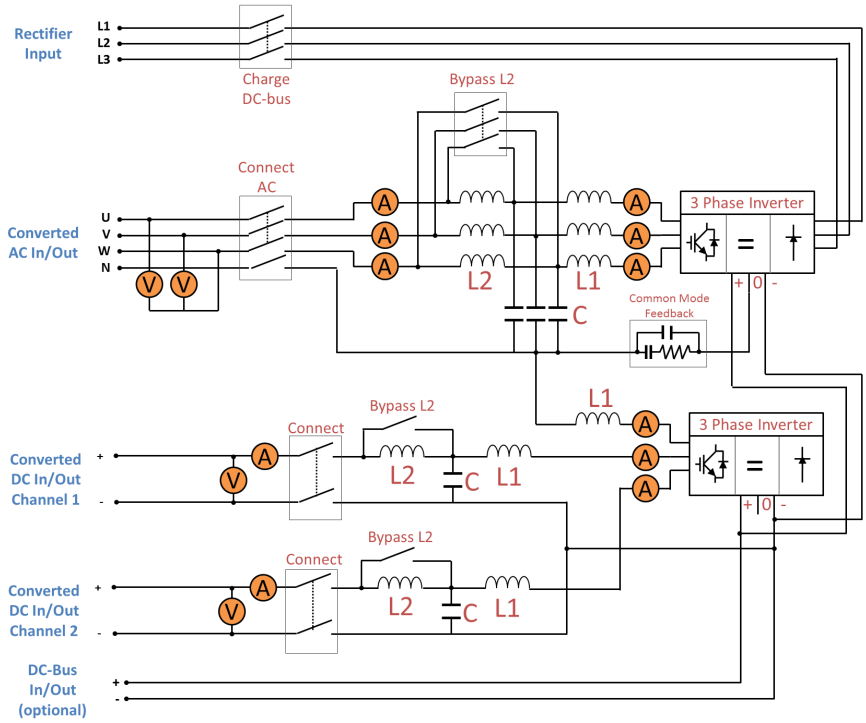

Figure 6.2: Schematic of the Triphase electrical connections [7]

The DC-link is also pre-charged by a 3-phase uncontrolled rectifier connected to the mains, but can also be connected to the 3-phase micro-grid, if complete stand alone operation of the micro-grid is required. When connected to the micro-grid, the operator is required to reset the Triphase PC every time the target is reprogrammed. Hence, it was connected to the mains for testing convenience.

The 3-phase converter currents, the DC link voltage, the 3-phase grid currents and voltages can be acquired from the current and voltage transducers available in the module. The grid voltage is taken as the voltage at the PCC. The other

parameters of the components of the Triphase power converter topology are listed in Table 6.2.

Parameter	Symbol	Value
Converter-side inductor	L_1	$2.3mH$
Effective resistance of L_1	R_1	0.2Ω
Grid-side inductor	L_2	$0.93mH$
Effective resistance of L_2	R_2	0.2Ω
LCL filter capacitance	C_f	$10\mu F$
DC-link capacitance	C_{dc}	$1000\mu F$
DC-link voltage	V_{dc}	$730V$

Table 6.2: Parameters of the PM15F42C power converter [7]

As mentioned previously, the Matlab/Simulink software interface of the Triphase provides an ad-hoc Triphase toolbox to design and develop new control techniques for specific applications. The software architecture shown in Fig.6.3 assists the control of the AC-side and the DC-side by providing access to the measurements acquired from the transducers of the power converter.

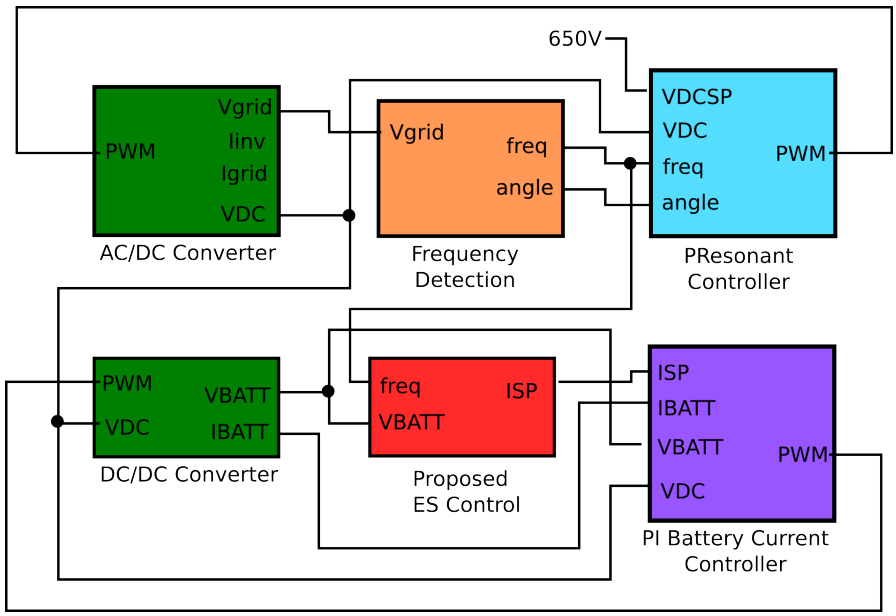

Figure 6.3: Schematic of the Triphase software user-interface [7]

The control PWM signals of both inverters are produced in real time depending on the control logic. With the control logic, inverter 1 is set to regulate the DC link (bus) at 650 V by injecting current to/from the 3-phase grid using a P-Resonant controller tuned to the grid power frequency. This is supplied by the frequency detection technique DSOGI-FLL designed in the Chapter 5.

The DSOGI-FLL also provides the phase angle for grid synchronisation of inverter 1. The control logic for inverter 2 is set to deliver a reference current to and from the energy storage (the battery) via the two channels, using a PI controller. Hence, the software configuration of the experiment is set out as shown in Fig.6.3.

The measured grid voltage (also V_{pcc}) is used to detect the frequency and the phase angle using a DSOGI-FLL. The energy storage control determines the required power that needs to be injected to the grid depending on the detected frequency. Depending on the real time battery voltage acquired, the battery current that is required to inject the necessary power to the grid is calculated. Inverter 2 then delivers this current to the DC-link using its PI control, resulting in an increase or a decrease in the DC bus voltage. Inverter 1 then reacts to regulate the DC bus voltage ultimately delivering the required power to the grid.

6.3 Experimental Set-up of The Prototype Micro-grid Emulation

In order to test the proposed energy storage control, a prototype micro-grid has been created with the help of the Triphase power converter. The two DC-channels of inverter 2 were connected to a $24kWh$ Lithium-ion battery, while the three legs of inverter 1 were connected to the Leroy-Somer generator powered by the diesel engine emulation explained in Chapter 3. The specifications of the battery subject to limited availability (due to commercial sensitivity of data) are listed in table 6.3.

Specification	Value
Energy capacity rating	$24kWh/70Ah$
Voltage	$250 - 380V$

Table 6.3: Specification of the Lithium-ion battery energy storage

The load-side of the micro-grid was configured with a resistive load connected via the 3-phase breaker C. Two 3-phase resistive loads equivalent to 57Ω ($2.78kW$)and 27.5Ω ($5.77kW$) were used to create two test cases, representing a low power and a high power loading respectively. The complete micro-grid prototype used for the experiment is shown in Fig.6.4.

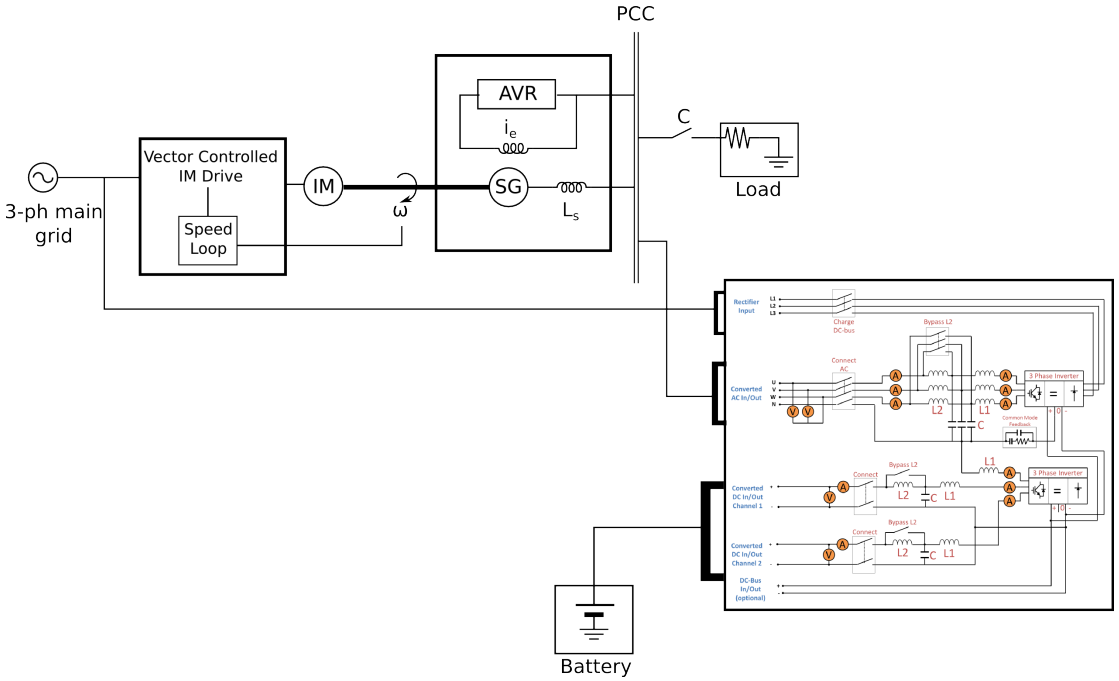

Figure 6.4: Schematic of the Triphase electrical connections

6.4 Experimental Results : Loading

The experiment was primarily conducted to observe the power frequency of the grid, for the two cases of with and without using the proposed energy storage control. The speed of the generator available from the IM drive and the 3-phase voltage at the PCC were recorded using an oscilloscope. Simultaneously, the battery current, the battery voltage, the grid voltage and the grid currents were recorded using the data logging facility in the Triphase. The results obtained are presented and discussed as follows.

case	per-phase resistive load	3-phase load	% generator rating
case 1	57Ω	2.78kW	35%
case 2	27.5Ω	5.77kW	72%

Table 6.4: Per-phase resistive loads considered for validating the energy storage control

The 3-phase loads used during the experiment is detailed in table 6.4. The frequency support achieved using the proposed control is eminent in both cases when conducted with a proportional gain $K_{ES} = 30$, as can be seen in Fig.6.5a and 6.5b respectively.

The experimental results confirm that the proposed method works by recovering the frequency at the threshold by supplying the additional active power

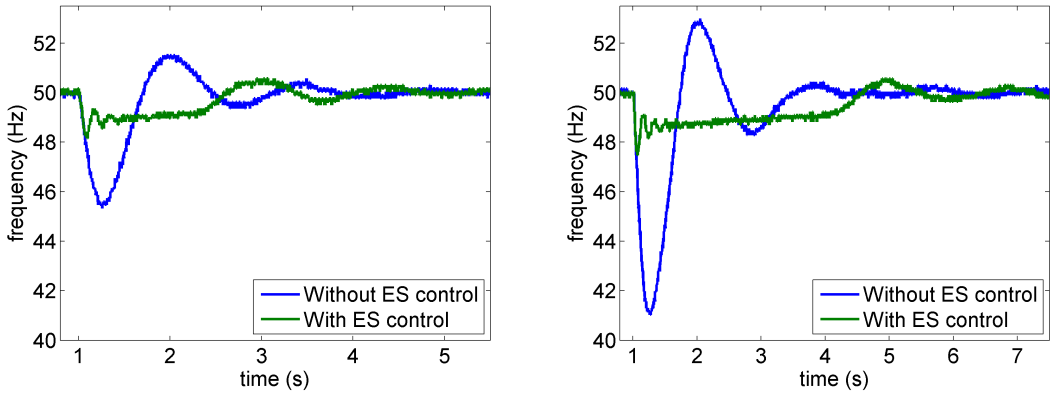

Figure 6.5: Frequency support achieved by applying the proposed ES control technique a) 35%; b) 72% loading, for $K_{ES} = 30$

needed via the Li-ion battery energy storage, while supporting the speed governor during the load transient. The energy storage has correctly activated when the detected frequency crosses the threshold value of 49 Hz. According to Fig.6.5a and Fig.6.5b, the frequency without ES support suffers a significant dip that nearly doubles when the loading was doubled. Yet the frequency with ES support has managed to contain the maximum dip to $<$ 2.5 Hz (i.e. 47.5 Hz). Hence, a significant frequency stabilisation is proven experimentally. One can also see that the settling time is doubled. This is because the governor only reacts to the frequency difference. The control of the ES system and the governor are completely independent and have no intercommunication. In both cases, this is approximately the same requiring double the time when the loading was doubled. Moreover, the delay in the frequency detection as expected has caused initial dampened oscillations similar to that observed in the simulation results.

In order to present the internal details of the experimental validation, the battery current drawn during loading is shown in Fig.6.7. Since the battery is discharging during ES support at loading, the current recorded is negative from the battery's perspective. The peak battery current and the duration of supply have both been increased proportional to the increasing loads. For the large load of 27.5 Ω, the battery has supplied a maximum current of nearly 25 A initially, which is close to the saturation limits (i.e. $\pm$25 A) imposed for the safe operation of the battery and the inverter. Both Fig.6.6a and Fig.6.6a show the triangular variation of the battery current characteristic of the proposed energy storage control presented in the simulations. The high amount of noise in the signals is due to several interdependent reasons. Due to the increase in

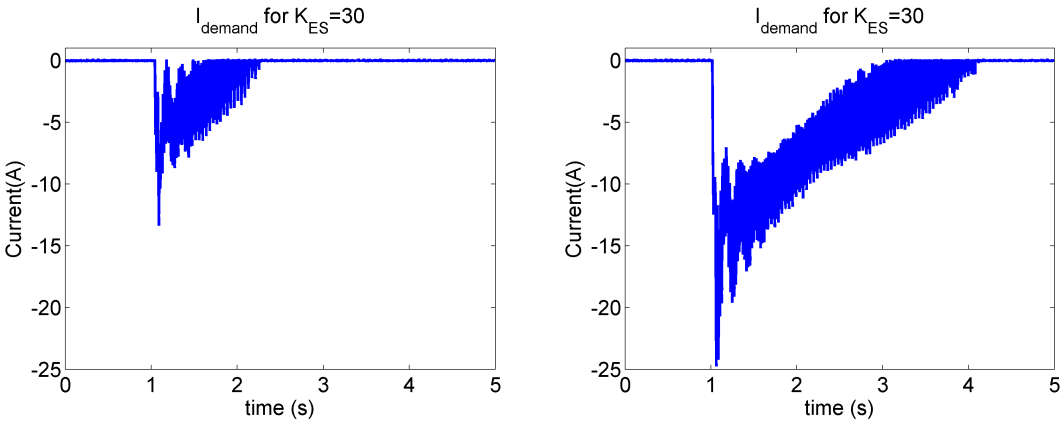

Figure 6.6: The reference demand current from the ES control to the battery energy storage to support frequency recovery: a) Case 1; b) Case 2, for $K_{ES} = 30$

harmonic content during power injection, the ripple in frequency detection increases. Thus, the current demand contains this ripple. Even though a filter could possibly be used, this inevitably introduces delay, which increases the initial frequency oscillations; hence, adding filters in this case is counter productive.

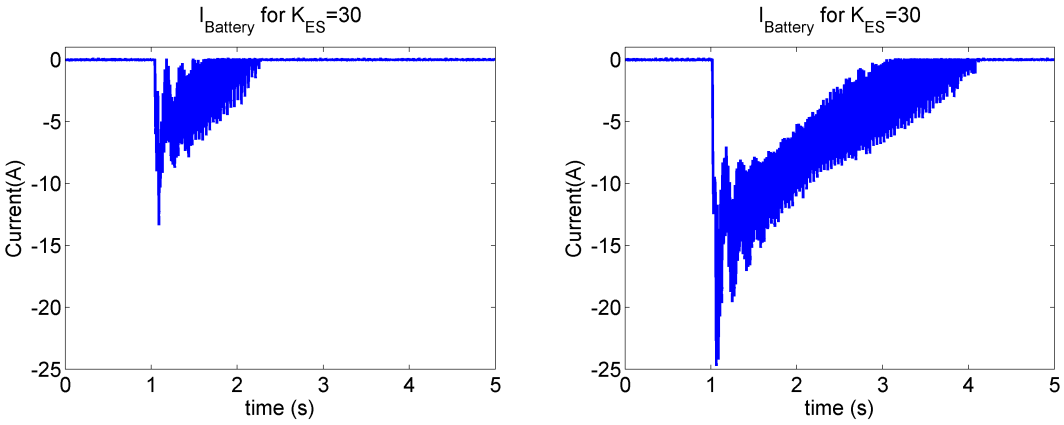

Figure 6.7: The current supplied by the battery energy storage to support frequency recovery a) Case 1; b) Case 2, for $K_{ES} = 30$

Due to the battery internal resistance, the battery voltage experiences a variation during the current drawing period as displayed in Fig.6.8. The level of battery charge is different in the two instances, hence the voltage levels before the energy storage activation is slightly different in the test cases. Due to the internal resistance, the larger the current, the more the battery voltage drops. From Fig.6.8a and Fig.6.8b, one can deduce that the internal resistance is approximately 0.13 Ω. Once, the energy storage automatically switches off as

soon as the frequency is recovered above the threshold, the voltage settles at a constant voltage level slightly less than what it was before the disturbance. As mentioned previously, this is due to the terminal voltage being dependant on the battery's state of charge.

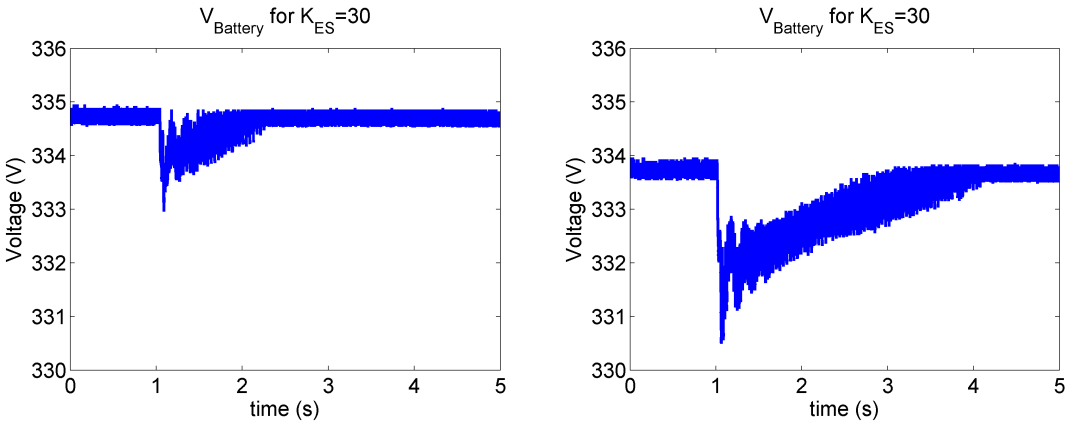

(a) **(b)**

Figure 6.8: The voltage of battery energy storage during frequency recovery a) Case 1; b) Case 2, for $K_{ES} = 30$

The total active power supplied by the battery in both cases are shown in Fig.6.9. For the 57Ω load, the maximum power supplied was about 4.5kW, whereas for 27.5Ω it was increased to 8.5kW confirming the increase in the active power requirement from the battery. The total energy used was also calculated by integrating the power curve in Fig. 6.9a and Fig.6.9b; hence the total energy was found to be 0.35 Wh and 1.76 Wh respectively.

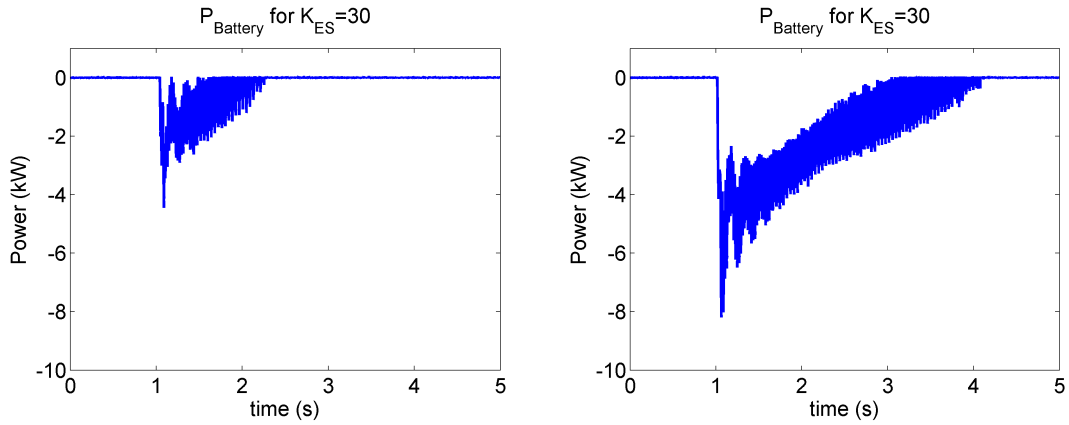

(a) **(b)**

Figure 6.9: The power supplied by the battery energy storage during frequency recovery a) Case 1; b) Case 2, for $K_{ES} = 30$

Finally, it is interesting to analyse the improvements in the voltage at the PCC due to energy storage support. As discussed in Chapter 3, the automatic volt-

age regulation of the generator forces the 3-phase voltage to dip below its nominal value during a heavy disturbance. This is more prominent in case 2, where the frequency drop is larger as shown in Fig. 6.10b. The voltage when the frequency was recovered with the ES support are shown in Fig. 6.10a and Fig.6.10b respectively. These figures illustrate the indirect improvement in voltage observed as a result of frequency support.

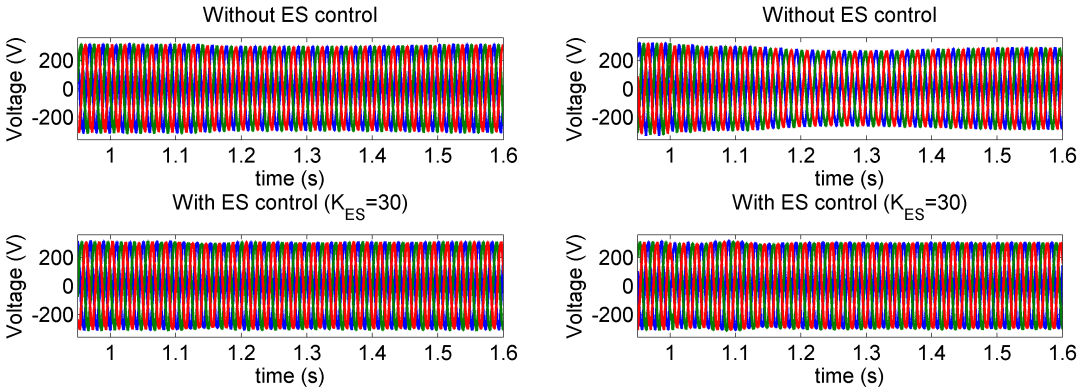

(a) **(b)**

Figure 6.10: The voltage at the PCC with and without energy storage control during loading a) Case 1; b) Case 2, for $K_{ES} = 30$

6.4.1 Comparison with Simulation

Upon observing the experimental validity of the proposed energy storage control, the experimental results are compared to the simulated results in this section. The main difference between the simulation and the experimental is the implementation of the vector control delivering the required current to the 3-phase grid. In order to find a simple transfer function for this current control, the required power input the battery control (i.e. PI controller) is compared with the power delivered at the 3-phase PCC (i.e. P-Resonant controller) by the Triphase in the experiments as shown in Fig.6.11a and Fig.6.11b.

According to Fig.6.11a and Fig.6.11b, there is an inherent delay in the delivered power as well as a reduction in noise. After trial and error, the first order delay was found to be approximately 11 ms for the best fit. The required power fed through this transfer function $\left(\frac{1}{0.011s+1}\right)$ is shown along with the actual power delivered in Fig.6.12a and Fig.6.12b.

For both cases of 27.5 Ω and 50 Ω, the transfer function represents the combined PI battery current control and P-resonant vector control delays of the Triphase.

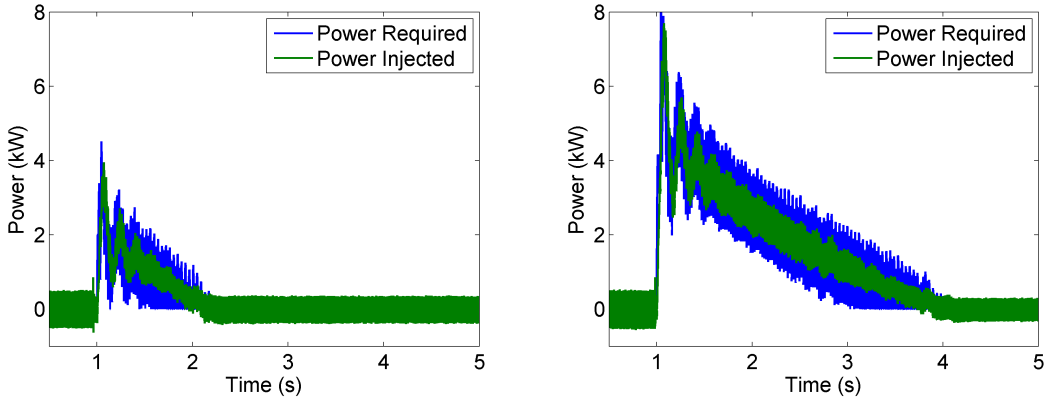

(a) **(b)**

Figure 6.11: The power required as determined by the ES control and the actual power delivered to the grid during loading a) Case 1; b) Case 2, for $K_{ES} = 30$

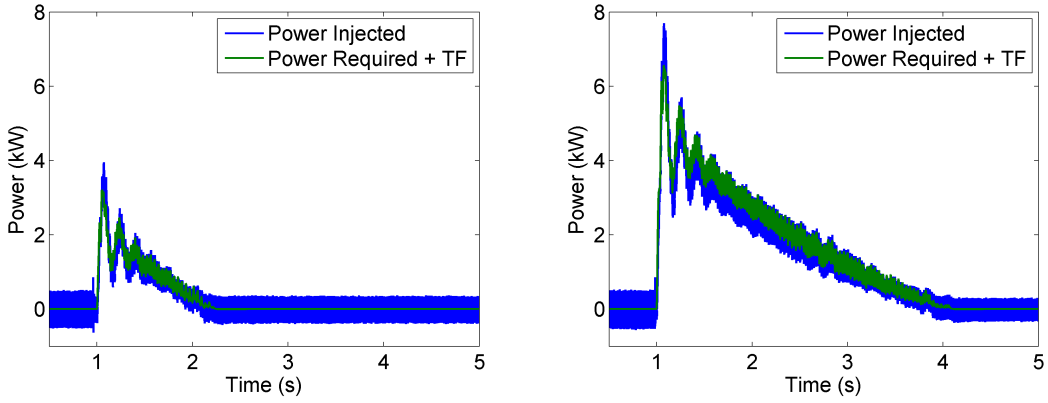

(a) **(b)**

Figure 6.12: The power required as determined by the ES control passed though an approximated transfer function of the vector control and the actual power delivered to the grid during loading a) Case 1; b) Case 2, for $K_{ES} = 30$

In the simulation, this transfer function of 11 *ms* first-order delay was inserted as the vector delay after determining the required d-axis current (I_d). The resultant simulated frequency response along with the corresponding experimental result is shown in Fig.6.13a and Fig.6.13b for 57 Ω and 27.5 Ω respectively.

As can be seen for $R_{Load} = 57\ \Omega$, the simulated frequency response matches with the experimental result reasonably well. The slight mismatch seen in this figure could also be seen in linearising the speed loop in Chapter 3. This can be interpreted as having a faster governor in the simulations. On the other hand, the initial response for $R_{Load} = 27.5\ \Omega$ matches well, but in the experimental result, the frequency response recovers above 49 Hz, 1 s after the simulation. This

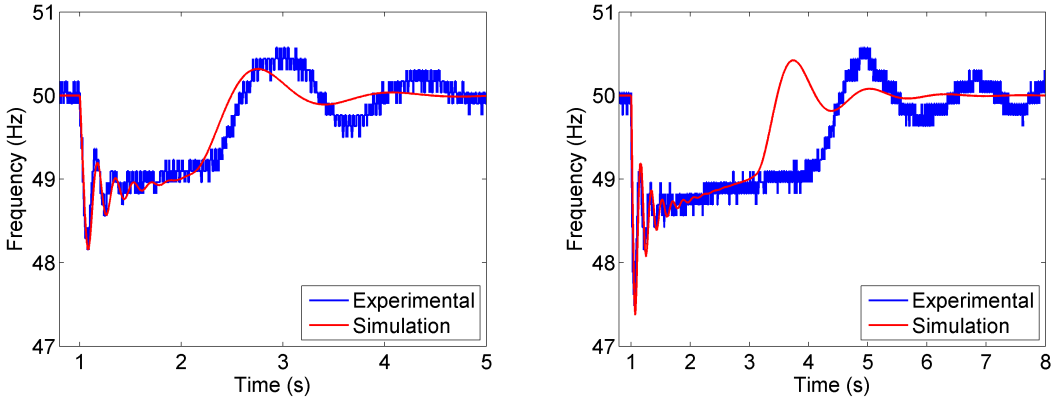

Figure 6.13: The frequency response of the simulation after inserting 11 *ms* vector control delay and the experimental frequency response during loading a) Case 1; b) Case 2, for $K_{ES} = 30$

is possibly due to the fact that the governor is slightly faster in the simulation or it might be a non-linear effect in the prime-mover. This should be investigated in a future work, comparing engine torques in the presence of ES control.

6.4.2 Loading Under Various Control Gains

In support of the proposed method, more experiments were conducted to observe the performance. When using higher gains for the proportional gain K_{ES}. From 4.7.1 in Chapter 4, the stability margin for the current system under test was found to be $\approx$ 60. The validity of this statement is investigated in this section.

The proportional gain was first increased to $K_{ES} = 50$ and the frequency was recorded for loadings of 37.5% and 72%, with the ES control. The results are presented in Fig.6.14 along with the experimental frequency in the absence of ES control and the frequency response predicted by the simulation under the same conditions. As explained in Chapter 4, increasing K_{ES} gives rise to a number of initial damped oscillations in the recovered frequency. As shown in Fig.6.14, the experimented results closely follow the simulated results with the exception of the settling time for the larger load due to the circumstances explained in the previous section for $K_{ES} = 30$. The only change from $K_{ES} = 30$ to $K_{ES} = 50$ is the increase in the damped oscillations in the latter case. This further confirms that the experimental system is stable at $K_{ES} = 50$.

The proportional gain was increased further in order to see whether the sta-

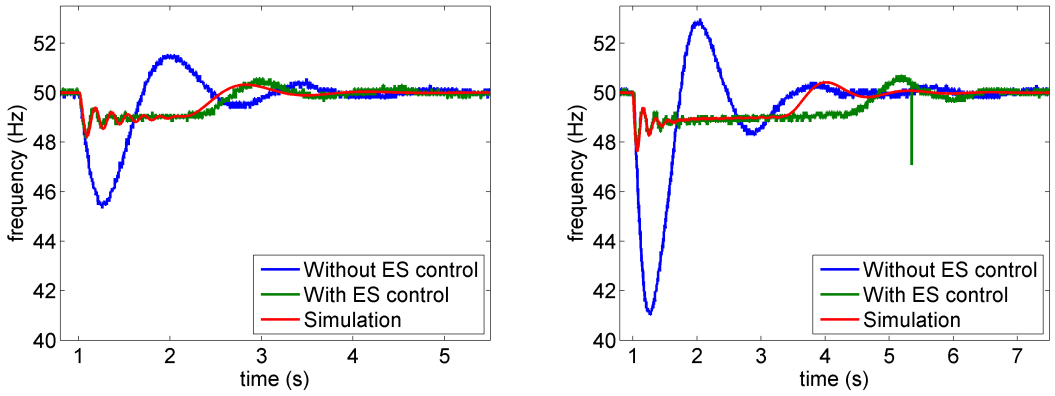

Figure 6.14: Frequency support achieved by applying the proposed energy storage technique a) Case 1; b) Case 2, for $K_{ES} = 50$

bility margin of $K_{ES} \leq 60$ predicted in the simulations is still valid. Fig.6.15 presents the frequency of the experimental system when $K_{ES} = 70$. The figure shows that the experimental results have a noisy response loosing the exponential decaying of the oscillations in frequency recovery at $K_{ES} = 70$. Thus, the experimental results can validate the theoretical stability margin of $K_{ES} = 60$.

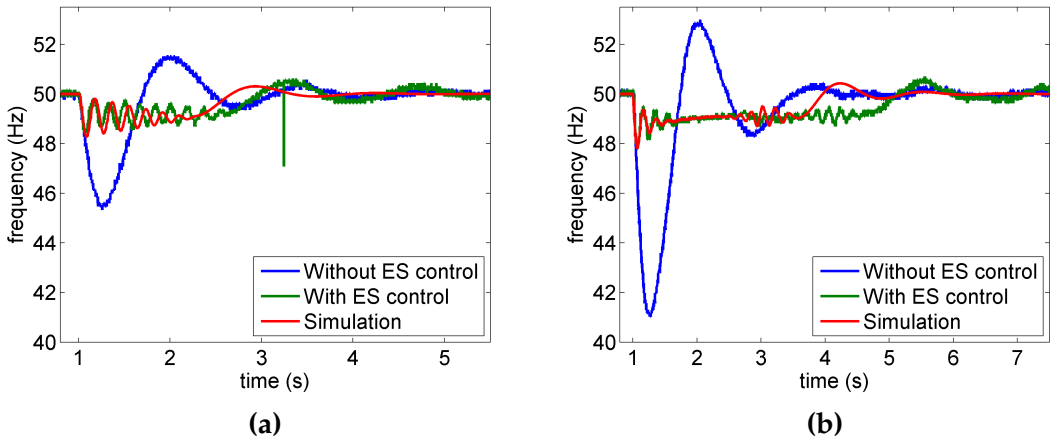

Figure 6.15: Frequency support achieved by applying the proposed energy storage technique a) Case 1; b) Case 2, for $K_{ES} = 70$

It is interesting to see that the initial oscillations are dampened less for the smaller load in the experimental results. For the larger load the experimental result shows more stability, though none of them show exponential decay of the oscillations. The reason is that the experimental system has a current limiter at 25 A, which affects the frequency response of the large load. In case of not having this current limiter in place, the frequency stabilization of the large load would have required a current well over 40 A, suggested by the simulation.

The simulation result shown in Fig.6.15 also has an equivalent current limiter in place ($I_d \leq 27\ A$) so that the power output limited in both the simulation and the experimental are the same. It is interesting to note that this barely affects for the smaller load as its required current even at $K_{ES} = 70$ does not reach 25 A. As a consequence for larger loads, the system shows increased stability by effective reduction of K_{ES}. This opens up an avenue for further study. It further shows that the system should not be operated beyond the stability margin, even though in theory or in practice it could be as the resultant frequency is still constrained; because then the frequency response would depend on the factors such as loading.

In summary, this section has verified the stability margin experimentally. The observation of the same stability margin for both cases of loads exhibits the consistent performance of the proposed energy storage control.

6.5 Experimental Results: Load Shedding

As opposed to the frequency drop during loading, the power frequency rises during load shedding. In this case, active power is in surplus and needs to be absorbed by the battery (i.e. charge) in order to constrain the frequency response. When designing the energy storage control, it has been assumed that the battery energy storage is equally capable of charging and discharging at the same rate. Therefore, a similar set of experiments were conducted in line with loading to observe the effectiveness of the energy storage in exploiting the surplus active power.

In Fig.6.16, the frequency rises as high as $54Hz$ and $59Hz$ when shedding 37% and 72% of the rated active power without energy storage support. In both cases, with the energy storage support the frequency could be successfully recovered at $51Hz$. Another interesting fact is that unlike the frequency recovery observed during loading in Fig.6.5, which showed similar initial oscillatory characteristics for a fixed K_{ES} but different loads, in shedding, the oscillatory profile has significantly changed for different loads (shed). This is also observable in the simulation results shown in Fig.6.16. The larger the load (power), the more oscillatory the frequency response with the energy storage support is - see Fig.6.16b. The battery current and the voltage supplied during the load shedding transient are shown in Fig.6.17 and Fig.6.18 respectively.

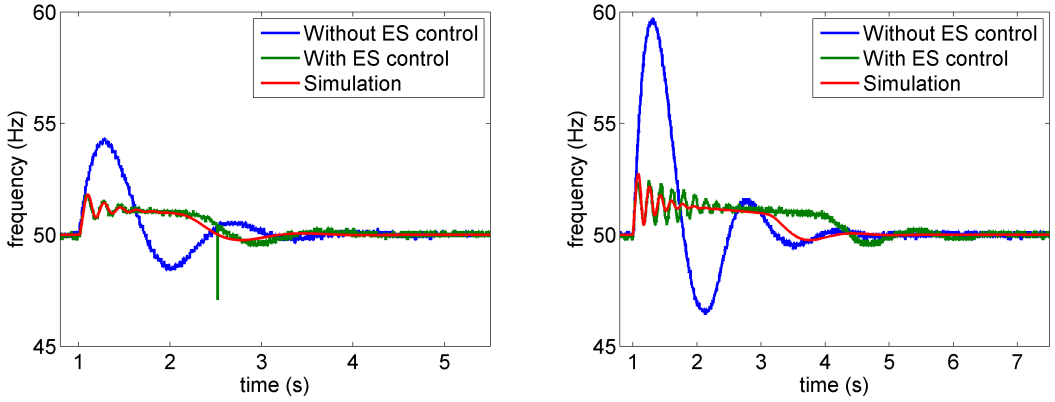

(a) **(b)**

Figure 6.16: Frequency support achieved by applying the proposed energy storage technique for load shedding a) Case 1; b) Case 2, for $K_{ES} = 30$

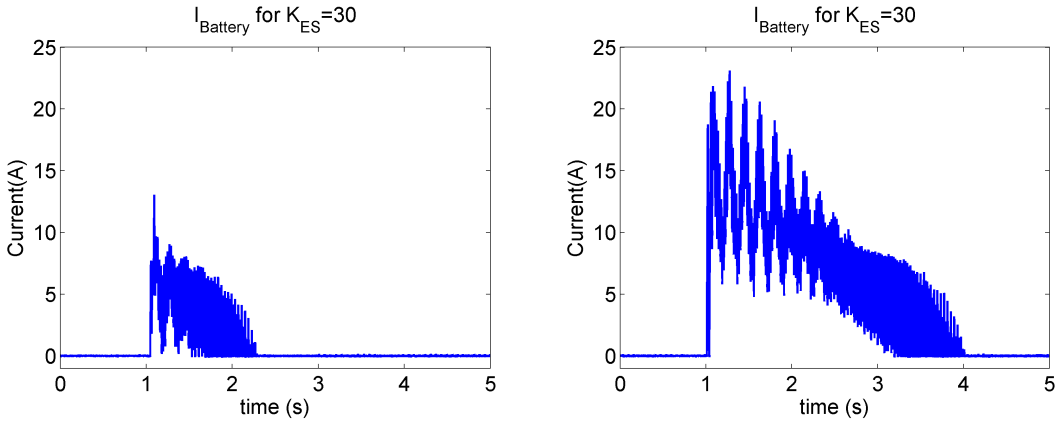

(a) **(b)**

Figure 6.17: The current absorbed by the battery energy storage during load shedding a) Case 1; b) Case 2, for $K_{ES} = 30$

As can be seen, the battery voltage experiences a rise in order to allow the charging current. Moreover, the active power absorbed by the battery is shown in Fig.6.19 confirming the effective use of the energy storage, restricting the frequency from reaching higher levels. Yet, none of these show a drastic difference from that of loading and follows an acceptable general trend.

The variations in the voltage at PCC can be observed in Fig.6.20. From Fig.6.20b, one can see a clear difference in the PCC voltage for load shedding, from that for loading. In all cases of loading the PCC voltage was also regulated as a consequence of frequency regulation because of AVR effects. For a small shed, the voltage is still regulated. But, for the higher load, the initial oscillations in the current injection will cause a variation in voltage due to the impedance as shown in Fig.6.20b. In order to overcome this, one would also require reactive

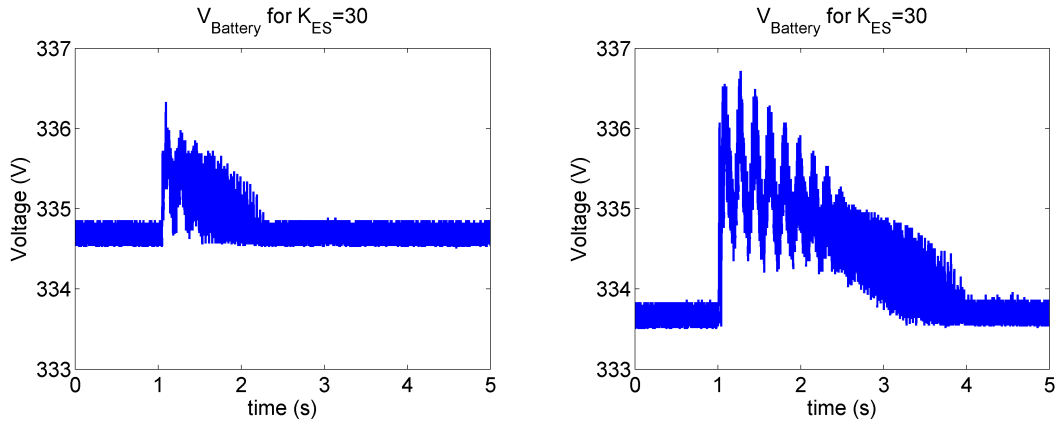

(a) **(b)**

Figure 6.18: The voltage of battery energy storage during load shedding a) Case 1; b) Case 2, for $K_{ES} = 30$

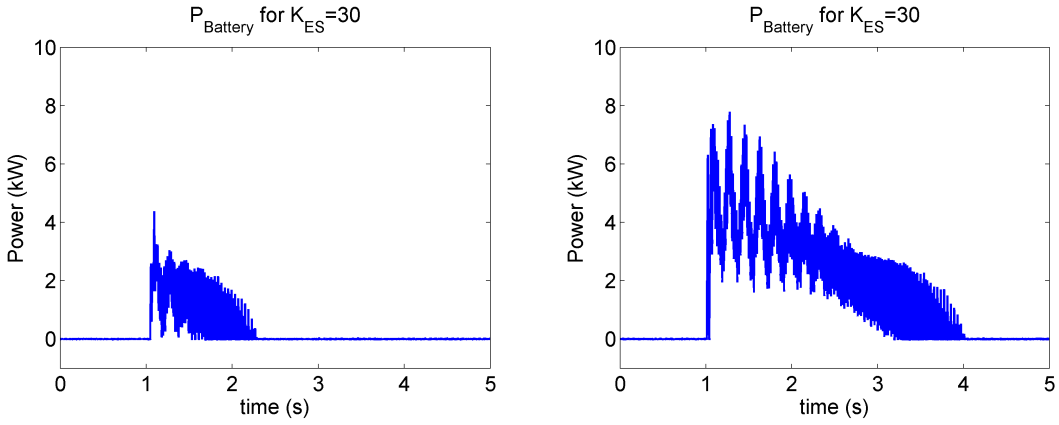

(a) **(b)**

Figure 6.19: The active power absorbed by the battery energy storage during load shedding a) Case 1; b) Case 2, for $K_{ES} = 30$

power control in addition to frequency control for an effective load-shedding to take place. While, this will open an interesting future work path, the existing method is shown to operate adequately in confining the frequency.

In order to observe the stability margin, the effects of load shedding on the frequency response for different control gains K_{ES} was tested next as conducted in loading. The frequency responses for load sheds of 35% and 72% of rated power when $K_{ES} = 50$ and $K_{ES} = 70$ are shown in Fig.6.21 and Fig.6.22 respectively. The corresponding simulation results also shown in the same figures depict that the frequency response is modelled adequately in the simulation. As a general rule, the oscillations are larger and last longer for larger load shedding, but they are constrained due to the current limiting of the Triphase. When K_{ES} is above the limit (i.e. $K_{ES} \geq 60$), the frequency oscillations for the large load are large

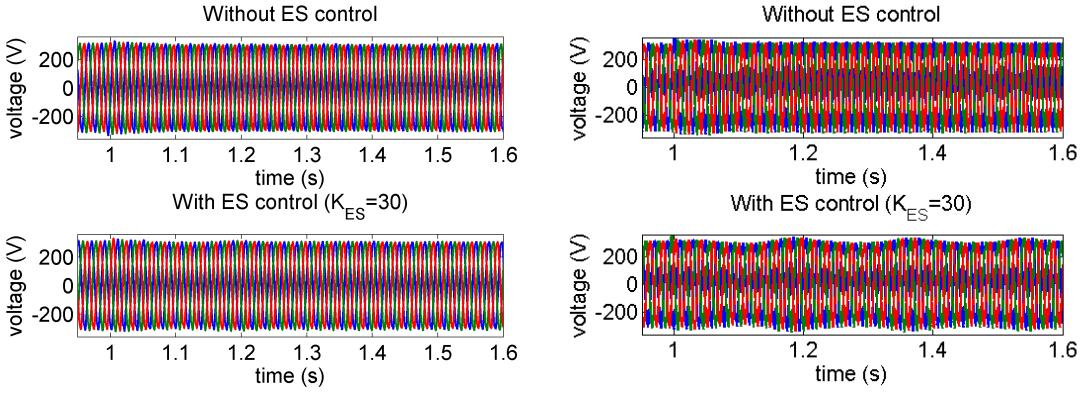

(a) **(b)**

Figure 6.20: The voltage at the PCC with and without energy storage control during load shedding a) Case 1; b) Case 2, for $K_{ES} = 30$

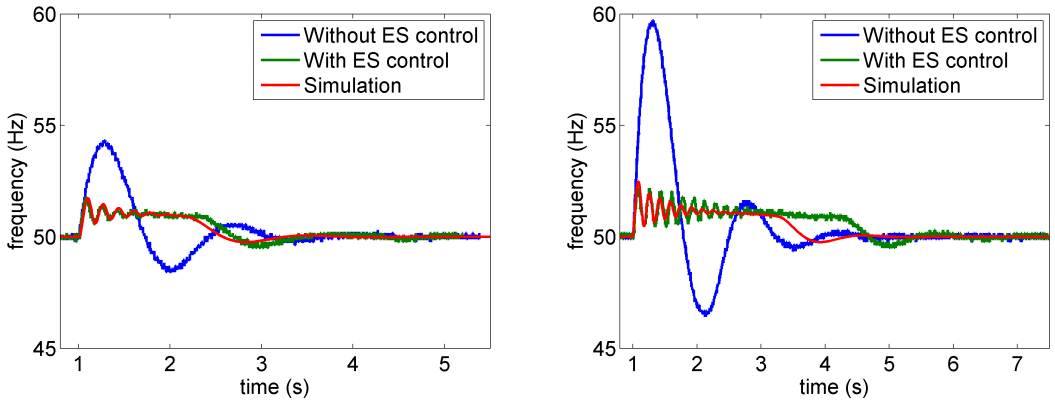

(a) **(b)**

Figure 6.21: Frequency support achieved with proposed ES control during load shedding: a) Case 1; b) Case 2, for $K_{ES} = 50$

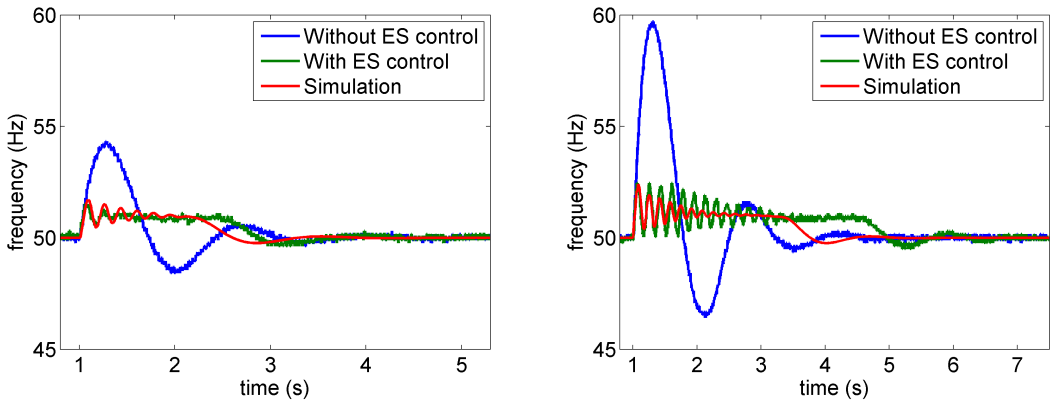

(a) **(b)**

Figure 6.22: Frequency support achieved with proposed ES control during load shedding: a) Case 1; b) Case 2, for $K_{ES} = 70$

enough to go below the nominal frequency (50 Hz). Hence, though practically possible due to the current limiting one should operate the ES control below the stability margin.

6.6 Effect of the Size of the Battery Current Limiter

The proposed energy storage control has been developed theoretically assuming that the size of the energy storage is same as that of the power system. This means that the energy storage is able to inject active power equivalent to the rated load disturbance experienced by the power system. In the previous experiments, the battery current was limited to 25 A, while the battery voltage was around 330 V or more. Thus, the battery can inject approximately 8.3 kW. Because of its capacity of 24 kWh, this power can be supplied for approximately 3 hours, though such capacity is unnecessary for this application. This is sufficient to supply the active power needed to recover the rated load disturbance in this case.

In order to see what to expect if the power converter available has a lower power rating, the current supplied by the battery was curtailed from 25 A to 5 A. If the voltage at the battery is assumed constant, this mimics a case where the battery energy storage is one fifth of the rating of the former.

The experimental results obtained for the frequency recovery for a small loading of 35% with $K_{ES} = 30$ and curtailed current of $5A$ is shown in Fig.6.23. As can be seen from Fig.6.24a, the battery has supplied a maximum current of $5A$.

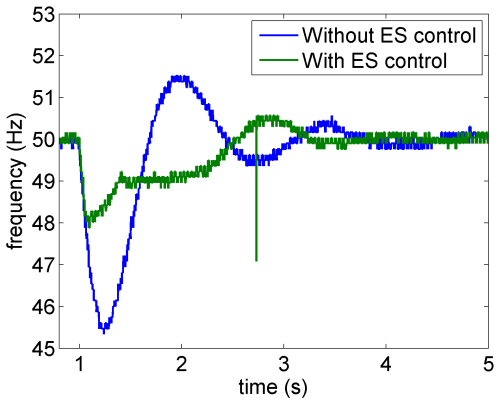

Figure 6.23: Frequency support achieved with proposed ES control, with $\pm 5A$ saturation limits ($K_{ES} = 30$)

With a lower current, the active power supplied was limited to about $1.8kW$ as seen in Fig. 6.24c. Therefore, the frequency recovery is taking a different shape as shown in Fig.6.23 to the typical response observed for loading in section 6.4. The frequency drops to the same level i.e. $\approx 48Hz$ before being recovered, and takes roughly the same time to settle at the threshold. Due to the relatively low active power supplied, the frequency is not over supported as in the case with the larger current supply. Therefore, the oscillations in the recovered frequency have become less prominent.

The voltage of the battery has also been restricted as shown in Fig.6.24b. Voltage, current and real power including the recovered frequency cannot maintain the typical exponential decaying due to the current rating restrictions.

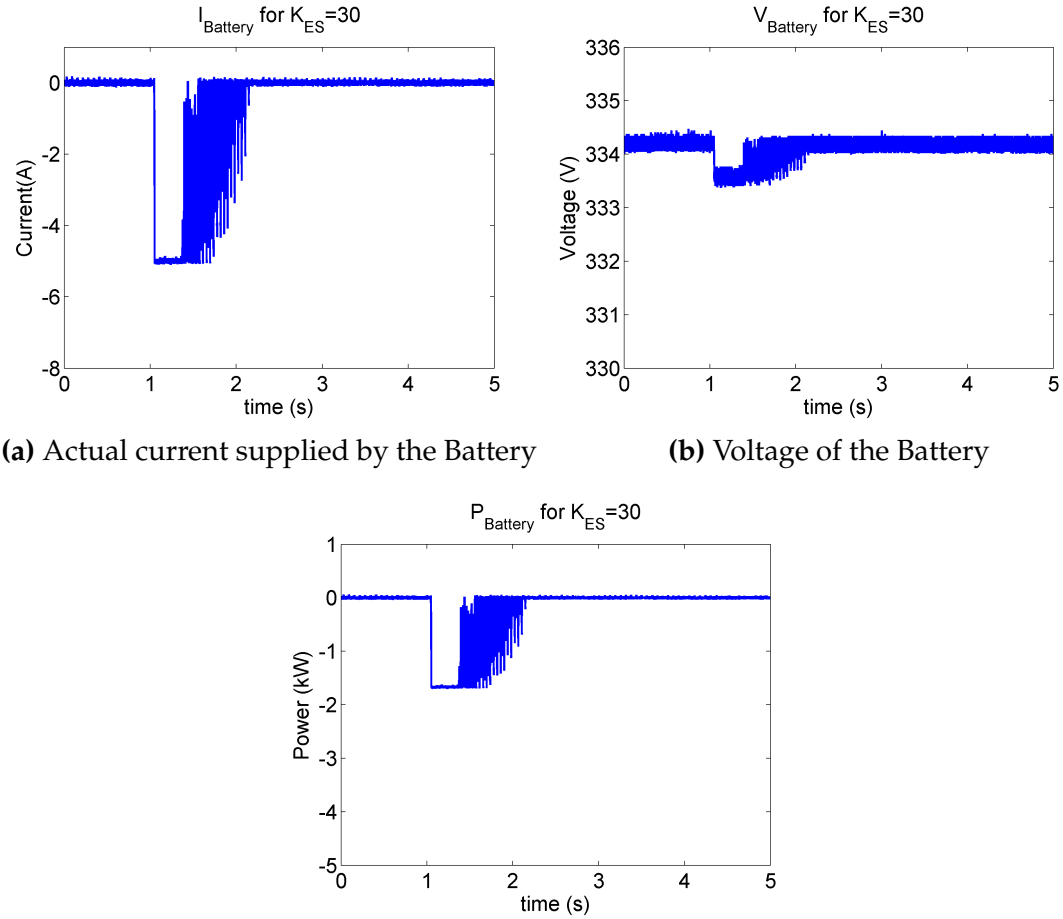

(a) Actual current supplied by the Battery

(b) Voltage of the Battery

(c) Power supplied by the battery

Figure 6.24: The performance of the energy storage with prosed control, with $\pm 5A$ saturation limits ($K_{ES} = 30$)

The frequency recovery with limited current rating was also observed for $K_{ES} = 50$ and 70. The results present in Fig.6.25 exhibit same characteristics to that of

$KES = 30$. Further, when the current is curtailed to a low value, the system does not experience an instability when $K_{ES} = 70$. Thus, when the current is limited to a low enough value, K_{ES} increase has no effect on the overall operation of the system.

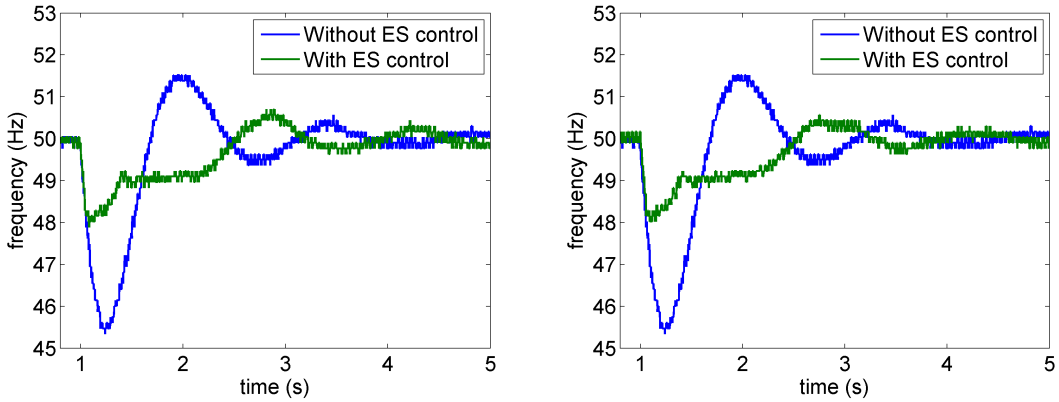

(a) $(K_{ES} = 50)$ **(b)** $(K_{ES} = 70)$

Figure 6.25: Frequency support achieved with proposed ES control, with $\pm 5A$ saturation limits $(K_{ES} = 50, 70)$

6.7 Effect of The Frequency Threshold

Until now, the energy storage control used a frequency threshold of 49 Hz. To observe the operation of the energy storage control for frequency support with tighter limits, the frequency response was observed with a lower-bound threshold of 49.5 Hz. Fig.6.26a and Fig.6.26b shows the corresponding frequency support achieved for loadings of 35% and 72% of the rated load obtained with $K_{ES} = 30$ as the control gain.

As can be seen, increasing the threshold by 0.5 Hz has successfully commanded the ES control to recover the power frequency at the new threshold of 49.5 Hz. The oscillations are smaller in magnitude but lasts about the same length of time when compared with Fig.6.5a and Fig.6.5b. Due to the reduced speed-error available for the governor action, the settling of the overall frequency response is lengthened compared to that when the threshold is 49 Hz. This is further elongated for the larger load as shown in Fig.6.26b. The reverse action of this was experienced when the same loads were unloaded as presented Fig.6.27. The effect of reactive power imbalance as discussed in section 6.5 has caused more oscillations in the shedding of the large load as shown in Fig.6.27b.

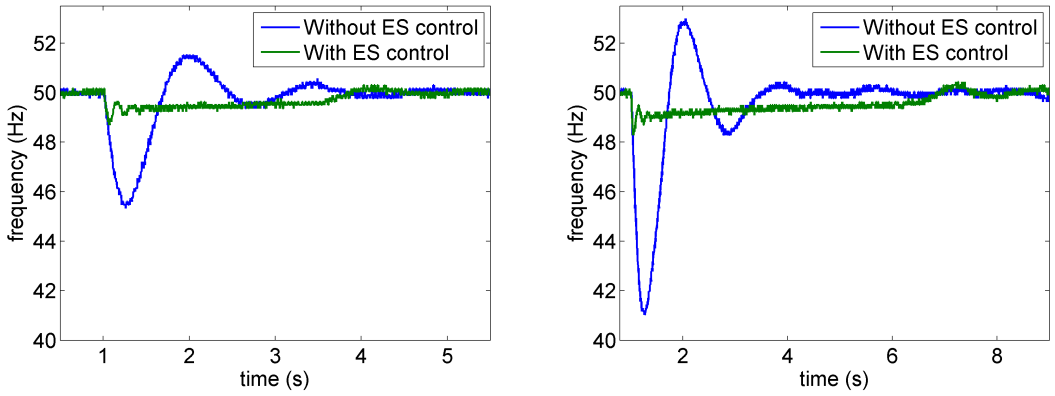

(a) case 1-35% rated power **(b)** case 2-72% rated power

Figure 6.26: Frequency support achieved with proposed energy storage technique with a threshold $f_{th} = 49.5\ Hz$, during loading ($K_{ES} = 30$)

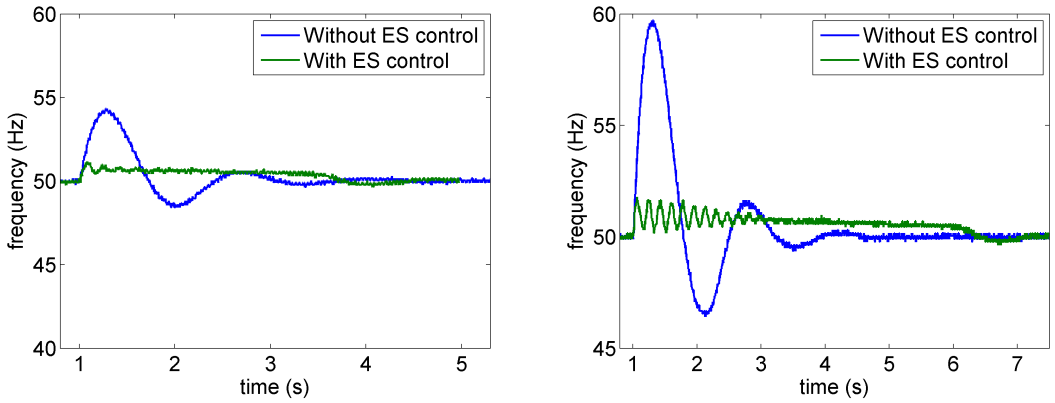

(a) case 1-35% rated power **(b)** case 2-72% rated power

Figure 6.27: Frequency support achieved with proposed energy storage technique with a threshold $f_{th} = 49.5\ Hz$, during load shedding ($K_{ES} = 30$)

Grid frequency regulations consider $\pm 0.5\ Hz$ from nominal as the normal operation limit for the frequency so that the frequency is regulated within 1% of the nominal [13]. Therefore, the successful performance delivered by the energy storage control experimentally for tighter limits can be recognised for improved frequency support when required.

6.8 Conclusion

The proposed energy storage control was experimentally validated successfully for different levels of loading and load shedding. The operation of the energy storage delivered the frequency support in a manner predicted by the simu-

lations. The stability margin of the proportional gain was experimentally observed to be closer to the margin of $K_{ES} \leq 60$ deduced by the simulation. The battery current limit was found to have an impact especially in recovering large load disruptions, due to significant curtailment of current. However, a reduced limit on the battery current increased the stability and masked the initial oscillations. The PCC voltage also benefited from the frequency support as its oscillations were smoothed out during the transient. However, PCC voltage during load shedding suffered from uncontrolled flow of reactive power visibly altering its envelope. The proposed energy storage control also successfully performed with an improved tighter threshold level to constraint the frequency to $\pm 0.5\ Hz$ in compliance with the normal operation requirements imposed by the Grid Code. In essence, the experimental results presented in this chapter not only validated the proposed energy storage control for frequency support in weak electrical grids, but also successfully verified the simulation model that the developed technique was based upon.

CHAPTER 7

Characterisation and Multiple Energy Storage Usage

7.1 Introduction

The proposed energy storage control technique has been modelled in a simulation in chapter 4 and was confirmed of its validity experimentally in chapter 6. Some investigation of the characteristics of the energy storage control was conducted in chapter 4 by varying the proportional gain K_{ES}. This chapter extends the characterisation study further into varying the frequency threshold and current limitation levels.

In practice, multiple energy stores may have to be used to improve the robustness of the energy storage solution. Hence, a study was conducted on employing multiple energy storage systems possibly at the same point of common coupling to determine the control parameters to share the energy injection between the multiple storage units.

7.2 Performance of The Energy Storage Control Algorithm for Varying Frequency Thresholds

In chapter 4, the total energy injected by the energy storage, the peak power injected, the maximum frequency drop and the settling time (the time to settle the frequency within $\pm 0.01\ Hz$ from nominal 50 Hz) were observed, varying the proportional energy storage controller gain K_{ES}. It was concluded that increasing K_{ES} in general increases both total energy and the peak power when

used during load compensation, while reducing the frequency drop and the settling time. Even though the effect of K_{ES} was small on the peak power, it was significant on the total energy used. Hence, it was concluded that K_{ES} should be chosen to match the energy storage capacity or vice versa.

In this spirit, the same observations were made by varying the threshold frequency, a parameter that was fixed at 49 Hz throughout the study to provide sufficient frequency error to the speed governor. The observations made using the rated load disturbance are recorded against the threshold frequency in Fig.7.1.

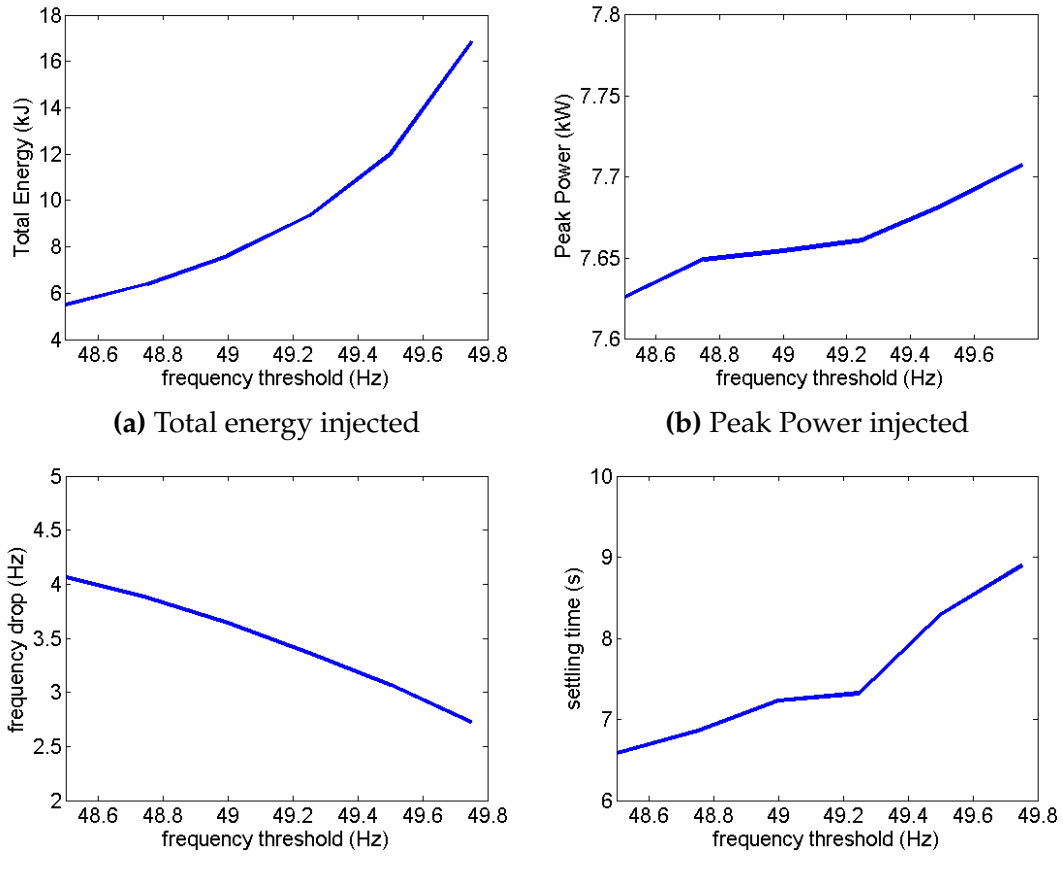

(a) Total energy injected

(b) Peak Power injected

(c) Maximum frequency drop

(d) Settling Time

Figure 7.1: Total energy used, peak power injection, maximum frequency drop, settling time when varying the frequency threshold f_{TH}, while keeping $K_{ES} = 30$ and current limit at 27 A.

According to Fig.7.1a, the total energy spent increases exponentially when the frequency threshold is raised. When the frequency threshold is raised, understandably, the energy required to bring the frequency above the threshold also rises, reaching infinity, when the frequency threshold is equal to the nominal frequency. The latter case was not considered as that would result in a neg-

ligible error for the generator governor to work on. Interestingly, the peak power used has not changed much when the frequency threshold was raised according to Fig.7.1b. This means that the maximum difference between the instantaneous frequency and the frequency threshold is almost the same despite varying the frequency threshold. This should be viewed in conjunction with Fig.7.1c, which shows that the maximum frequency drop has almost a linear relationship with the frequency threshold, decreasing when the threshold is raised. In fact, when the frequency threshold is raised, the overall power frequency gets raised by the same amount. The settling time however increases almost linearly when the frequency threshold is increased according to Fig.7.1d. This can be explained by the fact the frequency error seen by the governor gets reduced when the frequency threshold is raised, slowing down the settling at the threshold. This does not significantly affect the time to settle the frequency at the nominal after the energy storage controller is deactivated. Therefore, the total settling time shown in Fig.7.1d increases with increasing frequency threshold.

7.3 Performance of The Energy Storage Control Algorithm for Varying Current Thresholds

In chapter 4, it was concluded that the stability improves and the effective K_{ES} changes in the presence of current limiters, which are inevitably present in any power converter. In the experimental system considered, the d-axis current was effectively limited at 27 A. In this section, the effect of limiting the current on the total energy spent, frequency drop and settling time were observed on the rated load disturbance, and are shown in Fig.7.2.

Decreasing the current limit effectively decreases the rated power of the energy storage controller. According to Fig.7.2a, decreasing the current limit decreases the energy spent by the energy storage. Further, when the current limit is decreased, the frequency drop increases as shown in Fig.7.2b. Under decreased current limit, due to the large frequency drop, the governor sees larger frequency error and actuates the prime mover to provide more power quicker requiring less support from the energy storage. The fact that the energy storage has a lower power rating (lower current limit) means more energy is drawn from the prime mover and less from the energy storage during a transient.

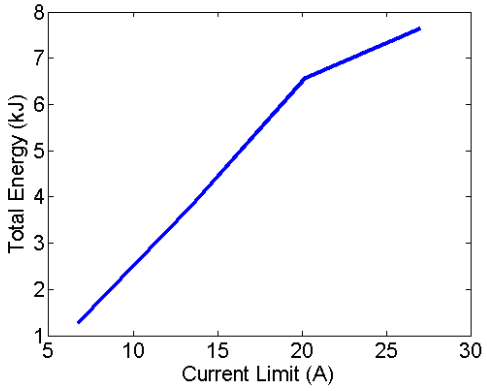

(a) Total energy injected

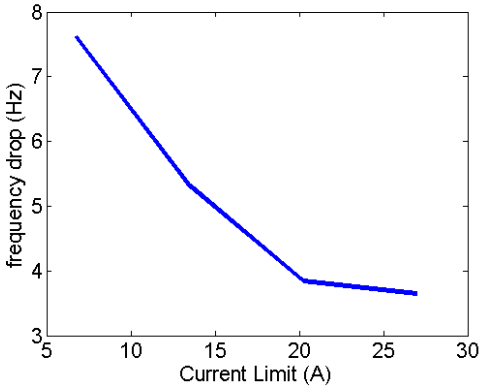

(b) Maximum frequency drop

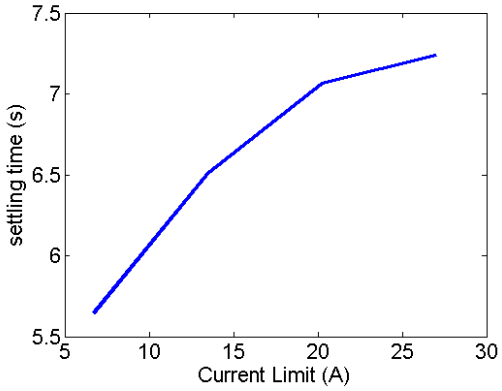

(c) Settling Time

Figure 7.2: Total energy spent, maximum frequency drop, settling time when varying the current limit, while keeping $f_{TH} = 49\ Hz$, $K_{ES} = 30$

The same phenomena also explains the decrease in settling time when the current limit is decreased. More governor action under reduced current limit also means quicker overall settling time. The main downside of reducing the current limit is the large initial frequency drop the system has to suffer due to lower power injection from the energy storage.

7.4 Fundamentals of Multiple Energy Stores

In order to improve the robustness, smaller multiple energy storage units can be a better solution than a single large energy storage. Up to now, it was understood that the proposed energy storage can work independent of the prime mover. By studying multiple energy storage systems, one can further explore the plug-and-play capabilities and limitations of the proposed energy storage control. In other words, this study will identify if any coordination between

energy storage is required to effectively constrain the power frequency without leading to instabilities.

When multiple energy storage units operate, they all share the same frequency information. If one keeps the frequency threshold the same, the frequency difference between the instantaneous frequency and the threshold will be the same for all energy storage controllers. Since, power supplied is additive, K_{ES} should also be added to come up with an effective K_{ES} figure for the multiple energy storage system.

To illustrate the above idea, the electrical system with two energy storage units was simulated with a threshold $f_{TH} = 49\ Hz$, $K_{ES1} = 22.5$ and $K_{ES2} = 7.5$ in the two energy storage controllers. The frequency response of the dual storage system is shown in Fig. 7.3 along with a single storage with $K_{ES} = 30$ and $f_{TH} = 49\ Hz$.

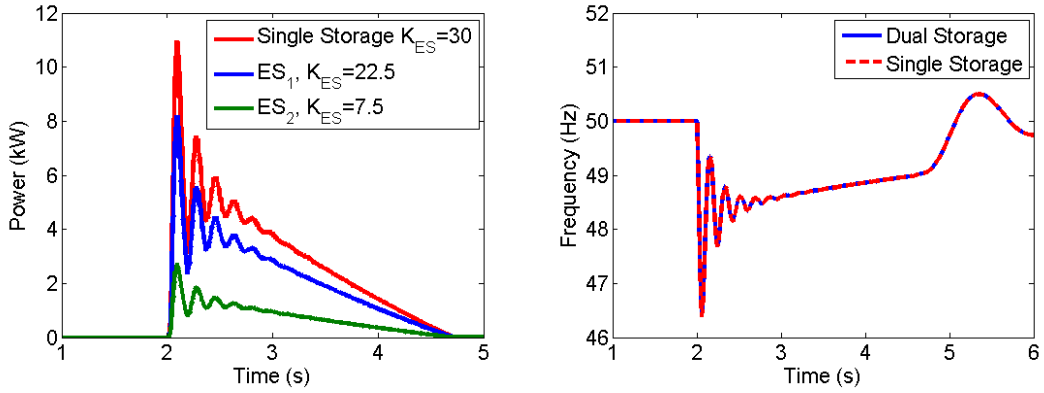

(a) Injected Power **(b)** Frequency

Figure 7.3: The injected power and the frequency for a dual storage system with $K_{ES1} = 22.5$, $K_{ES2} = 7.5$ and a single storage with $K_{ES} = 30$, while keeping $f_{TH} = 49\ Hz$.

From Fig.7.3a, one can see that the injected power is shared between the two storage units, where the sum of power injected by the two storage units are equivalent to the power injected by the single storage. This is further confirmed by Fig. 7.3b, where both systems provide equivalent frequency response confirming the linear addition of K_{ES}, when the frequency threshold of the storage control systems are the same.

In order to see the whether addition of K_{ES} is still valid when combining energy storage units of different f_{TH}, two energy storage units with $K_{ES1} = K_{ES2} = 15$ were used with two thresholds $f_{TH1} = 49\ Hz$ and $f_{TH2} = 49.2\ Hz$. The resulting frequency response is shown in Fig.7.4a along two single energy stor-

age systems, one with $K_{ES} = 30$, $f_{TH} = 49\ Hz$ and the other with $K_{ES} = 30$, $f_{TH} = 49.2\ Hz$ for comparison. Fig.7.4b shows the injected power for the three systems.

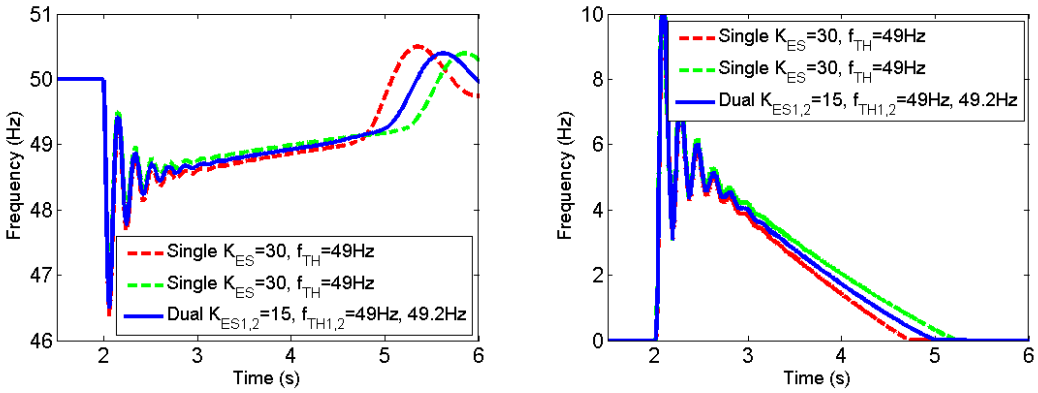

(a) Frequency **(b)** Power

Figure 7.4: The the frequency and the injected power for two storage units with $K_{ES1} = K_{ES2} = 15$, $f_{TH1} = 49\ Hz$,$f_{TH2} = 49.2\ Hz$ and two single storage systems with $K_{ES} = 30$, $f_{TH} = 49\ Hz$ and $K_{ES} = 30$, $f_{TH} = 49.2\ Hz$.

According to both Figs.7.4a, 7.4b, one can see that the oscillations are between the three systems. Since K_{ES} is the factor that affects the oscillations, one can conclude that all systems share the same K_{ES}. The system with two storage units, one with $f_{TH1} = 49\ Hz$ and $f_{TH2} = 49.2\ Hz$ performs in between the system, which has single storage units with thresholds of $f_{TH} = 49\ Hz$ and $f_{TH} = 49.2\ Hz$ individually. Thus, the addition of K_{ES} still holds for systems with different thresholds, but the performance in every aspect (i.e. energy, power, frequency drop, and settling time) is in between the single storage systems with the different thresholds.

Nonetheless, a quantitative analysis is now required to observe how the performance of multiple energy storage systems varies when K_{ES} is shared in different ratios with different frequency thresholds. The next sections discuss this matter.

7.5 Performance of Multiple Storage Units With Varying Parameters

From the above study, it could be said that when K_{ES} is shared between two energy storage units, the peak power and the total energy used also are shared

among the two storage units, even when the frequency thresholds are different. In order to quantify the effects, the peak injected power, total energy supplied, the maximum frequency drop and the settling time were measured for varying factors of K_{ES1}/K_{ES2} and different frequency thresholds. The frequency threshold of one controller was kept at $f_{TH1} = 49\ Hz$, while that of the other was varied.

7.5.1 K_{ES} Variation

The sharing of energy, sharing of peak power, the maximum frequency drop and the settling time was plotted against K_{ES} sharing-factors, for various frequency threshold differences $\Delta f_{TH} = f_{TH2} - f_{TH1}$ in Fig.7.5.

According to Fig.7.5a, one can immediately see that the share of energy injection is directly proportional to the K_{ES} share between the two energy storage units. Fig.7.5a also shows that the energy share can be changed by increasing the frequency threshold of the smaller K_{ES} controller. Thus, one can obtain the full control of how the energy injection should be shared between storage units, and this could be useful if the two units have different power or energy specifications. Fig.7.5b shows that the total energy does not vary much when K_{ES} is varied especially when the difference between the thresholds is low. In fact, the total energy varies between that of one storage with one threshold (i.e. f_{TH1}) and that of another storage with the other threshold (i.e. f_{TH2}) both with the same K_{ES} equal to the sum of that of the multiple storage system. Likewise, the share of peak power shown in Fig.7.5c follows the same rules defined for energy share.

The maximum frequency drop however, does not vary much with increasing K_{ES} share as seen in Fig.7.5d. When a controller with higher frequency threshold is involved, the frequency drop decrease as expected. The settling time does not show a significant variation with increasing K_{ES} share as seen in Fig 7.5e. Again, when higher thresholds are involved, the settling time is lengthened.

7.5.2 f_{TH} Variation

The sharing of energy, the sharing of peak power, the maximum frequency drop and the settling time are plotted against the frequency threshold differences Δf_{TH} for various K_{ES} sharing-factors in Fig.7.6.

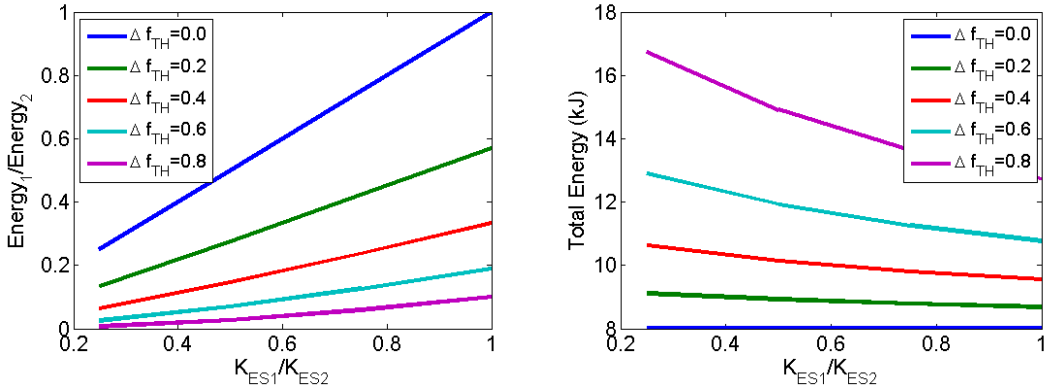

(a) Energy Share

(b) Total Energy

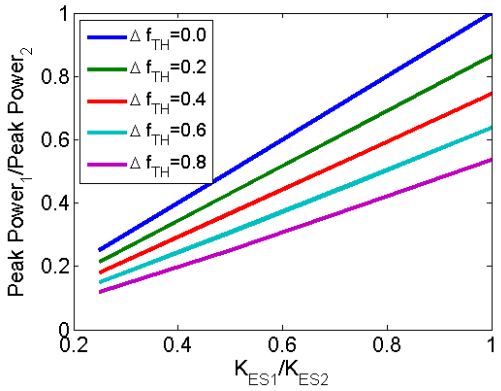

(c) Peak Power Share

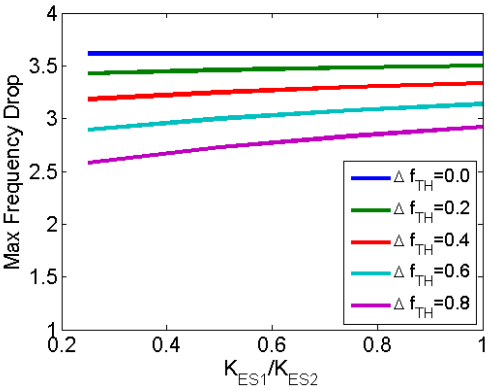

(d) Maximum Frequency Drop

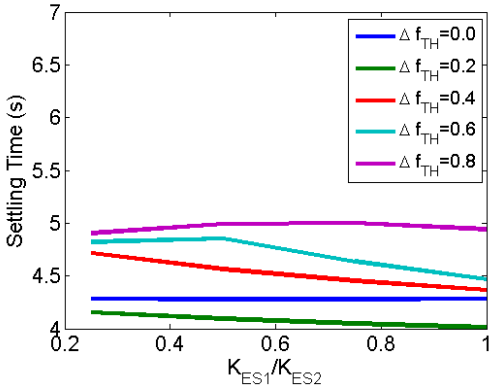

(e) Settling Time

Figure 7.5: Energy share, Total energy used, Power Share, maximum frequency drop, settling time when using two energy storage units with varying K_{ES} factor (i.e K_{ES1}/K_{ES2}) for different thresholds $\Delta f_{TH} = f_{TH2} - f_{TH2}$, while keeping $f_{TH1} = 49\ Hz$ and the sum of $K_{ES} = 30$.

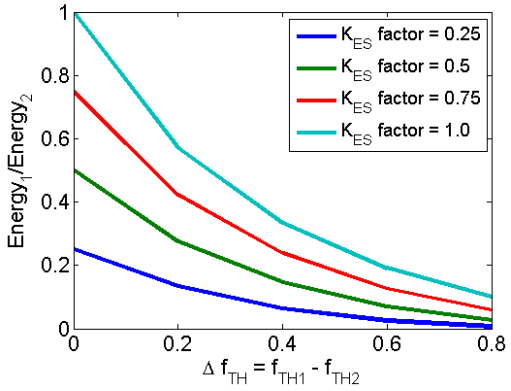

(a) Energy Share

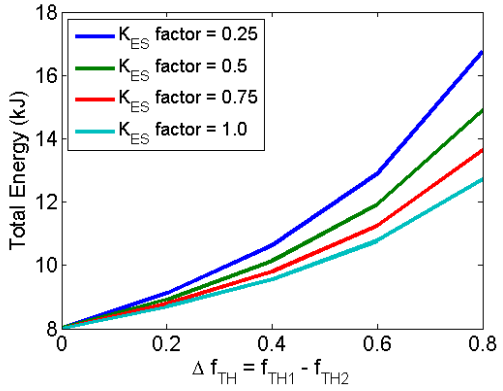

(b) Total Energy

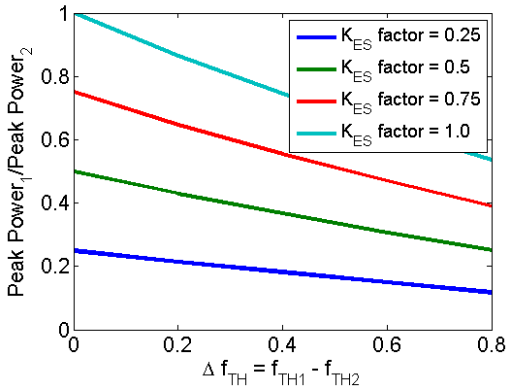

(c) Peak Power Share

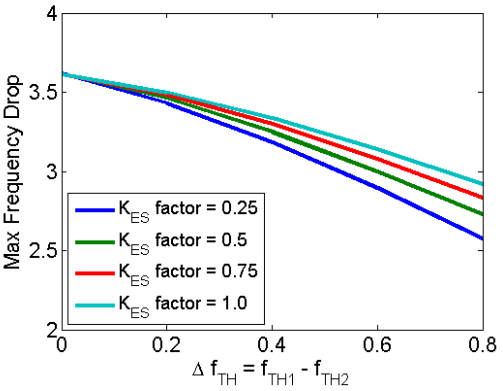

(d) Maximum Frequency Drop

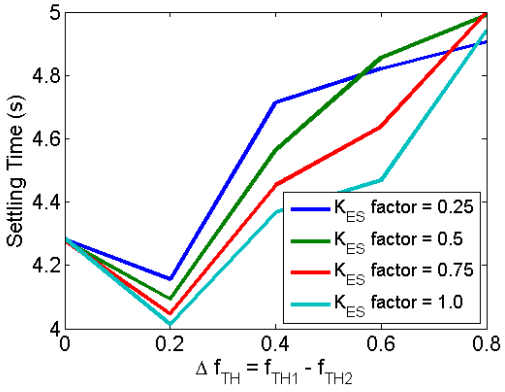

(e) Settling Time

Figure 7.6: Energy share, Total energy used, Power Share, maximum frequency drop, settling time when using two energy storage units with varying thresholds $\Delta f_{TH} = f_{TH2} - f_{TH2}$ for different K_{ES} factor (i.e K_{ES1}/K_{ES2}), while keeping $f_{TH1} = 49\ Hz$ and the sum of $K_{ES} = 30$.

According to Fig.7.6a, the energy share of the ES controller with a lower threshold becomes exponentially smaller when the threshold of the controller with higher threshold is raised. This is further aided if the lower threshold controller has a smaller K_{ES} share. As expected, the total energy shown in Fig.7.6b increases exponentially with the increase of the higher threshold. The peak power used on the other hand does not vary much with the threshold, but varies largely with K_{ES} as discussed for the single storage system.

The maximum frequency drop shown in Fig.7.6d is similar to the case where the frequency threshold of a single energy storage was varied, decreasing the frequency drop when one of the thresholds was increased. The frequency drop is further reduced when the K_{ES} share of the higher threshold controller is larger. The settling time in Fig.7.6e again shows similarity to the variation in settling time when the frequency threshold was varied.

In summary, multiple storage units when different frequency thresholds are used perform in between a single large system with the lower threshold and a single large system with the higher threshold. The K_{ES} share determines the bias towards one system or the other.

When the power ratings and the energy storage capacities of the energy storage units of a dual energy storage system are fixed, one can find the K_{ES}, f_{TH} values as follows. From Fig.7.5c and Fig.7.5b, a unique K_{ES} ratio and a Δf_{TH} that can satisfy the power rating ratio and the energy capacity ratio can be found out. The sum of K_{ES} values should be chosen so that the total energy used is less than the total capacity of the energy storage units. However, one has to make sure that the sum of K_{ES} does not violate the stability criterion. Hence, K_{ES1} and K_{ES2} values can be determined. From the specification of the allowable frequency drop in a given micro grid, one can decide the frequency threshold of the ES control, i.e the lower f_{TH}, hence completing the parameter selection of both storage units.

7.6 Conclusion

In this chapter, the performance of the energy storage control system was characterised when the frequency threshold was varied following the same conducted for varying K_{ES} in chapter 4. The discussion concluded that the frequency threshold shifts can shift the power frequency by approximately the

same amount, without observing a significant change in the peak power usage. Naturally, the total energy used increases and the settling time lengthens, when the threshold is raised. Varying the current threshold has expected variations of decreasing energy, increasing frequency drop and decreasing settling time, when the current threshold is reduced, since such a change makes the governor control more active.

When using multiple stores, it was understood that K_{ES} is additive once all storage units are triggered, even when the frequency thresholds of the controllers are different. The energy used by the controllers was shared according to the K_{ES} share between the controllers. Different shares of K_{ES} does not vary the maximum frequency drop and is only affected by frequency threshold changes. The settling time was the same for a system with different K_{ES} shares, as long as there is no variation in frequency thresholds. It was concluded that when using multiple storage units with different frequency thresholds, the resultant performance is in between a system with the lowest threshold and a system with the highest threshold within the multiple energy storage system. The exact behaviour depends on the K_{ES} share between the energy storage units.

CHAPTER 8

Conclusion

8.1 Conclusions of The Thesis

Weak electrical grids with distributed renewable energy resources suffer from regular off-nominal frequency excursions during load disturbances due to low system inertia. Supplementing system active power from an energy storage is one way of offering power system frequency support. This thesis describes a novel technique to dispatch active power from an independently controlled energy storage to constrain the system frequency within acceptable margins. This work identifies that supplying active power to support frequency to a level close but not equal to the nominal (i.e. a frequency threshold) is important, not only for the efficient use of energy storage but also for the unhindered operation of the speed governing of the power system to sustainably supply the load in the long run. These properties were realised by exploiting detected power system frequency as the main control input to the energy storage control. Due to this, the proposed energy storage control technique did not require dedicated intercommunication between the energy storage and the prime mover or among other power system elements.

The first objective was achieved by developing a proportional energy storage control using detected frequency as the control trigger in Chapter 4. The valuable property of power system frequency was employed in the control algorithm to indicate real time load-generation imbalance. The method was defined in such a way that the energy storage discharges when the frequency falls below the lower threshold (49 Hz) and charges when the frequency rises above the upper threshold (51 Hz), proportional to the frequency deviation from the threshold. Once the frequency is restored up to the threshold, the energy storage is

deactivated. In this way, the speed governor is provided with sufficient speed error for continuous operation. With the proposed ES control, the frequency could be recovered above the threshold within 3 s for the rated load disturbance of the 8kW microgrid and is well within the primary frequency response. As a consequence, the prime mover experiences less rigorous torque generation and smoother transition of active power supply from the energy storage to the speed governor controlled prime mover. The stability margin of the ES controller was found to depend upon the inertia of the grid and the inductive impedance at the PCC. However, these parameters can be pre-evaluated by means of regression analysis; hence have a minimal impact on the decoupling of the ES control from the host grid.

The second objective of identifying frequency detection requirements in order to replace power system frequency in the ES control algorithm with the detected frequency, was achieved in Chapter 4. The study revealed that the transient and the steady state response of the detected frequency should limit the ripple amplitude of the detected frequency to within $\Delta f \leq 0.5\ Hz$ and the transient delay of detection to within $T_d \leq 50\ ms$ in order to be sufficient for the optimum performance of the energy storage control. Three candidate frequency detection methods were compared under the same bandwidth specifically in weak electrical grid conditions to identify the best method in the Chapter 5. According to the comparison, the DSOGI-FLL was found to have the best performance in estimating frequency in a weak grid compared to a generalised DFT and the conventional SRF-PLL. A smoothing technique was developed for the DSOGI-FLL to mitigate the erroneous frequency dip occurring as a consequence of the weak grid voltage transients, which are a consequence of high inductive impedance. Also, the generalisation carried out on the modified DFT also showed competitive characteristics with accurate ROCOF estimation in power systems.

As a platform to design, develop and test the energy storage control technique and compare the frequency detection methods, a complete simulation model to replicate a worst-case weak grid was developed in Chapter 5, achieving the third objective. The model simulated speed control, automatic voltage regulation, harmonic distortion and effects of supply impedance derived from the observations made in a prototype 8 kW microgrid with resistive loads.

The fourth objective of validating the proposed method experimentally, using the 8 kW microgrid facility with a 70 Ah Li-ion battery energy storage was presented in Chapter 6. The experimental results showed a good proximity to

the simulated results including the stability margins deduced for loading and shedding of two resistive loads equivalent to 35% and 72% of rated loading.

In Chapter 7, general design rules for the ES control when applied as a singular entity or as multiple entities were discussed, achieving the final objective of this work. It was concluded that the main parameters of the ES control (i.e. K_{ES} and f_{TH}) may be varied to satisfy end users requirements, and hence determine the optimum sizing of the energy storage for a given power system.

8.2 Limitations and Future Work

This research is limited in certain ways, and some associated investigations may be suggested as future work to mitigate or eliminate these limitations. One clear limitation was that the harmonics and unbalances are created in the voltage during active power injection by the energy storage. Even though increasing the proportional gain K_{ES} of the ES control can offer benefits in frequency support by lessening the initial frequency drop followed by fast damped oscillations, the potential of using a higher K_{ES} is limited by the resulting distorted voltage waveform causing instability in the frequency support. An additional concurrent reactive power support to aid in voltage regulation may be suggested as future work to increase the practical stability margin of the proposed ES control.

Also, this work was developed for an agnostic energy storage technology, thus intentionally sidesteps from the inclusion of characteristics of the energy storage technology such as the state of charge. If the energy storage control is applied in a weak grid with continuous loading and load-shedding, a more in-depth analysis on the state of the energy storage may be beneficial for the uninterrupted application of the ES control. Therefore, the proportional control can be enhanced by considering additional parameters that are specific to energy storage technologies in the algorithm.

Moreover, this work may benefit from comparing the results with a method that uses direct speed to achieve frequency support as of [30]. Such an analysis can reveal the differences of using a plug-and-play technique as opposed to a generic method coupled to the host grid. Further, the technique as a whole should be extended to include effects of droop controlled power systems with multiple prime movers and multiple energy storage systems in order for this

system to be widely implemented.

Appendices

APPENDIX A

The Speed Signal Acquisition

The speed signal of the prime mover is accessible via the control board terminals panel available in the IM drive [8]. The control board panel facilitates data acquisition via digital and analogue outputs, as shown in Fig.A.1. Analogue output port C5 provides the speed-feedback signal as annotated in the figure.

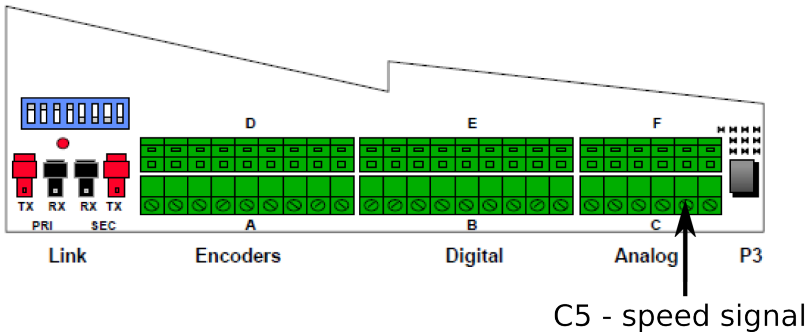

Figure A.1: User interface of the IM drive [8]

The speed feedback signal voltage is directly proportional to the rotor speed. In order to find the relationship between the speed and the voltage of the speed signal, several known speed points were set using the IM drive interface under no-load conditions and the voltage of the C5 terminal measured from the oscilloscope were recorded for each speed set point. These results are shown in Fig.A.2. By fitting these points to an equation of the form $y = mx + c$ we found that the relationship between the speed and the voltage signal is,

$$n = 201.5\ V_{ss} - 34.4255 \tag{A.0.1}$$

where n is the speed in rpm and V_{ss} is the speed signal voltage in V.

The resolution of the voltage signal is defined by the IM drive's digital to ana-

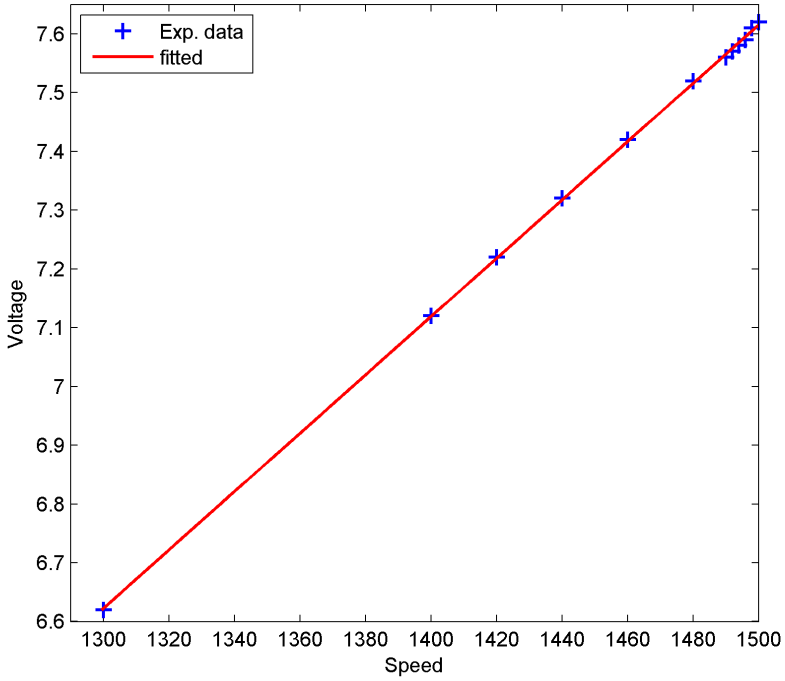

Figure A.2: Speed signal voltage recorded for IM drive speed set points (+) and a straight line fit (-)

logue converter's resolution as well as the resolution of the signal acquisition (i.e. oscilloscope). An oscilloscope (Tektronix® DPO 2024) was used to acquire the speed signal with a vertical scale of 500 mV/div, using a 1x probe.

In order to find the speed resolution, under no-load, the speed was increased linearly from zero up to 1500 rpm. During this time, the speed voltage signal was observed as shown in Fig.A.3.

From Fig.A.3, we can calculate the speed resolution the combined microprocessor and oscilloscope system is able to offer, using two adjacent voltage steps which define the maximum available resolution. This value was found to be $\Delta V_{ss} = 0.04V$. Using (A.0.1), the speed step was found to be,

$$\Delta n = 201.5\ \Delta V_{ss} = 8.06\ rpm$$

For a 4-pole synchronous generator the power frequency $f(Hz)$ can be calculated using,

$$f = \frac{np}{60} \tag{A.0.2}$$

where p is the number of pole pairs.

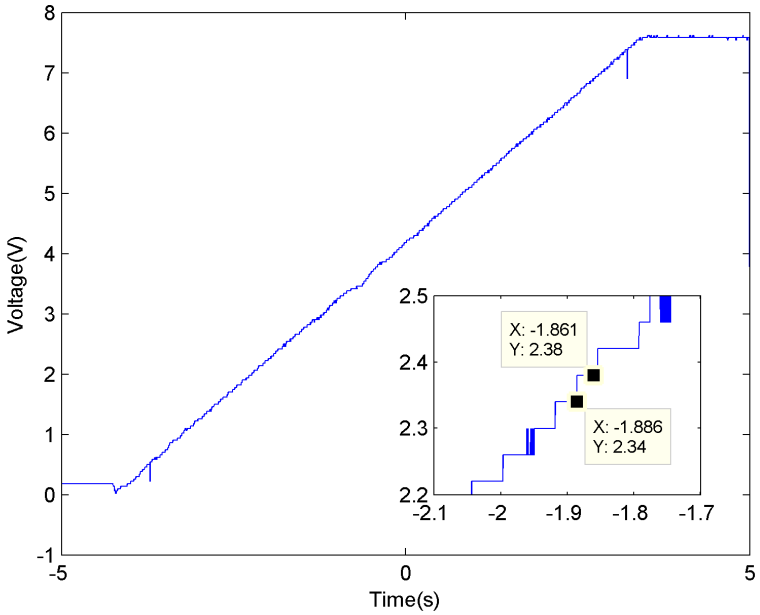

Figure A.3: Voltage measured with increasing speed in time [Inset : Zoomed in voltage in time]

Using this relationship we can write equation A.0.1,

$$f = 6.717\ V_{ss} - 1.1475 \tag{A.0.3}$$

In addition, the frequency step becomes,

$$\Delta f = 0.27\ Hz$$

Hence, the frequency resolution measured from the oscilloscope in the given scale taken from the IM drive speed feedback signal is 0.27 Hz.

References

[1] IA Erinmez, DO Bickers, GF Wood, and WW Hung. NGC experience with frequency control in england and wales-provision of frequency response by generators. In *Power Engineering Society 1999 Winter Meeting, IEEE*, volume 1, pages 590–596. IEEE, 1999.

[2] Youngho Cho, Jae Woong Shim, Seog-Joo Kim, Sang Won Min, and Kyeon Hur. Enhanced frequency regulation service using hybrid energy storage system against increasing power-load variability. In *Power and Energy Society General Meeting (PES), 2013 IEEE*, pages 1–5, July 2013. doi: 10.1109/PESMG.2013.6672784.

[3] PM Anderson and M Mirheydar. A low-order system frequency response model. *Power Systems, IEEE Transactions on*, 5(3):720–729, 1990.

[4] Alessandro Costabeber. *Advanced Control of Power Converters for Efficient Use of Distributed Energy Resources in Future Smart Microgrids*. PhD thesis, 2012.

[5] EMERSON Industrial Automation. Low voltage alternators - excitation and regulation systems shunt-pmg-arep. Technical report, Leroy Somer, 2013.

[6] Remus Teodorescu, Marco Liserre, and Pedro Rodriguez. *Grid converters for photovoltaic and wind power systems*, volume 29. John Wiley & Sons, 2011.

[7] Triphase. *Triphase PM15F42C Power Module*. http://www.triphase.be/.

[8] Eurotherm drives Ltd. *620 Vector Drive S/W Release 2.X - User Manual*, 2002.

[9] Leroy Somer. *Partner Alternators LSA 40 - 4 pole - Electrical and Mechnical Data*. Emerson Industrial Automation, www.leroy-somer.com, .

[10] Leroy Somer. *R220 A.V.R. Installation and Maintanance*, .

[11] J. Paska, P. Biczel, and M. Klos. Technical and economic aspects of electricity storage systems co-operating with renewable energy sources. In *Electrical Power Quality and Utilisation, 2009. EPQU 2009. 10th International Conference on*, pages 1–6, Sept 2009. doi: 10.1109/EPQU.2009.5318843.

[12] Egill Thorbergsson, Vaclav Knap, Maciej Swierczynski, Daniel Stroe, and Remus Teodorescu. Primary frequency regulation with li-ion battery based energy storage system - evaluation and comparison of different control strategies. In *Telecommunications Energy Conference 'Smart Power and Efficiency' (INTELEC), Proceedings of 2013 35th International*, pages 1–6, Oct 2013.

[13] National Grid Electricity Transmission plc. The grid code. Technical report, 2014.

[14] Olivia Leitermann. *Energy storage for frequency regulation on the electric grid*. PhD thesis, Massachusetts Institute of Technology, 2012.

[15] National Grid. Frequency response services, October 2014. URL `http://www2.nationalgrid.com/`.

[16] D Kottick, M Blau, and D Edelstein. Battery energy storage for frequency regulation in an island power system. *Energy Conversion, IEEE Transactions on*, 8(3):455–459, 1993.

[17] Tarek M Masaud, Keun Lee, and PK Sen. An overview of energy storage technologies in electric power systems: What is the future? In *North American Power Symposium (NAPS), 2010*, pages 1–6. IEEE, 2010.

[18] Energy Storage Association, February 2015. URL `http://www.energystorage.org/`.

[19] Irena Wasiak, Ryszard Pawelek, and Rozmyslaw Mienski. Energy storage application in low-voltage microgrids for energy management and power quality improvement. *Generation, Transmission & Distribution, IET*, 8(3): 463–472, 2014.

[20] Ioan Serban, Remus Teodorescu, and Corneliu Marinescu. Energy storage systems impact on the short-term frequency stability of distributed autonomous microgrids, an analysis using aggregate models. *IET Renewable Power Generation*, 7(5):531–539, 2013.

[21] John D Boyes. Overview of energy storage applications. In *Power Engineering Society Summer Meeting, 2000. IEEE*, volume 3, pages 1514–1516. IEEE, 2000.

[22] Sérgio Faias, Patrícia Santos, Jorge Sousa, and Rui Castro. An overview on short and long-term response energy storage devices for power systems applications. *system*, 5:6, 2008.

[23] Thomas Christen and Martin W Carlen. Theory of ragone plots. *Journal of power sources*, 91(2):210–216, 2000.

[24] M. Swierczynski, D.I Stroe, AI Stan, and R. Teodorescu. Primary frequency regulation with li-ion battery energy storage system: A case study for denmark. In *ECCE Asia Downunder (ECCE Asia), 2013 IEEE*, pages 487–492, June 2013. doi: 10.1109/ECCE-Asia.2013.6579141.

[25] DI Stroe, AI Stan, Robert Diosi, Remus Teodorescu, and Søren Juhl Andreasen. Short term energy storage for grid support in wind power applications. In *Optimization of Electrical and Electronic Equipment (OPTIM), 2012 13th International Conference on*, pages 1012–1021. IEEE, 2012.

[26] KC Divya and Jacob Østergaard. Battery energy storage technology for power systemsâĂŤan overview. *Electric Power Systems Research*, 79(4):511–520, 2009.

[27] Liang Liang, Jin Zhong, and Zaibin Jiao. Frequency regulation for a power system with wind power and battery energy storage. In *Power System Technology (POWERCON), 2012 IEEE International Conference on*, pages 1–6, Oct 2012. doi: 10.1109/PowerCon.2012.6401357.

[28] M.L. Lazarewicz and T.M. Ryan. Integration of flywheel-based energy storage for frequency regulation in deregulated markets. In *Power and Energy Society General Meeting, 2010 IEEE*, pages 1–6, July 2010. doi: 10.1109/PES.2010.5589748.

[29] Ning Lu, Mark R Weimar, Yuri V Makarov, FJ Rudolph, SN Murthy, Jim Arseneaux, and Clyde Loutan. Evaluation of the flywheel potential for providing regulation service in california. In *Power and Energy Society General Meeting, 2010 IEEE*, pages 1–6. IEEE, 2010.

[30] A Agbedahunsi, M Sumner, E Christopher, A Watson, A Costabeber, and R Parashar. Frequency control improvement within a microgrid, using

enhanced statcom with energy storage. In *Power Electronics, Machines and Drives (PEMD 2012), 6th IET International Conference on*, pages 1–6. IET, 2012.

[31] Rasool Aghatehrani, Rajesh Kavasseri, and Ravi Chandra Thapa. Power smoothing of the dfig wind turbine using a small energy storage device. In *Power and Energy Society General Meeting, 2010 IEEE*, pages 1–6. IEEE, 2010.

[32] MG Molina, PE Mercado, and EH Watanabe. Analysis of using facts controllers with superconducting magnetic energy storage in the primary frequency control of power systems. In *Transmission & Distribution Conference and Exposition: Latin America, 2006. TDC'06. IEEE/PES*, pages 1–7. IEEE, 2006.

[33] Susan M Schoenung and William V Hassenzahl. Long-vs. short-term energy storage technologies analysis. a life-cycle cost study. a study for the doe energy storage systems program. *Sandia National Laboratories*, 2003.

[34] Susan M Schoenung. Characteristics and technologies for long-vs. short-term energy storage. *United States Department of Energy*, 2001.

[35] John P Barton and David G Infield. Energy storage and its use with intermittent renewable energy. *Energy Conversion, IEEE Transactions on*, 19(2): 441–448, 2004.

[36] Robert H Lasseter. Microgrids. In *Power Engineering Society Winter Meeting, 2002. IEEE*, volume 1, pages 305–308. IEEE, 2002.

[37] M Perrin, YM Saint-Drenan, F Mattera, and P Malbranche. Lead–acid batteries in stationary applications: competitors and new markets for large penetration of renewable energies. *Journal of Power Sources*, 144(2):402–410, 2005.

[38] Prasanthi C Jayamaha. Assessment of technology requirements for off-grid rural electrification. Master's thesis, The University of Nottingham, 2009.

[39] International Electrotechnical Commission. White paper - electrical energy storage. *http://www.iec.ch/*, February 2015.

[40] IM Dudurych. Statistical analysis of frequency response of island power system under increasing wind penetration. In *Power and Energy Society General Meeting, 2010 IEEE*, pages 1–6. IEEE, 2010.

[41] Gauthier Delille, Bruno François, and Gilles Malarange. Dynamic frequency control support by energy storage to reduce the impact of wind and solar generation on isolated power system's inertia. *Sustainable Energy, IEEE Transactions on*, 3(4):931–939, 2012.

[42] Pascal Mercier, Rachid Cherkaoui, and Alexandre Oudalov. Optimizing a battery energy storage system for frequency control application in an isolated power system. *Power Systems, IEEE Transactions on*, 24(3):1469–1477, 2009.

[43] Wen Liang Zhang, Ming Qiu, and Xiao Kang LAI. Application of energy storage technologies in power grids [j]. *Power System Technology*, 7:004, 2008.

[44] Bo Yang, Yuri Makarov, John Desteese, Vilayanur Viswanathan, Preben Nyeng, Bart McManus, and John Pease. On the use of energy storage technologies for regulation services in electric power systems with significant penetration of wind energy. In *Electricity Market, 2008. EEM 2008. 5th International Conference on European*, pages 1–6. IEEE, 2008.

[45] MA Guerrero, E Romero, F Barrero, MI Milanés, and E González. Overview of medium scale energy storage systems. In *Compatibility and Power Electronics, 2009. CPE'09.*, pages 93–100. IEEE, 2009.

[46] Robert B Schainker. Executive overview: energy storage options for a sustainable energy future. In *Power Engineering Society General Meeting, 2004. IEEE*, pages 2309–2314. IEEE, 2004.

[47] Vaclav Knap, Rakesh Sinha, Maciej Jozef Swierczynski, Daniel Ioan Stroe, and Sanjay Chaudhary. Grid inertial response with lithium-ion battery energy storage systems.

[48] Alexandre Oudalov, Daniel Chartouni, and Christian Ohler. Optimizing a battery energy storage system for primary frequency control. *Power Systems, IEEE Transactions on*, 22(3):1259–1266, 2007.

[49] Costantino Citro, Alvaro Luna, Joan Rocabert, Raúl Santiago Munoz-Aguilar, Ignacio Candela, and Pedro Rodriguez. Overview of power processing structures for embedding energy storage in pv power converters. In *IECON 2011-37th Annual Conference on IEEE Industrial Electronics Society*, pages 2492–2498. IEEE, 2011.

[50] Alex Taiwo Agbedahunsi. *Frequency control for microgrids using enhanced STATCOM and supercapacitor energy storage*. PhD thesis, University of Nottingham, 2013.

[51] Rick Crispo and Ted KA Brekken. A motor-generator and supercapacitor based system for microgrid frequency stabilization. In *Technologies for Sustainability (SusTech), 2013 1st IEEE Conference on*, pages 162–166. IEEE, 2013.

[52] D.W.P. Thomas and Malcolm S. Woolfson. Evaluation of frequency tracking methods. *Power Delivery, IEEE Transactions on*, 16(3):367–371, Jul 2001. ISSN 0885-8977. doi: 10.1109/61.924812.

[53] M. Akke. Frequency estimation by demodulation of two complex signals. *Power Delivery, IEEE Transactions on*, 12(1):157–163, Jan 1997. ISSN 0885-8977. doi: 10.1109/61.568235.

[54] Pedro Rodriguez, Alvaro Luna, Mihai Ciobotaru, Remus Teodorescu, and Frede Blaabjerg. Advanced grid synchronization system for power converters under unbalanced and distorted operating conditions. In *IEEE Industrial Electronics, IECON 2006-32nd Annual Conference on*, pages 5173–5178. IEEE, 2006.

[55] Rubens M Santos Filho, Paulo F Seixas, Porfírio C Cortizo, Leonardo AB Torres, and André F Souza. Comparison of three single-phase pll algorithms for ups applications. *Industrial Electronics, IEEE Transactions on*, 55 (8):2923–2932, 2008.

[56] Pedro Rodriguez, Josep Pou, Joan Bergas, J Ignacio Candela, Rolando P Burgos, and Dushan Boroyevich. Decoupled double synchronous reference frame pll for power converters control. *Power Electronics, IEEE Transactions on*, 22(2):584–592, 2007.

[57] Tadeusz Lobos and Jacek Rezmer. Real-time determination of power system frequency. *Instrumentation and Measurement, IEEE Transactions on*, 46 (4):877–881, 1997.

[58] Elisabetta Lavopa, Pericle Zanchetta, Mark Sumner, and Francesco Cupertino. Real-time estimation of fundamental frequency and harmonics for active shunt power filters in aircraft electrical systems. *Industrial Electronics, IEEE Transactions on*, 56(8):2875–2884, 2009.

[59] M. Karimi-Ghartemani, A.R. Bakhshai, and M. Mojiri. Estimation of power system frequency using adaptive notch filter. In *Instrumentation and Measurement Technology Conference, 2005. IMTC 2005. Proceedings of the IEEE*, volume 2, pages 1494–1497, May 2005. doi: 10.1109/IMTC.2005.1604400.

[60] Masoud Karimi-Ghartemani and M Reza Iravani. A method for synchronization of power electronic converters in polluted and variable-frequency environments. *Power Systems, IEEE Transactions on*, 19(3):1263–1270, 2004.

[61] Houshang Karimi, Masoud Karimi-Ghartemani, and M Reza Iravani. Estimation of frequency and its rate of change for applications in power systems. *Power Delivery, IEEE Transactions on*, 19(2):472–480, 2004.

[62] Cheol-Hun Kim and Sang-Hee Kang. Frequency estimation algorithm based on dynamic phasor method in a power system. In *Advanced Power System Automation and Protection (APAP), 2011 International Conference on*, volume 1, pages 712–717, Oct 2011. doi: 10.1109/APAP.2011.6180491.

[63] Miroslav M Begovic, Petar M Djuric, Sean Dunlap, and Arun G Phadke. Frequency tracking in power networks in the presence of harmonics. *Power Delivery, IEEE Transactions on*, 8(2):480–486, 1993.

[64] Juan Carlos Rodríguez and Donald Grahame Holmes. A test bench for the evaluation of synchronisation techniques for grid-connected converters. In *Universities Power Engineering Conference (AUPEC), 2012 22nd Australasian*, pages 1–6. IEEE, 2012.

[65] Saeed Golestan, Mohammad Monfared, and Francisco D Freijedo. Design-oriented study of advanced synchronous reference frame phase-locked loops. *Power Electronics, IEEE Transactions on*, 28(2):765–778, 2013.

[66] Pedro Rodriguez, Alvaro Luna, Raúl Santiago Munoz-Aguilar, Ion Etxeberria-Otadui, Remus Teodorescu, and Frede Blaabjerg. A stationary reference frame grid synchronization system for three-phase grid-connected power converters under adverse grid conditions. *Power Electronics, IEEE Transactions on*, 27(1):99–112, 2012.

[67] Vikram Kaura and Vladimir Blasko. Operation of a phase locked loop system under distorted utility conditions. In *Applied Power Electronics Conference and Exposition, 1996. APEC'96. Conference Proceedings 1996., Eleventh Annual*, volume 2, pages 703–708. IEEE, 1996.

[68] N Hoffmann, R Lohde, M Fischer, FW Fuchs, L Asiminoaei, and PB Thogersen. A review on fundamental grid-voltage detection methods under highly distorted conditions in distributed power-generation networks. In *Energy Conversion Congress and Exposition (ECCE), 2011 IEEE*, pages 3045–3052. IEEE, 2011.

[69] Binita Sen, Dushyant Sharma, and B Chitti Babu. Dsrf and sogi based pll-two viable scheme for grid synchronization of dg systems during grid abnormalities. In *Engineering and Systems (SCES), 2012 Students Conference on*, pages 1–6. IEEE, 2012.

[70] Siyu Gao and Mike Barnes. Phase-locked loop for ac systems: Analyses and comparisons. 2012.

[71] P Rodriguez, L Sainz, and J Bergas. Synchronous double reference frame pll applied to a unified power quality conditioner. In *Harmonics and Quality of Power, 2002. 10th International Conference on*, volume 2, pages 614–619. IEEE, 2002.

[72] Pedro Rodriguez, Remus Teodorescu, I Candela, Adrian Vasile Timbus, M Liserre, and F Blaabjerg. New positive-sequence voltage detector for grid synchronization of power converters under faulty grid conditions. In *Power Electronics Specialists Conference, 2006. PESC'06. 37th IEEE*, pages 1–7. IEEE, 2006.

[73] A Nicastri and A Nagliero. Comparison and evaluation of the pll techniques for the design of the grid-connected inverter systems. In *Industrial Electronics (ISIE), 2010 IEEE International Symposium on*, pages 3865–3870. IEEE, 2010.

[74] Masoud Karimi-Ghartemani, Houshang Karimi, and M Reza Iravani. A magnitude/phase-locked loop system based on estimation of frequency and in-phase/quadrature-phase amplitudes. *Industrial Electronics, IEEE Transactions on*, 51(2):511–517, 2004.

[75] Eric Jacobsen and Richard Lyons. The sliding dft. *Signal Processing Magazine, IEEE*, 20(2):74–80, 2003.

[76] MS Reza, M Ciobotaru, and VG Agelidis. Tracking of time-varying grid voltage using dft based second order generalized integrator technique. In

Power System Technology (POWERCON), 2012 IEEE International Conference on, pages 1–6. IEEE, 2012.

[77] MS Padua, SM Deckmann, GS Sperandio, FP Marafão, and D Colon. Comparative analysis of synchronization algorithms based on pll, rdft and kalman filter. In *Industrial Electronics, 2007. ISIE 2007. IEEE International Symposium on*, pages 964–970. IEEE, 2007.

[78] Hatem A Darwish and Magdy Fikri. Practical considerations for recursive dft implementation in numerical relays. *Power Delivery, IEEE Transactions on*, 22(1):42–49, 2007.

[79] Aurobinda Routray, Ashok Kumar Pradhan, and K Prahallad Rao. A novel kalman filter for frequency estimation of distorted signals in power systems. *Instrumentation and Measurement, IEEE Transactions on*, 51(3):469–479, 2002.

[80] PK Dash, AK Pradhan, and G Panda. Frequency estimation of distorted power system signals using extended complex kalman filter. *Power Delivery, IEEE Transactions on*, 14(3):761–766, 1999.

[81] Adly A Girgis and William L Peterson. Adaptive estimation of power system frequency deviation and its rate of change for calculating sudden power system overloads. *Power Delivery, IEEE Transactions on*, 5(2):585–594, 1990.

[82] DWP Thomas and MS Woolfson. Voltage and current phasor estimation during abnormal conditions for transmission line protection schemes. 1997.

[83] Zoran Salcic, Zhenguo Li, UD Annakkage, and Nalin Pahalawaththa. A comparison of frequency measurement methods for underfrequency load shedding. *Electric power systems research*, 45(3):209–219, 1998.

[84] LR Limongi, R Bojoi, C Pica, Francesco Profumo, and Alberto Tenconi. Analysis and comparison of phase locked loop techniques for grid utility applications. In *Power Conversion Conference-Nagoya, 2007. PCC'07*, pages 674–681. IEEE, 2007.

[85] Prabha Kundur, Neal J Balu, and Mark G Lauby. *Power system stability and control*, volume 7. McGraw-hill New York, 1994.

[86] Magnetic. *Asynchronous vectorial servomotors MA series*.

[87] Norman S Nise. *Control systems engineering*. Benjamin-Cummings Publishing Co., Inc., 1991.

[88] V. Backmutsky, D. Kottick, B. Shklyar, M. BIau, and V. Zmudikov. Comparison of methods and algorithms for accurate frequency trend estimation following emergency transients in power systems. In *Athens Power Tech, 1993. APT 93. Proceedings. Joint International Power Conference*, volume 1, pages 271–274, Sep 1993. doi: 10.1109/APT.1993.686883.

[89] Ieee application guide for ieee std 1547(tm), ieee standard for interconnecting distributed resources with electric power systems. *IEEE Std 1547.2-2008*, pages 1–217, April 2009. doi: 10.1109/IEEESTD.2008.4816078.

[90] Simon S Haykin. *Adaptive filter theory*. Pearson Education India, 2008.

[91] Gene F Franklin, Michael L Workman, and Dave Powell. *Digital control of dynamic systems*. Addison-Wesley Longman Publishing Co., Inc., 1997.